THE UNIVERSITY OF CHICAGO

WATER AND PROTONS CONFINED IN ACIDIC ZEOLITES STUDIED WITH BROADBAND 2D IR SPECTROSCOPY

A DISSERTATION SUBMITTED TO

THE FACULTY OF THE DIVISION OF THE PHYSICAL SCIENCES

IN CANDIDACY FOR THE DEGREE OF

DOCTOR OF PHILOSOPHY

DEPARTMENT OF CHEMISTRY

BY

JOHN HARVARD KOLM HACK

CHICAGO, ILLINOIS

AUGUST 2023

Contents

List of Figures

List of Tables

Acknowledgments

Several people have contributed to making the work in this thesis possible. First, I would like to thank my advisor Andrei Tokmakoff for his support and guidance over the past six years. Andrei has a unique capacity for delivering feedback that is at one encouraging, while simultaneously highlighting the staggering amount of work left to do. In all seriousness, Andrei is an extraordinary scientist and a skilled communicator, and I have learned a great deal from him. Perhaps even more importantly, he is a supportive mentor who prioritizes the intellectual development of his students and provides the freedom to explore our scientific interests.

In the lab, I owe much of my knowledge and capabilities to the mentorship of Nick Lewis and Memo Carpenter, who trained me when I joined the group. Nick's wealth of technical knowledge and experience with ultrafast optics were invaluable to me in my first few years of graduate school. Throughout my PhD Nick has been a source of advice and support, and the group is fortunate to have him as a permanent member as a Research Assistant Professor. I first met Memo Carpenter when I was a prospective student, and the opportunity to work with him was a major contributing factor in my choice to attend the University of Chicago. Memo's enthusiasm and curiosity were a source of inspiration during my first three years of graduate study, and he set an excellent example for how to be a thoughtful, rigorous, and conscientious scientist.

I have had the pleasure of working with several other outstanding colleagues in the Tokmakoff group. In the water lab, I overlapped briefly with Joe Fournier who kept the group active, and for a few years with Bogdan Dereka whose scientific abilities are matched only by his photography skills. More recently, the number of water-polymer interfaces in the water lab has increased substantially with the addition of Sam Knight and Liv Mumma, who are taking the project in exciting new directions. I have also learned a great deal from my co-workers who study molecules

with more than three atoms, especially Sam Penwell, Paul Sanstead, Chi-Jui Feng, Yumin Lee, Lukas Whaley-Mayda, Brennan Ashwood, Ram Itani, Abhirup Guha, Melissa Bodine, Seung Yeon Lee, and anyone else not mentioned. Thank you all for your scientific insights and camaraderie over the years, and thanks to those who edited parts of this thesis.

I would like to thank my scientific collaborators from other research groups who contributed greatly to the work in this thesis and to my development as a scientist. The ultrafast IR studies on zeolites would not have been possible without the synthetic work of James Dombrowski and Yaxin Chen in Harold Kung's group at Northwestern University. And, the insight gained from those experiments was greatly enhanced by the simulation work of Xinyou Ma in Greg Voth's group at the University of Chicago. Many details and discoveries were worked out over video calls with Xinyou, James, and Yaxin, and those discussions helped keep me motivated while stuck at home during the COVID-19 pandemic.

I would also like to acknowledge the support of several others in my professional life at UChicago. In particular, I would like to thank Professors Ka Yee Lee and Sarah King for their advice and support, and for serving as members of my thesis committee. I would also like to thank Dr. Britni Ratliff for everything she taught me about being an effective teacher. I had the excellent opportunity to work with her as a TA during my 5th year, and her program is a boon to the Chemistry department for both undergraduate education and the pedagogical training of graduate students.

Outside of the scientific work, I would like to express my love and gratitude for my wife and partner Tatiana Hernandez Press. Her sense of humor, intellectual curiosity, and adventurous spirit ensure that our life together is always exciting. I would like to thank my family for their love and support, especially my parents Tina Kolm and Greg Hack, my sister Thea Hack, and my grandpa

Harvard Kolm. Finally, thanks to Richard Richey and Mike McKay for their continued friendship over the years.

I would like to thank the U.S. Department of Energy, Office of Basic Energy Sciences, and the Advanced Materials for Energy-Water Systems (AMEWS) Center for funding. Thanks to the Department of Chemistry at the University of Chicago for support during my 6th year through the Otto H. and Valerie Windt Memorial Fellowship.

Abstract

Acid-base chemistry is foundational to many chemical and biological processes. As chemists we often define acid strength in terms of acid dissociation equilibria, a description which is well-suited to aqueous solution where acid behavior is mediated by the extended hydrogen (H)-bonding network of liquid water. This description becomes complicated when considering solid acid sites in porous materials, since the extended H-bonding network of water is disrupted under confinement. Zeolites provide an ideal system for studying this behavior, where Brønsted acid sites (BAS) are present inside the regular, molecule-sized pores of these materials. Since zeolites are widely used acid catalysts, a molecular description of their acidity is highly relevant to several industrial processes including emerging bio-renewable processes where water is often present. However, many molecular details of zeolite-water interactions are not well understood. Central questions regarding the protonation state of the hydrated zeolite system, the extent and structure of water's disrupted H-bonding network inside small pores, and the evolution of these properties with increasing hydration had not been previously addressed experimentally.

The structure and protonation state of water at zeolite Brønsted acid sites were investigated over a wide range of hydration per BAS using infrared (IR) spectroscopy, which is sensitive to the H-bonding environment of water molecules. Several structural characteristics including anharmonic couplings, excited-state energies, and bond orientations were revealed with femtosecond two-dimensional IR (2D IR) spectroscopy, which had not been previously applied to this system. Measuring high-quality nonlinear spectra required several adaptations to the experimental design to mitigate artifacts from highly-scattering zeolite particles.

These spectroscopic studies present a detailed experimental characterization of water and protons under tight confinement near solid acid sites. When a single water molecule is adsorbed at

the BAS, the proton remains localized on the acid site displaying an IR spectrum with two broad bands centered near 2500 cm^{-1} and 2850 cm^{-1}. While the origin of this doublet feature has been a longstanding mystery, the 2D IR spectrum provides new experimental evidence to constrain the problem. Based on the relative frequencies and intensities of excited-state absorptions, we propose a model proton-transfer potential with excited-state tunneling, which is consistent with the experiment. As the hydration increases, new vibrational features appear corresponding to hydrated protons and water O-H bonds in various environments. Analysis of these features showed that the BAS is deprotonated in the presence of two or more water molecules, with the hydration saturating at approximately 8 H_2O molecules per BAS.

Finally, while 2D IR spectroscopy has proven to be an insightful tool for studying the structure and dynamics of water and protons, some information content is limited by the broad linewidths of these systems – relative to the bandwidth of available mid-IR laser pulses. To expand our 2D IR capabilities, we report the design and operation of a new light source which extends the mid-IR pulse bandwidth to ~1000 cm^{-1} with sufficient energy to excite molecular vibrations. The source is implemented in 2D IR experiments, demonstrating simultaneous excitation and detection across a broad range of mid-IR frequencies.

Chapter 1

Introduction

1.1. The relevance of zeolite-water interactions

The world today has been shaped in many ways by heterogeneous catalysis technology. In one example, over a fourth of world food production uses fertilizer generated by the Haber-Bosch process, where an iron or ruthenium-based solid catalyst converts nitrogen in the air into more readily-usable ammonia.[1–3] In another example, modern automobile transportation is enabled by heterogeneous catalysis, used to produce gasoline by cracking long-chain hydrocarbons, or synthesis from small molecules like methanol or carbon monoxide and hydrogen.[4,5] Furthermore, the toxicity of vehicle emissions from burning gasoline is greatly reduced by the catalytic converter. Adopted thanks to emissions regulations, these devices contain a mixture of precious metals including Pt, Pd, and Rh which oxidize CO and reduce NO_x in the exhaust of the internal combustion engine.[6]

Among the most prolific heterogeneous catalysts in industrial chemical synthesis are a class of materials called zeolites. Zeolites are crystalline aluminosilicates which can be prepared with Brønsted acid sites located inside molecular-sized pores.[7] They are used as acid catalysts in several reactions including the isomerization, cracking, and alkylation of hydrocarbons.[8–11] These are crucial steps in fossil hydrocarbon processing, which accounts for over 80% of energy

consumption worldwide[12] and the production of nearly all monomers used in plastics.[13] The zeolite ZSM-5, pictured in Fig. 1.1, is among the most widely used and studied zeolites in these processes. Originally developed by Mobil corporation in 1965 (ZSM stands for Zeolite Socony Mobil), its industrial applications include cracking of long-chain hydrocarbons in fuels production,[5] alkylation of benzene, xylene isomerization, and methanol-to-gasoline processes.[9]

Today, the existential challenge facing chemists and chemical engineers is the re-design of the industrial chemical processing system, to develop alternative synthetic routes for producing fuels and plastics from bio-renewable sources. Despite their sometimes-oily past, zeolites are poised to play an important role in these emerging synthetic processes,[14–18] where their catalytic and size-exclusion properties provide the same advantages as in fossil fuel applications. In particular, ZSM-5 has been identified as a promising catalyst for breaking down cellulose and other bio-feedstocks,[19,20] conversion of waste products like glycerol,[21] and upgrading of chemical intermediate molecules to higher-value products.[22]

Like all zeolites, ZSM-5 is composed of a collection of Si and Al atoms located in tetrahedral sites (T-sites), each coordinated to four oxygen atoms. These chemically simple building blocks can be arranged in a variety of ways, leading to variations in morphology and pore structure.[23] Nearly 250 different zeolite structures have been identified – some synthetic and some naturally occurring – each with a 3-letter code assigned by the International Zeolite Association.[24] For example, the 10-T-site pores of ZSM-5 (MFI) have a diameter of 5.5 Å, with the straight channels along the [010] dimension intersecting zig-zag channels along the [001] dimension.[25]

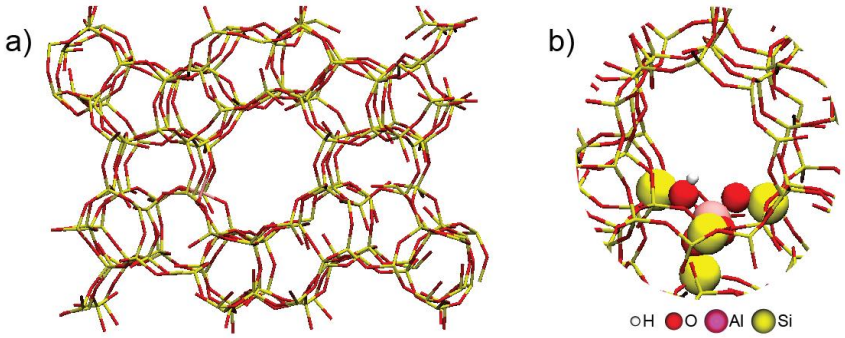

Figure 1.1. (a) Structure of zeolite ZSM-5 viewed along the [010] axis with two unit cells displayed. (b) Brønsted acid site with the Al atom, neighboring O and Si atoms, and acidic H atom emphasized using their van der Waals sizes. Images were rendered from a molecular dynamics simulation described in Chapter 6. White, H; red, O; Pink, Al; Yellow, Si.

Many of the useful properties of zeolites arise from their porosity on the molecular scale, with sizes ranging from ~2-10 Å depending on the number of T-sites at the pore opening. This makes them highly effective molecular sieves, able to efficiently separate small molecules based on relative size.[26–28] In chemical reactions, this size discrimination can lead to enhanced selectivity towards desired products. For example, in the acid-catalyzed disproportionation of methyl benzene the rapid isomerization rate often leads to a roughly equal mixture of o-, m-, and p-xylene. Though, the selectivity to the linear p-xylene can be greatly increased (to >80% over the bent isomers) by taking advantage of the difference in diffusivity through the small pores of a modified ZSM-5 catalyst.[10,29]

The catalytic properties of zeolites arise from the presence of Brønsted acid sites (BAS) at interfaces inside the pores. A BAS can occur at each T-site where Si is substituted for Al, which introduces a charge imbalance in the lattice. The excess negative charge from the Al atom is shared primarily between the four coordinated oxygen atoms, and is balanced with an extra-framework cation. The charge-balancing cation can assume many identities, and the ion-exchange capabilities

of zeolites have led to applications as ion-exchange membranes and as water softeners in detergents.[9,24,30] When the charge is balanced with H^+, the proton resides on one of the oxygen atoms neighboring Al, forming a Brønsted acid site at the bridging Al-O(H)-Si bond. An example BAS in HZSM-5 (H denoting the proton form) is displayed in Fig. 1.1b.

The density of Brønsted acid sites in a proton-form zeolite is therefore controlled by the Si:Al ratio. Nearest-neighbor Al sites are unstable, so this ratio is always greater than unity,[31] and BAS occur uniformly as Al-O(H)-Si. This uniformity of the acid sites is reflected in their acid strength, defined by the free energy of deprotonation in the absence of a solvent or other molecules. Using this definition, electronic structure calculations showed that the deprotonation energy of 1201 kJ/mol was independent of framework type, pore size, and local geometry like Al-O-Si bond angle.[32] Since this value is comparable to acids like HI (1294 kJ/mol) and H_2SO_4 (1264 kJ/mol),[33] zeolites are often referred to as strong Brønsted acids.[34,35]

While the deprotonation energy can be cleanly defined in a vacuum, the situation becomes rapidly more complex when even a single molecule is present at the acid site. This is reflected in experimental measures of zeolite acid strength, such as the adsorption enthalpy of a base like NH_3 or pyridine. In that case, confinement effects and van der Waals interactions between the adsorbate and zeolite lattice lead to differences in interaction strength across framework sites and pore sizes, as well as the size and chemical composition of the adsorbate.[34–36] In the context of acid catalysis the situation is complicated further, since the activity of the BAS as a catalyst depends on additional factors like the stabilization of intermediates, which are reaction-specific and do not necessarily correlate with other measures of acid strength.[34,35]

This raises definitional questions about the nature of acidity in the context of solid acids. What does it mean for a solid Brønsted acid site to be strong, and how does this differ from acidity in other systems? In aqueous solution, Brønsted acid strength is defined by the ability to donate a proton to bulk liquid water, quantified by the equilibrium constant for dissociation into an aqueous proton and conjugate base. In that context, the interactions between water, protons, and acid molecules are inherent to the definition of acid strength, and acid behavior is mediated by the extended H-bonding network of liquid water. In a zeolite pore, water cannot form an extended H-bonding network, but the interactions between water, protons, and zeolite acid sites can perhaps provide a basis for describing the acidity of solid acid sites.

Additionally, the molecular interactions between water and zeolite BAS are highly relevant to applications in emerging bio-renewable technologies. Compared to their fossil counterparts, bio-derived feedstocks like cellulose contain much more oxygen and therefore produce significant amounts of water in catalytic decomposition.[15] Water may also be present during reactions as a co-reactant[37] or solvent[38] in catalytic processes relevant to bio-renewable processing. This poses a challenge for the design and mechanistic description of these processes, since the role of water in zeolite-catalyzed reactions is not well understood. There are many factors to consider, with an interplay between water-zeolite and water-reactant interactions that modulate the nuclear and electronic re-arrangements occurring during chemical reaction.

Experimental and theoretical studies have shown that water can have a substantial effect on zeolite activity in a variety of chemical transformations. For example, the addition of water increased the selectivity to ring-opening products by ~50% in the ring-opening reaction of naphthalene over zeolite HY.[37] Water was also found to inhibit the zeolite-catalyzed dehydration

reactions of both propanol and cyclohexanol, but for different reasons. In propanol dehydration over HZSM-5, water stabilized the adsorbed propanol molecule, increasing the activation barrier.[39] While, in cyclohexanol dehydration over HBEA water molecules adsorbed preferentially, forming protonated water clusters with lower catalytic activity than the dry BAS.[40] In a study of C-H bond activation, the reaction rate was substantially promoted with the addition of small amounts of water (~1 H_2O / BAS), but suppressed at higher water loadings.[41] We observed a similar promotional effect at low water loadings in our own studies of methanol dehydration over HZSM-5, led by our collaborators in the research group of Harold Kung.[42]

To begin to unravel this behavior, we must first understand the basic molecular-scale interactions between water molecules and the zeolite BAS in the absence of complications from other adsorbates or chemical reactions. Central questions include: how do water molecules arrange near the solid acid under confinement? Where does the proton, or excess proton charge, go? And how do these properties depend on the number of water molecules present at the BAS? The scope of this thesis is aimed at investigating these questions, with the goal of providing a foundation for future studies on the role of water in zeolite-catalyzed reactions. While the chemical environment is quite different, the well-studied systems of liquid water and aqueous acid will provide valuable points of comparison. In the rest of this chapter, I will outline the principles of vibrational spectroscopy on H-bonding systems – which will be the primary tool used in these investigations – and an overview of the current literature on the hydration behavior of zeolite Brønsted acid sites.

1.2. O-H bond vibrations sense the H-bonding environment

1.2.1. Conventional H-bonds and Badger's rule

Addressing the foundational questions about water and proton structure at the interface of acidic zeolites requires experiments which are sensitive to the environment of a water molecule on the length scale of a chemical bond. In H_2O, intermolecular interactions are dominated by hydrogen (H)-bonding, and in zeolites the O-H bond at the BAS can donate a H-bond to adsorbed molecules.[43] The strength of a given H-bond is reflected in the frequency of the O-H stretch vibration, which can be measured directly by the absorption of infrared (IR) light. For this reason, vibrational spectroscopy has been used extensively to study the structure and dynamics of water molecules in a variety of environments including gas phase clusters,[44,45] the liquid phase,[46–48] concentrated electrolyte solutions,[49,50] the air-water interface,[51,52] and the surface of solid acids including zeolites.[43,53–56]

To relate the O-H stretch frequency to its molecular environment, consider a simplified representation of a H-bond from donor D-H to acceptor A, pictured schematically in Fig. 1.2a. This picture defines two distances of interest: the intramolecular D-H distance r_{DH} and the intermolecular donor-acceptor distance R_{DA}. In conventional H-bonds, the potential across r_{DH}, $V(r_{DH})$, can be described qualitatively with a double-well shape, as shown in Fig. 1.2b. The large barrier for proton transfer localizes the H atom in the potential well closer to the donor, with equilibrium value r_0 defined by the potential minimum. Near that minimum the potential is approximately harmonic, so I will refer to potentials with this qualitative shape as "weakly anharmonic."

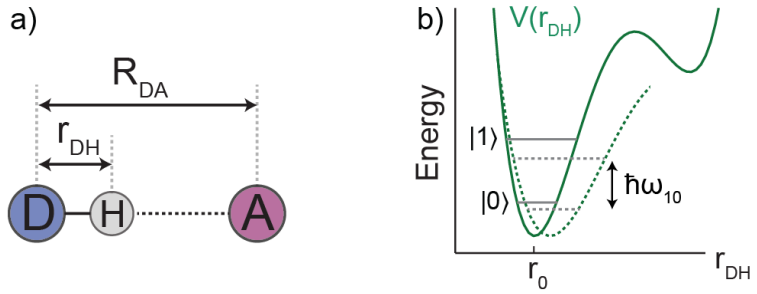

Figure 1.2. (a) Definition of H-bonding distances between donor (D), acceptor (A), and hydrogen (H) atoms. (b) Model potential across r_{DH} for a conventional H-bond. Dashed lines display a stretched potential, with increased equilibrium r_{DH} distance r_0.

The vibrational frequency of the O-H bond is determined by the potential. This connection is made explicit by solving the Schrödinger equation using the potential, returning energy eigenstates and wavefunctions. The fundamental transition frequency is defined by the difference between energies of the ground and first excited states, $\omega_{10} = (E_1 - E_0)/\hbar$. More intuitively, the vibrating bond can be pictured through the classical analogy of two masses, m_D and m_H, connected by a spring with force constant k_{DH}. In the harmonic limit, the vibrational frequency is given by $\omega_{DH} = \sqrt{k_{DH}/\mu_{DH}}$, where μ_{DH} is the reduced mass. Here, the vibrational frequency is connected to the potential through the force constant, which is defined as the second derivative of the potential evaluated at the minimum position r_0. In the classical analogy, it is clear that stretching the potential to increase r_0 corresponds to a lower force constant, and therefore a red-shift in the frequency as depicted with dashed lines in Fig. 1.2b.

This classical relationship between increasing equilibrium r_{DH} and decreasing vibrational frequency holds up well in practice. In fact, there is a well-established linear relationship with a negative slope between r_{DH} and ω_{10}, commonly referred to as Badger's rule.[57] For O-H stretch

vibrations in particular, this relationship has been shown to apply over a wide range of H-bond acceptors and H-bonding strength in both experiments and simulations.[58,59] Notably, the correlation applies not only between the harmonic frequency and the equilibrium value r_0 but also between the more experimentally-relevant anharmonic frequency and $\langle r_{OH} \rangle$, which is the proton position averaged over the vibrational motion.[58] This is the basis for the structural sensitivity of vibrational spectroscopy: the vibrational frequency reports on aspects of the shape of the potential, and correlates well with the D-H bond distance under most conditions.

1.2.2. Vibrational frequency and H-bonding strength

While Badger's rule relates the D-H stretch frequency to r_{DH}, it does not explain the connection between vibrational frequency and R_{DA}, which is one measure of the H-bonding strength. Typically, upon H-bonding the attractive force between the electronegative acceptor and the H atom causes an extension of the D-H bond, weakening D-H (decreasing k_{DH}) and causing the frequency to red-shift. This is the case for proper H-bonds, where D-H is highly polarized (e.g. D = O, F, or N). However, a blue-shift has been observed in improper H-bonds (e.g. D = C), where the H-bond instead causes the mildly-polarized D-H bond to contract.[60]

The characteristic red-shift with proper H-bonding can be observed for H_2O in Fig. 1.3, where the IR absorption spectrum is displayed for neat liquid H_2O and H_2O monomers in the non-H-bonding solvent acetonitrile (MeCN). The non-H-bonded O-H stretch of H_2O/MeCN vibrates with center frequencies 3550 cm^{-1} and 3610 cm^{-1}, and red-shifts to 3400 cm^{-1} in H_2O where approximately 84% form H-bonds to other water molecules at ambient temperature.[61] In the H_2O spectrum, a small high-frequency shoulder is observed from the 16% of H-bonds that are broken transiently.[62]

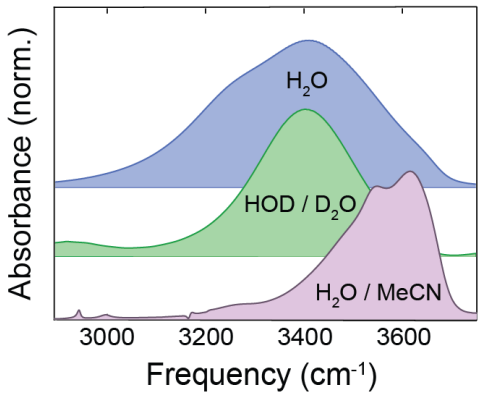

Figure 1.3. Infrared absorption spectra of H_2O monomers in acetonitrile (MeCN) with solvent background subtracted, 2% isotopically dilute HOD in D_2O, and neat liquid H_2O.

Notably, the O-H vibrations of H_2O are more complicated than the local-mode picture described in Fig. 1.2. Intramolecular coupling causes mixing between the local O-H stretch vibrations into symmetric and asymmetric normal modes. The ~60 cm^{-1} splitting between those two bands of non-H-bonded O-H stretch is resolved in the spectrum of water monomer in MeCN (Fig. 1.3). In neat H_2O, both intra- and inter-molecular coupling are significant,[46] causing the stretching vibration to extend over ~12 O-H bonds with approximately degenerate frequencies.[63] Among other effects, this vibrational delocalization washes out the resolution of symmetric and asymmetric bands in the IR spectrum and contributes to the broad absorption linewidth. Since these effects can complicate the interpretation, it is often useful to also study isotopically dilute HOD in D_2O. Since the H-bonded O-D stretch is red-shifted by ~900 cm^{-1}, the dilute O-H stretch of HOD is largely decoupled from the surrounding O-D vibrations and the local mode picture is more appropriate. Figure 1.3 shows that the O-H stretch vibration in dilute HOD is centered at the same frequency as in H_2O, reflecting the same average H-bonding strength in both systems.

1.3. Vibrational anharmonicity and the need for nonlinear spectroscopy

1.3.1. Coupled vibrations

The vibrations of O-H bonds can deviate significantly from simple harmonic motion, which complicates the relationship between the IR spectrum and the H-bonding environment but also encodes additional information. This leads to several anharmonic effects including dipole-forbidden excitations from the ground state to overtone or combination bands, coupling to lower-frequency vibrations including Fermi resonances, and excitonic delocalization as mentioned in the previous section. Without additional information, it can be difficult to identify these anharmonic effects or to distinguish them from dipole-allowed fundamental transitions in linear absorption spectra. While spectral simulations are invaluable, accurately capturing the shape of anharmonic vibrational potentials can require high-level, computationally expensive electronic structure methods.[64,65] On the other hand, capturing the static and dynamic disorder in the liquid phase requires molecular dynamics simulations,[66] which can only achieve reasonable statistics when integrated with less expensive density functional theory.[67]

Therefore, experiments which are sensitive to anharmonic effects are crucial for unraveling the complicated spectroscopy of H-bonding systems. In an infrared pump-probe (transient absorption) measurement, a pulse of infrared light excites the fundamental 0-1 transition of a resonant vibration, and a second light pulse probes the change in absorption at a later time. At short pump-probe delays, a decrease in absorption is observed at ω_{10} from the depletion of the ground state and stimulated emission, while an increase in absorption is observed at ω_{21} due to excited-state absorption. Therefore, transient absorption spectroscopy provides sensitivity to the

anharmonicity of a single vibration through the ratio of ω_{21}/ω_{10}. This ratio is less than unity for typical, weakly-anharmonic potentials such as the one pictured in Fig. 1.2.

Transient absorption spectroscopy is also sensitive to coupling between vibrations in the form of cross-peaks. These signatures are most commonly characterized in two-dimensional (2D) spectroscopy, where both pump (excitation) and probe (detection) frequencies are resolved in a pump-probe measurement.[68,69] A cross-peak appears when one vibration is excited and a change is absorption is observed at the frequency of a second vibration. Often, cross peaks come in the form of bleaching at the second frequency along with an increase in absorption corresponding to the excitation of a combination band.[68,70]

The 2D IR spectrum of isotopically dilute HOD/D_2O, Fig. 1.4, captures both the anharmonicity of the O-H stretch and the anharmonic coupling between O-H stretch and HOD bend.[71] When the O-H stretch is pumped at 3400 cm^{-1} both the fundamental and excited state transitions are measured in the 2D IR spectrum, with $\omega_{21}/\omega_{10}<1$ as expected for a conventional H-bond. Stretch-bend coupling is measured by the decreased absorption at the bend frequency of 1450 cm^{-1} after pumping the O-H stretch. In particular, these vibrations are coupled through Fermi resonance between the stretch fundamental and bend overtone, which is revealed by the 2D IR spectrum.[71] The excited state absorption near a detection frequency of ~2900 cm^{-1} arises from excitation of the bend overtone after pumping the stretch, and a small band can be observed at the same frequency in the linear absorption spectrum. This Fermi resonance is more prominent in the IR spectrum of H_2O (Fig. 1.3), since the H_2O bend is higher in frequency at ~3200 cm^{-1} and therefore closer to resonance with the O-H stretch. In both cases, the dipole-forbidden bend overtone appears in the linear IR spectrum due to anharmonic coupling to the bright O-H stretch.

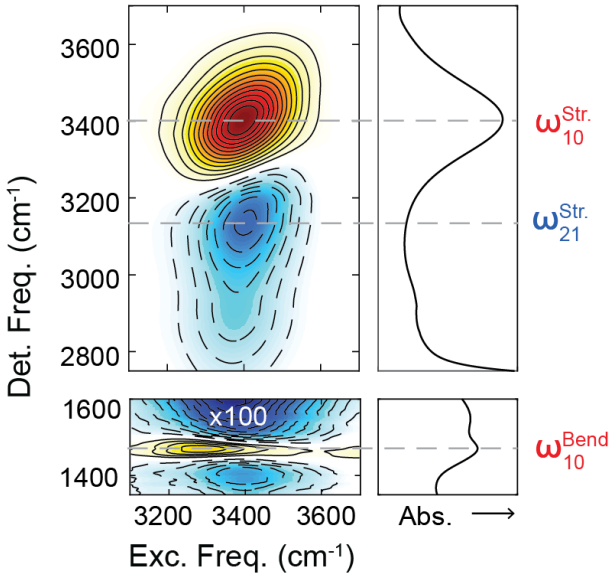

Figure 1.4. 2D IR spectrum of isotopically dilute HOD/D_2O at 100 fs pump-probe delay following excitation of the O-H stretch at 3400 cm^{-1}. Decreased absorption is plotted in red, increased absorption in blue. The spectrum at lower detection frequency is scaled for visualization. The linear absorption spectrum is plotted on the right. Center frequencies of the stretch fundamental (ω_{10}^{Str}), excited state absorption (ω_{21}^{Str}), and bend fundamental (ω_{10}^{Bend}) are denoted. The 2D IR spectrum is replotted with permission from De Marco, L.; Ramasesha, K.; Tokmakoff, A. *J. Phys. Chem. B* **2013**, *117* (49), 15319–15327. © 2013 American Chemical Society.

1.3.2. Short, strong H-bonds

In addition to coupling with other vibrations, the O-H stretch vibration itself can become highly anharmonic, particularly when participating in strong H-bonds with short donor-acceptor distances R_{DA}. In short, strong H-bonds (SHBs), the wavefunction overlap between H and A increases, leading to electronic redistribution across the bond and increased covalent character.[72–74] H-bonds of this type have been observed or inferred in enzymatic catalysis[72,73] ligand binding,[75] proton transport,[76] and aqueous ion solvation.[74,77,78] Strong H-bonds are often associated with systems where the H atom carries excess positive charge, which strengthens the electrostatic attraction to

electronegative donor and acceptor atoms. This is the case in aqueous acids, where the H-bonding environment is strengthened on average in the vicinity of the excess proton.[64,77–81]

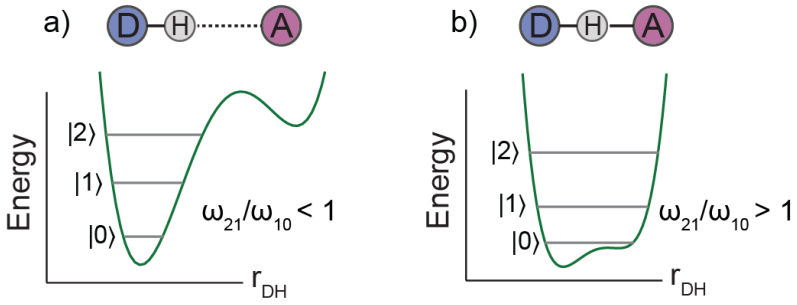

Figure 1.5. Model potentials representing (a) conventional and (b) short, strong H-bonds.

For sufficiently short H-bonds, the conventional relationship between H-bonding length and vibrational frequency breaks down, and we must return to the more direct relationship between O-H stretch potential and vibrational frequency to describe the spectroscopy. In the context of H-bonding solids, semiempirical models have been developed to describe the H-bonding potential as a function of R_{DA} and r_{DH} (as defined for a H-bond in Fig. 1.2).[82,83] In those models, decreasing R_{DA} causes the potential to transition from the conventional high-barrier, double well shape to a low-barrier single well. In this SHB potential, the proton-transfer barrier can decrease below the zero-point energy, and Pauli repulsion between H and A leads to a steep confining wall in the potential.[74,78,81] Example model potentials for these two limits are displayed in Fig. 1.5. Applied to liquid phase systems, these models provide a useful qualitative picture for the expected potential shape, and low-barrier single-well potentials have been observed in simulations of strong H-bonding systems in liquids.[65,74,81]

While the transition from conventional to SHB is accompanied by red-shifting as the potential well widens, it is not clear that the potential shapes depicted in Fig. 1.5 can be distinguished by

linear absorption spectroscopy alone. However, these distinct potential motifs can be distinguished by the ratio of ω_{21}/ω_{10} which is readily measured in 2D IR spectroscopy. In the SHB potential, the steep walls lead to quantum confinement with $\omega_{21}/\omega_{10} > 1,$ compared to $\omega_{21}/\omega_{10} < 1$ in the conventional H-bond potential.

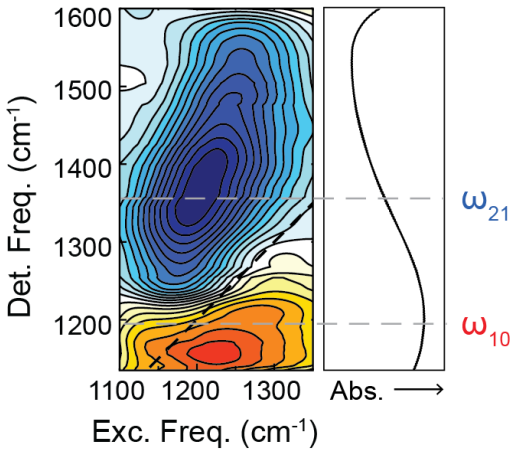

Figure 1.6. 2D IR spectrum of 2M HCl at 100 fs pump-probe delay following excitation of the proton stretch at 1200 cm^{-1}, with the corresponding spectrum of H_2O subtracted. Decreased absorption is plotted in red, increased absorption in blue. The linear absorption difference spectrum is plotted on the right. Center frequencies of the proton stretch fundamental (ω_{10}) and excited state absorption (ω_{21}) are denoted. The 2D IR spectrum is replotted with permission from Fournier, J. A.; Carpenter, W. B.; Lewis, N. H. C.; Tokmakoff, A. *Nat. Chem.* **2018**, *10*, 932–937. © 2018 Springer Nature.

A striking example of this inverted anharmonicity was measured in the 2D IR spectroscopy of aqueous HCl.[77,78] In this system, the excess aqueous proton becomes closely associated with nearby water molecules, and displays a broad vibration centered at 1200 cm^{-1} arising from the stretching motion of the proton between flanking oxygen atoms.[64,65,81] Exciting this proton stretch vibration resulted in intense absorption changes with a clear ratio $\omega_{21}/\omega_{10} > 1,$ shown in Fig. 1.6.[78] While the proton stretch vibration is complicated by coupling to nearby O-H bonds,[64,66] an inverted

anharmonicity ratio was also observed in the 2D IR spectrum of the F-H stretch of aqueous bifluoride (HF_2^-).[74] Both of these observations demonstrated experimentally that the H-bonding potential can assume a highly anharmonic shape when the H-bonding length is shortened, and that this is a crucial consideration when considering the IR spectroscopy of acids interacting with water.

1.4. IR spectroscopy of water at zeolite Brønsted acid sites

1.4.1. The singly-hydrated Brønsted acid site

Given the molecular-scale information content encoded in the vibrational spectrum, it is perhaps not surprising that IR spectroscopy has been among the most widely used techniques for studying water at zeolite Brønsted acid sites, alongside NMR spectroscopy and neutron scattering.[84,85] However, the subtle details of water O-H stretch spectroscopy and the substantial role of anharmonicity have not always been fully considered, and the advantages of 2D IR spectroscopy had not been applied prior to the work described in Chapter 5.[86]

Early IR studies of water in proton-form zeolites focused primarily on the low-hydration limit, where ≤ 1 water molecule is present on average per BAS.[53,54,87] In those studies, the hydration level was controlled through the partial pressure of water in the gas phase. The IR absorption spectra of HZSM-5 prepared with 1 equivalent (equiv.) H_2O/BAS and without any water present are displayed in Fig. 1.7. These spectra were collected from samples prepared with an *ex situ* hydration method described in Chapter 6, and display the same absorption features as the *in situ* hydrated samples reported in the literature. The dehydrated zeolite displays a prominent absorption peak at 3610 cm^{-1} from the non-H-bonded (NHB) O-H stretch of the BAS, with a narrow bandwidth of 50 cm^{-1} FWHM. This band does not appear when H^+ is substituted for Na^+,[88] and the

intensity grows linearly with Al content in the proton-form.[89] The band at 3720 cm^{-1} arises from the O-H stretch of terminal silenols, Si-OH. These are surface defects occurring from the curvature of finite zeolite crystals, and the intensity of this band correlates negatively with crystal size.[89] The sharp transitions sit atop a broad, low-intensity background centered near 3200 cm^{-1}, which has been attributed to a small fraction of BAS which form internal H-bonds to oxygen within the framework.[90,91]

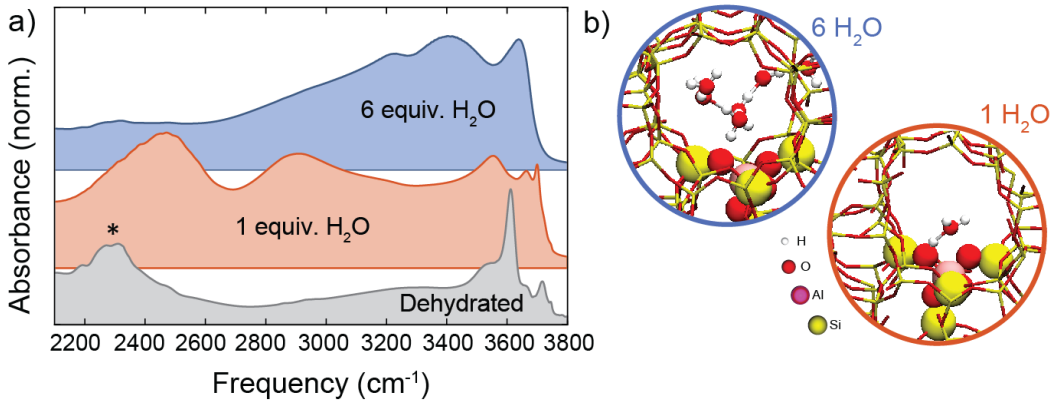

Figure 1.7. (a) Experimental IR absorption spectra of HZSM-5 with 0, 1, and 6 equiv. H_2O/BAS, normalized to their local maxima. The asterisk marks an artifact from the C-F overtone of oils used in the experiment. (b) Representative structures of 1 and 6 H_2O molecules equilibrated at the BAS of HZSM-5 from molecular dynamics simulations. Spectra and simulations were collected with the methods described in Chapter 6.

The IR absorption spectrum in the O-H stretch region changes dramatically with the addition of a single water molecule per Brønsted acid site, as shown in Fig. 1.7a. For reference, the structure of a singly-hydrated BAS is displayed in Fig. 1.7b, from a molecular dynamics simulation described in Chapter 6. In the experimental spectrum, the most prominent feature is a broad doublet with bands centered at 2500 cm^{-1} and 2850 cm^{-1}. These bands are dramatically broader than the sharp O-H stretch feature in dehydrated HZSM-5, each with a bandwidth exceeding 200 cm^{-1} and together spanning nearly 1000 cm^{-1} FWHM. In the higher-frequency NHB O-H stretch region,

there is a decrease in absorption at 3610 cm^{-1} as the zeolite BAS red-shifts upon H-bonding to the adsorbed water molecule. Additional, somewhat broader features appear in this region at both higher and lower frequencies than 3610 cm^{-1}, which can be attributed to NHB O-H stretching of the adsorbed water molecule.[92] These have been assigned to different environments of the two water O-H bonds, with the lower frequency 3550 cm^{-1} band shifted via a weak coordination to oxygen atoms in the lattice, relative to the free O-H bond at 3700 cm^{-1}.[92,93] Alternatively, they could be attributed to symmetric and asymmetric splitting through intramolecular coupling, like the case of water monomer in acetonitrile.

Based on the IR spectrum, Jentys *et* al. initially suggested that the singly-adsorbed water molecule deprotonates the BAS, forming a hydronium ion which donates an H-bond back to the deprotonated lattice.[53,54] They reasoned that an electronically neutral configuration would result in a single red-shifted BAS O-H stretch, while multiple vibrations of the hydronium ion could explain the multiple bands observed. An alternative hypothesis was proposed by Pelmenschikov *et* al., in which the doublet bands at 2500 cm^{-1} and 2850 cm^{-1} both arise from the H-bonded BAS which remains protonated in the presence of a single water molecule.[94,95] In that picture, the BAS O-H stretch is red-shifted by H-bonding and split into the doublet bands through Fermi resonance with the O–H–O bend overtone across the H-bond from BAS to adsorbed water.

Sauer and co-workers investigated this question with quantum chemistry calculations, finding that the electronically neutral complex was both more stable and had better spectral agreement with experiment compared to the protonated water molecule.[96,97] While the computed harmonic normal mode spectrum did not reproduce the experiment for either configuration, only the neutral cluster displayed any spectral density in the region of the doublet, with the BAS O-H stretch falling

in the range of 2600-2900 cm^{-1}.[97] Additional support for the neutral model came from an experimental study using ^{18}O labeling to distinguish between vibrations originating from BAS O-H and water O-H.[98] While no shift was observed in the doublet bands with ^{18}O labeled water, this is a somewhat difficult experiment to interpret since the O-H frequency shifts from oxygen labeling are small. Based on the reduced mass, the difference in frequency between a ^{16}O-H and ^{18}O-H stretch is only ~0.3%, corresponding to an ~8 cm^{-1} shift (at a center frequency of 2500 cm^{-1}) compared to a linewidth of >200 cm^{-1}.

The crucial experimental evidence on the protonation state of singly-hydrated zeolite BAS came from IR absorption studies where a series of H-bond acceptors were adsorbed at the BAS of HZSM-5, HY, and HMOR.[43,99] The same doublet feature was observed in the IR spectrum when adsorbed water was replaced with other H-bond acceptors including methanol, dimethyl ether (DME), and tetrahydrofuran (THF).[43] Therefore, the doublet bands must originate in some way from the O-H stretch vibration of the H-bonded BAS, since they appear with molecules like DME and THF which have no intramolecular O-H bonds. Around the same time, a series of studies reached a similar conclusion about HSAPO-34, a material where alternating P and Al atoms occupy T-sites in a zeolitic lattice. In that material, similar bridging Si-O(H)-Al Brønsted acid sites are formed at Si-substitution sites, which also remain protonated in the presence of a single water molecule according to neutron scattering experiments.[85,100,101]

1.4.2. The protonation state at elevated hydration

While the protonation state of the zeolite BAS is well-established in the presence of a single water molecule, a complete picture of protonation at elevated hydration has remained elusive. As additional water molecules accumulate at the BAS the propensity for deprotonation increases,

since larger clusters are better able to stabilize and solvate the excess charge.[102–104] In the gas phase, the calculated proton affinity increases from 166 kcal/mol for a single water molecule to 199 and 212 kcal/mol for the water dimer and trimer, respectively.[102] While these values do not account for van der Waals forces, confinement effects, or other complicating factors in the zeolite, the trend suggests that there is likely a minimum water cluster size above which the proton is stabilized on the water cluster.

The question of proton speciation at elevated hydration has been investigated thoroughly from the perspective of theory and simulation. While most simulation studies found that the BAS is protonated in the presence of 1 H_2O and deprotonated in the presence of 3 H_2O, there is broad disagreement over the protonation state of the adsorbed water dimer. Depending on the level of theory, definition of the protonation state, and treatment of nuclear quantum effects, various studies have concluded that the protonated BAS,[55,105] protonated water cluster,[106] or both[97,107–110] are stable species when 2 H_2O molecules are adsorbed.

Early simulation studies compared the energetics of optimized structures with different protonation states using electronic structure theory at the level of Hartree-Fock (HF), Møller-Plesset (MP2), and/or density functional theory (DFT).[97,106,110] Limited by computing power at the time, these studies truncated the zeolite lattice at 3 T-sites and mapped the energetics of only a few configurations. With increased computing power and the ability to perform mixed quantum-classical simulations, more recent *ab initio* molecular dynamics (AIMD) have captured a much larger configurational space.[108,109] In these studies, the statistics sampled over the MD trajectory were used to construct a free energy surface as a function of local or collective variables. Liu and Mei defined the protonation state by the nuclear coordinates of the H atoms,[108] while

Grifoni *et* al. used a spatial partitioning to assign the proton to an O atom.[109,111] Both studies concluded that there is an equilibrium between protonated BAS and protonated water dimer states, with roughly equal energetics and a low barrier for proton transfer.

Despite the extensive simulation literature, quantitative experimental studies at elevated hydration have been limited and largely unable to assess information about the protonation state. One practical challenge is quantitative control over the average hydration level. In most studies, this was controlled *in situ* by varying the water vapor pressure or temperature in contact with a zeolite pellet.[43,53,55,87] In the vapor pressure approach, the amount of adsorbed water must be inferred from a second gravimetric measurement, while the temperature approach induces temperature-dependent shifts in IR features in addition to the desired changes in hydration. Another challenge is the fact that the experimentally-prepared hydration level is always an average over a distribution of microscopic hydration states. This is not a problem when studying the singly-hydrated state, since the IR spectrum of dehydrated zeolite can be easily measured. But, it is not possible to isolate the spectroscopic signature of the adsorbed doublet, triplet, etc.

In addition to the practical experimental challenges, changes in the IR spectrum with increasing hydration can be difficult to interpret. Figure 1.7 displays the IR spectrum of 6 equiv. H_2O in HZSM-5, which has prominent high-frequency bands centered near 3400 cm^{-1} and 3650 cm^{-1} from water-water H-bonds and water NHB O-H stretch, respectively. At this hydration level, the broad doublet bands do not appear, but there is a broad continuous absorption extending to lower frequencies. Since the spectral features are broad and overlapping, it is not straightforward to identify spectral signatures associated with different protonation states or a clear transition between them as the hydration is increased. In a recent hydration-dependent IR study, spectral

changes were interpreted using calculated harmonic normal mode vibrations from DFT optimized structures.[55] Though, this approach for describing the highly-anharmonic water and acid vibrations should be considered with caution for the reasons discussed in Section 1.3.

1.4.3. The high hydration limit

As the number of water molecules at the BAS increases, the extent of H-bonding network formation and the structural arrangement of molecules under confinement is perhaps just as interesting as the protonation state. In the absence of hydrophilic Al T-sites, the zeolite pores are highly hydrophobic, as might be expected for a silica-based material. In fact, elevated pressures are required to introduce water molecules into the pores of Silicalite-1 (MFI structure with all T-sites occupied by Si).[112,113] When acid sites are present, the water uptake is proportional to the concentration of Al T-sites.[113,114] These observations suggest that there may be a maximum cluster size under saturated water conditions, limited by the hydrophobicity of the pores away from Al T-sites. An alternative hypothesis could involve water wire formation extending through the pores, akin to the water structure in carbon nanotubes with comparable pore diameters.[115]

This topic has been investigated primarily through bulk water adsorption studies, characterizing the heat of adsorption as a function of average water adsorbed per acid site.[87,113,114] Most recently, Eckstein *et* al. found that water adsorption in HZSM-5 saturated at approximately 7 equiv. H_2O, independent of Al content over a range of Si:Al from 15 – 110.[113] At that elevated water loading, the heat of adsorption per water molecule decreases to the heat of liquefaction, 45 kJ/mol, suggesting that water uptake in the pores is limited by condensation on the surface of the crystal. *Ab initio* simulations suggest that the changing heat of adsorption is driven by proton stabilization, which evens out for clusters larger than ~4 H_2O.[109] Interestingly, that picture implies

that the maximum cluster size of ~7-8 H_2O is not determined by pore size or structure, and should be independent of zeolite framework.

The extent of H-bond network formation and cluster size can be further investigated using IR spectroscopy, which provides molecular scale detail lacking in calorimetric adsorption measurements. These topics are important considerations in catalysis, since the presence of water and formation of protonated water clusters have been shown to modulate the adsorption thermodynamics of other molecules.[113,116,117]

1.4.4. A closer look at the broad doublet feature

From a spectroscopic perspective, perhaps the most intriguing mystery related to zeolite hydration is the vibrational assignment of the broad doublet feature in the spectrum of 1 equiv. H_2O (Fig. 1.7). Similar broad doublet features have also been observed in O-H and N-H vibrations of H-bonded systems including KH_2PO_4, $NaH_3(SeO_3)_2$, and other solids,[118] acetic acid[119,120] and phosphinic acid[121] heterodimers in the liquid, and trimethylamine heterodimers in the gas phase.[122] The common theme appears to be relatively strong H-bonding, with shorter Donor-Acceptor distances than between water molecules in the bulk liquid. In several cases, it has been shown that the doublet feature is sensitive to the H-bonding strength, modulated over a series of H-bond acceptors. In the case of zeolite BAS, the doublet does not appear when CO is adsorbed, which has a much lower proton affinity compared to H_2O.[43,123] A similar behavior was observed for trimethylamine in the gas phase, where the doublet appeared in heterodimers with H_2O and alcohols, but not with weaker proton acceptors like CO or Ar.[122]

Historically, two explanations have been considered which could plausibly explain the origin of these doublet features in strong H-bonding systems. The first, which was briefly mentioned

earlier, is Fermi resonance coupling between the O-H stretch vibration and the overtone of the O-H-O bend (Fig. 1.8a). In that picture, the O-H stretch is red-shifted to a center frequency of ~2700 cm^{-1} and broadened dramatically through coupling to lower frequency vibrations such as O-O stretching. It is split into two bands through coupling to the O-H-O bend overtone, which is much narrower and also centered near 2700 cm^{-1}. The doublet bands are quantum-mechanical mixtures of stretch fundamental and bend overtone, and equal mixtures in the case of perfect resonance. This concept has a long history, dating back at least to Evans who proposed this form of Fermi resonance splitting to explain broad vibrational transitions in the condensed phase.[124] In the context of strong H-bonding systems, both Hadzi[118] and Claydon and Shepherd[125] suggested the assignment to bend overtone, noting the frequencies of bend fundamentals in various H-bonding systems with doublet features. Based on these previous studies, Pelmenschikov *et* al. interpreted the doublet in hydrated zeolite BAS as Fermi resonance.[94,95]

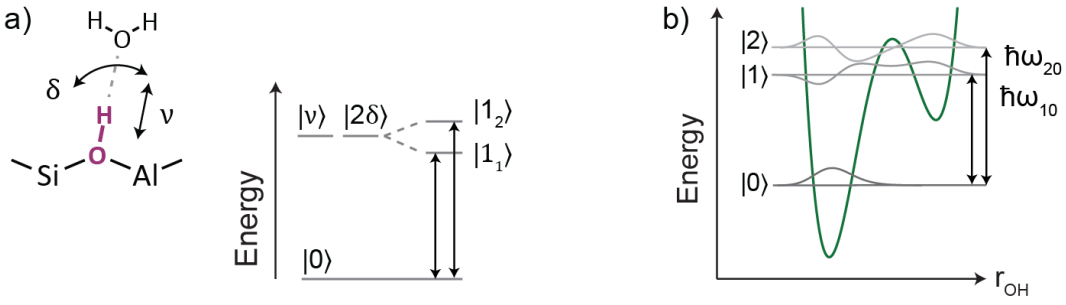

Figure 1.8. Schematic representations of proposed assignments for the doublet IR feature in 1 equiv. H_2O/BAS. (a) Fermi resonance mixing between zeolite O-H stretch ν and O-H-O bend overtone 2δ, forming mixed states $|1_1\rangle$ and $|1_2\rangle$ with a splitting of ~350 cm^{-1}. (b) An asymmetric double well O-H stretch potential, where tunneling in the first two excited states $|1\rangle$ and $|2\rangle$ leads to a splitting of ~350 cm^{-1}.

In an alternative picture, it was proposed that the doublet bands could arise from transitions on a double-well H-bonding potential with tunneling in the excited state.[118,126] This idea was

motivated in part by the semiempirical model for the H-bond potential developed by Lippincott and Schroeder.[82,83] When the double-well potential assumes an appropriate shape, the first and second excited states become nearly-degenerate, with wavefunctions that are approximately symmetric and antisymmetric combinations of states localized on the "left" and "right" wells (Fig. 1.8b). In these configurations the barrier height exceeds the first and second excited state energies, so this mixing occurs by tunneling. Somorjai and Horning explored this possibility using a quartic function, showing that the 0-1 and 0-2 transitions can fall in the range of the experimental doublet band frequencies for appropriate instantiations of the potential.[126]

Despite extensive study for over half a century, no experimental evidence has been found which can distinguish definitively between these two proposed pictures. One reason is that the two models predict a similar qualitative behavior in the linear absorption spectrum. The disappearance of the doublet with weak H-bond acceptors like CO can be explained by either model, since the blue-shifted O-H stretch becomes off-resonance with the bend overtone, and the proton transfer barrier increases substantially in weaker H-bonds. Another difficulty is that accurately modeling the shape of the highly-anharmonic potential requires complex computations using high-level electronic structure,[64,65] and the vibrational spectrum is not approximated well by harmonic normal mode calculations. So, neither the anharmonic bend overtone frequency nor the anharmonic tunneling potential have been captured in simulations of the zeolite BAS.

Despite a lack of definitive evidence to support one model over the other, the Fermi resonance interpretation has become widely accepted in the literature on zeolite hydration.[43,55,84,92,97,99,123] This is based largely on the fact that the O-H-O bend fundamental vibrates at the correct frequency for Fermi resonance mixing – roughly half the frequency at the local minimum between doublet

bands.[95,97] Though, that observation only suggests the Fermi resonance assignment is plausible, not necessarily that it is correct. Much like the previous studies on strong H-bonding in aqueous acid described in Section 1.3, this is a problem where 2D IR spectroscopy can provide valuable insight from its sensitivity to vibrational anharmonicity.

1.5. Thesis outline

This chapter motivated the relevance of water-zeolite interactions for industrial catalysis and emerging biorenewable technologies, outlined the current state of the field, and described some of the ways that linear and nonlinear infrared spectroscopy can deepen our understanding about the molecular-scale details of this intriguing system. In the rest of this thesis, I will describe how we have applied these techniques to address longstanding mysteries regarding the water speciation, protonation state, and spectroscopic assignments discussed in Section 1.4.

Chapter 2 describes the theoretical underpinnings of TA and 2D IR spectroscopy using the framework of time-dependent perturbation theory. Emphasis is placed on the details necessary for understanding and interpreting the experiments presented in later chapters. In particular, signal intensity, line broadening mechanisms, relaxation processes, polarization anisotropy, and 2D IR cross peaks are discussed.

Chapter 3 describes the experimental implementation of femtosecond TA and 2D IR spectroscopy and the instrumentation used for broadband spectral coverage across large portions of the mid-IR frequency range. The challenges associated with measuring broad vibrational transitions and scattering samples are discussed, and I describe the steps taken to capture scatter-free 2D IR spectra of highly-scattering zeolite particles without the use of pulse shaping.

Chapter 4 describes the development of a new mid-IR source for femtosecond pulses, which extends our capabilities for broadband excitation in 2D IR spectroscopy. This source was developed in parallel with the zeolite experiments, and the implications for future studies of water and protons in zeolites or other environments are discussed.

Chapter 5 details the first reported 2D IR measurements of hydrated zeolite, collected in the high-hydration limit. The 2D IR spectroscopy, with support from AIMD simulations, is used to assign spectral features in the linear absorption spectrum at elevated hydration levels. Using a signature of intramolecular coupling in the 2D IR spectrum, the speciation of water molecules in different H-bonding environments is calculated. We find good agreement with the statistics from simulations of protonated water octamer in HZSM-5, providing detailed molecular support for the saturation point at ~8 H_2O molecules per BAS. The shape of these water clusters and the disrupted H-bonding network under tight confinement in zeolite pores are explored.

Chapter 6 describes our investigation of the protonation state as a function of water loading by quantitative preparation and analysis of IR spectra with varying hydration. The many experimental challenges described in Section 1.4.2 are overcome with a combination of a quantitative zeolite hydration methodology, spectral decomposition, thermodynamic modeling, and comparison to hydration trends in 2D IR spectra. Distinct IR spectral signatures corresponding to protonated BAS and protonated water cluster are identified, and their hydration dependence is analyzed. The results show that two water molecules are sufficient to fully deprotonate the BAS with a deprotonation energy of approximately 1.6 kcal/mol, providing quantitative experimental insight into this longstanding question. Using the experimental result as a point of comparison, new AIMD

simulations are presented which provide further information about the extent of proton delocalization and location within the water cluster as a function of hydration level.

Finally, Chapter 7 details our investigation of the broad doublet feature in 1 equiv. H_2O in HZSM-5 using 2D IR spectroscopy. While linear absorption spectroscopy cannot distinguish between the proposed Fermi resonance and tunneling potential models outlined in Fig. 1.8, these models predict distinct 2D IR signatures from the differences in transition frequencies and intensities to higher-lying excited states. The model of Fermi resonance coupling predicts intense excited-state features which are not observed in the measured 2D IR spectrum, showing that this widely-accepted interpretation is inconsistent with the experiment. On the other hand, we show that the relative frequencies and amplitudes of all experimental transitions are reproduced with a 1-dimensional model of the tunneling double well potential. This result is discussed in the context of the theory of strong H-bonding described in Section 1.3.

1.6. References

(1) Humphreys, J.; Lan, R.; Tao, S. Development and Recent Progress on Ammonia Synthesis Catalysts for Haber–Bosch Process. *Adv. Energy Sustain. Res.* **2021**, *2* (1), 2000043. https://doi.org/10.1002/aesr.202000043.

(2) Erisman, J. W.; Sutton, M. A.; Galloway, J.; Klimont, Z.; Winiwarter, W. How a Century of Ammonia Synthesis Changed the World. *Nat. Geosci.* **2008**, *1* (10), 636–639. https://doi.org/10.1038/ngeo325.

(3) Smil, V. Nitrogen Cycle and World Food Production. *World Agric.* **2011**, *2*, 9–13.

(4) Armor, J. N. A History of Industrial Catalysis. *Catal. Today* **2011**, *163*, 3–9.

(5) Degnan, T. F.; Chitnis, G. K.; Schipper, P. H. History of ZSM-5 Fluid Catalytic Cracking Additive Development at Mobil. *Microporous Mesoporous Mater.* **2000**, *35–36*, 245–252. https://doi.org/10.1016/S1387-1811(99)00225-5.

(6) Farrauto, R. J.; Deeba, M.; Alerasool, S. Gasoline Automobile Catalysis and Its Historical Journey to Cleaner Air. *Nat. Catal.* **2019**, *2* (7), 603–613. https://doi.org/10.1038/s41929-019-0312-9.

(7) Corma, A. From Microporous to Mesoporous Molecular Sieve Materials and Their Use in Catalysis. *Chem. Rev.* **1997**, *97* (6), 2373–2419. https://doi.org/10.1021/cr960406n.

(8) Davis, M. E. Zeolite-Based Catalysts for Chemicals Synthesis. *Microporous Mesoporous Mater.* **1998**, *21* (4–6), 173–182. https://doi.org/10.1016/S1387-1811(98)00007-9.

(9) Tanabe, K.; Hölderich, W. F. Industrial Application of Solid Acid-Base Catalysts. *Appl. Catal. A Gen.* **1999**, *181* (2), 399–434. https://doi.org/10.1016/S0926-860X(98)00397-4.

(10) Corma, A. State of the Art and Future Challenges of Zeolites as Catalysts. *J. Catal.* **2003**, *216* (1–2), 298–312. https://doi.org/10.1016/S0021-9517(02)00132-X.

(11) Martínez, C.; Corma, A. Inorganic Molecular Sieves: Preparation, Modification and Industrial Application in Catalytic Processes. *Coord. Chem. Rev.* **2011**, *255* (13–14), 1558–1580. https://doi.org/10.1016/j.ccr.2011.03.014.

(12) BP. *BP Statistical Review of World Energy 2022*; 2022. https://www.bp.com/content/dam/bp/business-sites/en/global/corporate/pdfs/energy-economics/statistical-review/bp-stats-review-2022-full-report.pdf.

(13) Geyer, R.; Jambeck, J. R.; Law, K. L. Production, Use, and Fate of All Plastics Ever Made. *Sci. Adv.* **2017**, *3* (7), 25–29. https://doi.org/10.1126/sciadv.1700782.

(14) Ennaert, T.; Van Aelst, J.; Dijkmans, J.; De Clercq, R.; Schutyser, W.; Dusselier, M.; Verboekend, D.; Sels, B. F. Potential and Challenges of Zeolite Chemistry in the Catalytic Conversion of Biomass. *Chem. Soc. Rev.* **2016**, *45* (3), 584–611. https://doi.org/10.1039/c5cs00859j.

(15) Stanciakova, K.; Weckhuysen, B. M. Water–Active Site Interactions in Zeolites and Their Relevance in Catalysis. *Trends Chem.* **2021**, *3* (6), 456–468. https://doi.org/10.1016/J.TRECHM.2021.03.004.

(16) Galadima, A.; Muraza, O. Stability Improvement of Zeolite Catalysts under Hydrothermal Conditions for Their Potential Applications in Biomass Valorization and Crude Oil Upgrading. *Microporous Mesoporous Mater.* **2017**, *249*, 42–54. https://doi.org/10.1016/j.micromeso.2017.04.023.

(17) Taarning, E.; Osmundsen, C. M.; Yang, X.; Voss, B.; Andersen, S. I.; Christensen, C. H. Zeolite-Catalyzed Biomass Conversion to Fuels and Chemicals. *Energy Environ. Sci.* **2011**, *4*, 793–804. https://doi.org/10.1039/c004518g.

(18) Resasco, D. E.; Wang, B.; Crossley, S. Zeolite-Catalysed C-C Bond Forming Reactions for Biomass Conversion to Fuels and Chemicals. *Catal. Sci. Technol.* **2016**, *6* (8), 2543–2559. https://doi.org/10.1039/c5cy02271a.

(19) Mardiana, S.; Azhari, N. J.; Ilmi, T.; Kadja, G. T. M. Hierarchical Zeolite for Biomass Conversion to Biofuel: A Review. *Fuel* **2022**, *309*, 122119. https://doi.org/10.1016/J.FUEL.2021.122119.

(20) Shun, T.; Zhijun, Z.; Jianping, S.; Qingwen, W. Recent Progress of Catalytic Pyrolysis of Biomass by HZSM-5. *Chinese J. Catal.* **2013**, *34* (4), 641–650. https://doi.org/10.1016/S1872-2067(12)60531-2.

(21) Grzybek, G.; Greluk, M.; Patulski, P.; Stelmachowski, P.; Tarach, K.; Słowik, G.; Rotko, M.; Valencia, S.; Góra-marek, K. Adjustment of the ZSM-5 Zeolite Support towards the Efficient Hydrogen Production by Ethanol Steam Reforming on Cobalt Catalysts. *Chem. Eng. J.* **2023**. https://doi.org/10.1016/j.cej.2023.143239.

(22) Yan, T.; Zhang, M.; Liu, R.; Dai, W.; Guan, N.; Li, L. Acetone − Butanol − Ethanol Catalytic Upgrading into Aromatics over Ga-Modified HZSM-5 Zeolites. *ACS Catal.* **2023**, *13*, 7087–7102. https://doi.org/10.1021/acscatal.3c01491.

(23) *Database of zeolite structures*. Structure Commission of the International Zeolite Association. http://www.iza-structure.org/index.htm (accessed 2023-05-09).

(24) Masters, A. F.; Maschmeyer, T. Zeolites - From Curiosity to Cornerstone. *Microporous Mesoporous Mater.* **2011**, *142* (2–3), 423–438. https://doi.org/10.1016/j.micromeso.2010.12.026.

(25) Shamzhy, M.; Gil, B.; Opanasenko, M.; Roth, W. J.; Čejka, J. MWW and MFI Frameworks as Model Layered Zeolites: Structures, Transformations, Properties, and Activity. *ACS Catal.* **2021**, *11* (4), 2366–2396. https://doi.org/10.1021/acscatal.0c05332.

(26) Kosinov, N.; Gascon, J.; Kapteijn, F.; Hensen, E. J. M. Recent Developments in Zeolite Membranes for Gas Separation. *J. Memb. Sci.* **2016**, *499*, 65–79. https://doi.org/10.1016/j.memsci.2015.10.049.

(27) Bernardo, P.; Drioli, E.; Golemme, G. Membrane Gas Separation: A Review/State of the Art. *Ind. Eng. Chem. Res.* **2009**, *48* (10), 4638–4663. https://doi.org/10.1021/ie8019032.

(28) Khulbe, K. C.; Matsuura, T.; Feng, C. Y.; Ismail, A. F. Recent Development on the Effect of Water/Moisture on the Performance of Zeolite Membrane and MMMs Containing Zeolite for Gas Separation; Review. *RSC Adv.* **2016**, *6* (49), 42943–42961. https://doi.org/10.1039/c6ra03007f.

(29) Olson, D. H.; Haag, W. O. Structure-Selectivity Relationship in Xylene Isomerization and Selective Toluene Disproportionation. *ACS Symp. Ser.* **1984**, 276–307. https://doi.org/10.1021/bk-1984-0248.ch014.

(30) Sherman, J. D. Synthetic Zeolites and Other Microporous Oxide Molecular Sieves. *Proc. Natl. Acad. Sci.* **1999**, *96* (11), 3471–3478.

(31) Loewenstein, W. The Distribution of Aluminum in the Tetrahedra of Silicates and Aluminates. *Am. Miner.* **1954**, *39*, 92–96. https://doi.org/10.1002/anie.201004007.

(32) Jones, A. J.; Iglesia, E. The Strength of Brønsted Acid Sites in Microporous Aluminosilicates. *ACS Catal.* **2015**, *5* (10), 5741–5755. https://doi.org/10.1021/acscatal.5b01133.

(33) Koppel, I. A.; Taft, R. W.; Anvia, F.; Zhu, S.-Z.; Hu, L.-Q.; Sung, K.-S.; DesMarteau, D. D.; Yagupolskii, L. M.; Yagupolskii, Y. L.; Ignat'ev, N. V.; Kondratenko, N. V.; Volkonskii, A. Y.; Vlasov, V. M.; Notario, R.; Maria, P.-C. The Gas-Phase Acidities of Very Strong Neutral Bronsted Acids. *J. Am. Chem. Soc.* **1994**, *116*, 3047–3057.

(34) Gorte, R. J. What Do We Know about the Acidity of Solid Acids? *Catal. Letters* **1999**, *62* (1), 1–13. https://doi.org/10.1023/A:1019010013989.

(35) Derouane, E. G.; Védrine, J. C.; Ramos Pinto, R.; Borges, P. M.; Costa, L.; Lemos, M. A. N. D. A.; Lemos, F.; Ramôa Ribeiro, F. The Acidity of Zeolites: Concepts, Measurements and Relation to Catalysis: A Review on Experimental and Theoretical Methods for the Study of Zeolite Acidity. *Catal. Rev. - Sci. Eng.* **2013**, *55* (4), 454–515. https://doi.org/10.1080/01614940.2013.822266.

(36) Corma, A. Inorganic Solid Acids and Their Use in Acid-Catalyzed Hydrocarbon Reactions. *Chem. Rev.* **1995**, *95* (3), 559–614. https://doi.org/10.1021/cr00035a006.

(37) Wang, Q.; Fan, H.; Wu, S.; Zhang, Z.; Zhang, P.; Han, B. Water as an Additive to Enhance the Ring Opening of Naphthalene. *Green Chem.* **2012**, *14* (4), 1152–1158. https://doi.org/10.1039/c2gc16554f.

(38) Mei, D.; Lercher, J. A. Mechanistic Insights into Aqueous Phase Propanol Dehydration in H-ZSM-5 Zeolite. *AIChE J.* **2017**, *63* (1), 172–184. https://doi.org/10.1002/aic.15517.

(39) Zhi, Y.; Shi, H.; Mu, L.; Liu, Y.; Mei, D.; Camaioni, D. M.; Lercher, J. A. Dehydration Pathways of 1-Propanol on HZSM-5 in the Presence and Absence of Water. *J. Am. Chem. Soc.* **2015**, *137* (50), 15781–15794. https://doi.org/10.1021/jacs.5b09107.

(40) Mei, D.; Lercher, J. A. Effects of Local Water Concentrations on Cyclohexanol Dehydration in H-BEA Zeolites. *J. Phys. Chem. C* **2019**, *123* (41), 25255–25266.

https://doi.org/10.1021/acs.jpcc.9b07738.

(41) Chen, K.; Damron, J.; Pearson, C.; Resasco, D.; Zhang, L.; White, J. L. Zeolite Catalysis: Water Can Dramatically Increase or Suppress Alkane C-H Bond Activation. *ACS Catal.* **2014**, *4* (9), 3039–3044. https://doi.org/10.1021/cs500858d.

(42) Chen, Y.; Ma, X.; Hack, J. H.; Zhang, S.; Peng, A.; Dombrowski, J. P.; Voth, G. A.; Tokmakoff, A.; Kung, M. C.; Kung, H. H. Solvated Excess Proton: Active Site in ZSM-5-Catalyzed Methanol Dehydration. *(in submission)*.

(43) Zecchina, A.; Bordiga, S.; Spoto, G.; Scarano, D.; Spanò, G.; Geobaldo, F. IR Spectroscopy of Neutral and Ionic Hydrogen-Bonded Complexes Formed upon Interaction of CH3OH, C2H5OH, (CH3)2O, (C2H5)2O and C4H8O with H-Y, H-ZSM-5 and H-Mordenite: Comparison with Analogous Adducts Formed on the H-Nafion Superacidic Membrane. *J. Chem. Soc. - Faraday Trans.* **1996**, *92* (23), 4863–4875. https://doi.org/10.1039/ft9969204863.

(44) Headrick, J. M.; Diken, E. G.; Walters, R. S.; Hammer, N. I.; Christie, R. A.; Cui, J.; Myshakin, E. M.; Duncan, M. A.; Johnson, M. A.; Jordan, K. D. Spectral Signatures of Hydrated Proton Vibrations in Water Clusters. *Science* **2005**, *308* (5729), 1765–1769. https://doi.org/10.1126/science.1113094.

(45) Fournier, J. A.; Johnson, C. J.; Wolke, C. T.; Weddle, G. H.; Wolk, A. B.; Johnson, M. A. Vibrational Spectral Signature of the Proton Defect in the Three-Dimensional H+(H2O)21 Cluster. *Science* **2014**, *344* (6187), 1009–1012.

(46) Ramasesha, K.; De Marco, L.; Mandal, A.; Tokmakoff, A. Water Vibrations Have Strongly Mixed Intra- and Intermolecular Character. *Nat. Chem.* **2013**, *5* (11), 935–940. https://doi.org/10.1038/nchem.1757.

(47) Lock, A. J.; Bakker, H. J. Temperature Dependence of Vibrational Relaxation in Liquid H2O. *J. Chem. Phys.* **2002**, *117* (4), 1708–1713. https://doi.org/10.1063/1.1485966.

(48) Deàk, J. C.; Rhea, S. T.; Iwaki, L. K.; Dlott, D. D. Vibrational Energy Relaxation and Spectral Diffusion in Water and Deuterated Water. *J. Phys. Chem. A* **2000**, *104* (21), 4866–4875. https://doi.org/10.1021/jp994492h.

(49) Lewis, N. H. C.; Dereka, B.; Zhang, Y.; Maginn, E. J.; Tokmakoff, A. From Networked to Isolated: Observing Water Hydrogen Bonds in Concentrated Electrolytes with Two-Dimensional Infrared Spectroscopy. *J. Phys. Chem. B* **2022**, *126* (28), 5305–5319. https://doi.org/10.1021/acs.jpcb.2c03341.

(50) Lim, J.; Park, K.; Lee, H.; Kim, J.; Kwak, K.; Cho, M. Nanometric Water Channels in Water-in-Salt Lithium Ion Battery Electrolyte. *J. Am. Chem. Soc.* **2018**, *140* (46), 15661–

15667. https://doi.org/10.1021/jacs.8b07696.

(51) Inoue, K.; Ahmed, M.; Nihonyanagi, S.; Tahara, T. Reorientation-Induced Relaxation of Free OH at the Air/Water Interface Revealed by Ultrafast Heterodyne-Detected Nonlinear Spectroscopy. *Nat. Commun.* **2020**, *11* (1). https://doi.org/10.1038/s41467-020-19143-8.

(52) Das, S.; Imoto, S.; Sun, S.; Nagata, Y.; Backus, E. H. G.; Bonn, M. Nature of Excess Hydrated Proton at the Water-Air Interface. *J. Am. Chem. Soc.* **2020**, *142* (2), 945–952. https://doi.org/10.1021/jacs.9b10807.

(53) Jentys, A.; Warecka, G.; Derewinski, M.; Lercher, J. A. Adsorption of Water on ZSM5 Zeolites. *J. Phys. Chem.* **1989**, *93* (12), 4837–4843. https://doi.org/10.1021/j100349a032.

(54) Jentys, A.; Warecka, G.; Lercher, J. A. Surface Chemistry of H-ZSM5 Studied by Time-Resolved IR Spectroscopy. *J. Mol. Catal.* **1989**, *51* (3), 309–327. https://doi.org/10.1016/0304-5102(89)80010-0.

(55) Vjunov, A.; Wang, M.; Govind, N.; Huthwelker, T.; Shi, H.; Mei, D.; Fulton, J. L.; Lercher, J. A. Tracking the Chemical Transformations at the Brønsted Acid Site upon Water-Induced Deprotonation in a Zeolite Pore. *Chem. Mater.* **2017**, *29* (21), 9030–9042. https://doi.org/10.1021/acs.chemmater.7b02133.

(56) Bordiga, S.; Regli, L.; Lamberti, C.; Zecchina, A.; Bjorgen, M.; Lillerud, K. P. FTIR Adsorption Studies of H2O and CH3OH in the Isostructural H-SSZ-13 and H-SAPO-34: Formation of H-Bonded Adducts and Protonated Clusters. *J. Phys. Chem. B* **2005**, *109*, 7724–7732. https://doi.org/10.1021/jp04432b.

(57) Badger, R. M. A Relation between Internuclear Distances and Bond Force Constants. *J. Chem. Phys.* **1934**, *2* (3), 128–131. https://doi.org/10.1063/1.1749433.

(58) Boyer, M. A.; Marsalek, O.; Heindel, J. P.; Markland, T. E.; McCoy, A. B.; Xantheas, S. S. Beyond Badger's Rule: The Origins and Generality of the Structure-Spectra Relationship of Aqueous Hydrogen Bonds. *J. Phys. Chem. Lett.* **2019**, *10* (5), 918–924. https://doi.org/10.1021/acs.jpclett.8b03790.

(59) Steiner, T. The Hydrogen Bond in the Solid State. *Angew. Chemie - Int. Ed.* **2002**, *41* (1), 48–76. https://doi.org/10.1002/1521-3773(20020104)41:1<48::AID-ANIE48>3.0.CO;2-U.

(60) Joseph, J.; Jemmis, E. D. Red-, Blue-, or No-Shift in Hydrogen Bonds: A Unified Explanation. *J. Am. Chem. Soc.* **2007**, *129* (15), 4620–4632. https://doi.org/10.1021/ja067545z.

(61) Auer, B.; Kumar, R.; Schmidt, J. R.; Skinner, J. L. Hydrogen Bonding and Raman, IR, and 2D-IR Spectroscopy of Dilute HOD in Liquid D2O. *Proc. Natl. Acad. Sci. U. S. A.* **2007**,

104 (36), 14215–14220. https://doi.org/10.1073/pnas.0701482104.

(62) Eaves, J. D.; Loparo, J. J.; Fecko, C. J.; Roberts, S. T.; Tokmakoff, A.; Geissler, P. L. Hydrogen Bonds in Liquid Water Are Broken Only Fleetingly. *Proc. Natl. Acad. Sci.* **2005**, *102* (37), 13019–13022. https://doi.org/10.1073/pnas.0505125102.

(63) Auer, B. M.; Skinner, J. L. IR and Raman Spectra of Liquid Water: Theory and Interpretation. *J. Chem. Phys.* **2008**, *128* (22). https://doi.org/10.1063/1.2925258.

(64) Yu, Q.; Carpenter, W. B.; Lewis, N. H. C.; Tokmakoff, A.; Bowman, J. M. High-Level VSCF/VCI Calculations Decode the Vibrational Spectrum of the Aqueous Proton. *J. Phys. Chem. B* **2019**, *123* (33), 7214–7224. https://doi.org/10.1021/acs.jpcb.9b05723.

(65) Carpenter, W. B.; Yu, Q.; Hack, J. H.; Dereka, B.; Bowman, J. M.; Tokmakoff, A. Decoding the 2D IR Spectrum of the Aqueous Proton with High-Level VSCF/VCI Calculations. *J. Chem. Phys.* **2020**, *153* (12), 124506. https://doi.org/10.1063/5.0020279.

(66) Biswas, R.; Carpenter, W.; Fournier, J. A.; Voth, G. A.; Tokmakoff, A. IR Spectral Assignments for the Hydrated Excess Proton in Liquid Water. *J. Chem. Phys.* **2017**, *146* (15). https://doi.org/10.1063/1.4980121.

(67) Marx, D. Proton Transfer 200 Years after Von Grotthuss: Insights from Ab Initio Simulations. *ChemPhysChem* **2006**, *7* (9), 1849–1870. https://doi.org/10.1002/cphc.200600128.

(68) Hamm, P.; Zanni, M. *Concepts and Methods of 2D Infrared Spectroscopy*; Cambridge University Press: Cambridge, UK and New York, NY, USA, 2011.

(69) Cho, M. *Two-Dimensional Optical Spectroscopy*; CRC Press: Boca Raton, USA, 2009.

(70) Khalil, M.; Tokmakoff, A.; Tokmako, A. Signatures of Vibrational Interactions in Coherent Two-Dimensional Infrared Spectroscopy. *Chem. Phys.* **2001**, *266* (2–3), 213–230. https://doi.org/10.1016/S0301-0104(01)00230-0.

(71) De Marco, L.; Ramasesha, K.; Tokmakoff, A. Experimental Evidence of Fermi Resonances in Isotopically Dilute Water from Ultrafast Broadband IR Spectroscopy. *J. Phys. Chem. B* **2013**, *117* (49), 15319–15327. https://doi.org/10.1021/jp4034613.

(72) Cleland, W. W.; Kreevoy, M. M. Low-Barrier Hydrogen Bonds and Enzymic Catalysis. *Science* **1994**, *264* (5167), 1887–1890. https://doi.org/10.1126/science.8009219.

(73) Frey, P. A.; Whitt, S. A.; Tobin, J. B. A Low-Barrier Hydrogen Bond in the Catalytic Triad of Serine Proteases? Theory versus Experiment. *Science* **1994**, *264*, 1927–1930. https://doi.org/10.1126/science.278.5340.1128.

(74) Dereka, B.; Yu, Q.; Lewis, N. H. C.; Carpenter, W. B.; Bowman, J. M.; Tokmakoff, A. Crossover from Hydrogen to Chemical Bonding. *Science* **2021**, *371* (6525), 160–164. https://doi.org/10.1126/science.abe1951.

(75) Elias, M.; Wellner, A.; Goldin-Azulay, K.; Chabriere, E.; Vorholt, J. A.; Erb, T. J.; Tawfik, D. S. The Molecular Basis of Phosphate Discrimination in Arsenate-Rich Environments. *Nature* **2012**, *491* (7422), 134–137. https://doi.org/10.1038/nature11517.

(76) Dai, S.; Funk, L. M.; von Pappenheim, F. R.; Sautner, V.; Paulikat, M.; Schröder, B.; Uranga, J.; Mata, R. A.; Tittmann, K. Low-Barrier Hydrogen Bonds in Enzyme Cooperativity. *Nature* **2019**, *573* (7775), 609–613. https://doi.org/10.1038/s41586-019-1581-9.

(77) Dahms, F.; Fingerhut, B. P.; Nibbering, E. T. J.; Pines, E.; Elsaesser, T. Large-Amplitude Transfer Motion of Hydrated Excess Protons Mapped by Ultrafast 2D IR Spectroscopy. *Science* **2017**, *357* (6350), 491–495. https://doi.org/10.1126/science.aan5144.

(78) Fournier, J. A.; Carpenter, W. B.; Lewis, N. H. C.; Tokmakoff, A. Broadband 2D IR Spectroscopy Reveals Dominant Asymmetric H5O2+ Proton Hydration Structures in Acid Solutions. *Nat. Chem.* **2018**, *10*, 932–937. https://doi.org/10.1038/s41557-018-0091-y.

(79) Carpenter, W. B.; Fournier, J. A.; Lewis, N. H. C.; Tokmakoff, A. Picosecond Proton Transfer Kinetics in Water Revealed with Ultrafast IR Spectroscopy. *J. Phys. Chem. B* **2018**, *122* (10), 2792–2802. https://doi.org/10.1021/acs.jpcb.8b00118.

(80) Kim, J.; Schmitt, U. W.; Gruetzmacher, J. A.; Voth, G. A.; Scherer, N. E. The Vibrational Spectrum of the Hydrated Proton: Comparison of Experiment, Simulation, and Normal Mode Analysis. *J. Chem. Phys.* **2002**, *116* (2), 737–746. https://doi.org/10.1063/1.1423327.

(81) Daly, C. A.; Streacker, L. M.; Sun, Y.; Pattenaude, S. R.; Hassanali, A. A.; Petersen, P. B.; Corcelli, S. A.; Ben-Amotz, D. Decomposition of the Experimental Raman and Infrared Spectra of Acidic Water into Proton, Special Pair, and Counterion Contributions. *J. Phys. Chem. Lett.* **2017**, *8* (21), 5246–5252. https://doi.org/10.1021/acs.jpclett.7b02435.

(82) Schroeder, R.; Lippincott, E. R. Potential Function Model of Hydrogen Bonds. II. *J. Phys. Chem.* **1957**, *61* (7), 921–928. https://doi.org/10.1021/j150553a017.

(83) Reid, C. Semiempirical Treatment of the Hydrogen Bond. *J. Chem. Phys.* **1959**, *30* (1), 182–190. https://doi.org/10.1063/1.1729873.

(84) Wang, M.; Jaegers, N. R.; Lee, M. S.; Wan, C.; Hu, J. Z.; Shi, H.; Mei, D.; Burton, S. D.; Camaioni, D. M.; Gutiérrez, O. Y.; Glezakou, V. A.; Rousseau, R.; Wang, Y.; Lercher, J. A. Genesis and Stability of Hydronium Ions in Zeolite Channels. *J. Am. Chem. Soc.* **2019**, *141* (8), 3444–3455. https://doi.org/10.1021/jacs.8b07969.

(85) Smith, L.; Cheetham, A. K.; Morris, R. E.; Marchese, L.; Thomas, J. M.; Wright, P. A.; Chen, J. On the Nature of Water Bound to a Solid Acid Catalyst. *Science* **1996**, *271* (5250), 799–802.

(86) Hack, J. H.; Dombrowski, J. P.; Ma, X.; Chen, Y.; Lewis, N. H. C.; Carpenter, W. B.; Li, C.; Voth, G. A.; Kung, H. H.; Tokmakoff, A. Structural Characterization of Protonated Water Clusters Confined in HZSM-5 Zeolites. *J. Am. Chem. Soc.* **2021**, *143* (27), 10203–10213. https://doi.org/10.1021/jacs.1c03205.

(87) Ison, A.; Gorte, R. J. The Adsorption of Methanol and Water on H-ZSM-5. *J. Catal.* **1984**, *89* (1), 150–158. https://doi.org/10.1016/0021-9517(84)90289-6.

(88) Auroux, A.; Bolis, V.; Wierzchowski, P.; Gravelle, P. C.; Vedrine, J. C. Study of the Acidity of ZSM-5 Zeolite by Microcalorimetry and Infrared Spectroscopy. *J. Chem. Soc. Faraday Trans. 1 Phys. Chem. Condens. Phases* **1979**, *75*, 2544–2555. https://doi.org/10.1039/F19797502544.

(89) Jacobs, P. A.; Von Ballmoos, R. Framework Hydroxyl Groups of H-ZSM-5 Zeolites. *J. Phys. Chem.* **1982**, *86* (15), 3050–3052. https://doi.org/10.1021/j100212a046.

(90) Zholobenko, V. L.; Kustov, L. M.; Borovkov, V. Y.; Kazansky, V. B. A New Type of Acidic Hydroxyl Groups in ZSM-5 Zeolite and in Mordenite According to Diffuse Reflectance i.r. Spectroscopy. *Zeolites* **1988**, *8* (3), 175–178. https://doi.org/10.1016/S0144-2449(88)80303-8.

(91) Windeck, H.; Berger, F.; Sauer, J. Spectroscopic Signatures of Internal Hydrogen Bonds of Brønsted-Acid Sites in the Zeolite H-MFI. *Angew. Chemie Int. Ed.* **2023**, *e202303204*, 1–5. https://doi.org/10.1002/anie.202303204.

(92) Mihaleva, V. V.; Van Santen, R. A.; Jansen, A. P. J. Quantum Chemical Calculation of Infrared Spectra of Acidic Groups in Chabazite in the Presence of Water. *J. Chem. Phys.* **2004**, *120* (19), 9212–9221. https://doi.org/10.1063/1.1709896.

(93) Kondo, J. N.; Iizuka, M.; Domen, K.; Wakabayashi, F. IR Study of H2O Adsorbed on H-ZSM-5. *Langmuir* **1997**, *13* (4), 747–749. https://doi.org/10.1021/la9607565.

(94) Pelmenschikov, A. G.; Van Santen, R. A. Water Adsorption on Zeolites: Ab-Initio Interpretation of IR Data. *J. Phys. Chem.* **1993**, *97* (41), 10678–10680. https://doi.org/10.1021/j100143a025.

(95) Pelmenschikov, A. G.; van Wolput, J. H. M. C.; Jaenchen, J.; van Santen, R. A. (A,B,C) Triplet of Infrared OH Bands of Zeolitic H-Complexes. *J. Phys. Chem.* **1995**, *99* (11), 3612–3617. https://doi.org/10.1021/j100011a031.

(96) Sauer, J.; Horn, H.; Häser, M.; Ahlrichs, R. Formation of Hydronium Ions on Brønsted Sites in Zeolitic Catalysts: A Quantum-Chemical Ab Initio Study. *Chem. Phys. Lett.* **1990**, *173* (1), 26–32. https://doi.org/10.1016/0009-2614(90)85297-P.

(97) Krossner, M.; Sauer, J. Interaction of Water with Brønsted Acidic Sites of Zeolite Catalysts. Ab Initio Study of 1:1 and 2:1 Surface Complexes. *J. Phys. Chem.* **1996**, *100* (15), 6199–6211. https://doi.org/10.1021/jp952775d.

(98) Wakabayashi, F.; Kondo, J. N.; Domen, K.; Hirose, C. FT-IR Study of H218O Adsorption on H-ZSM-5: Direct Evidence for the Hydrogen-Bonded Adsorption of Water. *J. Phys. Chem.* **1996**, *100* (5), 1442–1444. https://doi.org/10.1021/jp953089h.

(99) Zecchina, A.; Geobaldo, F.; Spoto, G.; Bordiga, S.; Ricchiardi, G.; Buzzoni, R.; Petrini, G. FTIR Investigation of the Formation of Neutral and Ionic Hydrogen-Bonded Complexes by Interaction of H-ZSM-5 and H-Mordenite with CH3CN and H2O: Comparison with the H-NAFION Superacidic System. *J. Phys. Chem.* **1996**, *100* (41), 16584–16599. https://doi.org/10.1021/jp960433h.

(100) Termath, V.; Haase, F.; Sauer, J.; Hutter, J.; Parrinello, M. Understanding the Nature of Water Bound to Solid Acid Surfaces. Ab Initio Simulation on HSAPO-34. *J. Am. Chem. Soc.* **1998**, *120* (33), 8512–8516. https://doi.org/10.1021/ja981549p.

(101) Jeanvoine, Y.; Ángyán, J. G.; Kresse, G.; Hafner, J. On the Nature of Water Interacting with Brønsted Acidic Sites. Ab Initio Molecular Dynamics Study of Hydrated HSAPO-34. *J. Phys. Chem. B* **1998**, *102* (38), 7307–7310. https://doi.org/10.1021/jp981667z.

(102) Kawai, Y.; Yamaguchi, S.; Okada, Y.; Takeuchi, K.; Yamauchi, Y.; Ozawa, S.; Nakai, H. Reactions of Protonated Water Clusters H+(H2O) n (n = 1-6) with Dimethylsulfoxide in a Guided Ion Beam Apparatus. *Chem. Phys. Lett.* **2003**, *377* (1–2), 69–73. https://doi.org/10.1016/S0009-2614(03)01095-9.

(103) Cheng, H. P. Water Clusters: Fascinating Hydrogen-Bonding Networks, Solvation Shell Structures, and Proton Motion. *J. Phys. Chem. A* **1998**, *102* (31), 6201–6204. https://doi.org/10.1021/jp981433f.

(104) Kletnieks, P. W.; Ehresmann, J. O.; Nicholas, J. B.; Haw, J. F. Adsorbate Clustering and Proton Transfer in Zeolites: NMR Spectroscopy and Theory. *ChemPhysChem* **2006**, *7* (1), 114–116. https://doi.org/10.1002/CPHC.200500313.

(105) Vener, M. V.; Rozanska, X.; Sauer, J. Protonation of Water Clusters in the Cavities of Acidic Zeolites: (H2O)N·H-Chabazite, n = 1-4. *Phys. Chem. Chem. Phys.* **2009**, *11* (11), 1702–1712. https://doi.org/10.1039/b817905k.

(106) Zygmunt, S. A.; Curtiss, L. A.; Iton, L. E.; Erhardt, M. K. Computational Studies of Water

Adsorption in the Zeolite H-ZSM-5. *J. Phys. Chem.* **1996**, *100*, 6663–6671. https://doi.org/10.1021/jp952913z.

(107) Zygmunt, S. A.; Curtiss, L. A.; Iton, L. E. Protonation of an H2O Dimer by a Zeolitic Brønsted Acid Site. *J. Phys. Chem. B* **2001**, *105* (15), 3034–3038. https://doi.org/10.1021/jp003469p.

(108) Liu, P.; Mei, D. Identifying Free Energy Landscapes of Proton-Transfer Processes between Brønsted Acid Sites and Water Clusters Inside the Zeolite Pores. *J. Phys. Chem. C* **2020**, *124* (41), 22568–22576. https://doi.org/10.1021/acs.jpcc.0c07033.

(109) Grifoni, E.; Piccini, G. M.; Lercher, J. A.; Glezakou, V. A.; Rousseau, R.; Parrinello, M. Confinement Effects and Acid Strength in Zeolites. *Nat. Commun.* **2021**, *12*. https://doi.org/10.1038/s41467-021-22936-0.

(110) Olson, D. H.; Zygmunt, S. A.; Erhardt, M. K.; Curtiss, L. A.; Iton, L. E. Evidence for Dimeric and Tetrameric Water Clusters in HZSM-5. *Zeolites* **1997**, *18*, 347–349. https://doi.org/10.1016/S0144-2449(97)00024-9.

(111) Grifoni, E.; Piccini, G. M.; Parrinello, M. Microscopic Description of Acid–Base Equilibrium. *Proc. Natl. Acad. Sci. U. S. A.* **2019**, *116* (10), 4054–4057. https://doi.org/10.1073/pnas.1819771116.

(112) Humplik, T.; Raj, R.; Maroo, S. C.; Laoui, T.; Wang, E. N. Effect of Hydrophilic Defects on Water Transport in MFI Zeolites. *Langmuir* **2014**, *30* (22), 6446–6453. https://doi.org/10.1021/la500939t.

(113) Eckstein, S.; Hintermeier, P. H.; Zhao, R.; Baráth, E.; Shi, H.; Liu, Y.; Lercher, J. A. Influence of Hydronium Ions in Zeolites on Sorption. *Angew. Chemie - Int. Ed.* **2019**, *58* (11), 3450–3455. https://doi.org/10.1002/anie.201812184.

(114) Bolis, V.; Busco, C.; Ugliengo, P. Thermodynamic Study of Water Adsorption in High-Silica Zeolites. *J. Phys. Chem. B* **2006**, *110* (30), 14849–14859. https://doi.org/10.1021/jp061078q.

(115) Dalla Bernardina, S.; Paineau, E.; Brubach, J. B.; Judeinstein, P.; Rouzière, S.; Launois, P.; Roy, P. Water in Carbon Nanotubes: The Peculiar Hydrogen Bond Network Revealed by Infrared Spectroscopy. *J. Am. Chem. Soc.* **2016**, *138* (33), 10437–10443. https://doi.org/10.1021/jacs.6b02635.

(116) Khalid, M.; Joly, G.; Renaud, A.; Magnoux, P. Removal of Phenol from Water by Adsorption Using Zeolites. *Ind. Eng. Chem. Res.* **2004**, *43* (17), 5275–5280. https://doi.org/10.1021/ie0400447.

(117) Li, S.; Tuan, V. A.; Falconer, J. L.; Noble, R. D. Separation of 1,3-Propanediol from Glycerol and Glucose Using a ZSM-5 Zeolite Membrane. *J. Memb. Sci.* **2001**, *191* (1–2), 53–59. https://doi.org/10.1016/S0376-7388(01)00448-3.

(118) Hadzi, D. Infrared Spectra of Strongly Hydrogen-Bonded Systems. *Pure Appl. Chem.* **1965**, *11*, 435–453.

(119) Petersen, P. B.; Roberts, S. T.; Ramasesha, K.; Nocera, D. G.; Tokmakoff, A. Ultrafast N-H Vibrational Dynamics of Cyclic Doubly Hydrogen-Bonded Homo- and Heterodimers. *J. Phys. Chem. B* **2008**, *112* (42), 13167–13171. https://doi.org/10.1021/jp805338h.

(120) Stingel, A. M.; Petersen, P. B. Couplings Across the Vibrational Spectrum Caused by Strong Hydrogen Bonds : A Continuum 2D IR Study of the 7-Azaindole−Acetic Acid Heterodimer. *J. Phys. Chem. B* **2016**, *120*, 10768–10779. https://doi.org/10.1021/acs.jpcb.6b05049.

(121) Asfin, R. E.; Denisov, G. S.; Tokhadze, K. G. The ν(OH/OD) Band Shape of Strong Hydrogen Bonded Dimers of Phosphinic Acids. Phenomenology and Formation Models. *J. Mol. Struct.* **2006**, *790* (1–3), 11–17. https://doi.org/10.1016/j.molstruc.2006.03.037.

(122) Huang, Q. R.; Shishido, R.; Lin, C. K.; Tsai, C. W.; Tan, J. A.; Fujii, A.; Kuo, J. L. Strong Fermi Resonance Associated with Proton Motions Revealed by Vibrational Spectra of Asymmetric Proton-Bound Dimers. *Angew. Chemie - Int. Ed.* **2021**, *60* (4), 1936–1941. https://doi.org/10.1002/anie.202012665.

(123) Bordiga, S.; Lamberti, C.; Bonino, F.; Travert, A.; Thibault-Starzyk, F. Probing Zeolites by Vibrational Spectroscopies. *Chem. Soc. Rev.* **2015**, *44* (20), 7262–7341. https://doi.org/10.1039/c5cs00396b.

(124) Evans, J. C. Further Studies of Unusual Effects in the Infrared Spectra of Certain Molecules. *Spectrochim. Acta* **1960**, *16* (9), 994–1000. https://doi.org/10.1016/0371-1951(60)80138-5.

(125) Claydon, M. F.; Sheppard, N. The Nature of "A,B,C"-Type Infrared Spectra of Strongly Hydrogen-Bonded Systems; Pseudo-Maxima in Vibrational Spectra. *J. Chem. Soc. D Chem. Commun.* **1969**, 1431–1433. https://doi.org/10.1039/C29690001431.

(126) Somorjai, R. L.; Horning, D. F. Double-Minimum Potentials in Hydrogen-Bonded Solids. *J. Chem. Phys.* **1962**, *36*, 1980–1987. https://doi.org/https://doi.org/10.1063/1.1732814.

Chapter 2

Theory and interpretation of 2D IR spectroscopy

2.1. Time domain spectroscopy and perturbation theory

2.1.1. Semiclassical treatment of light-matter interactions

A theoretical framework is needed to describe and interpret the vibrational spectroscopy experiments in this thesis. In coherent spectroscopy, which includes linear absorption and nonlinear changes in absorption, incident light fields create a macroscopic polarization in the matter of interest (the sample). The time-varying polarization in turn emits a signal field which is detected. Several properties of the absorbing material are encoded in the measured electric field, according to mathematical relationships which will be explored and summarized here. The underlying theory is well-documented in several textbooks[1–5] and previous PhD theses,[6–8] so I will not attempt to restate the full development of these concepts. The goal of this chapter is to describe the observable signals specific to nonlinear 2D IR and transient absorption (TA) spectroscopy of molecular vibrations in the liquid phase, with the aim of providing a basis for interpreting the experimental results presented in subsequent chapters.

To describe the light-matter interactions at the heart of spectroscopy, we use the semiclassical time-dependent perturbation theory popularized by Mukamel.[1] The matter is described as a collection of quantum-mechanical dipole moments $\boldsymbol{\mu}$, whose ensemble average gives the

macroscopic polarization of the sample **P**. The electric field **E** is described classically and is coupled to the system under the dipole approximation through the semiclassical term $V = -\boldsymbol{\mu} \cdot \mathbf{E}$. The governing equations of motion are the coupled Maxwell-Liouville equations,

$$\nabla^2 \mathbf{E}(\mathbf{r},t) - \frac{1}{c^2}\frac{\partial^2}{\partial t^2}\mathbf{E}(\mathbf{r},t) = \frac{4\pi}{c^2}\frac{\partial^2}{\partial t^2}\mathbf{P}(\mathbf{r},t) \tag{2.1}$$

$$i\hbar\frac{\partial \rho}{\partial t} = [H, \rho] \tag{2.2}$$

where the state of the system is described by the density operator $\rho = |\psi\rangle\langle\psi|$. The system evolves under the Hamiltonian *H*,

$$\begin{aligned} H &= H_0 + V \\ &= H_0 - \boldsymbol{\mu} \cdot \mathbf{E} \end{aligned} \tag{2.3}$$

where H_0 holds the degrees of freedom (DOF) of the unperturbed system. We assume that *V* can be treated as a perturbation on H_0, which is appropriate for our experiments where the incident electric field is orders of magnitude smaller than intermolecular field in the liquid.

The macroscopic polarization of the sample is the sum over the dipole moments of all molecules (in the focus of the laser). Quantum mechanically, it can be evaluated as the expectation value of the dipole operator calculated using the trace.

$$\mathbf{P}(\mathbf{r},t) = \sum\nolimits_i \boldsymbol{\mu}_i(\mathbf{r},t) = \langle \boldsymbol{\mu}(\mathbf{r},t)\rho(t)\rangle \tag{2.4}$$

The electric field is treated as a collection of incident laser pulses with envelope A_j, polarization e_j, carrier frequency ω_j, wavevector k_j, and phase φ_j, plus the generated signal field E_{Sig}. The time-dependent phase will be important for describing pulse dispersion and compression in

Chapter 3, but for now we will treat the pulses as perfectly compressed with $\varphi(t) = 0$. The electric field is a real-valued function, ensured by the complex conjugate (c.c.).

$$\begin{aligned}\mathbf{E}(\mathbf{r},t) &= \sum\nolimits_j A_j(\mathbf{r},t)\mathbf{e}_j e^{-i\omega_j t + i\mathbf{k}_j\mathbf{r} + i\varphi_j(t)} + c.c. + \mathbf{E}_{sig}(\mathbf{r},t) \\ \mathbf{E}_{sig}(\mathbf{r},t) &= A_{sig}(\mathbf{r},t)\mathbf{e}_{sig} e^{-i\omega_{sig} t + i\mathbf{k}_{sig}\mathbf{r} + i\varphi_{sig}(t)} + c.c.\end{aligned} \tag{2.5}$$

Ultimately, we wish to relate the observed signal field to the properties of the system (vibrational frequencies, correlation times, etc.). In principle, Eqs. (2.1)-(2.5) contain these relationships, but they are intractable to solve without further approximations. As we go through the mathematics in the rest of this section, I find it helpful to keep two guiding questions in mind: 1) how does the sequence of light pulses in our experiment generate the macroscopic polarization in the sample, and 2) how is the measured signal field related to that macroscopic polarization?

2.1.2. Perturbative expansion of the density matrix

The incident light pulses generate a macroscopic polarization in the sample, which can be described using time-dependent perturbation theory to iteratively solve the quantum Liouville equation.[1] The result is a perturbative expansion of the density matrix, represented in the interaction picture.

$$\begin{aligned}\rho(t) &= \rho^{(0)}(t) + \rho^{(1)}(t) + \rho^{(2)}(t) + \ldots \\ \rho^{(n)}(t) &= \left(\frac{-i}{\hbar}\right)^n \int_{t_0}^{t} dt_n \ldots \int_{t_0}^{t_3} dt_2 \int_{t_0}^{t_2} dt_1 [V(t_n)\ldots[V(t_2),[V(t_1),\rho(t_0)]]]\end{aligned} \tag{2.6}$$

Evaluating the trace in Eq. (2.4) results in a corresponding expansion of the macroscopic polarization, ignoring vector direction and spatial dependence for now. The polarization is expressed as a sum of terms, where the n^{th} term arises from n light-matter interactions and scales to the n^{th} power in the incident electric field.

$$P(t) = P^{(0)}(t) + P^{(1)}(t) + P^{(2)}(t) + ...$$
$$P^{(n)}(t) = \left(\frac{-i}{\hbar}\right)^n \int_{t_0}^{t} dt_n ... \int_{t_0}^{t_3} dt_2 \int_{t_0}^{t_2} dt_1 \left\langle \mu(t)[V(t_n)...[V(t_2),[V(t_1),\rho(t_0)]]]\right\rangle \quad (2.7)$$

Substituting the interaction term, setting $t_0 = -\infty,\ t_1 = 0,$ and defining time intervals $\tau_i = t_{i+1} - t_i$ leads to the general result for the n^{th} order polarization and molecular response function $R^{(n)}$. Setting $t_0 = -\infty$ is appropriate under the assumption that the system is at equilibrium before the first interaction, so $\rho(t_0) = \rho_{eq}$.

$$P^{(n)}(t) = \int_{-\infty}^{\infty} d\tau_n ... \int_{-\infty}^{\infty} d\tau_2 \int_{-\infty}^{\infty} d\tau_1 E(t-\tau_n)E(t-\tau_n-\tau_{n-1})...E(t-\tau_n-...-\tau_1)R^{(n)}(\tau_1...\tau_n) \quad (2.8)$$

$$R^{(n)}(\tau_1...\tau_n) = \left(\frac{i}{\hbar}\right)^n \left\langle [\mu(\tau_n+...+\tau_2+\tau_1),...[\mu(\tau_2+\tau_1),[\mu(\tau_1),\mu(0)]]...]\rho_{eq}\right\rangle \theta(\tau_1)...\theta(\tau_n) \quad (2.9)$$

Equations (2.8)-(2.9) comprise a crucial result. Equation (2.8) separates the electric field DOF from the matter DOF, which are entirely contained in the response function *R*. Equation (2.9) shows that $R^{(n)}$ is, in general, a sum of dipole correlation functions each evaluated at $n+1$ time points. Like all correlation functions, the terms in $R^{(n)}$ depend only on time intervals and are invariant to time translation. The terms $\theta(\tau_i)$ are step functions which enforce causality; light-matter interactions cannot occur out of order. The response function is evaluated by tracing over the equilibrium eigenstates of the system independent of the applied perturbation. Therefore, Eqs. (2.8)-(2.9) take the form of a fluctuation-dissipation relationship,[9] relating equilibrium fluctuations to the time-dependent response following a perturbation from the incident electric field. So, the molecular response function is the quantity we are interested in since it contains information about the eigenstates and dynamics of the system.

How should we begin to interpret the response function? To start, we can put $R^{(n)}$ into a more intuitive form by expanding the time dependence of the dipole operators in Eq. (2.9), which are written in the interaction picture.

$$\mu(\tau) = U_0^{\dagger}(\tau)\mu U_0(\tau) \tag{2.10}$$

Here, U_0 is the time-evolution operator under H_0.

$$\begin{aligned} U_0(t,t_0) &= \sum_{n=0}^{\infty}\left(\frac{-i}{\hbar}\right)^n \int_{t_0}^{t} d\tau_n ... \int_{t_0}^{t} d\tau_1 H_0(\tau_n)...H_0(\tau_1) \\ &= \exp_+\left(\frac{-i}{\hbar}\int_{t_0}^{t} d\tau H_0(\tau)\right) \end{aligned} \tag{2.11}$$

The second line of (2.11) defines the time-ordered exponential notation, and time-evolution is propagated under the unperturbed system Hamiltonian H_0. Next, we can define the operators Υ and G_0 by their action on a general operator *A*.

$$\begin{aligned} \Upsilon A &= [\mu, A] \\ G_0(\tau)A &= U_0^{\dagger}(\tau)AU_0(\tau) \end{aligned} \tag{2.12}$$

The operator Υ represents one action of the dipole operator and $G_0(\tau)$ represents time-propagation under H_0 during the time period τ, which can be used to rewrite $R^{(n)}$ as follows,

$$R^{(n)}(\tau_1...\tau_n) = \left\langle \Upsilon G_0(\tau_n)\Upsilon...G_0(\tau_2)\Upsilon G_0(\tau_1)\Upsilon\rho_{eq}\right\rangle \theta(\tau_1)...\theta(\tau_n) \tag{2.13}$$

In this form, the response function can be read as a sequence of events which are ordered in time and each influence the state of the system, tracked by the density matrix ρ. The system begins at equilibrium, and first experiences one dipole interaction Υ. Next, the system evolves in time under H_0 during τ_1, $G_0(\tau_1)$, until the second dipole interaction Υ. This pattern repeats itself until the

final time period τ_n, followed by the final dipole interaction. The final dipole term is distinct from the rest because it arises from taking the trace to calculate $P(t)$, not from a coupling term $-\boldsymbol{\mu}\cdot\mathbf{E}$. This is why the n^{th} order polarization scales with E^n and μ^{n+1}. The last dipole term is evaluated at time t when the emitted signal is observed in the experiment.

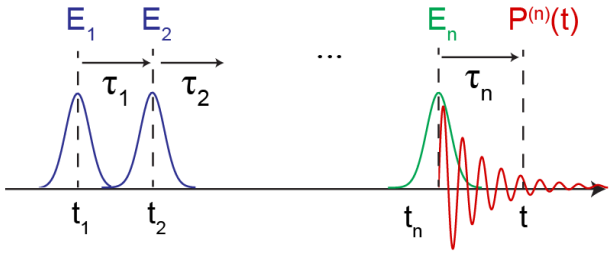

Figure 2.1. Pulse sequence and time variables corresponding to the generation of the n^{th} order polarization. In a time-domain spectroscopy experiment, interaction times t_i are controlled by the time delays τ_i between pulses.

In a time-domain spectroscopy experiment the time delays between the n light-matter interactions are controlled by the experimental delays between n short pulses. The resulting generation of a macroscopic n^{th} order polarization $P^{(n)}$ is illustrated schematically in Fig. 2.1. The electric field pulses E_i are peaked at times t_i to represent the pulse sequence. Figure 2.1 implicitly assumes that each light-matter interaction occurs at a peak in the electric field, which is exact only for infinitely short pulses. In practice, the finite pulse width sets a limit on the time resolution of the experiment.

2.1.3. Evaluation of the dipole correlation function

Under the perturbative treatment, the molecular response of the system is encoded in response function as a sum of dipole correlation functions. So, the next step is to evaluate these dipole correlation functions. This is the most straightforward in the linear case where there are only two

time points and one time interval. Then, there are two correlation functions to consider, distinguished by the ordering of dipole interactions on the bra- and ket- sides of ρ. Many of the interesting details can be seen in this case, and much of the effort for describing higher-order response functions will be dedicated to keeping track of the greater number of terms.

Consider an incident electric field which is weak enough that the polarization can be truncated at the linear term $P^{(1)}(t)$ in the expansion; $P^{(0)}$ is the static dipole moment which vanishes for an isotropic medium.

$$P^{(1)}(t) = \int_{-\infty}^{\infty} d\tau E(t-\tau) R^{(1)}(\tau) \tag{2.14}$$

$$\begin{aligned} R^{(1)}(\tau) &= \left(\frac{i}{\hbar}\right)\left\langle [\mu(\tau), \mu(0)]\rho_{eq} \right\rangle \theta(\tau) \\ &= \left(\frac{2}{\hbar}\right)\theta(\tau)\Im\left(C_{\mu\mu}(\tau)\right) \end{aligned} \tag{2.15}$$

To evaluate Eq. (2.15), it is sufficient to consider only one dipole correlation function, since the other term is the complex conjugate.

$$C_{\mu\mu}(\tau) = \left\langle \mu(\tau)\mu(0)\rho_{eq} \right\rangle \tag{2.16}$$

The dipole correlation function is related to the linear absorption spectrum through the Fourier transform of Eq. (2.14). In the frequency domain the linear polarization is proportional to the linear susceptibility $\chi^{(1)}(\omega)$, which is proportional to the Fourier transform of $R^{(1)}(\tau)$. The imaginary part of $\chi^{(1)}(\omega)$ encodes the linear absorption spectrum, which will be shown in section 2.1.4.

$$P^{(1)}(\omega) = \chi^{(1)}(\omega)E(\omega) \tag{2.17}$$

For a single isolated particle with unperturbed Hamiltonian H_0, the correlation function can be computed straightforwardly in the basis of H_0 eigenstates.

$$\begin{aligned} C_{\mu\mu}(\tau) &= \sum_a p_a \left\langle a \left| e^{iH_0\tau/\hbar} \mu e^{-iH_0\tau/\hbar} \mu \right| a \right\rangle \\ &= \sum_a \sum_b p_a \left| \mu_{ba} \right|^2 e^{-i\omega_{ba}\tau} \end{aligned} \tag{2.18}$$

Here, p_a is the Boltzmann factor for occupation of state |a⟩ at equilibrium and $\omega_{ba} = (E_b - E_a)/\hbar$. Working in the basis of H_0, the time-evolution operator U_0 is simplified from a time-ordered exponential to a simple exponential, since H_0 is time-independent and therefore $[H_0(0), H_0(\tau)] = 0$. The correlation function oscillates in time at the difference frequencies between eigenstates, with each oscillating term weighed by the norm-squared value of the corresponding transition dipole matrix element.

Taking the Fourier transform of (2.18) would result in a sum of delta functions at the transition frequencies ω_{ba}. For a collection of particles at finite temperature, collisions between molecules effectively induce some mixing between eigenstates, since during a collision the molecule is no longer isolated. This leads to dephasing, resulting in a nonzero linewidth in the frequency domain. In the gas phase, the mixing between eigenstates is typically small enough that it is appropriate to simply modify (2.18) by adding a phenomenological relaxation term with dephasing rate Γ_{ba} for each pair of eigenstates |a⟩ and |b⟩.

$$C_{\mu\mu}(\tau) = \sum_a \sum_b p_a \left| \mu_{ba} \right|^2 e^{-i\omega_{ba}\tau} e^{-\Gamma_{ba}\tau} \tag{2.19}$$

In the condensed phases however, particle-particle interactions are much stronger, further complicating the evaluation of the time-dependent dipole correlation function. At a given point in time, otherwise identical molecules may be embedded in different environments which modulate their eigenstates (for example, donating a H-bond can shift the frequency of an O-H stretch by hundreds of wavenumbers). Furthermore, the environment can fluctuate causing time-dependent changes in the molecular eigenstates. Both of these factors contribute to the linewidth, which can be quite broad in the condensed phases. In effect, (2.19) is not necessarily valid, and evaluating $C_{\mu\mu}(\tau)$ requires the full time-ordered exponential treatment of U_0.

To obtain a tractable solution, a common treatment is to separate the DOF in H_0 into the "system" H_S containing the spectroscopically bright states observed in the experiment and the "bath" H_B containing the lower-frequency dark states, with system-bath coupling H_{SB}.[1]

$$H_0 = H_S + H_B + H_{SB} \tag{2.20}$$

Assuming an adiabatic separation between system and bath DOF with weak coupling, the correlation function can be expressed as,

$$C_{\mu\mu}(\tau) = \sum_a \sum_b p_a \left\langle \mu_{ba}(\tau)\mu_{ba}(0)e^{-i\int_0^\tau d\tau' \omega_{ba}(\tau')} \right\rangle_B \tag{2.21}$$
$$\mu_{ba}(\tau) = e^{iH_B\tau/\hbar}\mu_{ba}e^{-iH_B\tau/\hbar}$$

where the trace is over the bath DOF and time-evolution occurs under H_B. The advantage of this formulation is that the transition frequencies and transition dipole moments correspond to system eigenstates, and the time-dependence arises from fluctuations of the bath.

Evaluating Eq. (2.21) is still not always straightforward, so two additional approximations are often applied to reach a more convenient form. First, under the Condon approximation there is an adiabatic separation between electronic and nuclear DOF. This means the transition dipole moment μ is independent of the bath DOF and can be evaluated outside of the trace. The expression can be further simplified by taking the cumulant expansion of the trace and truncating at second order.[1] This is akin to assuming that the bath fluctuations are Gaussian (i.e., treating the bath as a collection of harmonic oscillators). For a single transition between states |a⟩ to |b⟩, the correlation function under these approximations becomes:

$$C_{\mu\mu}^{\ Non-Condon}(\tau) = e^{-i\bar{\omega}_{ba}\tau}\left\langle \mu_{ba}(\tau)\mu_{ba}(0)e^{-i\int_0^\tau d\tau'\delta\omega_{ba}(\tau')}\right\rangle \tag{2.22}$$

$$C_{\mu\mu}^{\ Condon}(\tau) = |\,\mu_{ba}\,|^2\, e^{-i\bar{\omega}_{ba}\tau}\left\langle e^{-i\int_0^\tau d\tau'\delta\omega_{ba}(\tau')}\right\rangle \tag{2.23}$$

$$\begin{aligned} C_{\mu\mu}^{\ Cumulant}(\tau) &= |\,\mu_{ba}\,|^2\, e^{-i\bar{\omega}_{ba}\tau}e^{-g(\tau)} \\ g(\tau) &= \int_0^\tau d\tau'(\tau-\tau')\left\langle \delta\omega_{ba}(\tau')\delta\omega_{ba}(0)\right\rangle \end{aligned} \tag{2.24}$$

So, under the Condon and cumulant approximations the lineshape is encoded in the lineshape function $g(\tau)$ which is determined by the autocorrelation function of frequency fluctuations $\delta\omega$ away from the mean frequency $\bar{\omega}_{ba}$. An insightful comparison between these levels of approximation in the context of O-H stretch spectroscopy was illustrated by Schmidt *et* al.[10]

To demonstrate the influence on the linear absorption spectrum, consider the Gaussian-stochastic model,[3,11] which treats the frequency-frequency correlation function (FFCF) as a single decaying exponential with correlation time τ_c.

$$\langle \delta\omega_{ba}(\tau)\delta\omega_{ba}(0)\rangle = \Delta^2 e^{-\tau/\tau_c} \tag{2.25}$$

$$g(\tau) = \Delta^2 {\tau_c}^2 \left(e^{-\tau/\tau_c} + \tau/\tau_c - 1\right) \tag{2.26}$$

If the frequency fluctuations caused by the bath are much slower than the timescale of the experiment, $\tau_c >> \tau$, the linewidth is determined by the static distribution Δ of oscillators with different frequencies. This is the inhomogeneous or static limit, where the dipole correlation function is Gaussian in time. The corresponding lineshape in frequency space is also Gaussian with FWHM 2.35Δ.

$$\begin{aligned} g(\tau) &= \Delta^2\tau^2/2 \\ C_{\mu\mu}(\tau) &= |\mu_{ba}|^2 e^{-i\bar{\omega}_{ba}\tau} e^{-\Delta^2\tau^2/2} \end{aligned} \tag{2.27}$$

In the limit of fast bath fluctuations, $\tau_c << \tau$, the linewidth is instead determined by the dephasing rate $\Gamma = \Delta^2\tau_c$. This is the homogeneous limit, where the dipole correlation function decays exponentially in time and transforms to a Lorentzian in frequency with FWHM 2Γ.

$$\begin{aligned} g(\tau) &= \Delta^2\tau_c\tau = \Gamma\tau \\ C_{\mu\mu}(\tau) &= |\mu_{ba}|^2 e^{-i\bar{\omega}_{ba}\tau} e^{-\Gamma\tau} \end{aligned} \tag{2.28}$$

So, line broadening in the absorption spectrum is a combination of homogeneous and inhomogeneous contributions. Those contributions are illustrated in Fig. 2.2 under the approximations of the Gaussian stochastic model, resulting in a Gaussian distribution of Lorentzian transitions. Because homogeneous and inhomogeneous broadening are convolved, it is in general not possible to separate these contributions in the linear absorption spectrum. This is one advantage of 2D spectroscopy where homogeneous and inhomogeneous linewidths are separated in the 2D lineshape, described in section 2.3.3.

The illustration in Fig. 2.2 provides an intuitive picture of the contributions of homogeneous and inhomogeneous broadening. However, for vibrations in condensed phase systems we should be cautious when applying the Condon and cumulant approximations. For example, in the spectrum of the O-H stretch of liquid water a prominent non-Condon effect has been observed both experimentally[12] and in spectral simulations.[10] And, ultrafast vibrational spectroscopy experiments sensitive to the FFCF have revealed non-Gaussian fluctuations in the H-bonding network of liquid water.[13–15] Spectral simulations comparing the treatments in Eqs. (2.22) - (2.24) showed that both the frequency-dependence of $\mu(\omega)$ and non-Gaussian fluctuations contribute meaningfully to the water O-H stretch lineshape. Therefore, the more general form of Eq. (2.22) is more appropriate for realistic spectral simulations of lineshape dynamics in the complicated vibrations of liquid water.[10]

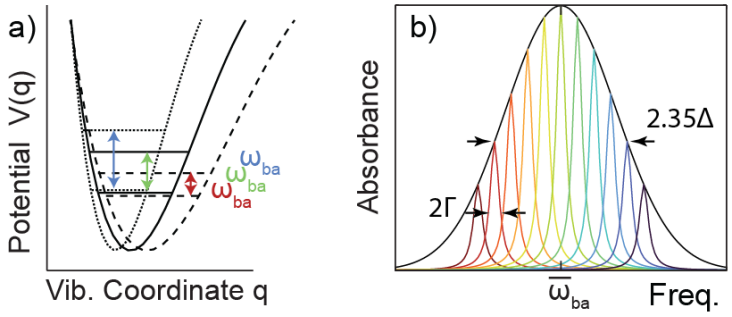

Figure 2.2. Illustration of inhomogeneous broadening in linear absorption. (a) The distribution of molecular environments in the ensemble is reflected in (b) a distribution of frequencies Δ, with oscillators in each environment experiencing homogeneous broadening Γ.

2.1.4. Generated electric field from the macroscopic polarization

So far, it has been shown that the bright system DOF are encoded in the molecular response function, which is a sum of dipole time correlation functions. When a sequence of short pulses are

used to interrogate the sample, as in ultrafast experiments, it is common to treat the incident electric field as a sum of delta functions in time for the purpose of evaluating Eq. (2.8). Under this treatment, referred to as the impulsive approximation, the macroscopic polarization $P^{(n)}(t)$ is proportional to the response function $R^{(n)}(t)$, evaluated at the experimentally-controlled time delays between electric field pulses. Next, we will explore how the macroscopic polarization – and therefore the response function – is encoded in the measured signal field.

In the case of linear absorption, the macroscopic polarization is linear in the electric field. In the frequency domain, the linear susceptibility $\chi^{(1)}(\omega)$ is proportional to the Fourier transform of $R^{(1)}(t)$, shown in Eq. (2.17). The linear susceptibility can be related to the index of refraction *n* and absorption coefficient κ through the dielectric function $\varepsilon(\omega)$.

$$\begin{aligned} \varepsilon(\omega) &= 1 + 4\pi\chi^{(1)}(\omega) \\ \sqrt{\varepsilon(\omega)} &= n(\omega) + i\kappa(\omega) \end{aligned} \tag{2.29}$$

For simplicity, consider the absorption of a plane wave with fixed frequency ω propagating along the *z* direction, interacting with a sample of length *L*.

$$E(z,t) = Ae^{-i\omega t + ikz} + c.c. \tag{2.30}$$

Using Eqs. (2.1) and (2.17), the dispersion relation is,

$$\varepsilon(\omega) = k^2c^2 / \omega^2 \tag{2.31}$$

Plugging this expression back into Eq. (2.30) and integrating $I(z) = \left|E(z,t)\right|^2$ over the sample from $z = [0, L]$ recovers Beer's law.

$$\begin{aligned} I(L) &= I(0)e^{-\alpha(\omega)L} \\ \alpha(\omega) &= 2\omega\kappa(\omega)/c \end{aligned} \tag{2.32}$$

Finally, rearranging Eqs. (2.29) and (2.32) shows that the absorbance per unit length $\alpha(\omega)$ at frequency ω is proportional to the imaginary part of the linear susceptibility, defining the relationship between the linear absorption spectrum and first-order response function $R^{(1)}(t)$.

$$\alpha(\omega) = \frac{4\pi\omega}{n(\omega)c}\Im\left(\chi^{(1)}(\omega)\right) \tag{2.33}$$

In linear spectroscopy, Beer's law is the fundamental equation relating light absorption to the linear susceptibility. In nonlinear spectroscopy, a few additional steps are needed to relate the emitted field to the nonlinear response function. First, separating the polarization into linear and nonlinear terms $P(\mathbf{r},t) = P^{(1)}(\mathbf{r},t) + P^{NL}(\mathbf{r},t)$ puts Eq. (2.1) into a convenient form.

$$\nabla^2\mathbf{E}(\mathbf{r},t) - \frac{n^2}{c^2}\frac{\partial^2}{\partial t^2}\mathbf{E}(\mathbf{r},t) = \frac{4\pi}{c^2}\frac{\partial^2}{\partial t^2}\mathbf{P}^{NL}(\mathbf{r},t) \tag{2.34}$$

Here, Eqs. (2.17) and (2.29) were used to rewrite $\mathbf{E} + 4\pi\mathbf{P}$ in terms of the refractive index. Next, take a single oscillating term in the macroscopic polarization with frequency ω_p and a generated electric field of the form,

$$\begin{aligned} P(\mathbf{r},t) &= \mathrm{P}(t)e^{-i\omega_p t + i\mathbf{k}_p\mathbf{r}} + c.c. \\ E_{sig}(\mathbf{r},t) &= A_{sig}(\mathbf{r},t)e^{-i\omega_p t + i\mathbf{k}'_p\mathbf{r}} + c.c. \end{aligned} \tag{2.35}$$

The frequency and wavevector of the macroscopic polarization are a combination of the incident fields, and the wavevector of the generated field depends on the refractive index of the sample: $k'_p = n\omega_p / c.$

$$\begin{aligned} \omega_p &= \pm\omega_1 \pm \omega_2 \pm \omega_3 ... \\ \mathbf{k}_p &= \pm\mathbf{k}_1 \pm \mathbf{k}_2 \pm \mathbf{k}_3 ... \end{aligned} \tag{2.36}$$

Consider our sample of length *L*, with the electric field propagating along the *z* direction. Under conditions where light absorption is small, changes in the incident electric fields or the polarization along *z* can be neglected. We assume that the envelopes $P(t)$ and $A_{Sig}(\mathbf{r},t)$ vary slowly compared to the oscillation frequencies, referred to as the slowly-varying envelope approximation. Then, Eq. (2.34) can be integrated to find the crucial result relating P^{NL} to the measured electric field.[1]

$$E(L,t) = \frac{2\pi i}{n(\omega_p)} \frac{\omega_p L}{c} P^{NL}(t) \operatorname{sinc}\left(\frac{\Delta k_p L}{2}\right) e^{\Delta k_p L/2} \qquad (2.37)$$
$$\Delta k_p = k_p - k_p'$$

There are two important results contained in Eq. (2.37). First, the generated electric field is proportional to the nonlinear polarization with a phase shift of π. Therefore, the measured field reports directly on the nonlinear polarization, which is in turn proportional to the response function under the impulsive approximation. Second, the generated field has a spatial dependence through the sinc function, $\operatorname{sinc}(x) = \sin(x)/x$, which is sharply peaked at $x = 0$. The generated electric field radiates efficiently only in the direction determined by $\Delta k_p = 0$, referred to as the phase-matched direction. Using this relationship, the direction of the emitted field can be predicted based on the directions of incident beams and the type of nonlinear interaction.

Notably, phase matching is not a result of momentum conservation, as it may first appear. Instead, the phase-matched direction is the direction in which the radiating dipoles in the sample add constructively. This explains the dependence on sample length *L*, as perfect constructive interference occurs only among dipoles in the same plane perpendicular to the *z*-axis. Finally, it is important to note that the phase-matching condition is determined not only by the direction of each incident electric field, but also the frequency-dependent refractive index in the sample,

$k(\omega) = n(\omega)\omega / c.$ This can be neglected in our spectroscopy experiments, where the frequency dispersion of the liquid is small and the pathlength through the sample is short (1-50 μm). However, the dispersion of $n(\omega)$ will be a crucial factor for describing IR pulse generation by wave mixing in crystals (Chapter 3), where the interaction length is on the order of 1 mm.

2.1.5. Heterodyne detection

The emitted signal field in nonlinear experiments is detected as a function of frequency, either by interferometry or using a spectrometer. However, the detector can only directly measure the field intensity, not the phase. To obtain phase information, the signal is overlapped with a second field with known amplitude and phase called the local oscillator E_{LO}. The local oscillator could be a separately introduced beam or the probe pulse E_3 depending on the geometry of the experiment. The intensity measured by the detector is,

$$\begin{aligned} I(\omega) &= \frac{nc}{4\pi}\left|E_{Sig}(\omega) + E_{LO}(\omega)\right|^2 \\ &= \frac{nc}{4\pi}\left|E_{Sig}(\omega)\right|^2 + \frac{nc}{4\pi}\left|E_{LO}(\omega)\right|^2 + \frac{nc}{2\pi}\Re\left(E_{Sig}(\omega)E_{LO}(\omega)\right) \\ &\simeq \frac{nc}{4\pi}\left|E_{LO}(\omega)\right|^2 + \frac{nc}{2\pi}\left|E_{Sig}(\omega)\right|\left|E_{LO}(\omega)\right|\cos(\phi_{Sig}) \end{aligned} \tag{2.38}$$

The intensity of the signal is neglected since it is much smaller than the intensity of the local oscillator. What's left is the spectrum of the local oscillator and the interference between E_{LO} and E_{Sig}, which contains the phase of the signal ϕ_{Sig} relative to E_{LO}. The interference term can be isolated in a differential measurement, and independent measurement of the local oscillator spectrum $\left|E_{LO}\right|^2$ allows for the full characterization of signal field.

$$S(\omega) = \Delta I(\omega) \simeq \frac{nc}{2\pi} \left| E_{Sig}(\omega) \right| \left| E_{LO}(\omega) \right| \cos(\phi_{Sig}) \tag{2.39}$$

So, heterodyne detection enables measurement of both the amplitude and phase of the signal field. Together with Eq. (2.37) and the impulsive approximation, these relationships show that we can directly relate the observables in nonlinear spectroscopy to dipole time correlation functions which encode the molecular response.

2.2. Third order nonlinear response

Two-dimensional and transient absorption spectroscopy are third-order nonlinear techniques, where the corresponding macroscopic polarization is generated by three interactions with the electric field. Starting from Eq. (2.9), the third order nonlinear response can be written as follows. Expanding the commutators, the response function is the sum of eight total correlation functions $R_j^{(3)}$, four of which are complex conjugates of the other denoted by the asterisk in $R_j^{(3)*}$.

$$\begin{aligned} R^{(3)}(\tau_1,\tau_2,\tau_3) &= \left(\frac{i}{\hbar}\right)^3 \theta(\tau_1)\theta(\tau_2)\theta(\tau_3)... \\ &\quad \left\langle \Big[\mu(\tau_3+\tau_2+\tau_1), \Big[\mu(\tau_2+\tau_1), \big[\mu(\tau_1), \mu(0) \big] \Big] \Big] \rho_{eq} \right\rangle \\ &= \left(\frac{i}{\hbar}\right)^3 \sum_{j=1}^{4} R_j^{(3)}(\tau_1,\tau_2,\tau_3) - R_j^{(3)*}(\tau_1,\tau_2,\tau_3) \end{aligned} \tag{2.40}$$

The four unique correlation functions, also referred to as Liouville space pathways, are written in Eq. (2.41). Like linear absorption spectroscopy, the third order molecular response is encoded in a sum of dipole time correlation functions. Though, in the third order case there are more correlation functions to consider, and each is evaluated at four points in time with three time delays.

$$
\begin{aligned}
R_1^{(3)}(\tau_1,\tau_2,\tau_3) &= \left\langle \mu(\tau_3+\tau_2+\tau_1)\mu(0)\rho_{eq}\mu(\tau_1)\mu(\tau_2+\tau_1)\right\rangle \theta(\tau_1)\theta(\tau_2)\theta(\tau_3) \\
R_2^{(3)}(\tau_1,\tau_2,\tau_3) &= \left\langle \mu(\tau_3+\tau_2+\tau_1)\mu(\tau_1)\rho_{eq}\mu(0)\mu(\tau_2+\tau_1)\right\rangle \theta(\tau_1)\theta(\tau_2)\theta(\tau_3) \\
R_2^{(3)}(\tau_1,\tau_2,\tau_3) &= \left\langle \mu(\tau_3+\tau_2+\tau_1)\mu(\tau_2+\tau_1)\rho_{eq}\mu(0)\mu(\tau_1)\right\rangle \theta(\tau_1)\theta(\tau_2)\theta(\tau_3) \\
R_4^{(3)}(\tau_1,\tau_2,\tau_3) &= \left\langle \mu(\tau_3+\tau_2+\tau_1)\mu(\tau_2+\tau_1)\mu(\tau_1)\mu(0)\rho_{eq}\right\rangle \theta(\tau_1)\theta(\tau_2)\theta(\tau_3)
\end{aligned}
\tag{2.41}
$$

Using the cyclic invariance of the trace, the correlation functions are written so that dipole terms appear either on the ket-side (left) or bra-side (right) of the density matrix depending on the time ordering of the interactions. The correlation functions can be read as a sequence of events. For example, in $R_1^{(3)}$ the dipole operator acts on the density matrix from the ket-side at time 0, then from the bra-side at time τ_1, from the bra-side at $\tau_1+\tau_2$, then from the ket-side at $\tau_1+\tau_2+\tau_3$. The final interaction is always placed on the ket-side by convention.

Next, using the system-bath separation with a similar approach as Eq. (2.21) and taking the Condon approximation, the correlation functions can be re-written in terms of transition dipole matrix elements, oscillation center frequencies, and a lineshape function $F(\tau_1,\tau_2,\tau_3)$.[6] For generality, the functions are evaluated over four system eigenstates labeled |a⟩, |b⟩, |c⟩, and |d⟩. Without additional constraints, these could represent any states of the system. The result shows that each correlation function scales to the fourth order in transition dipole moment, and the dipole matrix elements included depend on the particular transitions induced by interactions with the electric field. During the delay periods between interactions the correlation function oscillates at difference frequencies between system energy levels.

$$
\begin{aligned}
R_1^{(3)}(\tau_1,\tau_2,\tau_3) &= \sum_{abcd} p_a \mu_{cd} \mu_{cb}{}^* \mu_{ba}{}^* \mu_{da} \exp(-i\omega_{da}\tau_1 - i\omega_{db}\tau_2 - i\omega_{dc}\tau_3) F^{abcd}(\tau_1,\tau_2,\tau_3) \\
R_2^{(3)}(\tau_1,\tau_2,\tau_3) &= \sum_{abcd} p_a \mu_{cd} \mu_{cb}{}^* \mu_{da} \mu_{ba}{}^* \exp(-i\omega_{ab}\tau_1 - i\omega_{db}\tau_2 - i\omega_{dc}\tau_3) F^{abcd}(\tau_1,\tau_2,\tau_3) \\
R_3^{(3)}(\tau_1,\tau_2,\tau_3) &= \sum_{abcd} p_a \mu_{cd} \mu_{da} \mu_{cb}{}^* \mu_{ba}{}^* \exp(-i\omega_{ab}\tau_1 - i\omega_{ac}\tau_2 - i\omega_{dc}\tau_3) F^{abcd}(\tau_1,\tau_2,\tau_3) \\
R_4^{(3)}(\tau_1,\tau_2,\tau_3) &= \sum_{abcd} p_a \mu_{ab} \mu_{bc} \mu_{cd} \mu_{da} \exp(-i\omega_{da}\tau_1 - i\omega_{ca}\tau_2 - i\omega_{ba}\tau_3) F^{abcd}(\tau_1,\tau_2,\tau_3)
\end{aligned}
\tag{2.42}
$$

These correlation functions are often represented diagrammatically using the notation in Fig. 2.3. In the diagram, time increases in the upwards direction and light-matter interactions occur at time points denoted by horizontal lines. The state of the system before the first interaction, and during the time delays $\tau_1 - \tau_3$, is represented by the density matrix. For example, in $R_1^{(3)}$ during τ_1 the system is in the state |d⟩⟨a|, corresponding to the oscillating term $\exp(-i\omega_{da}\tau_1)$. Each light-matter interaction contributes one dipole matrix element term to the correlation function. For example, in $R_1^{(3)}$ the first interaction occurs on the left side from state |a⟩ to state |d⟩, with the corresponding dipole matrix element μ_{da}. Interactions from the right follow the same rules but contribute the complex conjugate of the dipole matrix element. For example, the second interaction in $R_1^{(3)}$ contributes dipole matrix element μ_{ba}^*.

While the correlation functions contain only system DOF, some information about the field can be incorporated under appropriate considerations. In a 2D IR experiment, the incident electric field is composed of three pulses of light, each with a carrier frequency ω_j and sharply peaked in time at a controllable time t_j (Eq. (2.5)). First, assume that the pulses interact with the sample in the order that they arrive, referred to as the pulse-ordering approximation.

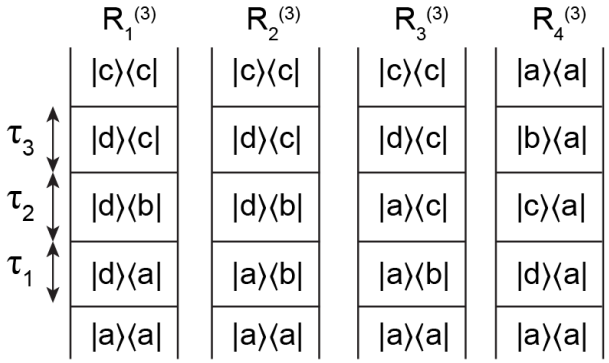

Figure 2.3. Diagrammatic representation of the third-order Liouville pathways.

Next, consider a resonant interaction of the first pulse with the sample. Since the electric field is real-valued, it contains oscillating terms $\exp\left(-i\omega_j t\right)$ and $\exp\left(+i\omega_j t\right)$. However, only one of these terms will be resonant with the oscillating term in the response function, and the other will result in an oscillation at approximately $\pm 2\omega_j$. When calculating the polarization (Eq. (2.8)), the integral of this rapidly-oscillating term will tend towards 0, and can therefore be neglected. This is referred to as the rotating wave approximation (RWA). Since the signs of the electric field frequency and wavevector are related, the RWA implies that each transition between states in the correlation function constrains the wavevector of the interacting electric field.

To illustrate the implications of the RWA, let's reduce the number of pathways we need to consider by describing a model system in a fixed experimental geometry. Consider a system with eigenstates labeled |ν⟩, with $\nu = 1, 2, 3...$ which follows harmonic dipole selection rules, $\Delta\nu = \pm 1$. Begin each pathway in the ground state |0⟩⟨0|, which is appropriate for vibrations in the mid-IR where $\omega_{10} / 2\pi c >> k_B T / hc \approx 207\,\mathrm{cm}^{-1}$ at room temperature. Then, select for only signals emitted in the direction of the third pulse, $+\mathbf{k}_3$. Experimentally, this is accomplished by aligning the first

two pump pulses in a collinear geometry, crossed with the third probe pulse and placing the detector in the beam line of the probe after the sample. This is referred to as the pump-probe geometry,[16,17] which was used in all experiments in this thesis. In order for the emitted signal to radiate efficiently in the direction of the probe, the wavevectors of the first two pulses must cancel, so the phase-matching condition is $\mathbf{k_{Sig}} = \pm\mathbf{k_1} \mp \mathbf{k_2} + \mathbf{k_3}$.

In diagrammatic perturbation theory, electric field wavevectors are incorporated in the form of arrows pointing in or out of the diagram. Arrows pointing right denote a positive wavevector; left denotes negative wavevector. Under the RWA, arrows pointing inwards correspond to upwards transitions in the density matrix (from a lower-energy state to a higher-energy state); outward pointing arrows correspond to downwards transitions.

Figure 2.4 shows the six Liouville space pathways which meet the phase-matching and dipole selection rule criteria for our model system in the pump-probe geometry. The pathways can be further characterized based on the transition frequencies and oscillation phases during time periods τ_1 and τ_3. Under the conditions considered, the system is always in a population state during τ_2 and therefore does not oscillate. However, for a general system coherence pathways are also possible; for example if two different resonances fall within the bandwidth of the pump pulses.[18] During τ_1 and τ_3 the system is in a coherence state, and oscillates with either positive or negative phase. Dephasing occurs during τ_1, which continues during τ_3 if the oscillation phases are equal (nonrephasing pathway). If the oscillation phases are opposite during τ_1 and τ_3, then some or all of the dephasing is reversed during τ_3 (rephasing pathway).

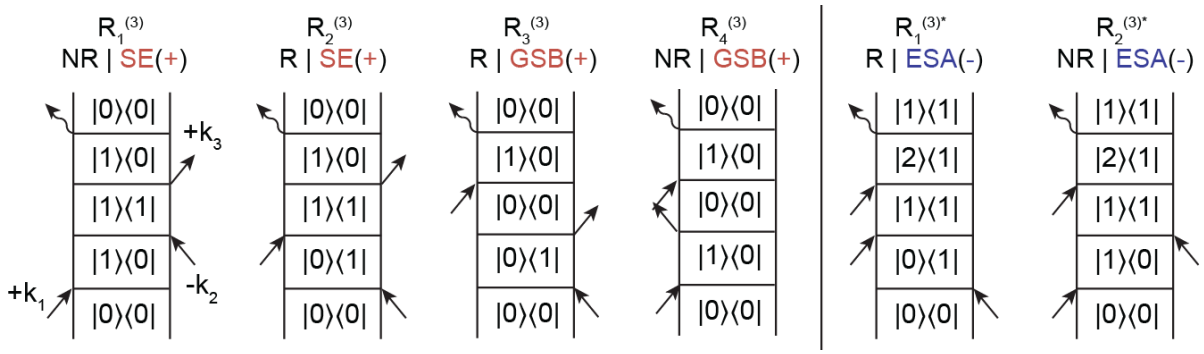

Figure 2.4. Diagrammatic representation of the Liouville space pathways for the phase matching condition $\mathbf{k_{Sig}} = \pm\mathbf{k_1} \mp \mathbf{k_2} + \mathbf{k_3}$ and a single vibration obeying harmonic dipole selection rules. Pathways are labeled with the corresponding $R_j^{(3)}$ terms, rephasing (R) or nonrephasing (NR), as ground state bleach (GSB), stimulated emission (SE), or excited state absorption (ESA), and with the sign of the term (+/-). The wavevectors implied by arrows are denoted for $R_1^{(3)}$.

The oscillation frequency during τ_1 indicates the center excitation frequency of the pathway, and oscillation frequency during τ_3 indicates the center detection frequency. In the pathways shown in Fig. 2.4 GSB and SE pathways both oscillate at ω_{10} during both of those time periods, and are differentiated by the population state during τ_2. ESA pathways instead oscillate at ω_{21} during τ_3, and are negatively signed. The sign of a pathway can be determined by the number of bra-side dipole interactions, since each one contributes a negative sign from the commutators in Eq. (2.40). In the differential 2D IR and TA experiments, the sign determines whether the signal from that pathway is measured as an increase (+) or decrease (-) in transmitted light at the corresponding detection frequency.

2.3. 2D IR and TA spectroscopy

2.3.1. 2D IR and TA signal

In 2D IR spectroscopy, the third order molecular response is represented in the mixed frequency-time domain by taking the Fourier transforms over time delays τ_1 and τ_3. The measured signal is plotted as a 2D map with frequencies ω_1 (excitation frequency) and ω_3 (detection frequency) on the axes at a fixed τ_2 (waiting time).

$$S_{2D}(\omega_1,\tau_2,\omega_3) \propto \Re\left[\int_{-\infty}^{\infty} d\tau_3 e^{i\omega_3\tau_3} \int_{-\infty}^{\infty} d\tau_1 e^{i\omega_1\tau_1} R^{(3)}(\tau_1,\tau_2,\tau_3)\right] \tag{2.43}$$

In TA, or "pump-probe," spectroscopy all measurements are made with $\tau_1 = 0$ and therefore the excitation frequency is not resolved. This is formally equivalent to integrating the 2D IR spectrum across ω_1 by the projection-slice theorem.[17] Clearly, less information is present in the TA measurement, but in practice it is very useful when we wish to efficiently sample many points along τ_2.

$$S_{TA}(\tau_2,\omega_3) \propto \int_{-\infty}^{\infty} d\omega_1 S_{2D}(\omega_1,\tau_2,\omega_3) \tag{2.44}$$

When interpreting spectra, we typically do not include all terms in $R^{(3)}$ in Eq. (2.43). Instead, we select a set of pathways based on phase-matching conditions, selection rules, and the other considerations discussed in the previous section. For example, consider the case of a single vibration with a weakly-anharmonic potential energy surface, which led to the six pathways pictured in Fig. 2.4. In general, the third-order lineshape functions $F(\tau_1,\tau_2,\tau_3)$ could be quite

complicated, but for the sake of illustration consider a simple case with dephasing with rate Γ during τ_1 and τ_3, and population relaxation with time constant T_1 during τ_2.

$$F(\tau_1,\tau_2,\tau_3)=\theta(\tau_1)\theta(\tau_2)\theta(\tau_3)e^{-\Gamma\tau_1-\tau_2/T_1-\Gamma\tau_3} \tag{2.45}$$

Since the Fourier transform of a decaying exponential is a Lorentzian, Eq. (2.45) results in a two-dimensional Lorentzian lineshape in the 2D IR spectrum. Model 2D IR and TA spectra of this system are presented in Fig. 2.5. Since there are equal numbers of rephasing (R) and nonrephasing (NR) pathways in Fig. 2.4, the resulting spectra have purely absorptive lineshapes. This can be shown by writing out the terms for $R_j^{(3)}$ using Eqs. (2.42) and (2.45).[6] Absorptive 2D lineshapes are a feature of the pump-probe geometry, where both rephasing $(-\mathbf{k_1}+\mathbf{k_2}+\mathbf{k_3})$ and nonrephasing $(+\mathbf{k_1}-\mathbf{k_2}+\mathbf{k_3})$ pathways are phase-matched in the direction of the probe and added perfectly *in situ*. The R and NR pathways can be separated using the boxcars geometry,[4,17,19] but for the work in this thesis absorptive lineshapes are desirable since they are more straightforward to interpret.

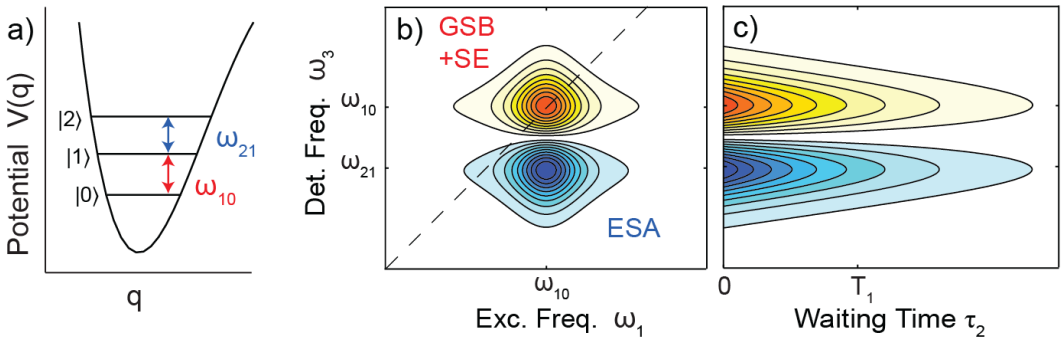

Figure 2.5. A model three-level system with (a) weakly anharmonic potential and the corresponding (b) 2D IR and (c) TA spectra from the pathways in Fig. 2.4. Positive amplitudes are in red and negative amplitudes in blue.

Much information is contained in the 2D IR and TA spectra, even for the simple model system considered in Fig. 2.5. The excitation and detection frequencies report on the coherence states occupied during τ_1 and τ_3, respectively. Therefore, ω_{10} and ω_{21} can be read off the peak positions along the detection frequency axis, providing constraints on the shape of the corresponding potential energy surface. In a harmonic potential $\omega_{21} = \omega_{10}$, so the difference $\chi = \omega_{10} - \omega_{21}$ provides a measure of anharmonicity. In most cases, molecular vibrations experience potentials qualitatively similar to the one pictured in Fig. 2.5 with $\chi > 0$ $\left(\omega_{21}/\omega_{10} < 1\right)$.[4] Though, as discussed in Chapter 1, 2D IR experiments of some strong H-bonding systems have revealed vibrations with $\chi < 0$,[20–22] providing evidence of vibrational potentials with large deviations from a harmonic oscillator.

The amplitude of each feature in the 2D IR spectrum is determined by the number of pathways centered at the same excitation and detection frequencies and the corresponding transition dipole matrix elements. Each feature scales to the fourth power with the transition dipole moment, as shown in Eq. (2.42), though the particular elements depend on the pathway. In the system considered in Figs. 2.4-2.5, the two SE and two GSB pathways scale with $|\mu_{10}|^4$, while the two ESA pathways scale with $|\mu_{21}|^2 |\mu_{10}|^2$. Assuming the dipole moment surface is harmonic, then $|\mu_{21}| = \sqrt{2}|\mu_{10}|$. Under that approximation, the positive and negative features in Fig. 2.5b have equal amplitudes of $4|\mu_{10}|^4$.

2.3.2. Population relaxation

In section 2.1.3 it was shown that the lineshape of a vibrational transition contains information about both the static distribution of molecular environments (inhomogeneous broadening) and dynamics including population relaxation, orientational diffusion, and collisions or bath fluctuations (homogeneous broadening). While these are convolved in the linear absorption spectrum, they can be measured independently with 2D IR spectroscopy. From Eq. (2.24), the lineshape is determined by the frequency-frequency correlation function, which in turn is expressed in terms of a homogeneous dephasing rate Γ and inhomogeneous distribution Δ, under the appropriate approximations. The homogeneous dephasing rate can be further decomposed into contributions from the molecular rate processes which contribute to the linewidth.

$$\Gamma = \frac{1}{T_2^*} + \frac{1}{2T_1} + \frac{1}{\tau_{or}} \tag{2.46}$$

Here, T_2^* is the timescale of pure dephasing, T_1 is the population relaxation timescale, and τ_{or} is the timescale of orientational diffusion.

The population relaxation, or lifetime, can be measured straightforwardly in TA (or 2D) spectroscopy. All six of the pathways in Fig. 2.4 decay in amplitude during τ_2 with the depopulation of the first excited state $\rho_{11} = |1\rangle\langle 1|$. This is clear for the SE and ESA pathways, which are in the state $|1\rangle\langle 1|$ during τ_2. The GSB pathways, on the other hand, decay in amplitude as the ground state $|0\rangle\langle 0|$ is repopulated, which occurs at the same rate as $|1\rangle\langle 1|$ relaxes in the model system. Therefore, T_1 can be measured by the decay rate of either the positive or negative diagonal

feature. When measuring population relaxation, care must be taken to separate the contribution from orientational diffusion, discussed in section 2.3.4.

2.3.3. 2D IR lineshape

In 2D IR spectroscopy, the lineshape of a feature is a correlation map between oscillation frequencies at the times of excitation and detection. At the time of excitation, an ensemble of oscillators are vibrationally excited with a distribution of instantaneous frequencies reflecting their molecular environments (eg., O-H bonds with a distribution of H-bonding strengths). During τ_2 fluctuations in the bath cause these molecular environments to exchange, leading to a decay in the correlation. This is displayed schematically in Fig. 2.6 where the lineshape is calculated using the Gaussian stochastic model,[11] Eqs. (2.25)-(2.26). Here, τ_c is the timescale for bath fluctuations.

The lineshape evolution of the 2D IR feature reflects the dynamics of the FFCF during τ_2, $\langle \delta\omega_{10}(0)\delta\omega_{10}(\tau_2)\rangle$. There are several lineshape parameters which can be related to the FFCF including the slope of the center line through the local maxima,[23] the slope of the nodal line between positive and negative features,[24] the ellipticity of the band,[25] and the slope in phase space.[26] In Fig. 2.6 the center line and corresponding time-dependent center line slope (CLS) are plotted to illustrate one method for obtaining this information from an experiment. The numerical correspondence between CLS, or other metrics, and the FFCF rely on the Condon and cumulant approximations, but can capture more complex dynamics than the single exponential form in the Gaussian stochastic model.

Furthermore, since inhomogeneous broadening is reflected only along the diagonal, the homogeneous and inhomogeneous linewidths are separated in the early-time $(\tau_2 << \tau_c)$ 2D

lineshape. The anti-diagonal linewidth is homogeneously broadened, while the diagonal linewidth is broadened by both homogeneous and inhomogeneous mechanisms. Therefore, the homogeneous dephasing rate Γ can be measured directly from the anti-diagonal linewidth. Together with T_1, the unknown information in Eq. (2.46) can be narrowed down to T_2^* and τ_{or}.

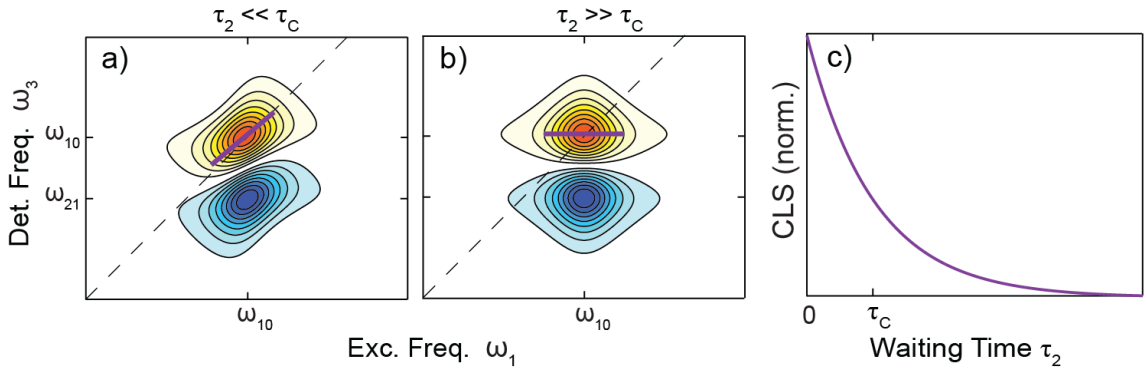

Figure 2.6. 2D IR spectrum of a two-level system with $\omega_{21}/\omega_{10} = 0.88$, modeled using the Gaussian stochastic model with $\tau_c = 30\,\text{fs}$ and $\Delta = 1100\ \text{cm}^{-1}$ for (a) $\tau_2 = 0$ and (b) $\tau_2 = 100\,\tau_c$. The center line is drawn in purple and the center line slope (CLS) decay with time is shown in (c), which decays with the same timescale as the FFCF.

2.3.4. Polarization anisotropy

Transient absorption and 2D IR spectroscopy can measure orientational diffusion through the correlation between transition dipole moment directions. Until this point, the vectorial nature of both the electric fields and transition dipole matrix elements have been ignored. However, each field-matter interaction depends on the angle φ between the transition dipole and the polarization of the electric field. So, the probability of absorption or emission depends on the polarization of the field.

$$V = -\boldsymbol{\mu} \cdot \mathbf{E} = \mu E \cos(\varphi) \tag{2.47}$$

In the experiments in this thesis all fields are linearly polarized along laboratory frame directions X, Y, or Z. The medium is isotropic, so the measured signal can be treated as the ensemble average over a collection of randomly oriented dipoles. The pump pulses E_1 and E_2, polarized in the same direction, preferentially excite the sub-ensemble of transition dipoles pointing along the polarization direction with a $\cos^2(\varphi)$ distribution, according to Eq. (2.47). The subsequent interaction with E_3 and emission of E_{Sig} also occurs with a $\cos^2(\varphi')$ probability distribution, where φ' is the angle between $\boldsymbol{\mu}$ and $\mathbf{E_3}$. Therefore, control over the probe polarization (relative to the pump) is the basis for measuring orientational correlation in the sample.

To work out the relationship between polarization and dipole orientational correlation, the third order response functions are separated into a product of the correlation functions R_j^{abcd}, which contain only the vibrational dynamics, and orientational tensors Y_{IJKL}^{abcd} which contain only the orientational dynamics. The indices *IJKL* correspond to the field polarizations along the laboratory frame directions {X,Y,Z}, while the indices *abcd* correspond to the directions of the dipole moments in the molecular frame, each evaluated at the four time points of interaction.

$$R_j^{(3)}(\tau_1,\tau_2,\tau_3) = \sum_{IJKL}\sum_{abcd} Y_{IJKL}^{abcd}(\tau_1,\tau_2,\tau_3) R_j^{abcd}(\tau_1,\tau_2,\tau_3) \tag{2.48}$$

The tensor elements Y_{IJKL}^{abcd} are a map between the molecular frame and the laboratory frame. The dipole moment can reorient during time delays according to the orientational diffusion equation.

$$\frac{\partial W(\Omega,t)}{\partial t} = D_{or}\nabla^2 W(\Omega,t) \tag{2.49}$$

Here, $W(\Omega,t)$ is the probability that the dipole moment is orientated at the set of Euler angles Ω at time t and D_{or} is the orientational diffusion constant.[27,28] The tensor elements Y_{IJKL}^{abcd} have been derived elsewhere[6,27] by averaging over all possible orientations in an isotropic medium. Most of the tensor elements vanish in an isotropic system; only four are nonzero: Y_{ZZZZ}, Y_{ZZYY}, Y_{ZYYZ}, and Y_{ZYZY}, three of which are independent. For a single transition the upper indices are all the same, so they have been dropped for simplicity. For the experiments described here only two elements need to be considered, Y_{ZZZZ} which corresponds to all fields polarized in the same direction, and Y_{ZZYY} which corresponds to perpendicular pump-probe polarization.

$$\begin{aligned} Y_{ZZZZ}(\tau_1,\tau_2,\tau_3) &= \frac{1}{9}C_1(\tau_1)C_1(\tau_3)\left(1+\frac{4}{5}C_2(\tau_2)\right) \\ Y_{ZZYY}(\tau_1,\tau_2,\tau_3) &= \frac{1}{9}C_1(\tau_1)C_1(\tau_3)\left(1-\frac{2}{5}C_2(\tau_2)\right) \end{aligned} \tag{2.50}$$

Here, $C_1(\tau)$ and $C_2(\tau)$ are two-point dipole correlation functions which track the orientational correlation between the transition dipole moment direction at the times 0 and τ through the angle $\theta(\tau)$ between them.[28,29] These are expanded in Eq. (2.51), where P_k is the k^{th} order Legendre polynomial.

$$\begin{aligned} C_1(\tau) &= \left\langle P_1\left(\boldsymbol{\mu}(\tau)\cdot\boldsymbol{\mu}(0)\right)\right\rangle = \left\langle\cos(\theta)\right\rangle \\ C_2(\tau) &= \left\langle P_2\left(\boldsymbol{\mu}(\tau)\cdot\boldsymbol{\mu}(0)\right)\right\rangle = \left\langle\frac{1}{2}\left(3\cos^2(\theta)-1\right)\right\rangle \end{aligned} \tag{2.51}$$

Together, Eqs. (2.50) and (2.51) show the orientational dependence of the third order nonlinear signal, which is encoded in $C_2(\tau_2)$ during the waiting time. Experimentally, the tensor elements of the third order signal S_{ZZZZ} and S_{ZZYY} can be measured by rotating the probe polarization parallel (ZZZZ) or perpendicular (ZZYY) to the pump polarization. During τ_2, these signals depend on both population relaxation $B(\tau_2)$ (which decays with the lifetime T_1) and orientational correlation $C_2(\tau_2)$. Taking the appropriate sums or differences can isolate either the isotropic population relaxation, which is independent of orientation, or the orientational anisotropy.

$$\begin{aligned} B(\tau_2) &= \frac{1}{3} S_{Iso} = \frac{1}{3}\left(S_{ZZZZ} + 2S_{ZZYY}\right) \\ r(\tau_2) &= \frac{S_{ZZZZ} - S_{ZZYY}}{S_{ZZZZ} + 2S_{ZZYY}} = \frac{2}{5} C_2(\tau_2) \end{aligned} \tag{2.52}$$

The isotropic component of the spectrum S_{Iso} is isolated by taking the sum of $S_{ZZZZ} + 2S_{ZZYY}$, which cancels the orientational dependence shown in Eq. (2.50). This is equivalent to measuring the spectrum with probe polarized at the "magic angle" of 54.7˚ relative to the pump, which is the zero of $P_2(\cos\theta)$. The anisotropy $r(\tau_2)$ is isolated by taking the difference $S_{ZZZZ} - S_{ZZYY}$ and dividing by the isotropic component, providing a measurement of the orientational correlation function. The anisotropy has a maximum value of 0.4, corresponding to perfect orientational correlation; $r = 0$ corresponds to total orientational decorrelation. Isotropic and anisotropic spectra are resolved as a function of ω_3 in TA and both ω_1 and ω_3 in 2D IR spectra.

In the case of small-angle orientational diffusion, the orientational correlation function decays as a single exponential $C_2(\tau_2) = \exp(-6\tau_2 / \tau_{or})$.[28,30] Often, orientational relaxation is measured

with TA spectroscopy for efficient τ_2 sampling. A model TA spectrum with single-exponential population and orientational relaxation is displayed in Fig. 2.7. In the experiments in this thesis, the ZZZZ and ZZYY components of the spectrum were measured simultaneously, as described in Chapter 3, then the isotropic spectrum and anisotropy were calculated using Eq. (2.52).

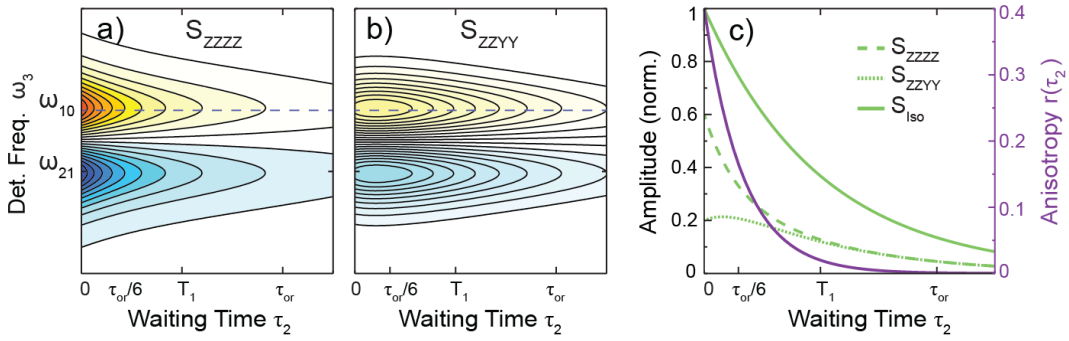

Figure 2.7. Model TA spectrum with single exponential population relaxation $B(\tau_2)=\exp(-\tau_2/T_1)$ and orientational relaxation $C_2(\tau_2)=\exp(-6\tau_2/\tau_{or})$, plotted with $\tau_{or}=2T_1$. (a) ZZZZ and (b) ZZYY spectral components are displayed with (c) traces of the isotropic spectrum, ZZZZ and ZZYY components, and anisotropy at $\omega_3=\omega_{10}$.

2.3.5. Cross peaks

The description so far has examined the 2D IR and TA observables corresponding to a single vibration, focusing largely on the implications for dynamics. When two or more vibrations are present, 2D IR spectroscopy can also provide information about correlations between those vibrations. This is revealed by a change in absorbance at the frequency of one vibration after the excitation of a second vibration, referred to as a cross peak. Such signals also contribute to TA spectra, but are more clearly resolved from overlapping features at the same detection frequency in 2D IR spectroscopy. Cross peaks therefore contain structural information from the

two-dimensional potential energy surface along two vibrational coordinates, as well as the relative angles between transition dipole moments.

For an example, consider two vibrations with fundamental frequencies and transition dipole moments labeled ω^{α}, $\boldsymbol{\mu}^{\alpha}$ and ω^{β}, $\boldsymbol{\mu}^{\beta}$. In the case of weak coupling, with constant $\Delta << \left|\omega^{\alpha} - \omega^{\beta}\right|$, the coupling is a perturbation on the unmixed states, and the mixed states can be labeled according to the unmixed states that they most closely resemble. The six lowest lying states are {|0⟩, |β⟩, |α⟩, |2β⟩, |αβ⟩, |2α⟩}, where |α⟩ and |2α⟩ represent the first and second excited states of oscillator α and the combination band |αβ⟩ represents one quantum of excitation in each α and β. The energy level diagram for the resulting 6-level system is depicted in Fig. 2.8a, with the corresponding model 2D IR spectrum plotted in Fig. 2.8b plotted with homogeneous lineshapes.

Along the diagonal $\left(\omega_3 = \omega_1\right)$, positive and negative features arise from transitions of a single vibration. Peaks labeled I & I' correspond to the six diagrams in Fig. 2.4, with frequencies determined by ω_{10}^{α} and ω_{21}^{α}. Similarly, peaks labeled II & II' arise from transitions associated with only oscillator β.

The cross peaks labeled III & III' appear near ω_{10}^{β} following excitation of ω_{10}^{α}. Peak III arises from bleaching at ω_{10}^{β} due to the depletion of the shared ground state. Peak III' arises from excited state absorption to the combination band |αβ⟩ from |α⟩, which occurs at the frequency difference between those states. Therefore, the splitting between cross peak features III & III' measures a change in the potential energy surface of ω^{β} when one quantum of energy is put into oscillator α. Of course, for uncoupled oscillators there is no change, and no cross peak would be observed.

The amplitudes and transition dipole scaling of the cross peak features can be calculated from the Liouville space pathways, which are displayed diagrammatically for peaks III & III" in Fig. 2.8c. Each peak arises from two pathways, one rephasing and one nonrephasing, which all scale as $\left|\mu_{10}^{\alpha}\right|^2\left|\mu_{10}^{\beta}\right|^2$, assuming a harmonic transition dipole surface. This implies that the positive and negative cross-peak features have equal amplitude. And, since half as many pathways contribute to peak III than peak I, the cross peaks are typically lower intensity than diagonal features (if the two vibrations have similar transition dipole strengths).

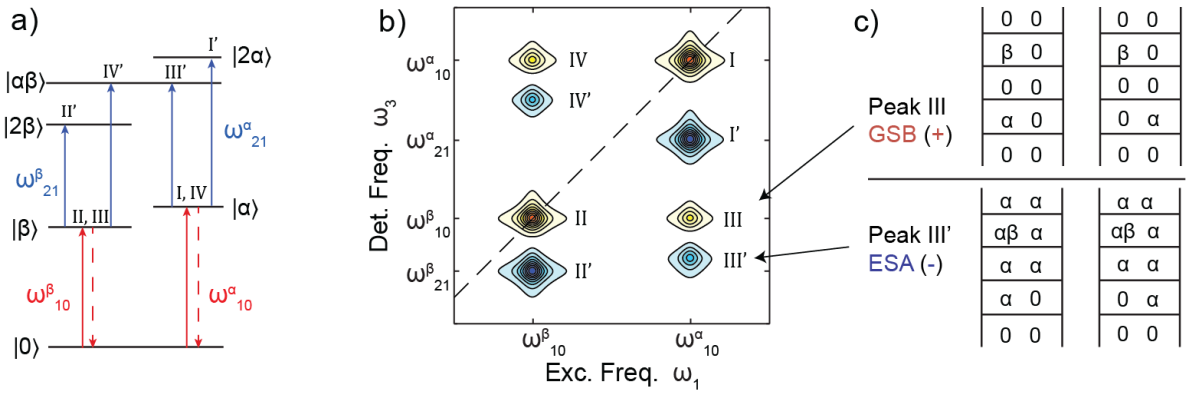

Figure 2.8. Model 2D IR spectrum of two coupled oscillators labeled ω^{α} and ω^{β}. (a) Energy level diagram. (b) Model 2D IR spectrum with homogeneous lineshapes. Peak labels I-IV and I'-IV' correspond to transitions labeled in (a). (c) Diagrams for the cross peak doublet labeled III and III'.

In addition to the downhill cross peaks III & III', a corresponding set of uphill cross peaks IV & IV' appear when ω_{10}^{β} is excited. These carry the same information as the downhill cross peaks, with the same splitting and dipole scaling, and the Liouville space pathways can be constructed simply by exchanging α and β in Fig. 2.8c. In practice, one cross peak may be more straightforward to measure or interpret than the other due to spectral overlap with other features.

In addition to anharmonic coupling between oscillators, depicted in Fig. 2.8, cross peaks can also arise from chemical exchange. By chemical exchange, we mean a dynamical switching between configurations with distinct vibrational spectra. For example, an O-H stretch vibration could exchange between H-bonded and non-H-bonded configurations, or a molecule could exchange between protonated and deprotonated states. In that case, the cross peak arises from oscillators which are in state α when they are excited, then in state β when they are detected after the time delay τ_2. Chemical exchange cross peaks will not be present at $\tau_2 = 0,$ and will grow in intensity with the timescale of chemical exchange. Therefore, they can be distinguished from anharmonic coupling cross peaks (which are present at $\tau_2 = 0$) by the time-dependence of the cross peak amplitude. An analysis of time-dependent cross peak amplitude must also account for energy transfer between coupled oscillators.[4] In this thesis, most 2D IR spectra presented were collected at $\tau_2 = 100\,\text{fs},$ which was the earliest measurable waiting time outside of pulse overlap. Chemical exchange can be neglected in the analysis of cross peaks at these early waiting times, since 100 fs is much shorter than the picosecond timescales for atomic rearrangements of water and hydrated protons in the liquid phase.[31–34]

Importantly, cross peaks can also arise from transitions that break harmonic selection rules, which have been excluded from all model spectra so far. In the system described in Fig. 2.8, consider the dipole-forbidden transition from $|\alpha\rangle$ to $|2\beta\rangle$. This would lead to an ESA feature centered at ω_{10}^{α} in excitation frequency and a detection frequency below peak III'. For weakly-anharmonic vibrations, such dipole-forbidden transitions will have extremely low intensity, and are often not considered for that reason. However, dipole-forbidden transitions could

be quite intense for vibrations with highly-anharmonic potentials.[35] This possibility is examined in detail for a double-well O-H stretch potential in Chapter 7.

Cross peak anisotropy

Cross peaks arising from anharmonic coupling between two vibrations also carry information about the relative angle between the transition dipole moments of those vibrations. Consider the system in Fig. 2.8, where two coupled vibrations have fundamental frequencies and transition dipole moments ω^{α}, $\boldsymbol{\mu}^{\alpha}$ and ω^{β}, $\boldsymbol{\mu}^{\beta}$. The orientational component of the cross peak spectrum can be obtained by calculating the anisotropy from S_{ZZZZ} and S_{ZZYY} according to Eq. (2.52). By accounting for all orientational factors that contribute to these signals,[6,28] it can be shown that the anisotropy of the cross peak, at $\tau_2 = 0,$ is related to the angle between transition dipole moments $\theta_{\alpha\beta}$ according to Eq. (2.53).

$$r\left(\omega^{\alpha},\omega^{\beta}\right) = \frac{2}{5}\left\langle P_2\left(\cos\left(\theta_{\alpha\beta}\right)\right)\right\rangle \tag{2.53}$$

The cross peak anisotropy ranges from 0.4 for parallel dipoles $\left(\theta_{\alpha\beta} = 0\right)$ to -0.2 for perpendicular dipoles $\left(\theta_{\alpha\beta} = \pi/2\right)$. An anisotropy value of 0 could correspond to either a fixed magic-angle orientation in the molecular frame or to uncorrelated, randomly-oriented dipoles.

2.4. References

(1) Mukamel, S. *Principles of Nonlinear Optical Spectroscopy*; New York, 1995.

(2) Boyd, R. J. *Nonlinear Optics*, 3rd ed.; Rochester, NY, 2007.

(3) Tokmakoff, A. *Time-Dependent Quantum Mechanics and Spectroscopy*. http://tdqms.uchicago.edu/.

(4) Hamm, P.; Zanni, M. *Concepts and Methods of 2D Infrared Spectroscopy*; Cambridge University Press: Cambridge, UK and New York, NY, USA, 2011.

(5) Cho, M. *Two-Dimensional Optical Spectroscopy*; CRC Press: Boca Raton, USA, 2009.

(6) De Marco, L. The Molecular Dynamics of Hydrogen-Bonding Explored with Broadband Two Dimensional Infrared Spectroscopy, Massachusetts Institute of Technology, 2016.

(7) Ramasesha, K. Dynamics of Water and Aqueous Protons Studied Using Ultrafast Multi-Dimensional Infrared Spectroscopy, Massachusetts Institute of Technology, 2013.

(8) Carpenter, W. B. Aqueous Proton Structures and Dynamics Observed with Nonlinear Infrared Spectroscopy, University of Chicago, 2020. https://knowledge.uchicago.edu/record/2584.

(9) Chandler, D. *Introduction to Modern Statistical Mechanics*; 1987. https://doi.org/10.1016/j.jcrs.2007.12.047.

(10) Schmidt, J. R.; Corcelli, S. A.; Skinner, J. L. Pronounced Non-Condon Effects in the Ultrafast Infrared Spectroscopy of Water. *J. Chem. Phys.* **2005**, *123* (4). https://doi.org/10.1063/1.1961472.

(11) Kubo, R. A Stochastic Theory of Line Shape. *Adv. Chem. Phys.* **1969**, *XV* (1), 101. https://doi.org/10.1002/9780470143605.ch6.

(12) Loparo, J. J.; Roberts, S. T.; Nicodemus, R. A.; Tokmakoff, A. Variation of the Transition Dipole Moment across the OH Stretching Band of Water. *Chem. Phys.* **2007**, *341* (1–3), 218–229. https://doi.org/10.1016/j.chemphys.2007.06.056.

(13) Fecko, C. J.; Loparo, J. J.; Roberts, S. T.; Tokmakoff, A. Local Hydrogen Bonding Dynamics and Collective Reorganization in Water: Ultrafast Infrared Spectroscopy of HOD/D2O. *J. Chem. Phys.* **2005**, *122* (5), 054506. https://doi.org/10.1063/1.1839179.

(14) Eaves, J. D.; Tokmakoff, A.; Geissler, P. L. Electric Field Fluctuations Drive Vibrational Dephasing in Water. *J. Phys. Chem. A* **2005**, *109* (42), 9424–9436. https://doi.org/10.1021/jp051364m.

(15) Eaves, J. D.; Loparo, J. J.; Fecko, C. J.; Roberts, S. T.; Tokmakoff, A.; Geissler, P. L. Hydrogen Bonds in Liquid Water Are Broken Only Fleetingly. *Proc. Natl. Acad. Sci.* **2005**, *102* (37), 13019–13022. https://doi.org/10.1073/pnas.0505125102.

(16) DeFlores, L. P.; Nicodemus, R. A.; Tokmakoff, A. Two-Dimensional Fourier Transform Spectroscopy in the Pump-Probe Geometry. *Opt. Lett.* **2007**, *32* (20), 2966. https://doi.org/10.1364/ol.32.002966.

(17) Faeder, S. M. G.; Jonas, D. M. Two-Dimensional Electronic Correlation and Relaxation Spectra: Theory and Model Calculations. *J. Phys. Chem. A* **1999**, *103* (49), 10489–10505. https://doi.org/10.1021/jp9925738.

(18) Khalil, M.; Demirdöven, N.; Tokmakoff, A. Coherent 2D IR Spectroscopy: Molecular Structure and Dynamics in Solution. *J. Phys. Chem. A* **2003**, *107* (27), 5258–5279. https://doi.org/10.1021/jp0219247.

(19) Khalil, M.; Demirdöven, N.; Tokmakoff, A. Coherent 2D IR Spectroscopy: Molecular Structure and Dynamics in Solution. *J. Phys. Chem. A* **2003**, *107* (27), 5258–5279. https://doi.org/10.1021/jp0219247.

(20) Fournier, J. A.; Carpenter, W. B.; Lewis, N. H. C.; Tokmakoff, A. Broadband 2D IR Spectroscopy Reveals Dominant Asymmetric H5O2+ Proton Hydration Structures in Acid Solutions. *Nat. Chem.* **2018**, *10*, 932–937. https://doi.org/10.1038/s41557-018-0091-y.

(21) Dahms, F.; Fingerhut, B. P.; Nibbering, E. T. J.; Pines, E.; Elsaesser, T. Large-Amplitude Transfer Motion of Hydrated Excess Protons Mapped by Ultrafast 2D IR Spectroscopy. *Science* **2017**, *357* (6350), 491–495. https://doi.org/10.1126/science.aan5144.

(22) Dereka, B.; Yu, Q.; Lewis, N. H. C.; Carpenter, W. B.; Bowman, J. M.; Tokmakoff, A. Crossover from Hydrogen to Chemical Bonding. *Science* **2021**, *371* (6525), 160–164. https://doi.org/10.1126/science.abe1951.

(23) Kwak, K.; Park, S.; Finkelstein, I. J.; Fayer, M. D. Frequency-Frequency Correlation Functions and Apodization in Two-Dimensional Infrared Vibrational Echo Spectroscopy: A New Approach. *J. Chem. Phys.* **2007**, *127* (12). https://doi.org/10.1063/1.2772269.

(24) Kwac, K.; Cho, M. Two-Color Pump - Probe Spectroscopies of Two- and Three-Level Systems: 2-Dimensional Line Shapes and Solvation Dynamics. **2003**, 5903–5912.

(25) Roberts, S. T.; Loparo, J. J.; Tokmakoff, A. Characterization of Spectral Diffusion from Two-Dimensional Line Shapes. *J. Chem. Phys.* **2006**, *125* (8), 1–8. https://doi.org/10.1063/1.2232271.

(26) Nicodemus, R. A. Hydrogen Bond Reorganization and Vibrational Relaxation in Water Studied with Ultrafast Infrared Spectroscopy. **2011**.

(27) Golonzka, O.; Tokmakoff, A. Polarization-Selective Third-Order Spectroscopy of Coupled Vibronic States. *J. Chem. Phys.* **2001**, *115* (1), 297–309. https://doi.org/10.1063/1.1376144.

(28) Tokmakoff, A. Orientational Correlation Functions and Polarization Selectivity for Nonlinear Spectroscopy of Isotropic Media. I. Third Order. *J. Chem. Phys.* **1996**, *105* (July),

1–12.

(29) Tao, T. Time-Dependent Fluorescence Depolarization and Brownian Rotational Diffusion Coefficients of Macromolecules. *Biopolymers* **1969**, *8* (5), 609–632. https://doi.org/10.1002/bip.1969.360080505.

(30) Sung, J.; Silbey, R. J. Four Wave Mixing Spectroscopy for a Multilevel System. *J. Chem. Phys.* **2001**, *115* (20), 9266–9287. https://doi.org/10.1063/1.1413979.

(31) Nicodemus, R. A.; Ramasesha, K.; Roberts, S. T.; Tokmakoff, A. Hydrogen Bond Rearrangements in Water Probed with Temperature-Dependent 2D IR. *J. Phys. Chem. Lett.* **2010**, *1* (7), 1068–1072. https://doi.org/10.1021/jz100138z.

(32) Nicodemus, R. A.; Corcelli, S. A.; Skinner, J. L.; Tokmakoff, A. Collective Hydrogen Bond Reorganization in Water Studied with Temperature-Dependent Ultrafast Infrared Spectroscopy. *J. Phys. Chem. B* **2011**, *115* (18), 5604–5616. https://doi.org/10.1021/jp111434u.

(33) Ramasesha, K.; Roberts, S. T.; Nicodemus, R. A.; Mandal, A.; Tokmakoff, A. Ultrafast 2D IR Anisotropy of Water Reveals Reorientation during Hydrogen-Bond Switching. *J. Chem. Phys.* **2011**, *135*, 054509. https://doi.org/10.1063/1.3623008.

(34) Carpenter, W. B.; Lewis, N. H. C.; Fournier, J. A.; Tokmakoff, A. Entropic Barriers in the Kinetics of Aqueous Proton Transfer. *J. Chem. Phys.* **2019**, *151* (3), 034501. https://doi.org/10.1063/1.5108907.

(35) Somorjai, R. L.; Horning, D. F. Double-Minimum Potentials in Hydrogen-Bonded Solids. *J. Chem. Phys.* **1962**, *36*, 1980–1987. https://doi.org/https://doi.org/10.1063/1.1732814.

Chapter 3

Experimental implementation of 2D IR spectroscopy with broadband detection

3.1. Overview of the instrument

While the description of third order nonlinear spectroscopy in Chapter 2 may sound simple, in practice the experimental implementation is somewhat involved. To perform these experiments, a sequence of short, mid-IR laser pulses with sufficient pulse energy and spectral bandwidth are required, incident on the sample of interest with controlled time delays between them. The aim of this chapter is to describe how those light pulses are generated and manipulated to measure 2D IR spectra, and the reasoning behind the choices made.

This year marks the 25th anniversary of the first reported 2D IR measurements,[1] and in that time several practices have gained widespread adoption across the field. However, there is no "standard" 2D IR instrument, and there are many choices to be made about pulse generation,[2–4] compression,[5,6] beam geometry,[7,8] and detection with implications for the accessible information in the experiment. Furthermore, technical advances continue to improve the capabilities for generating, controlling, and measuring mid-IR light, enabling 2D IR spectroscopy at increased repetition rates and with greater spectral coverage, among other advantages.[9–14]

3.1. Overview of the instrument

The 2D IR and TA experiments in this thesis were collected on the instrument summarized in Fig. 3.1. This instrument is designed to study water and aqueous solutions, which have broad vibrational transitions at frequencies across the mid-IR fingerprint region of ~1000-4000 cm^{-1}. The broad absorption linewidths and ultrafast vibrational relaxation of those systems continue to push the boundaries of what is possible to measure in 2D IR spectroscopy.[15–18] As a result, the instrument design is dynamic and updated periodically to incorporate the shortest, most spectrally broad IR pulses that can be generated.[3,4] A particularly notable component of this instrument is the extraordinarily broadband detection source, which can simultaneously probe the mid-IR region and was first incorporated in 2D IR spectroscopy in the Tokmakoff group.[19,20]

In this thesis, there are two instrumentation advances to report since the instrument was last documented.[20–22] The highly-scattering zeolite particles studied herein posed new challenges for signal detection and processing. The capabilities we developed for collecting scatter-free 2D IR and TA spectroscopy of scattering samples without pulse shaping are described in section 3.6. In addition, a new source for mid-IR excitation pulses was developed, which is reported in Chapter 4. While we plan to incorporate that source for future studies, this chapter describes the instrumentation used for zeolite measurements discussed in chapters 5-7. First, I will summarize the instrument, the basic principles behind femtosecond mid-IR pulse generation and characterization, and a few additional considerations particular to broadband 2D IR spectroscopy.

An overview of the instrument is displayed in Fig. 3.1. The system is sourced from a Ti:Sapphire regenerative amplifier (Coherent Legend Elite) which produces 800 nm, 5 mJ pulses at 1 kHz. A series of waveplates and polarizing beamsplitters divide this output into three separate lines. During operation, the energy is split between one of the optical parametric amplifiers (OPAs)

and to the broadband IR (BBIR) probe source. Pulses are compressed to 25 fs with independent compressors (Comp.) in each line, allowing for independent optimization.

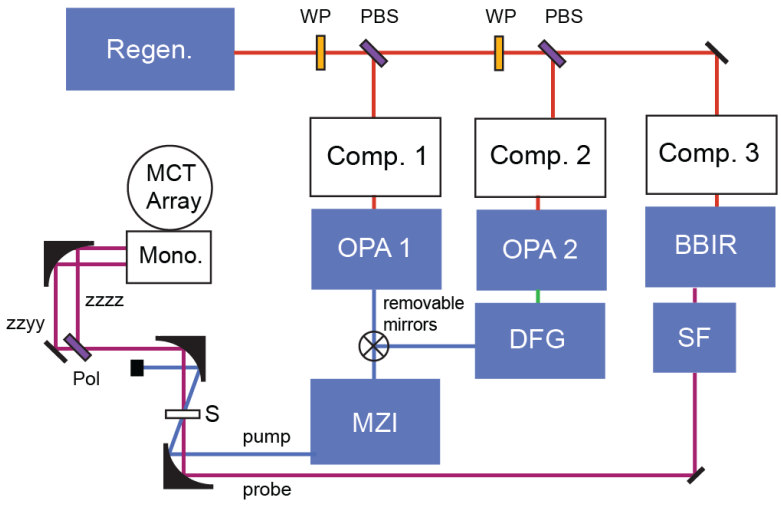

Figure 3.1. Overview of the instrumentation for mid-IR pulse generation and TA and 2D IR spectroscopy experiments. BBIR, broadband IR generation; Comp., compressor; DFG, difference frequency generation; MCT, Hg-Cd-Te detector; Mono., monochromator; MZI, Mach-Zehnder interferometer; OPA, optical parametric amplification; PBS, polarizing beamsplitter; Pol, polarizer; Regen., regenerative amplifier; S, sample; SF, spatial filter.

The laser fundamental is down-converted to the mid-IR using a different method in each line. After Comp. 1, a home-built OPA generates ~3 μJ, 45 fs pulses centered near 3 μm in $KNbO_3$ (KNB).[3] Alternatively, after Comp. 2 a commercial OPA (Light Conversion, TOPAS Prime) generates a pair of pulses in the near-IR with frequencies that sum to 800 nm (12500 cm^{-1}). Then, mid-IR light is generated by difference frequency generation (DFG) in $AgGaS_2$ (AGS) or GaSe. The resulting mid-IR pulses are tunable from ~1200 – 2800 cm^{-1} with pulse energies of several microjoules and durations ≤ 70 fs. Together, these two sources enable tunable excitation across much of the mid-IR, described further in sections 3.2.2 – 3.2.3.

A set of removable mirrors direct the output of either the 3 μm OPA or the DFG into a Mach-Zehnder interferometer (MZI), which splits the beam into a pair of approximately identical pulses. The excitation (pump) pulse pair E_1 and E_2 is separated in time by τ_1 using a computer-controlled state (Aerotech ANT-95-L) in the moving arm of the interferometer. The stage is accurate to < 300 nm, corresponding to a time delay of < 1 fs. The output of the MZI is directed to the sample, with the pulses in phase at $\tau_1 = 0$. The second output of the MZI, where the pulses out of phase at $\tau_1 = 0$, is monitored with an energy meter (Coherent J-10MB-HE) enabling simultaneous measurement of the pump interferogram during 2D IR data collection.

The detection (probe) pulse is generated after Comp. 3 by filamentation in N_2 gas.[4] The generated plasma radiates coherent light spanning the mid-IR with ~1 nJ pulse energy and a duration of 50 fs. While far too weak to excite molecular vibrations, this source provides a suitable probe pulse E_3. The pump-probe delay τ_2 is controlled using a second stage in the 800 nm line before BBIR generation. The probe is polarized at 45˚ relative to the pump using transmission through a rotated silicon wafer.

The three pulses meet at the sample in the pump-probe geometry,[7,8] where the two pump pulses are collinear and crossed with the probe. The signal is emitted in the direction of the probe and with the same polarization. A polarizer splits the signal into the parallel (ZZZZ) and perpendicular (ZZYY) components relative to the pump, which are dispersed with a grating and detected simultaneously in the frequency domain on the two stripes of a 2x64 Hg-Cd-Te (MCT) detector (Infrared Associates). The probe acts as the local oscillator for heterodyne detection. Simultaneous detection of ZZZZ and ZZYY components enables anisotropy measurements where both

components contain the same shot-to-shot noise. The noise is also monitored on a reference single-channel MCT detector using a ~1% BaF_2 pickoff mirror before the polarizer.

3.2. Generation of tunable pulses by optical parametric amplification

3.2.1. Principle of OPA and DFG

The generation of short (~45-70 fs), broadband (~200-350 cm^{-1}), high-energy (~3-10 μJ), tunable mid-IR pulses is accomplished with optical parametric amplification, which is a second-order nonlinear process based on DFG. We can describe the DFG process using perturbation theory, where an electric field is generated from the polarization induced by two interactions with the incident electric field. Since this process is nonresonant, we can assume that the material responds instantaneously to the electric field.[23] Then, the second order nonlinear polarization is expressed in terms of the second-order susceptibility $\chi^{(2)}$, electric field *E*, and the permittivity of free space ε_0.

$$P^{(2)}(t) = \varepsilon_0 \chi^{(2)} E^2(t) \tag{3.1}$$

Since the polarization scales with $E^2(t)$, it oscillates at sum and difference frequencies of the incident fields. The nonresonant nature of the interaction simplifies the molecular response function compared to the case of resonant interactions for 3rd order spectroscopy described in Chapter 2. In the context of DFG, the three fields of interest will be referred to as pump, signal, and idler defined by their relative frequencies: $\omega_P > \omega_S \geq \omega_I$. In DFG, the incident fields are the pump and signal, and the generated field is the idler with $\omega_I = \omega_P - \omega_S$. The relevant tensor element of the susceptibility is $\chi^{(2)}(\omega_I; \omega_P, \omega_S)$, which is a time-independent constant that

depends only on the mixing frequencies and the nonlinear medium. For this reason, it is often referred to as (twice) the effective nonlinearity, d_{eff}.[24]

Optical parametric amplification and DFG are distinguished by the relative intensities of the input beams. In DFG, the intensities I_P and I_S are comparable, so we can assume that neither beam is significantly depleted by the perturbative interaction. Solving the equations for propagation along a crystal of length L shows that the generated idler intensity I_I grows quadratically with crystal length and d_{eff}.[23,24]

$$I_I^{DFG}(L) = \left(\frac{d_{eff} L \omega_I^2}{2c^2 k_I} \right)^2 I_P(0) I_S(0) \operatorname{sinc}^2(\Delta k L / 2) \tag{3.2}$$

Here, Δk is the phase mis-match, $\Delta k = k_P - k_S - k_I$. Importantly, the efficiency of DFG is sharply peaked around $\Delta k = 0$.

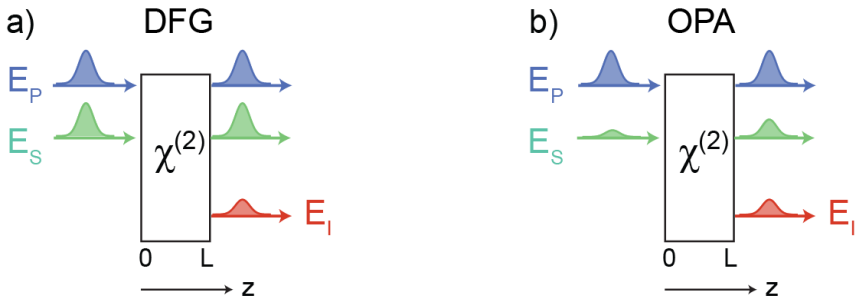

Figure 3.2. Collinear (a) DFG and (b) OPA in a medium of length L. In DFG $|E_P| \sim |E_S|$; in OPA $|E_P| >> |E_S|$ and the signal is amplified along with the idler.

In OPA, the pump intensity is much larger than the signal, $I_P(0) >> I_S(0)$. As a result, multiple cascading DFG events occur over the length of the medium leading to net generation at both ω_I

and ω_S. Under these conditions, the system of equations for propagation are solved neglecting pump depletion,[24] leading both signal and idler intensity to grow exponentially with crystal length.

$$\begin{aligned} I_I{}^{OPA}(L) &\propto \frac{\omega_I}{\omega_S} I_S(0) e^{2gL} \\ I_S{}^{OPA}(L) &\propto I_S(0) e^{2gL} \\ g &= \sqrt{\frac{2{d_{eff}}^2 \omega_S \omega_I}{c^3 \varepsilon_0 n_P n_S n_I} I_P - \frac{\Delta k^2}{4}} \end{aligned} \tag{3.3}$$

In Eq. (3.3) the exponential gain of the signal and idler is controlled by the parameter *g*. The gain in maximized at the phase-matching condition $\Delta k = 0,$ and increases with both d_{eff} and I_P. Here, n_I, n_S, and n_P are the refractive index of the medium evaluated at the corresponding frequencies.

In a sense, parametric amplification can be pictured as "splitting" high-energy pump photons each into a signal and idler photon. Due to energy conservation, the ratio of signal and idler intensities is fixed by their relative frequencies since equal numbers of signal and idler photons are generated (Manley-Rowe relations).[25] The exponential scaling with crystal length and d_{eff} is a significant improvement over the scaling in DFG. In practice, exponential scaling is an upper bound, limited by pump depletion, and temporal pulse walk-off,[24] which are important to consider in OPA design.

Phase matching

The phase-matching condition has crucial implications for DFG in nonlinear crystals. Together with energy conservation, this places two simultaneous constraints on the wave mixing process at maximum efficiency.

$$\omega_P - \omega_S - \omega_I = 0 \tag{3.4}$$

$$\begin{aligned} k_P - k_S - k_I &= 0 \\ n(\omega_P)\omega_P - n(\omega_S)\omega_S - n(\omega_I)\omega_I &= 0 \end{aligned} \tag{3.5}$$

In Eq. (3.5) the second line is re-written in terms of the frequency-dependent refractive index $n(\omega)$. The refractive index of most materials is a monotonic function of frequency, in which case the two conditions cannot be satisfied simultaneously. This is resolved by using a birefringent crystal with one beam polarized perpendicular to the other two. The phase-matching condition is called Type-I when signal and idler have the same polarization, and Type-II when they are cross-polarized. In the birefringent crystal, one or more beams is polarized along the ordinary direction (perpendicular to the optical axis) with refractive index $n_o(\omega)$, while the cross-polarized beam(s) experience the extraordinary refractive index $n_e(\omega)$, depicted in Fig. 3.3a. While both indices are frequency-dependent, the extraordinary index also depends on the angle θ between the propagation direction $\vec{k}$ and the optical axis according to Eq. (3.6).

$$\frac{1}{n_e(\theta)^2} = \frac{\cos^2(\theta)}{n_o^{\,2}} + \frac{\sin^2(\theta)}{n_e^{\,2}} \tag{3.6}$$

Therefore, the phase-matching angle controls the refractive index of the beam(s) polarized in the extraordinary direction, providing tunability over the phase-mismatch Δk independent of pulse frequencies. While phase matching is not guaranteed in general, it is straightforward to check by solving Eqs. (3.4)-(3.6) together, and software with this functionality is freely available.[26] The solution is referred to as the phase-matching curve, which defines the internal crystal angle where $\Delta k = 0$ at a given pump frequency. An example phase-matching curve is plotted in Fig. 3.3 for Type-II DFG in AGS with a pump wavelength of 1.33 μm (7500 cm^{-1}). When the crystal is tuned

to $\theta = 52°$ the generated idler is centered at 2500 cm^{-1} with a corresponding signal frequency of 5000 cm^{-1} (not displayed).

The phase-matching curve is the critical property of the nonlinear crystal, and determines the bandwidth of the generated pulse(s). For example, Fig. 3.3 shows that decreasing the phase-matching angle in AGS also decreases the center frequency of the generated idler (at a constant pump frequency). For a given internal crystal angle there is only one perfectly phase-matched idler frequency, but nearby frequencies are also generated less efficiently with increasing Δk further from the center frequency. Therefore, the bandwidth of the generated pulse depends on the steepness of the phase-matching curve (in addition to the crystal length).

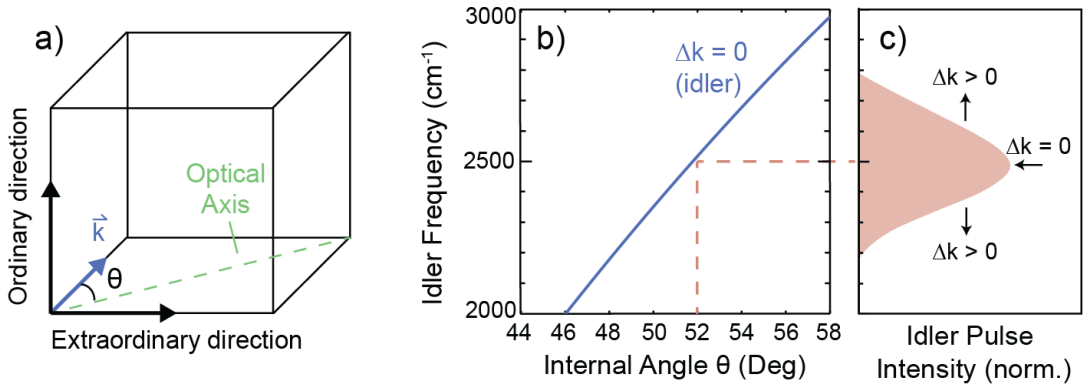

Figure 3.3. (a) Ordinary and extraordinary directions in a uniaxial birefringent crystal with beam propagation in the direction $\vec{k}$. (b) Phase-matching curve for Type-II DFG in $AgGaS_2$ with pump wavelength 1.33 μm and (c) idler pulse spectrum generated under these conditions.

3.2.2. Generation of pulses at 3 μm

Excitation pulses in the 3 μm spectral region were generated using a home-built, two-stage OPA which is described in detail elsewhere.[3] In the first stage of the OPA, a 1-mm β-$Ba(BO_2)_2$ (BBO) is pumped at 800 nm and seeded with white light generated in a 1-mm sapphire crystal. The BBO is turned to $\theta = 21.5°$ which phase-matches the amplification of signal at 1.1 μm in a

Type-I process. In the second stage, ~500 nJ of 1.1 μm light from the first stage acts as the signal for Type-I phase matching in a 1-mm KNB crystal pumped at 800 nm. The idler is generated with a center frequency of 3 μm at the phase-matching angle $\theta = 41°$

The mid-IR idler is separated from the near-IR pump and signal with a Ge window, which has a bandgap of 1.8 μm. The center frequency is tunable from ~2800 – 3400 cm^{-1} by adjusting the phase-matching angles of the two OPA crystals. At 3400 cm^{-1} the pulse energy is typically 3 μJ, and increases to 5 μJ at lower frequencies, with durations of ~50 fs measured by interferometric autocorrelation. Energy stability is typically 1.5 – 2 % rms. Generated pulse spectra centered near 2850 cm^{-1}, 3100 cm^{-1}, and 3350 cm^{-1} are displayed in blue in Fig. 3.4, with parameters in Table 3.1, corresponding to excitation pulses for measurements reported in Chapters 5-7.

3.2.3. Tunable pulse generation by DFG

Lower-frequency mid-IR excitation pulses were generated by sequential down-conversion in the TOPAS OPA followed by DFG between the signal and idler. The TOPAS is a two-stage BBO OPA, where the seed for the first stage is generated by white light generation in sapphire. Both BBO stages are Type-I, generating pulses in the range of 1.3 – 1.45 μm (signal) and 2.0 – 1.8 μm (idler). The total output energy is typically 450 μJ, with energy divided between signal and idler according to Eq. (3.3): $I_S / \omega_S = I_I / \omega_I$.

The near-IR signal and idler from the TOPAS are further down-shifted in a home-built single stage DFG, which has been described in detail in previous group theses.[21,22] First, any time delay between the beams is corrected in a Michelson interferometer using a dichroic as the beamsplitter and a manual moving stage. The retimed pulses are combined collinearly for DFG in either AGS (Type-II) or GaSe (Type-I). The signal and idler from the TOPAS become the pump and signal,

respectively, for the DFG process. A mid-IR idler is generated at the difference frequency, tunable between 1200 – 2800 cm^{-1}. The phase-matching curve for generation at 2500 cm^{-1} (1.33 μm pump) in AGS is shown in Fig. 3.3.

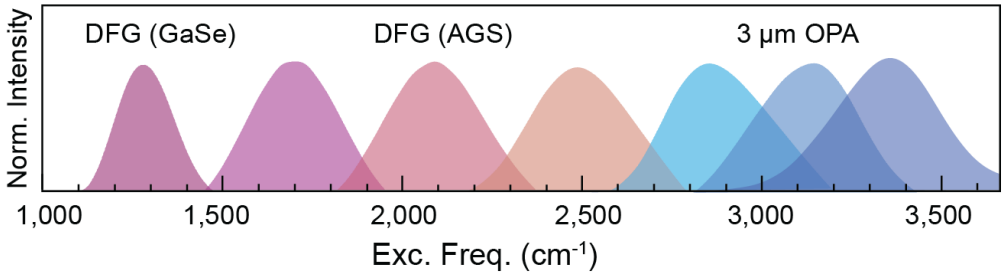

Figure 3.4. Excitation pulse spectra. Pulses in red-orange were generated by DFG in either GaSe or AGS; pulses in blue were generated in the 3 μm OPA.

Figure 3.4 shows the spectra of pulses generated in a 0.5-mm AGS crystal with center frequencies near 1700 cm^{-1}, 2100 cm^{-1}, and 2500 cm^{-1}. The AGS crystal was cut at 42˚ (Eksma) and rotated based on the desired mid-IR frequency. We measured durations of 50 – 60 fs for these pulses using interferometric autocorrelation. The pulse centered near 1280 cm^{-1} shown in Fig. 3.4 was generated instead by Type-I DFG in a 0.5 mm GaSe crystal. The phase-matching bandwidths in both AGS and GaSe are narrower in this frequency range compared to the higher mid-IR frequencies, but GaSe has both broader phase matching and a higher effective nonlinearity here, yielding pulses with a duration of 67 fs. Typical energies of 7 – 10 μJ were achieved for the DFG pulses with energy stability ≤ 1% rms.

Table 3.1: Excitation pulse parameters

Center Frequency (cm^{-1})	Bandwidth FWHM (cm^{-1})	Pulse Duration (fs)	Pulse Energy (μJ)	Generation Source
3360	350	46	3	3 μm OPA
3140	330	49	4	3 μm OPA
2860	340	46	5	3 μm OPA
2490	320	57	8	DFG in AGS
2090	310	51	8	DFG in AGS
1700	290	50	7	DFG in AGS
1280	180	67	10	DFG in GaSe

3.3. Generation of BBIR detection pulses

3.3.1. Filamentation and IR generation mechanism

While second-order wave mixing in nonlinear crystals can produce mid-IR pulses with microjoule energies, the bandwidth is typically limited to a few hundred wavenumbers by phase matching. Filamentation in gas provides an alternative approach capable of producing broad bandwidth pulses spanning the mid-IR, at a significant cost to pulse energy. Incorporating this source as a probe is the basis for 2D IR spectroscopy with broadband detection.

In BBIR generation, the laser fundamental is focused along with the second harmonic $(\omega / 2\omega)$ or second and third harmonics $(\omega / 2\omega / 3\omega)$ into a gas, typically air or N_2. The high peak power of the focused pulse ionizes a fraction of the gas particles forming a plasma. The spatial profile of the plasma refractive index causes de-focusing, which is balanced against self-focusing from the optical Kerr effect. The combined focusing and de-focusing allow the beam to propagate at a focused spot size over a distance much greater than the Rayleigh length. This filamentation extends

the effective length for light generation processes, and the plasma radiates coherent light pulses at THz-MIR frequencies.

While the mechanism of light generation remains somewhat mysterious, a leading interpretation is rectification by four-wave mixing (FWM).[27–29] In that picture, wave mixing generates photons near zero-frequency: $(3\omega - 2\omega - \omega = \omega_0)$ or $(2\omega - \omega - \omega = \omega_0)$. While the center frequencies of the generating pulses sum to zero, THz-MIR photons are generated due to the nonzero bandwidth of the pulses. Evidence in support of the FWM interpretation includes the power scaling with the energies of generating pulses in both $\omega / 2\omega$ and $\omega / 2\omega / 3\omega$ schemes.[19,27] In addition, Fuji and Nomura observed a ring-shaped spatial mode of generated MIR,[29] consistent with the phase-matching condition for FWM in a focused, collinear geometry.[30] However, the extremely high peak pulse energies perhaps call into question a straightforward perturbation theory interpretation, or at least suggest that other processes may play a role.

In another picture, light generation near zero-frequency is described by the tunnel current in the plasma.[31–33] In that picture, the gas is partially ionized at high-amplitude peaks in the driving electric field by tunneling through the barrier binding electrons to the nucleus. Following tunnel ionization, the motion of liberated electrons is driven by the electric field of the pulse. This process is typically described with a semi-classical model that has been successfully applied to several high-field phenomena including high harmonic generation.[34,35] The addition of the 2ω component creates an asymmetry in the driving field, leading to a DC component in the power spectrum of the generated current which could account for the generation of low-frequency photons.[32] This model predicts oscillations in the generated THz power with the phase between ω and 2ω components, which matches experimental observations.[31–33] While the dominant mechanism is not

entirely clear, it seems plausible that both FWM and tunnel ionization contribute. And, they are not necessarily incompatible descriptions since the FWM model does not predict the microscopic origin of the optical nonlinearity in the $\chi^{(3)}$ process.

3.3.2. BBIR generation scheme

In our lab, broadband IR pulses are generated using a scheme designed by Petersen and Tokmakoff,[4] depicted in Fig. 3.5. The 800 nm fundamental, 400 nm second harmonic, and 267 nm third harmonic are focused in a collinear geometry into a stream of N_2 gas. First, 400 nm light is generated by Type-I second harmonic generation (SHG) in a 200 μm BBO cut at 29.2˚ (Eksma). Timing between the 400 nm and 800 nm pulses is adjusted using a delay plate: a 2-mm BBO cut at 66˚ (Eksma), which does not phase-match any nonlinear process. The delay plate uses the birefringence of the BBO to control the relative delay between the cross-polarized beams. Next, the polarization of the 800 nm beam is rotated with a dual frequency waveplate (6.5λ at 800 nm and 14λ at 400 nm). Then, the third harmonic is generated by Type-I sum frequency generation (SFG) in a 100 μm BBO cut at 44.6˚ (Eksma).

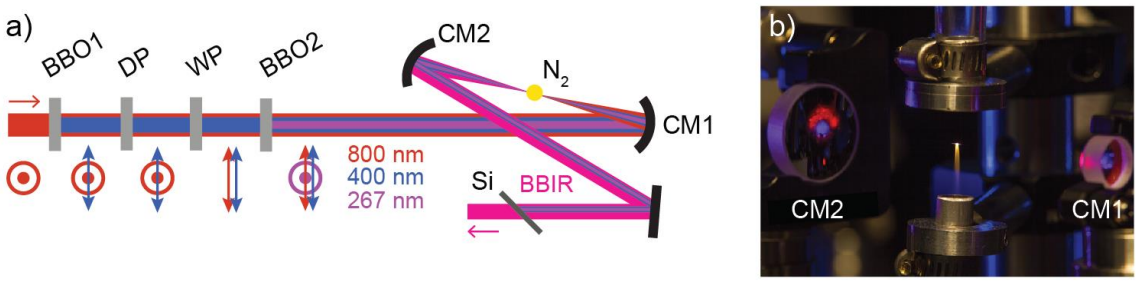

Figure 3.5. (a) Beam diagram for BBIR generation. (b) Picture of plasma formed in flowing N_2 (photo credit: Bogdan Dereka). BBO, β-Barium borate; CM, curved mirror; DP, delay plate; WP, waveplate. All beams are linearly polarized vertical (circle with dot) or horizontal (double-sided arrow) relative to the table.

The three beams are focused with a dielectric spherical mirror, $f = 5\,\mathrm{cm}$ (Layertec Art 100600), which is coated for 800 nm and 400 nm and has high reflectivity at 267 nm. A tube placed above the focus flows N_2 gas at a pressure of ~5 atm and a second tube pulls vacuum from below (pictured in Fig. 3.5b). The flowing N_2 and vacuum protect nearby mirrors from ozone generated in the laser focus. The generated BBIR pulse is recollimated with a silver spherical mirror, $f = 5\,\mathrm{cm}$ (Thorlabs). The focusing and recollimating mirrors are arranged in an x-fold geometry with an angle of 7˚, which was the smallest achievable angle given the size of the optics. The mid-IR is separated from the generating pulses by transmission through at 0.5-mm Si window at Brewster's angle along the horizontal axis and at 45˚ along the vertical axis, yielding transmitted BBIR linearly polarized at 45˚ relative to vertical. After the filter, the BBIR is overlapped spatially with a visible tracer using a flipper mirror.

The spatial mode of the generated BBIR is poor, as a result of aberrations from the off-axis operation in the x-fold geometry. The mode and focal properties are greatly improved with spatial filtering using a 150 μm pinhole at the focus of two bare gold off-axis parabolic mirrors, $f = 10\,\mathrm{cm}$. The spatially filtered BBIR profile is approximately Gaussian. While only ~70% of the BBIR is transmitted through the spatial filter, the nonlinear signal in 2D IR spectroscopy is increased by a factor of ~1.5-2 because of tighter focusing into the sample.

The BBIR spectrum is displayed in Fig. 3.6, from independent measurements with frequency and time domain detection. In the frequency-domain measurement, the beam was dispersed with a grating (6 μm blaze) onto a 64-element MCT array. The 1000-3800 cm^{-1} region was covered by scanning 6 grating positions with overlapping frequencies and matching the intensities in overlap regions. In the time-domain measurement, a Mach-Zehnder interferometer was used to measure

the interferogram on a single-channel MCT. In both cases, the spectrum was corrected for the frequency-dependent sensitivity of the detector.

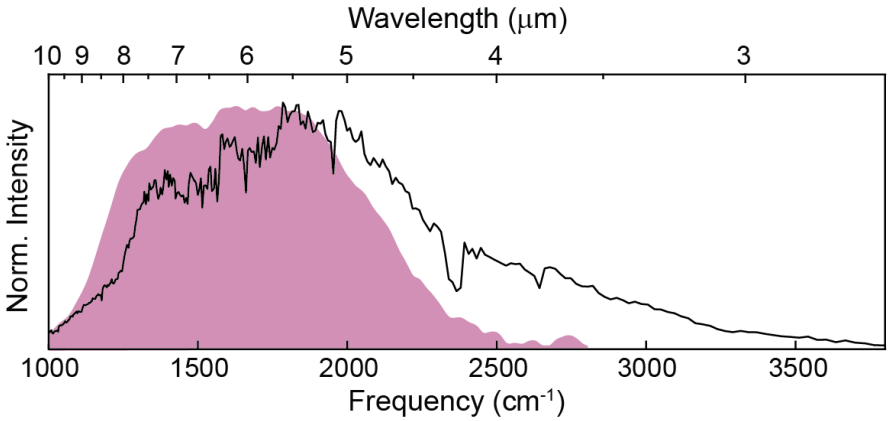

Figure 3.6. Broadband IR probe spectrum measured in the frequency domain (solid line) and time domain (shaded).

Both time- and frequency-domain measurements in Fig. 3.6 record a spectrum peaked near 6 μm with a bandwidth of >1000 cm^{-1} and a tail extending to higher frequencies. Some differences between the spectra can be explained by the fact that they were measured under slightly different conditions. For example, the air purging was better in the time-domain measurement, as water (5.5-7 μm) and CO_2 (4.25 μm) lines are clearly seen in the frequency-domain spectrum. The most notable difference is that higher mid-IR frequencies appear more prominently in the frequency-domain spectrum. This may be a result of the dynamic range of the detector, which makes it difficult to simultaneously measure the high intensities at 6 μm and low intensities at 3 μm when both are incident on a single element. That is not an issue in the spectrometer where the frequency components are dispersed.

There are several factors which make the BBIR pulses more challenging to work with than the narrower OPA-based pulses. The energy noise is greater, ~3-5% rms for the BBIR pulse, requiring

increased averaging during data collection. This shot-to-shot noise is managed with referencing and simultaneous detection of parallel and perpendicular signal components. The low pulse energy is another challenge. The beam does not register above the ~10 nJ detection limit of our energy meter, so the exact pulse energy is not precisely known. In addition, overlap with the visible tracer is cumbersome, requiring an MCT or pyroelectric detector. Furthermore, the broad bandwidth limits our options for pulse manipulation. In particular, transmission through any material causes temporal dispersion, and the influence on pulsewidth increases with bandwidth. For this reason, lenses are avoided and only mirrors are used for focusing. In the current design, the probe passes through only the 0.5-mm Si window and the window for sample housing, typically 1-mm CaF_2.

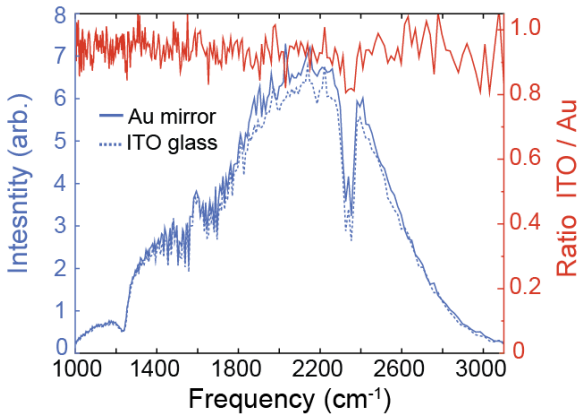

Figure 3.7. Broadband mid-IR reflectivity of ITO coated glass.

To further reduce transmissive material in the probe line, we investigated a reflective alternative for separation of mid-IR from the generating pulses. Thin layers of indium tin oxide (ITO), coated onto glass, have a high broadband reflectivity across the mid-IR while transmitting the 800 nm, 400 nm, and 267 nm beams. We found that lower resistivity (longer film thickness) corresponded to greater mid-IR reflectivity. This was based on our own measurements, since IR

reflectivity was not specified by most vendors. The reflectivity of a BBIR pulse off ITO coated glass (surface resistivity 7 Ohms/sq., PGO CEC007S) is displayed in Fig. 3.7. The spectrum was measured first after reflection off an unprotected Au mirror at 45° incidence, then after replacing the Au mirror with ITO glass. The ITO reflectivity is ~95% relative to the Au mirror, consistent across at least 1000-3000 cm^{-1}. Four bounces off ITO glass were required to fully remove the generating pulses. While we could not measure the pulse energy directly, we estimate that the BBIR energy lost after 4 ITO reflections is roughly equal to the reflective losses from transmission through the Si wafer using the counts on an MCT detector. In addition to removing transmissive material from the beam path, reflective pulse separation also provides a more convenient overlap with the visible tracer, which can be transmitted through the last piece of ITO glass. During the experiments in this thesis the probe source used the Si window for separation, but the ITO glass was implemented for BBIR separation in the new OPA described in Chapter 4.

3.4. Pulse compression and measurement

3.4.1. The spectral phase

Pulse compression and temporal measurement are crucial, since the time resolution of ultrafast measurements depends on the ability to deliver short pulses to the sample. The electric field of the laser pulse in the time domain $E(t)$ can be described as an envelope function $A(t)$ with oscillation at center frequency ω_0 and phase $\varphi(t)$, ignoring the spatial dependence for this discussion.

$$E(t) = A(t)e^{-i\omega_0 t + i\varphi(t)} \tag{3.7}$$

The same electric field is expressed in the frequency domain in terms of the spectral intensity $I(\omega)$ and spectral phase $\varphi(\omega)$.

$$E(\omega) = \sqrt{I(\omega)}e^{i\varphi(\omega)} \tag{3.8}$$

As Fourier conjugates, $E(t)$ and $E(\omega)$ obey the uncertainty relation $\tau_P \Delta\omega \leq C,$ where τ_P and $\Delta\omega$ are the FWHM of $E(t)$ and $E(\omega)$, respectively and C is a constant that depends on the shape of the pulse spectrum. So, the bandwidth of the pulse $\Delta\omega$ places a lower bound on the pulsewidth τ_P. This bound C in the time-bandwidth product (TBP) can be calculated straightforwardly through the Fourier transform of the pulse spectrum; for example $C = 0.44$ for a Gaussian pulse.

The TBP implies that a broad spectrum is necessary, but not sufficient, to support a short pulse. The other necessary condition is that all frequency components have a fixed phase relationship such that they add constructively at a localized point in time. This relationship between frequency components is encoded in the spectral phase, yielding the shortest pulse when $\varphi(\omega) = 0.$ In that case, the pulsewidth is determined only by the TBP, and is referred to as transform-limited (TL). When $\varphi(\omega) \neq 0,$ different frequency components are delayed relative to each other and the pulse is stretched, or chirped, in time with a pulsewidth greater than the TL. It is useful to describe the spectral phase with an expansion around the center frequency.

$$\begin{gathered}\varphi(\omega) = \varphi(\omega_0) + \varphi_1(\omega_0)(\omega-\omega_0) + \frac{1}{2}\varphi_2(\omega_0)(\omega-\omega_0)^2 + \frac{1}{6}\varphi_3(\omega_0)(\omega-\omega_0)^3 + \ldots \\ \varphi_n(\omega_0) = \left.\frac{\partial^n \varphi}{\partial \omega^n}\right|_{\omega_0}\end{gathered} \tag{3.9}$$

The first term $\varphi(\omega_0)$ is the carrier-envelope phase (CEP), which defines the phase between the peak of the envelope and the oscillation of the carrier. While the CEP is important for processes like high-harmonic generation which depend on each oscillation of the field,[35] it does not affect the 2D IR measurement and we can neglect it here. The second term $\varphi_1(\omega_0)$ is the group delay

(GD), which simply delays all frequency components equally. This is the term that controls timing between pulses, but it plays no role in pulse compression. The next term $\varphi_2(\omega_0)$ is the group delay dispersion (GDD), which imparts a linear relationship on the relative delay of each frequency component. Positive GDD means lower frequencies arrive at earlier times, and vice-versa. Similarly, $\varphi_3(\omega_0)$ is the third order dispersion (TOD), which imparts a quadratic delay on the frequency components. For short pulses, we can assume that higher-order dispersion terms are small enough to be neglected.

The influence of leading terms in the spectral phase is illustrated in Fig. 3.8 for a model Gaussian pulse. The shortest pulse occurs at the TL $(\varphi(\omega) = 0)$. Adding GDD stretches the pulse in time, and the arrival of lower frequencies at earlier times can be visualized in the electric field in Fig. 3.8c. The addition of TOD stretches the pulse asymmetrically in an oscillating pattern as shown in Fig. 3.8d.

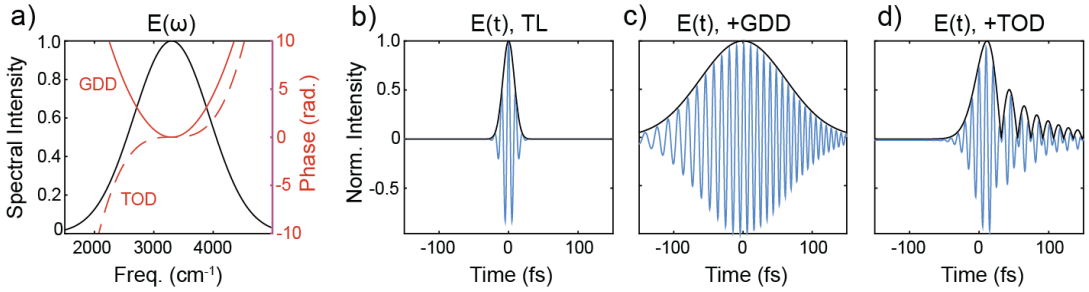

Figure 3.8. Effect of temporal dispersion on a model Gaussian pulse. (a) Spectral intensity and spectral phase with positive GDD (solid) and positive TOD (dashed). The pulse in the time domain is plotted with (b) zero spectral phase, (c) GDD, and (d) TOD corresponding to the curves in (a). The field intensity is in blue, envelope in black.

3.4.2. Pulse compression in the mid-IR

For short pulses, where higher-order terms in the spectral phase are negligible, compression and stretching can be described by accounting for the GDD and TOD of the pulse. Changing the GDD or TOD is accomplished by imparting a frequency-dependent delay. In a grating or prism compressor (or stretcher), frequency components are spatially dispersed and travel different pathlengths before spatial recombination.[36] Additional control over the spectral phase can be achieved with modifications, for example by using a deformable mirror,[37] or an acousto-optic modulator[6] to further adjust the relative delay between spectral components. Alternatively, temporal dispersion can be imparted on a pulse when it passes through any transmissive material due to the frequency dependence of the refractive index $n(\omega)$.

In our lab, the 800 nm pulses are stretched with a grating pair before regenerative amplification, then recompressed to 25 fs afterwards with a second grating pair. The compressed 800 nm pulses are used to generate mid-IR pump pulses by OPA (and DFG). Temporal dispersion is imparted onto those pulses when they travel through the generating crystals, as well as any transmissive optics including spectral filters, beamsplitters, polarizers, and sample windows. The dispersion from those optics must be compensated to deliver TL, or nearly-TL, pulses to the sample.

Compression with a grating or prism pair is possible in the mid-IR, but these optics are lossy and/or difficult to align when the beam is not visible to the eye. In the visible wavelengths, chirped mirrors can deliver a controlled dispersion on each bounce, providing convenient control over pulse compression. However, efficient chirped mirrors have not been developed for mid-IR wavelengths. Therefore, our strategy is to add material to the beam path with the appropriate sign GDD. IR transmissive materials can be found with either positive or negative GDD, as shown in

Fig. 3.9. In practice, we estimate the amount of material needed to reach GDD ≈ 0 from all transmissive materials (for example, adding CaF_2 to compensate for positive GDD from a Ge filter). Then, the amount of material is adjusted to minimize the measured pulsewidth.

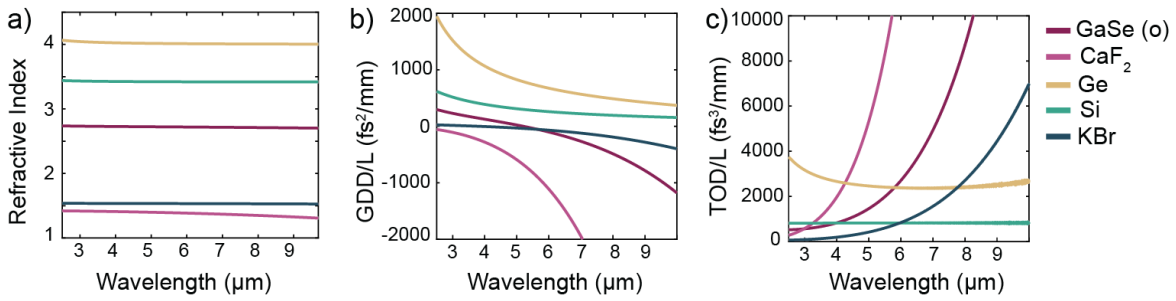

Figure 3.9. (a) Refractive index of selected materials in the mid-IR with (b) the GDD and (c) TOD per millimeter pathlength.

The drawback of this approach is that the TOD from material transmission is positive in the mid-IR. So, it is generally desirable to minimize the total material in the beam. This is accomplished by adjusting the materials used for beamsplitters and polarizers. For example, more CaF_2 is needed to compensate for the GDD of the Ge filter at shorter wavelengths, due to the shape of the GDD curves in Fig. 3.9b. So, in the MZI we use CaF_2 beamsplistters when working with the 3 μm OPA and switch to KBr beamsplitters for lower-frequency DFG pulses.

3.4.3. Interferometric autocorrelation and FROG

While pulse dispersion and compression are straightforward to describe, measuring these properties experimentally is more challenging and the methodology of femtosecond pulse characterization is an interesting topic in its own right. Ideally, we would like to fully characterize the electric field $E(t)$ through knowledge of both the spectrum and spectral phase. The spectrum is readily obtained from the time-domain measurement of the interferogram $I_{IG}(\tau)$, where τ is the time delay in the MZI.

$$\begin{aligned} I_{IG}(\tau) &= \int dt \,|\, E(t) + E(t-\tau) \,|^2 \\ &= \int dt \left(I(t) + I(t-\tau) \right) + 2 \int dt \, \Re \left(E(t) E^*(t-\tau) \right) \end{aligned} \tag{3.10}$$

Here, $I(t)$ is the electric field intensity $I(t) = \left| E(t) \right|^2$, ignoring proportionality constants. In Eq. (3.10) the first term is a constant baseline, while the second oscillates at the center frequency ω_0 and Fourier transforms to the spectrum $I(\omega)$. So, the interferogram encodes the minimum pulse length, based on the TL, but contains no information about the spectral phase.

Measuring the spectral phase requires a nonlinear process that depends on the time profile of the pulse. Several methods exist, with varying levels of sophistication and information content.[23] In our case, fully characterizing $E(t)$ is often not necessary, and it is sufficient to simply measure the pulsewidth τ_P. The general approach is to measure a nonresonant interaction (for example SFG or SHG) as a function of time delay between pulses. Since the nonresonant interaction occurs only during pulse overlap, the measured signal carries information about $E(t)$. If the two pulses are different, the shorter reference pulse can be used to effectively map out the envelope of the longer pulse. However, for the femtosecond pulses we wish to measure, much shorter pulses are not readily accessible in our lab. So, a second copy of the pulse is used as its own reference. Crossing the two copies of $E(t)$ in an SHG crystal measures the intensity autocorrelation (AC).

$$I_{AC}(\tau) = \int dt I(t) I(t-\tau) \tag{3.11}$$

Since the pulse pair exits the MZI collinearly, it is more convenient for us to use a modification of this measurement called interferometric autocorrelation (IAC). We focus the collinear pulses into an SHG crystal (0.5-mm AGS), block the fundamental with a short-pass filter, and send the generated second harmonic to a single-channel MCT detector.

$$\begin{aligned} I_{IAC}(\tau) &= \int dt \left| \left(E(t) + E(t-\tau) \right)^2 \right|^2 \\ &= \int dt \left(I(t)^2 + I(t-\tau)^2 \right) + 4\int dt I(t) I(t-\tau) \\ &+ 4\int dt \left(I(t) + I(t-\tau) \right) \Re\left(E(t) E^*(t-\tau) \right) + 2\int dt \Re\left(E(t)^2 E^*(t-\tau)^2 \right) \end{aligned} \tag{3.12}$$

The measured IAC intensity, Eq. (3.12), can be broken into four terms. The first is a constant offset; the second is the intensity autocorrelation; the third is proportional to the interferogram and oscillates at $\omega_0 \tau$; and the fourth oscillates at $2\omega_0 \tau$. The autocorrelation is isolated in signal processing by applying a filter in the Fourier domain to isolate the zero-frequency component of I_{IAC}. An example is displayed in Fig. 3.10 for a pulse centered at 2500 cm^{-1}.

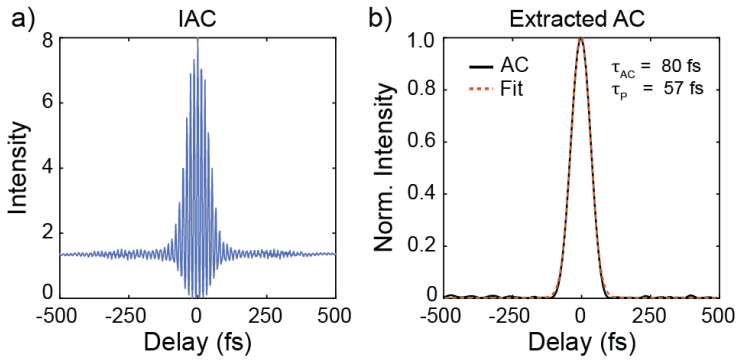

Figure 3.10. Example (a) interferometric autocorrelation with the (b) extracted autocorrelation for a pulse centered at 2500 cm^{-1}. The autocorrelation is fitted to a Gaussian with τ_{AC} = 80 fs FWHM, corresponding to a Gaussian pulsewidth of τ_P = 57 fs.

The pulsewidth is obtained by fitting the autocorrelation to a Gaussian, as shown in Fig. 3.10b. Assuming the pulse is Gaussian in time, the pulse duration is $\tau_P = \sqrt{2}\tau_{AC}$, where τ_{AC} is the FWHM of the autocorrelation. In addition, at $\tau = 0$ all of the terms in Eq. (3.12) add constructively with a ratio of 8:1 to the constant baseline. That ratio is highly sensitive to the alignment through the

interferometer and bleed-through of the fundamental through the filter, so it can be used to check the quality of the measurement.

Notably, the autocorrelation does not measure the spectral phase, and fitting is necessary to obtain the pulsewidth. This is acceptable for the DFG and 3 μm OPA pulses, since they are approximately Gaussian and the dispersion is relatively small. Additional information could be obtained with a more involved fitting procedure. For example, the IAC trace could be fit using Eq. (3.12) and modeling $E(t)$ with the measured pulse spectrum and assuming linear chirp (only GDD). That approach returns a value for the GDD, but still requires assuming a model for $E(t)$.

For pulses that are more complicated – or when a more detailed characterization of the spectral phase is desired – more information-rich characterization techniques are available. A powerful and relatively simple method is frequency-resolved optical gating (FROG),[38] which is essentially a frequency-resolved autocorrelation. The experimental geometry is similar to the standard autocorrelation: two copies of the pulse are crossed in a nonlinear medium and the generated signal is detected. However, in the FROG measurement the signal is measured as a function of both interferometer delay and frequency. The resulting spectrogram $I_{FROG}(\tau,\omega)$ can be expressed in terms of the field and a gating function $g(t-\tau)$.

$$I_{FROG}(\tau,\omega)=\left|\int dt e^{-i\omega t}E(t)g(t-\tau)\right|^2 \tag{3.13}$$

The gating function is determined by the type of nonlinear interaction. For SHG $g(t-\tau)=E(t-\tau)$, and for transient grating or transient birefringence $g(t-\tau)=\left|E(t-\tau)\right|^2$. The spectrogram resolves information about the time delay between frequency components, and can be inverted to almost fully characterize the spectral phase using an algorithm developed by Trebino

and co-workers.[38] In principle, this returns the spectral phase with the exception of the CEP, and the sign of GDD is not resolved in SHG FROG. The GDD sign is resolved in third-order FROG measurements,[38] and the CEP can be measured with additional steps[39,40] if necessary. While we typically do not use FROG for the OPA or DFG pulses, it was used for characterization of the broadband excitation pulses generated with the new OPA reported in Chapter 4, and the details are reported there.

3.5. 2D IR spectroscopy with broadband detection

3.5.1. Spectral coverage by tuning excitation frequency

2D IR spectra are collected in the pump-probe geometry as depicted in Fig. 3.1. The pump is tuned within the range depicted in Fig. 3.4 and crossed with the BBIR probe. At a fixed waiting time τ_2, the coherence time τ_1 is scanned in the MZI. The oscillating signal along τ_1 is Fourier transformed to the frequency domain, generating the ω_1 frequency axis. In the 3 μm region we typically scan ω_1 from -520:300 fs in steps of 4 fs, which is below the Nyquist frequency at 3 μm. For narrower features, the frequency resolution can be improved by increasing the maximum τ_1 value. While all mid-IR frequencies can be resolved along ω_1, a large nonlinear signal is only generated where the pump has sufficient intensity. So, the effective observation window in ω_1 is determined by the bandwidth of the pump.

During 2D IR data collection, the pump interferogram is collected simultaneously in the second output of the MZI. This allows us to monitor the pump spectrum and to correct for time-zero errors or misalignment through the interferometer. Those errors manifest as asymmetry in the pump

interferogram, which should be symmetric since the spectrum is purely real-valued. The asymmetry is quantified and corrected using the Mertz method.[41] First, the interferogram is truncated so that the time axis is symmetric (eg. -300:300 fs) and a low-resolution spectrum $S(\omega_1)$ is obtained by Fourier transform. Using the real and imaginary parts of the spectrum, a low-resolution phase is computed which accounts for the errors in data collection.

$$\phi = \tan^{-1}\left(\Im(S(\omega_1)) / \Re(S(\omega_1))\right) \tag{3.14}$$

Next, the high-resolution spectrum is calculated using the full interferogram. The low-resolution phase is interpolated to the full resolution of the spectrum, and the spectrum is corrected by multiplication with $\exp(-i\phi)$. Finally, the interpolated high-resolution phase is also applied to the 2D IR spectrum along ω_1.

After the sample, the nonlinear signal is detected in the frequency domain using a grating blazed for 6 μm with 75 grooves/mm, dispersed onto 64 MCT pixels. The frequency resolution along ω_3 is ~20 nm, which corresponds to ~1-2 cm^{-1} at 9 μm and ~25 cm^{-1} at 3 μm. The 64 pixels cover a ω_3 frequency range of ~150 cm^{-1} (near 9 μm) to ~1500 cm^{-1} (near 3 μm). So, the effective ω_3 window in a single measurement is determined by our detection capabilities. Since the probe spectrum covers the mid-IR, we can cover that entire spectral region along ω_3 by scanning several grating positions, which does not require any re-alignment between scans. Grating positions are chosen which overlap by several pixels, and the 2D IR spectrum is stitched along the detection frequency by matching the amplitudes in the overlap region. Since the signal is measured as a change in absorption of the probe, stitching along ω_3 is in principle exact, and mis-match between measurements is due to noise.

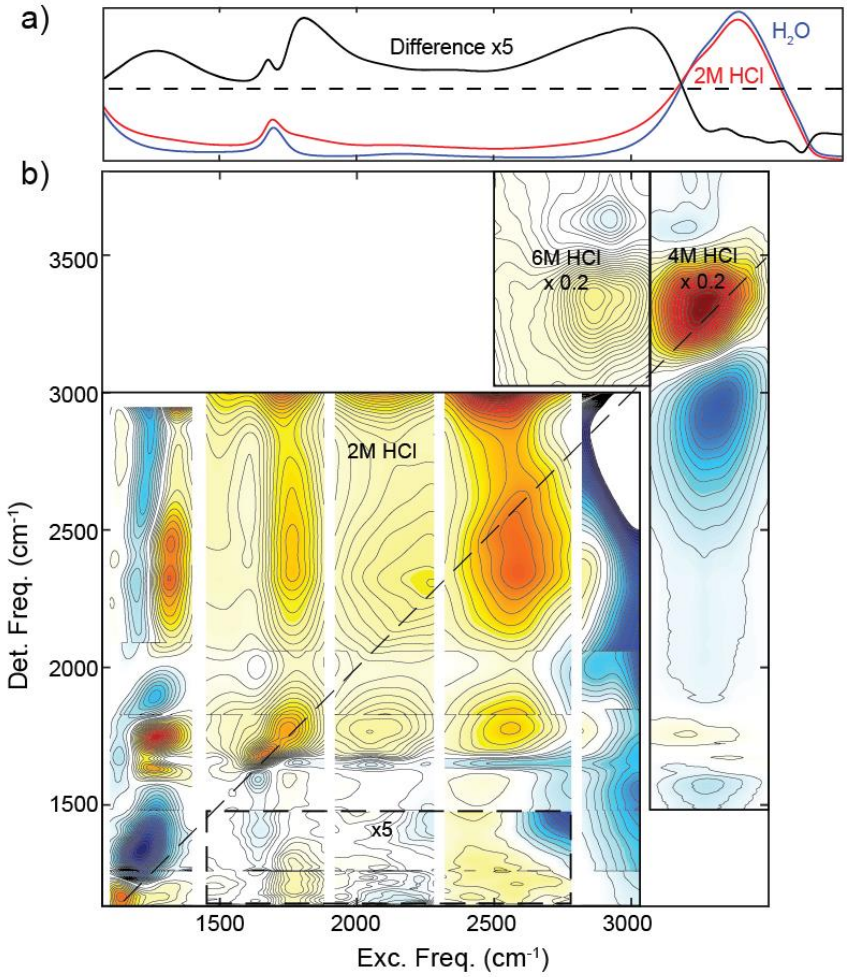

Figure 3.11. Isotropic 2D IR spectrum of aqueous HCl at τ_2 = 100-150 fs covering most of the mid-IR spectral range. The BBIR pulse provides broad coverage along the detection frequency; broad coverage along the excitation frequency is achieved by tuning the OPA(s), with pulse spectra reported in Fig. 3.4. The linear spectrum is shown in (a). The 2M 2D IR spectrum is replotted with permission from Fournier, J. A.; Carpenter, W. B.; Lewis, N. H. C.; Tokmakoff, A. *Nat. Chem.* **2018**, *10*, 932–937. © 2018 Springer Nature. The 4M 2D IR spectrum is from Thämer, M.; De Marco, L.; Ramasesha, K.; Mandal, A.; Tokmakoff, A.. *Science* **2015**, *350* (6256), 78–82. Replotted with permission from AAAS.

Since the pump spectra are much narrower than the probe, broad coverage along the excitation axis requires realignment between each experiment to tune the pump spectrum. Tuning across the mid-IR is achievable, as shown in Fig. 3.4, so in principle full spectral coverage is possible.

However, this approach is very time-consuming so only a few examples can be found which approach full 2D IR spectral coverage.[17,42] One example from the Tokmakoff group is the broadband 2D IR characterization of concentrated HCl in water, summarized in Fig. 3.11. This system has broad absorption bands across the mid-IR, necessitating broad spectral coverage. Figure 3.11 combines several isotropic spectra from both published[17,43] and unpublished data. All spectra were measured at $\tau_2 = 100\,\text{fs}$ except the lowest excitation frequency spectrum, measured at $\tau_2 = 150\,\text{fs}$.

In Fig. 3.11, each tall rectangular 2D IR spectrum corresponds to a different pump frequency, separated by white space for clarity. The 2M 2D IR spectra were collected with the DFG pump source, with center frequencies corresponding approximately to spectra in Fig. 3.4. The other 2D IR spectra were collected with the 3 μm OPA tuned to 2800 cm^{-1} (6M HCl) and 3400 cm^{-1} (4M HCl). Along the detection frequency axis, slight discontinuities can be seen from stitching together grating positions, for example at ω_3 ~1200, 1500, 1800, and 2100 cm^{-1} in the 2M spectra.

3.5.2. Pump normalization and stitching

While broad 2D IR coverage is possible with the tunable pump source and BBIR probe, as shown in Fig. 3.11, there are additional complications which must be considered. First, it is not immediately clear how to scale the relative intensities of 2D IR spectra collected with different pump frequencies. Consider for example the 2D IR spectra of 2M HCl collected with pump spectra centered at 1700 cm^{-1} and 2100 cm^{-1}, which are plotted again in Fig. 3.12a. The amplitude of the measured 2D IR signal scales with the intensity of the pump, but the two pump pulses have different pulse energies and spectra, and may have slightly different focused spot sizes depending on the realignment between measurements. This is a frustrating limitation, since relative peak

amplitudes encode information about the concentrations of different species or molecules in different environments.[44,45]

Second, the 2D IR lineshapes of broad spectral features are distorted by the shape of the pump spectrum. For example, in the spectra excited at 2100 cm^{-1} and 2500 cm^{-1} in Fig. 3.11, features appear to be peaked in ω_1 around the peak of the excitation pulse spectrum. Though, there is no corresponding peak in the FTIR spectrum. This is almost certainly a distortion from the spectrum of the pump, which is narrower than the molecular transition. For many molecular vibrations, the linewidth is much smaller than 300-400 cm^{-1}, and this windowing effect is not an issue. But, it becomes an important consideration for the broad vibrational features of the aqueous proton and other H-bonding systems. Notably, much of the information in Fig. 3.11 is not distorted by pump windowing. For example, band positions along ω_3 are undistorted and amplitudes at constant ω_1 can be compared quantitatively. But, the pump windowing hides the true 2D IR lineshape which encodes valuable information about the dynamics of spectral diffusion, as discussed in Chapter 2.

In light of these pump windowing distortions, what is the most accurate representation of the 2D IR data? One option is to simply display the data in panels as collected, without any overlapping ω_1, as shown in Fig. 3.11. Another similar option is to display an overlapping ω_1 region marking a line of equal ω_1, as in Fig. 3.12a. Alternatively, we can attempt to correct the pump distortion by normalizing the 2D IR spectrum by the pump spectrum along ω_1. The spectra can then be stitched along ω_1 by scaling one panel to the other using the overlap region, in the same way grating positions were stitched along ω_3. This option is displayed in Fig. 3.12b.

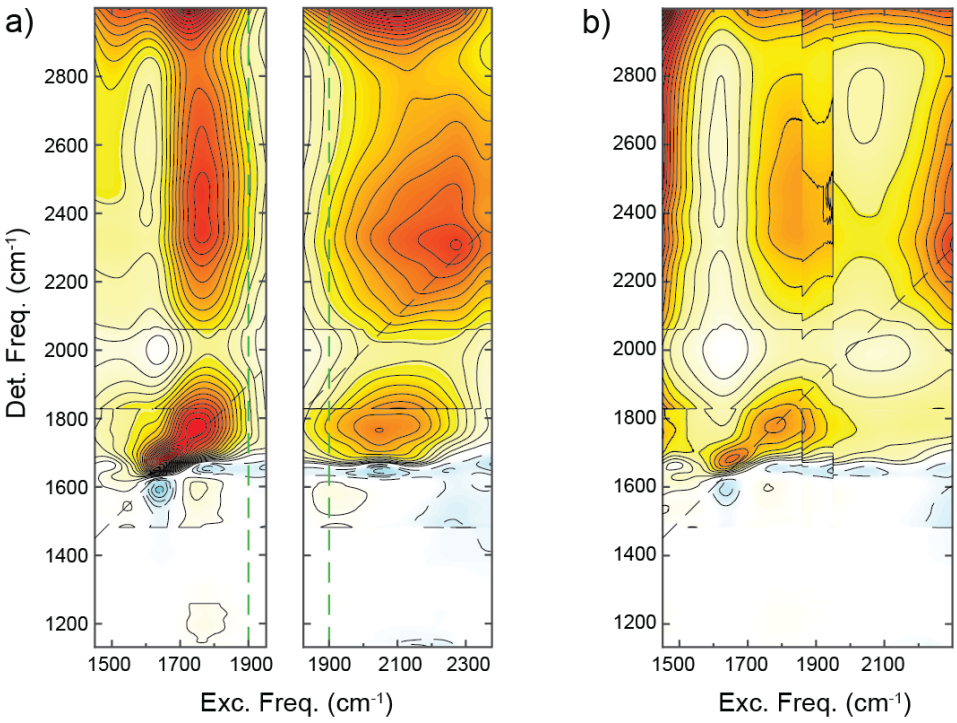

Figure 3.12. Isotropic 2D IR spectra of 2M HCl at τ_2 = 100 fs with two overlapping excitation pulses, plotted (a) without and (b) with pump normalization and stitching. In (a) the dashed green lines mark equal excitation frequencies in the two panels. In (b) discontinuities can be seen along exc. freq. from stitching the two panels. Spectra are replotted with permission from data in Fournier, J. A.; Carpenter, W. B.; Lewis, N. H. C.; Tokmakoff, A. *Nat. Chem.* **2018**, *10*, 932–937. © 2018 Springer Nature.

While pump normalization can be useful, it should be performed, presented, and interpreted with care. In principle, normalization is appropriate if the 2D IR spectrum contains only population pathways (where the system is in a population state during τ_2). In those pathways, the excitation frequencies are equal at both light-matter interactions with the pump, and therefore the pathway should be proportional to the pump intensity at that frequency. However, this is clearly not the case for coherence pathways, which interact with the pump at two different excitation frequencies

to create a coherence state during τ_2. So, pump normalization is not appropriate when coherence pathways are expected to be prominent.

A more practical complication is the fact that the signal/noise ratio is lowest on the wings of the pump spectrum. So, pump normalization increases the amplitude of the noisiest parts of the 2D IR spectrum, and then uses those noisy regions for stitching. It also seems that pump normalization artificially over-inflates the amplitude of the wings, though this is difficult to verify. This can be observed, for example, in Fig. 3.12b near $\omega_1 = 1500\,\mathrm{cm}^{-1}$ and 2250 cm^{-1}. In practice, I have found that a reasonable rule of thumb is to use only ω_1 frequencies where the pump intensity is at least 25% of its maximum value. Though, a more conservative window may be necessary if the signal/noise ratio is poor.

In Chapters 5-7, some 2D IR spectra are presented with and some without pump normalization, using the approaches displayed in Fig. 3.12. Where pump normalized is applied, it is clearly labeled and the spectral overlap between pump spectra is greater than in Fig. 3.12. Ideally, the complications from broad spectral features in 2D IR spectroscopy can be overcome by constructing a mid-IR excitation source with bandwidth exceeding the IR features of interest. This is the motivation for the work discussed in Chapter 4, which made progress towards that goal particularly in the 3 μm region.

3.6. Scatter management without pulse shaping

In addition to the broad spectral features of water and protons, the zeolite particles studied in this thesis posed an additional experimental challenge in the form of scattered light from the pump onto the detector, causing large-amplitude artifacts in nonlinear spectra. Most commonly, scatter

is managed in 2D IR spectroscopy with pulse shaping.[6,10,44,46] In a mid-IR pulse shaper, a Ge-based acousto-optic modulator (AOM) provides direct control over the relative phase between the two pump pulses.[6] This enables phase-cycling schemes where the phase of the oscillating scatter artifact is flipped between successive shots and cancels in averaging.[44] Using this approach, 2D IR spectra of highly-scattering silica, zeolites, and other solid particles have been measured with the scatter artifacts either removed or significantly suppressed.[10,46] In those studies, additional steps were also required: either suspension in index-matching oils,[46] or significantly increasing the pump intensity[10] which scales up the 2D IR signal relative to the scattered light.

While pulse shaping is a powerful tool, there are two drawbacks of Ge-AOM-based pulse shaping the mid-IR which led us to pursue a different approach. First, the AOM supports a finite bandwidth, which is typically narrower than the DFG or 3 μm OPA pulses. Second, the AOM must compensate for any dispersion from passing through the Ge material, in addition to the desired shaping.[47] This becomes more difficult at higher mid-IR frequencies as the GVD of Ge increases,[5] limiting mid-IR pulse shaping to ~4 μm and longer wavelengths.

In lieu of pulse shaping, we used a combination of several strategies for scatter suppression. The hydrated zeolite particles were filtered by size and suspended in a mixture of index-matching oils. The filtering removed the largest, most highly scattering particles and the oil reduced the change in refractive index at the particle interface. Additional details about the sample preparation can be found in Chapter 5. In addition, scatter was subtracted or suppressed during data collection by measuring a negative-time 2D IR surface, adding a chopper in the probe beam, and implementing quasi-phase cycling. To describe the influence of each of these methods, it is useful to consider the different types of scatter observed in 2D IR and TA spectroscopy.

3.6.1. Scatter in 2D IR and TA spectra

In the pump-probe geometry the 2D IR signal S_{2DIR} is heterodyned with the probe E_3 and the two beams travel collinearly to the detector. Scattered light from the two pump pulses E_1 and E_2 also reaches the detector and can interfere with the probe or with each other. In the absence of any chopping, the light reaching a given pixel on the array detector (ω_3) can be expressed as a sum of the 2D IR signal, TA signals, and scatter terms with their dependence on time delays τ_1 and τ_2.[10]

$$\begin{aligned} S(\tau_1,\tau_2,\omega_3) = {} & S_{2DIR}^{(1,2,3)}E_3 + S_{TA}^{(1,3)}E_3 + S_{TA}^{(2,3)}E_3 \\ & + a_{12}E_1E_2 + a_{13}E_1E_3 + a_{23}E_2E_3 + {E_1}^2 + {E_2}^2 + {E_3}^2 \end{aligned} \tag{3.15}$$

$$a_{ij} = \cos\left(\omega_3 T_{ij} + \phi_{ij}\right) \tag{3.16}$$

The term $S_{2DIR}^{(1,2,3)}$ represents the 2D IR signal, heterodyned with E_3, generated by light-matter interactions with E_1, E_2, and E_3 (and therefore depending on τ_1 and τ_2). The system can also interact twice with E_1 to generate the TA signal $S_{TA}^{(1,3)}$, or twice with E_2 to generate $S_{TA}^{(2,3)}$. In a 2D IR measurement these terms are distinct, while in a TA measurement $\tau_1 = 0$ so all three signal terms reduce to $S_{TA}^{(2,3)}$.

The scatter terms in Eq. (3.15) are denoted as the interference between two fields, for example E_1E_2 for the interference between fields E_1 and E_2. The a_{ij} factor keeps track of the dependence on the time delays. In Eq. (3.16) T_{ij} is the time delay between pulses *i* and *j*, and ϕ_{ij} is the relative phase. So, $T_{12} = \tau_1$, $T_{23} = \tau_2$, and $T_{13} = \tau_1 + \tau_2$. The terms E_i^2 are the pulse spectra incident on the

detector, which do not depend on any time delays. Since the scatter terms all oscillate at frequency ω_3, the resulting artifact appears along the diagonal in the 2D IR spectrum.

When considering the contributions of scatter terms, there is a crucial difference between 2D IR and TA measurements, since 2D IR spectra are processed with a Fourier transform over τ_1. Therefore, any scatter or TA term which is independent of τ_1 is Fourier-filtered out (appearing only near $\omega_1 = 0$). This includes all E_i^2 terms, $S_{TA}^{(2,3)}$ and E_2E_3 scatter. However, this is not the case in a TA measurement. Therefore, the TA spectra were collected with a constant time step and Fourier filtered along τ_2 to remove E_2E_3 scatter. In the frequency domain, the slowly-varying TA signal appeared near $\omega_2 = 0$ and was isolated from the scatter which appeared near $\omega_2 = \omega_3$. Otherwise, the same processing was applied to both 2D IR and TA spectra.

The simplest scatter subtraction method used was a negative time subtraction at $\tau_2 = -5\,\text{ps}$. The negative waiting time was chosen to be much longer than the oscillation period (10 fs at 3 μm), such that any interference between pump and probe has decayed. The only term present at this negative waiting time (besides the pulse spectra) is the E_1E_2 scatter, with the signature shown in Fig. 3.13a. Therefore, E_1E_2 scatter is suppressed by subtracting the negative time surface.

3.6.2. Optical Chopping

Optical chopping enables subtraction on a shot-to-shot basis. Under normal operating conditions, the stationary pump pulse E_2 is chopped at 500 Hz, half the repetition rate of the laser. All terms that depend on E_2 are incident on the detector in every-other shot. So, subtraction

between successive shots removes the E_2-independent terms including E_1E_3 scatter and $S_{TA}^{(1,3)}$. Even when no scatter is present, chopping is used for differential measurement of the 2D IR signal.

In principle, the combination of chopping E_2, negative time subtraction, and Fourier filtering are sufficient to remove all scatter and TA terms in Eq. (3.15), leaving only the 2D IR spectrum. In practice, scatter from the zeolite particles was intense enough that these steps alone were not sufficient. The direct E_1E_2 scatter was further suppressed by adding a second chopper to the probe line E_3. Just like the E_2 chopper, the E_3 chopper subtracts terms which do not depend on E_3, including the E_1E_2 scatter. The second chopper operated at 250 Hz, so S_{2DIR} was present in one out of every four shots. The four consecutive shots are labeled S_{OO}, S_{OC}, S_{CO}, S_{CC}, where the indices are the states of the E_2 and E_3 choppers, respectively (O for open, C for closed). The double-chopped signal is constructed as $S_{DC} = (S_{OO} - S_{OC}) - (S_{CO} - S_{CC})$.

$$\begin{aligned}
S_{OO} &= S_{2DIR}E_3 + a_{12}E_1E_2 + a_{13}E_1E_3 + a_{23}E_2E_3 + E_1^2 + E_2^2 + E_3^2 \\
S_{OC} &= a_{12}E_1E_2 + E_1^2 + E_2^2 \\
S_{CO} &= + a_{13}E_1E_3 + E_1^2 + E_3^2 \\
S_{CC} &= E_1^2 \\
S_{DC} &= S_{2DIR}E_3 + a_{23}E_2E_3
\end{aligned} \tag{3.17}$$

3.6.3. Quasi-Phase Cycling

While the probe chopper subtracted residual E_1E_2 scatter, E_1E_3 scatter was further suppressed with the implementation of quasi-phase cycling.[48] In quasi-phase cycling, the relative phase ϕ_{13} between E_1 and E_3 is shifted in successive shots by introducing a variation in τ_2 on the order of the optical period $2\pi/\omega_3$. This can be accomplished in multiple ways, for example using a

wobbling Brewster window to modulate the optical delay of one pulse.[48] In our experiments, we oscillated the τ_2 stage over a distance of 1.1 μm, corresponding to a maximum delay of 7 fs. The oscillation distance was set empirically to minimize scatter before beginning an experiment. The oscillation period of the stage was 10 Hz, so the stage completed 5 cycles for each data point, averaged over 500 shots at 1 kHz.

Quasi-phase cycling perfectly cancels scatter only at the center frequency ω_0 (as opposed to proper phase cycling using a pulse shaper, which does not have this restriction), and slightly narrows the 2D IR spectrum. The scatter grows with frequency as $\sin(\pi\omega/\omega_0)$ and the 2D IR signal is suppressed as $\sin(\pi\omega/2\omega_0)$.[48] For a center frequency of 3400 cm^{-1}, ~72% of scatter is suppressed at ±200 cm^{-1}, where the 2D IR signal is suppressed by only <0.5%. Therefore, the scatter suppression is significant over the bandwidth of the excitation pulse and the narrowing effect is negligible. We found that quasi-phase cycling dramatically improved the signal quality for excitation pulses from the 3 μm OPA, as shown in Fig. 3.13. However, it provided no benefit for DFG pulses. This is likely due to the much longer pathlength between separation and recombination for DFG/BBIR pulses, compared to 3 μm OPA/BBIR, which scrambles the relative phase ϕ_{13} and suppresses E_1E_3 scatter without the need for phase cycling.

The combination of index-matching oils, double chopping, quasi-phase cycling, and negative time subtraction enabled the measurement of scatter-free 2D IR spectra of the highly-scattering zeolite particles, as shown in Fig. 3.13. In Fig. 3.13b, E_1E_2 scatter is largely suppressed by the probe chopper, and the most prominent signal is E_1E_3 scatter which appears along the diagonal and oscillates because of its dependence on τ_2. The oscillation period in the 2D IR spectrum is

$\sim 330\,\mathrm{cm}^{-1} = 1/\mathrm{c}\tau_2$ at $\tau_2 = 100\,\mathrm{fs}$. That E_1E_3 scatter is largely removed by quasi-phase cycling in Fig. 3.13c, and residual E_1E_2 scatter is removed by the negative time subtraction to produce the final result in Fig. 3.13d.

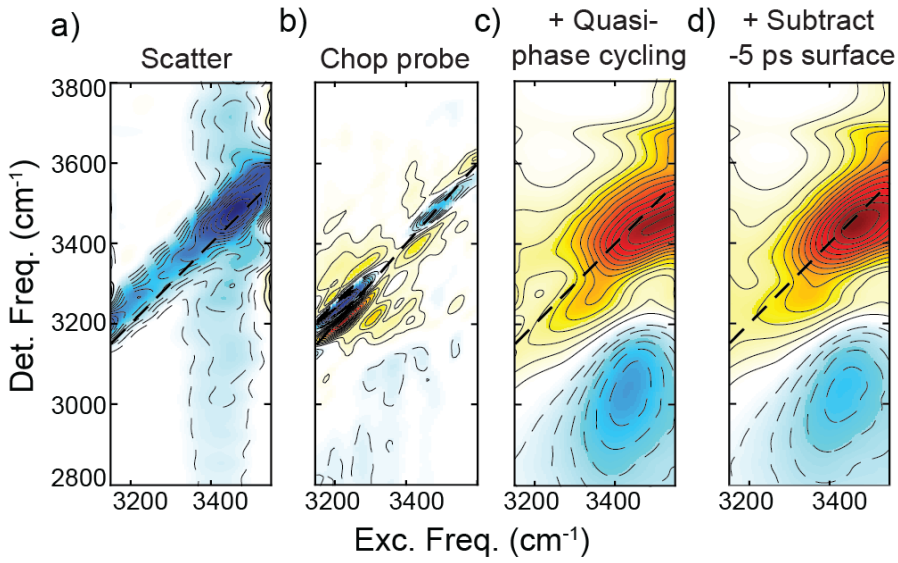

Figure 3.13. 2D IR spectra of hydrated HZSM-5 with scatter suppression methods. (a) The signature of direct scatter, measured at -5 ps. (b-d) Signal at 100 fs with (b) double chopping, (c) double chopping and quasi-phase cycling, (d) double chopping, quasi-phase cycling, and negative time subtraction.

3.7. References

(1) Hamm, P.; Lim, M.; Hochstrasser, R. M. Structure of the Amide I Band of Peptides Measured by Femtosecond Nonlinear-Infrared Spectroscopy. *J. Phys. Chem. B* **1998**, *102* (31), 6123–6138. https://doi.org/10.1021/jp9813286.

(2) Kaindl, R. A.; Wurm, M.; Reimann, K.; Hamm, P.; Weiner, A. M.; Woerner, M. Generation, Shaping, and Characterization of Intense Femtosecond Pulses Tunable from 3 to 20 Mm. *J. Opt. Soc. Am. B* **2000**, *17* (12), 2086. https://doi.org/10.1364/JOSAB.17.002086.

(3) Fecko, C. J.; Loparo, J. J.; Tokmakoff, A. Generation of 45 Femtosecond Pulses at 3 Mm with a KNbO3 Optical Parametric Amplifier. *Opt. Commun.* **2004**, *241*, 521–528.

https://doi.org/10.1016/j.optcom.2004.07.038.

(4) Petersen, P. B.; Tokmakoff, A. Source for Ultrafast Continuum Infrared and Terahertz Radiation. *Opt. Lett.* **2010**, *35* (12), 1962. https://doi.org/10.1364/OL.35.001962.

(5) Demirdöven, N.; Khalil, M.; Golonzka, O.; Tokmakoff, A. Dispersion Compensation with Optical Materials for Compression of Intense Sub-100-Fs Mid-Infrared Pulses. *Opt. Lett.* **2002**, *27* (6), 433–435. https://doi.org/10.1364/ol.27.000433.

(6) Shim, S.-H.; Strasfeld, D. B.; Fulmer, E. C.; Zanni, M. T. Femtosecond Pulse Shaping Directly in the Mid-IR Using Acousto-Optic Modulation. *Opt. Lett.* **2006**, *31* (6), 838. https://doi.org/10.1364/ol.31.000838.

(7) DeFlores, L. P.; Nicodemus, R. A.; Tokmakoff, A. Two-Dimensional Fourier Transform Spectroscopy in the Pump-Probe Geometry. *Opt. Lett.* **2007**, *32* (20), 2966. https://doi.org/10.1364/ol.32.002966.

(8) Faeder, S. M. G.; Jonas, D. M. Two-Dimensional Electronic Correlation and Relaxation Spectra: Theory and Model Calculations. *J. Phys. Chem. A* **1999**, *103* (49), 10489–10505. https://doi.org/10.1021/jp9925738.

(9) Donaldson, P. M.; Greetham, G. M.; Shaw, D. J.; Parker, A. W.; Towrie, M. A 100 KHz Pulse Shaping 2D-IR Spectrometer Based on Dual Yb:KGW Amplifiers. *J. Phys. Chem. A* **2018**, *122* (3), 780–787. https://doi.org/10.1021/acs.jpca.7b10259.

(10) Donaldson, P. M.; Howe, R. F.; Hawkins, A. P.; Towrie, M.; Greetham, G. M. Ultrafast 2D-IR Spectroscopy of Intensely Optically Scattering Pelleted Solid Catalysts. *J. Chem. Phys.* **2023**, *158* (11), 114201. https://doi.org/10.1063/5.0139103.

(11) Stingel, A. M.; Petersen, P. B. Full Spectrum 2D IR Spectroscopy Reveals Below-Gap Absorption and Phonon Dynamics in the Mid-IR Bandgap Semiconductor InAs. *J. Chem. Phys.* **2021**, *155*, 104202. https://doi.org/10.1063/5.0056217.

(12) Hack, J. H.; Lewis, N. H. C.; Carpenter, W. B.; Tokmakoff, A. Amplification of Mid-IR Continuum for Broadband 2D IR Spectroscopy. *Opt. Lett.* **2023**, *48* (4), 960–963. https://doi.org/10.1364/OL.481088.

(13) Al-Mualem, Z. A.; Chen, X.; Shirley, J. C.; Xu, C.; Baiz, C. R. BoxCARS 2D IR Spectroscopy with Pulse Shaping. *Opt. Express* **2023**, *31* (2), 2700. https://doi.org/10.1364/oe.471984.

(14) Farrell, K. M.; Yang, N.; Zanni, M. T. A Polarization Scheme That Resolves Cross-Peaks with Transient Absorption and Eliminates Diagonal Peaks in 2D Spectroscopy. *Proc. Natl. Acad. Sci. U. S. A.* **2022**, *119* (6). https://doi.org/10.1073/pnas.2117398119.

(15) Eaves, J. D.; Loparo, J. J.; Fecko, C. J.; Roberts, S. T.; Tokmakoff, A.; Geissler, P. L. Hydrogen Bonds in Liquid Water Are Broken Only Fleetingly. *Proc. Natl. Acad. Sci.* **2005**, *102* (37), 13019–13022. https://doi.org/10.1073/pnas.0505125102.

(16) Ramasesha, K.; De Marco, L.; Mandal, A.; Tokmakoff, A. Water Vibrations Have Strongly Mixed Intra- and Intermolecular Character. *Nat. Chem.* **2013**, *5* (11), 935–940. https://doi.org/10.1038/nchem.1757.

(17) Fournier, J. A.; Carpenter, W. B.; Lewis, N. H. C.; Tokmakoff, A. Broadband 2D IR Spectroscopy Reveals Dominant Asymmetric H5O2+ Proton Hydration Structures in Acid Solutions. *Nat. Chem.* **2018**, *10*, 932–937. https://doi.org/10.1038/s41557-018-0091-y.

(18) Dahms, F.; Fingerhut, B. P.; Nibbering, E. T. J.; Pines, E.; Elsaesser, T. Large-Amplitude Transfer Motion of Hydrated Excess Protons Mapped by Ultrafast 2D IR Spectroscopy. *Science* **2017**, *357* (6350), 491–495. https://doi.org/10.1126/science.aan5144.

(19) Petersen, P. B.; Tokmakoff, A. Source for Ultrafast Continuum Infrared and Terahertz Radiation. *Opt. Lett.* **2010**, *35* (12), 1962. https://doi.org/10.1364/ol.35.001962.

(20) Ramasesha, K. Dynamics of Water and Aqueous Protons Studied Using Ultrafast Multi-Dimensional Infrared Spectroscopy, Massachusetts Institute of Technology, 2013.

(21) De Marco, L. The Molecular Dynamics of Hydrogen-Bonding Explored with Broadband Two Dimensional Infrared Spectroscopy, Massachusetts Institute of Technology, 2016.

(22) Carpenter, W. B. Aqueous Proton Structures and Dynamics Observed with Nonlinear Infrared Spectroscopy, University of Chicago, 2020. https://knowledge.uchicago.edu/record/2584.

(23) Diels, J.-C.; Rudolph, W. *Ultrashort Laser Pulse Phenomena*, 2nd ed.; Academic Press: Amsterdam, 2006.

(24) Manzoni, C.; Cerullo, G. Design Criteria for Ultrafast Optical Parametric Amplifiers. *J. Opt.* **2016**, *18* (10), 103501. https://doi.org/10.1088/2040-8978/18/10/103501.

(25) Armstrong, J. A.; Bloembergen, N.; Ducuing, J.; Pershan, P. S. Interactions between Light Waves in a Nonlinear Dielectric. *Phys. Rev.* **1962**, *127* (6), 1918–1939. https://doi.org/10.1103/PhysRev.127.1918.

(26) Smith, A. V. SNLO Nonlinear Optics Code. AS-Photonics: Albuquerque, NM. https://as-photonics.com/products/snlo/.

(27) Cook, D. J.; Hochstrasser, R. M. Intense Terahertz Pulses by Four-Wave Rectification in Air. *Opt. Lett.* **2000**, *25* (16), 1210. https://doi.org/10.1364/OL.25.001210.

(28) Fuji, T.; Suzuki, T. Generation of Sub-Two-Cycle Mid-Infrared Pulses by Four-Wave Mixing through Filamentation in Air. *Opt. Lett.* **2007**, *32* (22), 3330. https://doi.org/10.1364/OL.32.003330.

(29) Fuji, T.; Nomura, Y. Generation of Phase-Stable Sub-Cycle Mid-Infrared Pulses from Filamentation in Nitrogen. *Appl. Sci.* **2013**, *3* (1), 122–138. https://doi.org/10.3390/app3010122.

(30) Bjorklund, G. C. Effects of Focusing on Third-Order Nonlinear Processes in Isotropic Media. *IEEE J. Quantum Electron.* **1975**, *11* (6), 287–296.

(31) Kress, M.; Löffler, T.; Eden, S.; Thomson, M.; Roskos, H. G. Terahertz-Pulse Generation by Photoionization of Air with Laser Pulses Composed of Both Fundamental and Second-Harmonic Waves. *Opt. Lett.* **2004**, *29* (10), 1120. https://doi.org/10.1364/ol.29.001120.

(32) Kim, K.-Y.; Glownia, J. H.; Taylor, A. J.; Rodriguez, G. Terahertz Emission from Ultrafast Ionizing Air in Symmetry-Broken Laser Fields. *Opt. Express* **2007**, *15* (8), 4577. https://doi.org/10.1364/oe.15.004577.

(33) Dai, J.; Karpowicz, N.; Zhang, X. C. Coherent Polarization Control of Terahertz Waves Generated from Two-Color Laser-Induced Gas Plasma. *Phys. Rev. Lett.* **2009**, *103* (2), 1–4. https://doi.org/10.1103/PhysRevLett.103.023001.

(34) Corkum, P. B. Plasma Perspective on Strong Field Multiphoton Ionization. *Phys. Rev. Lett.* **1993**, *71* (13), 1994–1997. https://doi.org/10.1103/PhysRevLett.71.1994.

(35) Krausz, F.; Ivanov, M. Attosecond Physics. *Rev. Mod. Phys.* **2009**, *81* (1), 163–234. https://doi.org/10.1103/RevModPhys.81.163.

(36) Treacy, E. B. Optical Pulse Compression with Diffraction Gratings. *IEEE J. Quantum Electron.* **1969**, *5* (9), 454–458. https://doi.org/10.1109/JQE.1969.1076303.

(37) Balasubramanian, M.; Courtney, T. L.; Gaynor, J. D.; Khalil, M. Compression of Tunable Broadband Mid-IR Pulses with a Deformable Mirror Pulse Shaper. *J. Opt. Soc. Am. B* **2016**, *33* (10), 2033. https://doi.org/10.1364/JOSAB.33.002033.

(38) Trebino, R.; DeLong, K. W.; Fittinghoff, D. N.; Sweetser, J. N.; Krumbügel, M. A.; Richman, B. A.; Kane, D. J. Measuring Ultrashort Laser Pulses in the Time-Frequency Domain Using Frequency-Resolved Optical Gating. *Rev. Sci. Instrum.* **1997**, *68* (9), 3277–3295. https://doi.org/10.1063/1.1148286.

(39) Nomura, Y.; Shirai, H.; Fuji, T. Frequency-Resolved Optical Gating Capable of Carrier-Envelope Phase Determination. *Nat. Commun.* **2013**, *4*, 1–11. https://doi.org/10.1038/ncomms3820.

(40) Shirai, H.; Kumaki, F.; Nomura, Y.; Fuji, T. High-Harmonic Generation in Solids Driven by Subcycle Midinfrared Pulses from Two-Color Filamentation. *Opt. Lett.* **2018**, *43* (9), 2094. https://doi.org/10.1364/OL.43.002094.

(41) Mertz, L. Auxiliary Computation for Fourier Spectrometry. *Infrared Phys.* **1967**, *7* (1), 17–23. https://doi.org/10.1016/0020-0891(67)90026-7.

(42) Stingel, A. M.; Petersen, P. B. Couplings Across the Vibrational Spectrum Caused by Strong Hydrogen Bonds : A Continuum 2D IR Study of the 7-Azaindole−Acetic Acid Heterodimer. *J. Phys. Chem. B* **2016**, *120*, 10768–10779. https://doi.org/10.1021/acs.jpcb.6b05049.

(43) Thämer, M.; De Marco, L.; Ramasesha, K.; Mandal, A.; Tokmakoff, A. Ultrafast 2D IR Spectroscopy of the Excess Proton in Liquid Water. *Science* **2015**, *350* (6256), 78–82. https://doi.org/10.1126/science.aab3908.

(44) Hamm, P.; Zanni, M. *Concepts and Methods of 2D Infrared Spectroscopy*; Cambridge University Press: Cambridge, UK and New York, NY, USA, 2011.

(45) Donaldson, P. M. Spectrophotometric Concentration Analysis Without Molar Absorption Coefficients by Two-Dimensional-Infrared and Fourier Transform Infrared Spectroscopy. *Anal. Chem.* **2022**, *94* (51), 17988–17999. https://doi.org/10.1021/acs.analchem.2c04287.

(46) Yamada, S. A.; Shin, J. Y.; Thompson, W. H.; Fayer, M. D. Water Dynamics in Nanoporous Silica: Ultrafast Vibrational Spectroscopy and Molecular Dynamics Simulations. *J. Phys. Chem. C* **2019**, *123* (9), 5790–5803. https://doi.org/10.1021/acs.jpcc.9b00593.

(47) Middleton, C. T.; Woys, A. M.; Mukherjee, S. S.; Zanni, M. T. Residue-Specific Structural Kinetics of Proteins through the Union of Isotope Labeling, Mid-IR Pulse Shaping, and Coherent 2D IR Spectroscopy. *Methods* **2010**, *52* (1), 12–22. https://doi.org/10.1016/j.ymeth.2010.05.002.

(48) Bloem, R.; Garrett-Roe, S.; Strzalka, H.; Hamm, P.; Donaldson, P. Enhancing Signal Detection and Completely Eliminating Scattering Using Quasi-Phase-Cycling in 2D IR Experiments. *Opt. Express* **2010**, *18* (26), 1747–1756. https://doi.org/10.1364/OE.18.027067.

Chapter 4

Amplification of mid-IR continuum for broadband 2D IR spectroscopy

Much of the work in this chapter has been published and is adapted with permission from:
Hack, J. H., Lewis, N. H. C., Carpenter, W. B., Tokmakoff, A. Amplification of mid-IR continuum for broadband 2D IR spectroscopy. *Optics Letters*, **48**, 960-963 (2023).

4.1. Introduction

The studies presented in the next three chapters were conducted using the technology described in Chapter 3. In parallel, we developed a new source for broadband mid-IR light pulses with increased pulse energy, with the goal of expanding the accessible excitation bandwidth in 2D IR spectroscopy experiments. That work is described in this chapter.

The generation of few-cycle IR pulses has advanced rapidly in recent years, with applications in high-harmonic generation,[1] terahertz generation,[2] solid state physics,[3] and infrared spectroscopy.[4] While all operating in the mid-IR (MIR) spectral range, these various applications have different design and implementation requirements for pulse energy, spectrum, bandwidth, and compression, and a wide range of generation strategies have been tailored to different needs.[5] For ultrafast IR spectroscopy, design criteria

include compression at the sample, broad bandwidth and smoothly-varying spectrum for spectral coverage, microjoule pulse energies to excite molecular vibrations, and shot-to-shot stability for averaging, as discussed in Chapter 3. Increasing pulse bandwidth – and thus spectral coverage – while meeting all other requirements would dramatically improve capabilities for measuring broad vibrational lineshapes, simultaneous measurement of multiple transitions, and data collection efficiency. Major practical challenges include generating suitable pulses and delivering compressed pulses to the sample through the transmissive optics required in experiments for interferometry and sample housing. While often manageable for narrower pulses, the temporal and spatial dispersion accumulated from transmissive optics increases with pulse bandwidth. Dispersion compensation is more difficult in the MIR than in the visible, as chirp mirrors are unavailable and prism or grating compressors are lossy and difficult to align.

Ultrafast two-dimensional infrared (2D IR) spectroscopy has been used extensively to measure vibrational structure and dynamics in molecular systems.[6] In state-of-the-art experiments, microjoule pulse energies are obtained by down-conversion via optical parametric amplification (OPA) or difference frequency generation (DFG) on Ti:Sapphire systems, with bandwidths limited to 150-400 cm^{-1} and pulse durations of 45-70 fs.[4,7–9] This covers only a fraction of the MIR spectral range of 500-4000 cm^{-1}, making tuning a necessity for broad spectral coverage,[4,9] for example using the strategy and technology described in Chapter 3.

Alternative generation schemes include laser filamentation in gases, which produced pulses with broad, smooth spectra covering the MIR with typical pulse energies on the order of 10-100 nJ.[10,11] These broadband IR (BBIR) continuum sources have been implemented as a probe in 2D IR spectroscopy, dramatically increasing the accessible detection bandwidth,[4,9] though pulse energies are too low to excite molecular vibrations. Microjoule pulse energies have been reached via OPA or DFG in non-oxide crystals

such as GaSe, $ZnGeP_2$ (ZGP), and $CdSiP_2$ (CSP) which support broad phase-matching when pumped near 2 μm.[1,12–14] A variety of pump sources and repetition rates were used, reaching large power by optical parametric chirped pulse amplification,[1,12] lasing near 2 μm in Cr^{2+}:ZnS or Tm-doped systems,[15,16] or down-conversion from 1 μm lasers.[14] Large average MIR powers were attained by intra-pulse DFG, though pulse energies were sub-microjoule at high repetition rates.[15,16] While the generation of extraordinarily short, intense, or broadband IR pulses has been reported,[5] suitable pulses which meet all requirements for 2D IR vibrational spectroscopy – while significantly improving on a bandwidth of 400 cm^{-1} – have not yet been demonstrated and implemented in experiments.

In this chapter, we report the generation and implementation of broadband, microjoule MIR pulses spanning >1000 cm^{-1} for excitation and detection in 2D IR spectroscopy of O-H and N-H molecular vibrations. Because the BBIR source meets all requirements but pulse energy, our strategy is to amplify that pulse by OPA with a 2 μm pump in GaSe, which supports a broader phase-matching bandwidth and transparency range than CSP or ZGP.[13] The OPA and 2D IR apparatus are designed to minimize transmissive optics, and amplified pulses are compressed at the sample using bulk material. Based on Ti:Sapphire and TOPAS technology, this light source operates on systems readily available in many ultrafast spectroscopy labs.

4.2. Description of the OPA

Figure 4.1 shows a schematic of the OPA and 2D IR interferometer and spectrometer. The output of a Ti:Sapphire regenerative amplifier (Coherent Legend Elite, 25 fs, 1 kHz) is split into two paths: 0.7 mJ is used to generate the seed and 1.8 mJ to generate the pump. The 2 μm pump (50 fs, 105 μJ ±0.5% at the

GaSe crystal) is generated as the idler from a commercial OPA (Light Conversion TOPAS Prime) and expanded to a diameter of ~13 mm $1/e^2$ with a Galilean telescope.

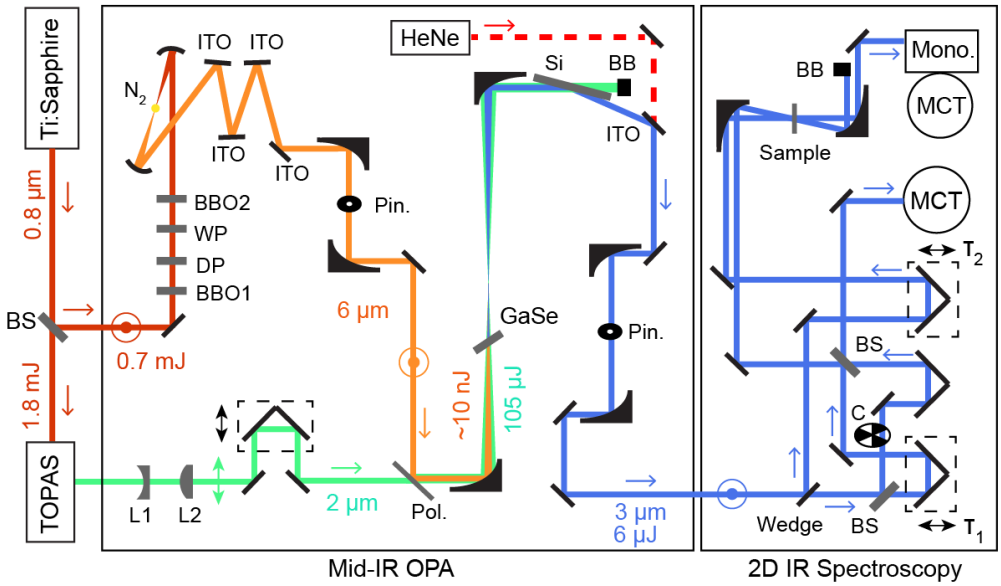

Figure 4.1. Mid-IR OPA and 2D IR interferometer and spectrometer. BB, beam block; BBO, β-Barium borate; BS, beamsplitter; C, optical chopper; DP, delay plate; L, lens; MCT, HgCdTe detector; Mono., monochromator; Pin, pinhole; Pol, polarizer; WP, waveplate. Color scheme: red, Ti:Sapphire fundamental; orange, seed; green, pump; blue, signal; dashed red, visible tracer.

In the seed line, continuum MIR is generated using a scheme that has been described in detail previously,[11] and in Chapter 3. The 800 nm fundamental and its second and third harmonics are tightly focused into N_2 gas to generate a plasma which radiates light from 2.5-10 µm with a spectrum peaked near 6 µm. The generated BBIR is recollimated and separated from the other fields with four consecutive reflections off ITO coated glass (PGO CEC007S). The BBIR is spatially filtered to improve the beam profile and focusing using a 150 µm pinhole at the focus of two bare gold coated 90° off-axis parabolic mirrors (Au-OAP), f = 100 mm, resulting in a 20% improvement in OPA efficiency. The resulting 50 fs BBIR seed has an energy of ~10 nJ with 3-5% rms shot-to-shot noise.

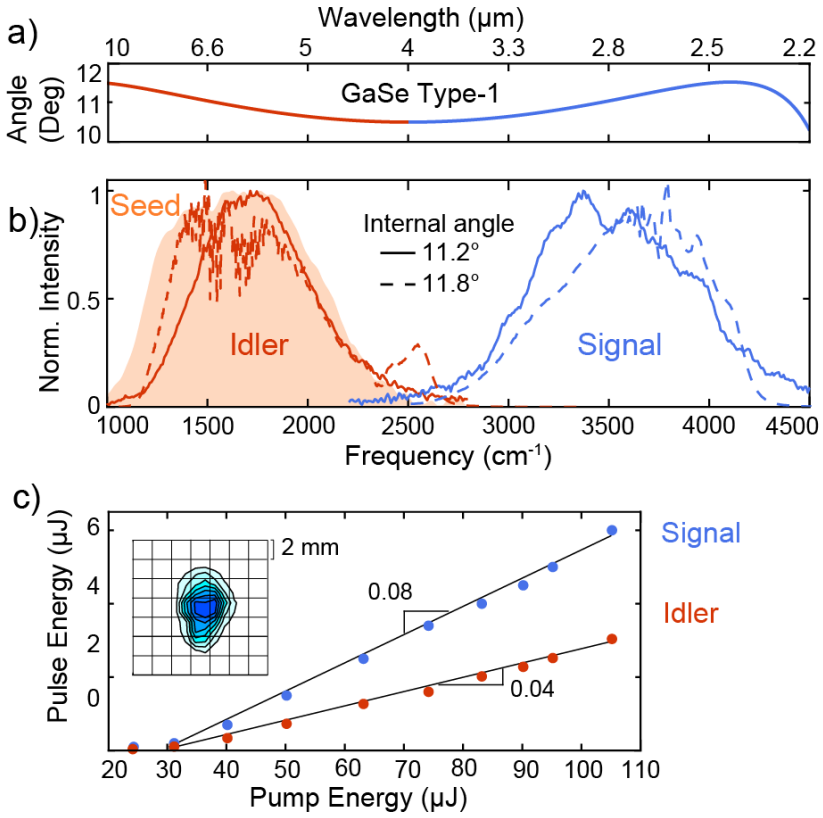

Figure 4.2. (a) Type-1 phase matching curve for GaSe pumped at 2 μm. (b) Pulse spectra at phase matching angle 11.2° (solid) and 11.8° (dashed). (c) Pulse energy scaling with linear fit; inset, signal spatial profile.

After pulse retiming, the pump and seed are spatially overlapped with orthogonal polarization by reflecting the BBIR off a CaF_2 wire grid polarizer (Specac) which transmits the pump. The collinear pump and seed pulses are focused into a 1-mm GaSe crystal (z-cut, Eksma) using a Au-OAP (f = 200 mm). The crystal is placed 25 mm before the focus where pump and seed diameters are 1.6 mm and 0.5 mm $1/e^2$, (with approximate peak intensities 200 and 0.2 GW/cm^2 assuming a Gaussian profile) respectively. Type-1 phase matching in GaSe at a phase-matching angle (θ_{PM}) of 11.2-11.8° supports a broad bandwidth (Fig. 4.2a), producing amplified BBIR signal and idler displayed in Fig. 4.2b. The amplified pulses have spectra spanning over 1000 cm^{-1}, somewhat narrower than the seed due to phase matching. Parametric

amplification with $\theta_{PM} = 11.2°$ yields a slope efficiency of 8% and 4% for signal and idler, respectively (Fig. 4.2c), and pulse energies of 6 μJ and 3 μJ (±1% rms) with a 105 μJ pump, consistent with the ~2:1 ratio of output frequencies. This represents a 20% total photon conversion efficiency considering the ~16% Fresnel reflection off the GaSe crystal, and the lack of saturation suggests further scalability. Spatial profiles of the collimated (focused) beams were measured by transmission through a 400 (100) μm pinhole mounted on an x-y stage.

After recollimation to a diameter of 7 mm $1/e^2$, amplified BBIR is separated from residual pump by reflection off a Si wafer at Brewster's angle, which transmits the horizontally polarized pump and reflects 72% of the amplified BBIR. This approach was chosen to minimize dispersion and more efficiently transmit the pump compared to the polarizer used to combine the beams. The signal and idler exit the GaSe crystal at a small angle (<1°) with respect to each other due to refraction, which we use to separate the beams by passing one through a 200 μm pinhole at the focus of two matched Au-OAPs (f = 100 mm).

4.3. Pulse compression and characterization

Minimizing the total transmissive material before the sample is an important consideration for pulse compression. While group delay dispersion (GDD) can be compensated in the MIR using oppositely signed GDD materials, third-order dispersion (TOD) is positive for all materials and grows rapidly with increasing wavelength for many materials including CaF_2.[17] The amplified BBIR pulse exits the OPA having transmitted through only the 1-mm GaSe crystal with GDD of 230 fs^2 at 3 μm. Considering also the 3-mm KBr beamsplitter (51 fs^2) in the 2D IR interferometer used here (Fig. 4.1) suggests that the 3 μm signal can be compressed with 3 mm of CaF_2 (GDD = –318 fs^2), which is also a desirable material for sample

windows.[18] Idler compression poses a greater practical challenge because of the large TOD from transmissive material at 6 μm and longer wavelengths.

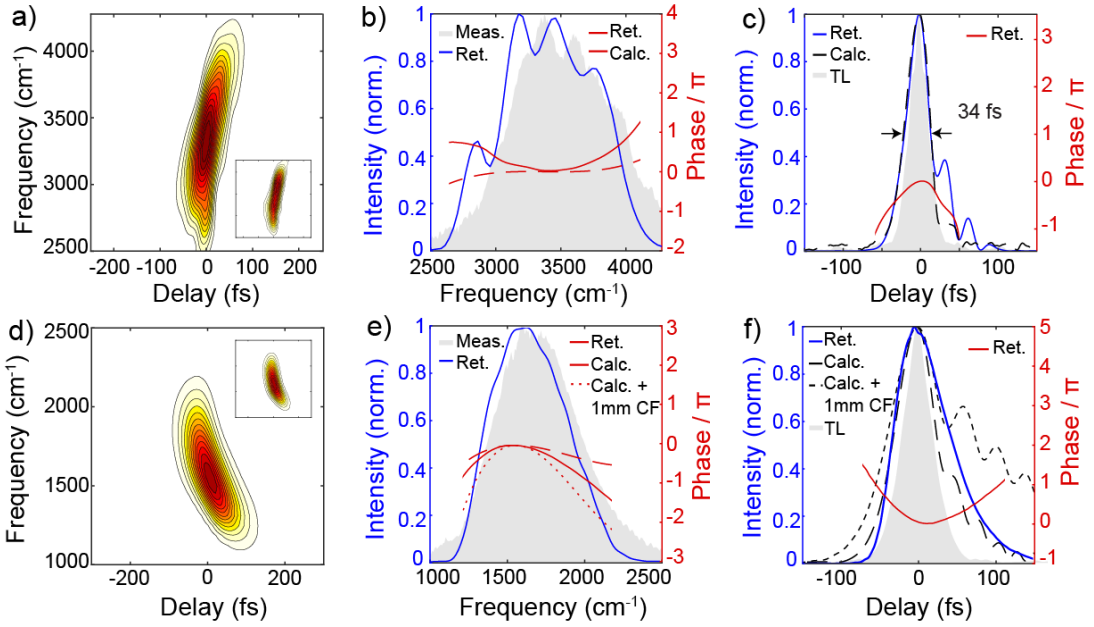

Figure 4.3. FROG characterization of (a-c) signal using nonresonant response in 0.5 mm Si with 3 mm CaF_2 added in the beam path and (d-f) idler using 1 mm Ge. (a & d) Retrieved FROG spectrogram (inset: measured spectrogram). (b & e) Retrieved spectral intensity (blue) and spectral phase (red), along with measured spectrum (shaded) and calculated spectral phase accounting for transmissive material in the beam (dashed) and addition of 1 mm CaF_2 (dotted). (c & f) Retrieved time-domain intensity (blue) and phase (red), along with the transform limit (shaded) and calculated intensity (dashed, dotted) from the measured spectrum and calculated spectral phases in (b & e).

Pulse compression was measured with frequency resolved optical gating (FROG)[19] using the interferometer and spectrometer in Fig. 4.1 with slight modification. A noncollinear pulse pair was generated in a Mach-Zehnder interferometer (MZI) with two 3-mm AR coated 50/50 KBr beamsplitters. This was achieved by displacing the retro-reflector in the stationary arm of the interferometer horizontally using a translation stage. Signal (or idler) pulses were crossed in a 0.5 mm Si (or 1 mm Ge) window at the sample position using a Au-OAP (f = 100 mm) and one pulse was dispersed with a monochromator onto a

HgCdTe (MCT) detector. The third-order non-resonant response was collected as a function of wavelength and interferometer delay. This measurement carries the same information as transient grating FROG,[20,21] and was analyzed this way using commercial software (Femtosoft). This third-order FROG method was chosen to avoid phase matching limitations in second-order processes such as SHG FROG.

Figure 4.3 displays the FROG measurements and retrievals for signal (a-c) and idler (d-f). For the signal characterization, 3 mm CaF_2 was placed before the MZI. The retrieved pulsewidth was 34 fs FWHM, corresponding to <4 optical cycles at 3 μm; the transform limit is 26 fs. For comparison, the spectral phase was calculated accounting for the GDD and TOD of the GaSe, KBr, and CaF_2 material in the beam path (dashed line in 3c) using tabulated data for the refractive index.[22] Together with the measured spectrum, the calculated spectral phase was used to model the pulse intensity in the time domain (dashed black line in Fig. 4.3c). The residual positive GDD in the retrieved FROG is likely the result of the Si window used for characterization, as suggested by the calculated spectral phase when Si dispersion is neglected.

Signal compression was optimized by measuring the FROG trace as a function of CaF_2 added to the beam before the interferometer, shown in Fig. 4.4. The FROG trace displays positive GDD accumulated in the GaSe crystal, which decreases as CaF_2 is added. When 5-7 mm CaF_2 is added, some curvature is observed in the FROG trace due to TOD, which increases with addition of transmissive material. As expected, the retrieved pulsewidth is minimized with the addition of 3 mm CaF_2.

Idler FROG characterization (Fig. 4.3 d-f) was measured without additional material in the beam path. The retrieved pulsewidth was 80 fs FWHM, due to uncompensated negative GDD in GaSe at 6 μm and positive TOD from GaSe and KBr; the transform limit is 40 fs. For comparison, the spectral phase was calculated accounting for 1 mm GaSe and 3 mm KBr (dashed line), with the addition of 1 mm CaF_2 (dotted line). This suggests that the GDD can be compensated by a material such as Ge with positive GDD, and

that spectroscopic experiments will require an alternative to CaF_2 sample windows such as thin Si_3N_4 windows.[23]

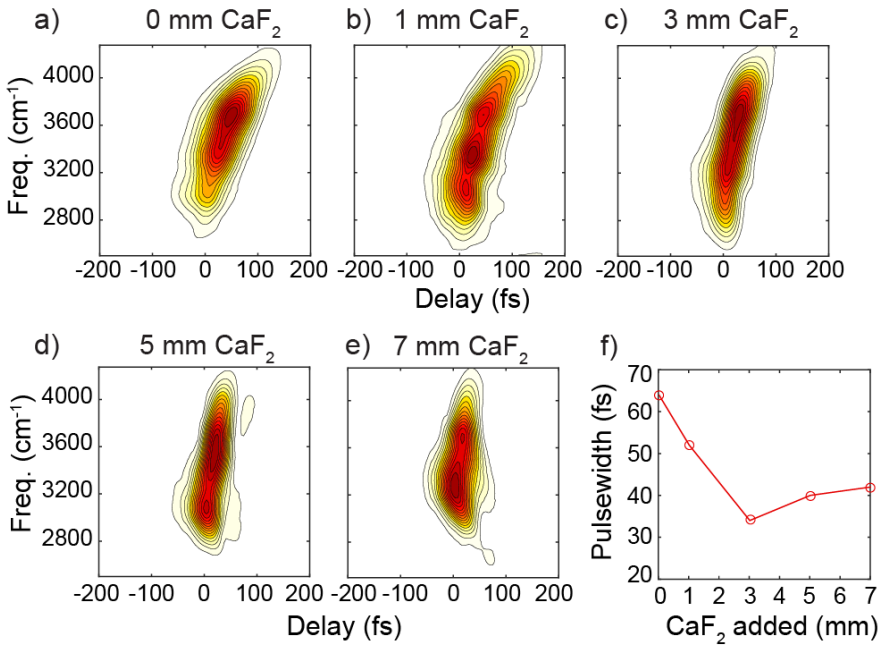

Figure 4.4. FROG characterization of the signal pulse as a function of CaF_2 bulk material added before the interferometer. (a-e) Experimental FROG traces using the nonresonant response in 0.5 mm Si. (f) Retrieved pulsewidth as a function of CaF_2 added.

4.4. 2D IR spectroscopy with broadband excitation and detection

To demonstrate the utility of this light source for spectroscopy, 2D IR measurements were collected with the experimental apparatus in Fig. 4.1 using the compressed signal for excitation and detection. The detection pulse is a 1% reflection off a 1-mm CaF_2 wedge, and the excitation pulse pair exit the MZI collinearly. Pulses meet at the sample in the pump-probe geometry.[24,25] The nonlinear signal is measured as an absorption change in the frequency domain with a monochromator and MCT detector. For

compression, 1 mm CaF_2 was added in the beam path before and after the wedge such that all beams pass through at total of 3 mm including the sample window.

The instrument response function is determined by the nonresonant response of the 1-mm CaF_2 window before the sample. The transient absorption of that window is displayed in Fig. 4.5, and decays before 100 fs waiting time (τ_2) or earlier, suggesting that any signal measured in experiments at $\tau_2 \geq 100\,\text{fs}$ can be attributed to the sample of interest. To reproduce the conditions of 2D IR measurements, both excitation and detection pulses pass through 2 mm CaF_2 before reaching the window in the focus.

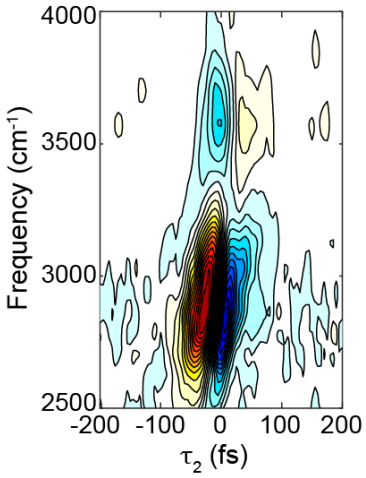

Figure 4.5. Transient absorption of a 1-mm CaF_2 window using the signal pulse for excitation and detection.

The early-time 2D IR spectrum of isotopically dilute HOD in D_2O in the O-H stretch region (a benchmark that has been studied both experimentally and theoretically)[26,27] demonstrates the improved capabilities for lineshape measurements with broadband excitation (Fig. 4.6a) compared to excitation with 300 cm^{-1} bandwidth FWHM (Fig. 4.6b) generated in a $KNbO_3$ OPA.[8] With BBIR excitation, the 2D IR spectrum reproduces the fundamental (red) and excited state absorption (ESA, blue) features, and quantitatively reproduces the nodal line slope of the previous measurement. Notably, broadband excitation

reveals that the maximum of the O-H stretch in the 2D IR spectrum is red-shifted in excitation frequency relative to the linear absorption spectrum, which is not observed in Fig. 4.6b where the 2D IR lineshape is artificially narrowed by the excitation bandwidth. This difference between the 2D IR and linear absorption peak positions is an expected result of the frequency-dependent transition dipole moment of the O-H stretch.[27]

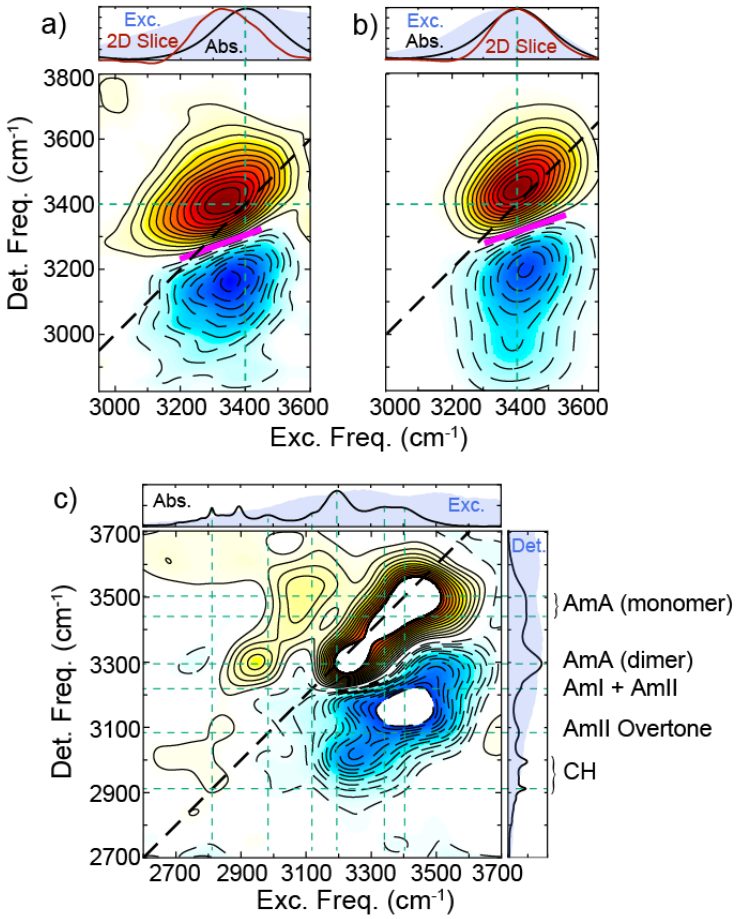

Figure 4.6. 2D IR spectra of (a-b) 1% HOD in D_2O and (c) 1 M NMA in DMSO-d6, collected at τ_2 = 100 fs with parallel polarization. Samples were excited with (a & c) the signal pulse reported in this work and (b) the 3 μm source described in ref. 8. Preliminary assignments in (c) are based on ref. 28. Color scheme: black, normalized linear absorption spectra; shaded, pulse spectra; red, diagonal 2D IR slice through the maximum; dashed green, selected transitions; magenta, nodal line.

The 2D IR spectrum of N-methylacetamide (NMA) dimers in DMSO-d6 (Fig. 4.6c) demonstrates the capabilities of broadband excitation for cross peak measurements, simultaneously exciting features spanning ~1000 cm^{-1}. This spectrum displays numerous resonances that arise from the coupled fundamental and overtone vibrations of the amide group, based on previous 2D IR measurements by De Marco *et* al.[28] The Amide A (AmA) fundamental appears at frequencies characteristic of both monomers and H-bonded dimers, while the rich cross peak structure arises from couplings to overtones and combination bands of Amide I and Amide II (AmI & AmII), which shift in frequency upon dimerization. Notably, uphill cross peaks can be observed simultaneously with diagonal features, which is necessary for quantitative comparison.

In summary, we report a source for broadband, multi-μJ MIR pulses centered at 3 μm and 6 μm and illustrate 2D IR spectroscopy with broadband excitation using the signal pulse. In principle, this source can be applied between 1000-4000 cm^{-1} covering the vibrational fingerprint region, making it particularly useful for broad molecular vibrations in aqueous solutions. The gain curve of the OPA is not saturated, suggesting further energy scalability with increased pump energy or crystal length, though tradeoffs with self-phase modulation or reduced phase matching bandwidth may arise. With future work to independently manipulate, compress, and combine signal and idler, we envision broad bandwidth 2D IR spectroscopy that measures time-resolved vibrational correlations simultaneously across the entire mid-infrared spectrum.

4.5. Outlook

The results above demonstrate that the signal of this OPA can be applied as an excitation source in 2D IR experiments. While proof-of-principle experiments were demonstrated by using the

signal for detection as well, integration with a separate BBIR probe source is a better long-term solution. This is because the signal is limited to ~2700 cm^{-1} and higher frequencies, while the BBIR probe can be applied across the entire MIR. Currently, our plan is to replace the 3 μm KNB OPA with this OPA in our working instrument detailed in Chapter 3. This will be straightforward in principle, but will require careful management of table space to achieve the correct beam path lengths and incorporation of the visible tracer in a new location.

Broadband excitation at 3 μm with continuum MIR detection will enable an exciting round of experiments on O-H stretch vibrations in liquid water and aqueous solutions. The O-H stretch vibration of isotopically pure H_2O has a linewidth of ~400 cm^{-1}, which is commensurate with the bandwidth of our current 3 μm excitation source, so I expect some improvement in the linewidth measurement with broadband excitation. In particular, it may be interesting to resolve the linewidth on the red side of the band where the Fermi resonance with the bend overtone plays a role in both isotopically pure and isotopically dilute spectra.[26] The aqueous excess proton is another system of great interest with extraordinarily broad transitions in the 3 μm region[9] which will be intriguing to study with the broadband excitation source. In that system there are longstanding questions about the ultrafast dynamics of the proton.[29,30] Clues about those dynamics may be encoded in the 2D lineshapes of the O-H vibrations, and in principle the shorter pulses generated in this OPA should enable 2D IR experiments with sub-100 fs instrument response time. On the blue side of the O-H stretch band, the broadband OPA will enable excitation of free O-H stretch vibrations. These are prominent in confined water systems including zeolites[31] and metal-organic frameworks[32] but are outside of the tuning range of our current excitation sources.

Another notable direction is expanding on the idler compression and characterization work shown in Fig. 4.3 to deliver compressed idler pulses to the sample. As described above, the crucial task will be finding a reliable alternative to CaF_2 windows, which are untenable at long MIR wavelengths with broadband pulses due to dispersion. Possible alternatives include thin Si_3N_4 windows,[23] or thin liquid jets which would eliminate sample windows altogether.[33] Furthermore, an additional round of pulsewidth characterization is needed to compensate for residual GDD in the idler. I expect AR coated Ge will be a good option for pulse compression, though there will still be some reflective losses. Access to broadband excitation in the 6 μm region can expand the information content in our studies of bending vibrations in H_2O and aqueous protons, as well as Amide I and Amide II vibrations in molecules like NMA and proteins. While broadband excitation is certainly not required for Amide I diagonal spectroscopy, valuable information may be revealed by simultaneously measuring the Amide I & Amide II region at 6 μm and Amide A region at 3 μm, since overtones and combination bands play a role in the 3 μm spectrum of NMA (Fig. 4.6).

4.6. References

(1) Liang, H.; Krogen, P.; Wang, Z.; Park, H.; Kroh, T.; Zawilski, K.; Schunemann, P.; Moses, J.; Dimauro, L. F.; Kärtner, F. X.; Hong, K. H. High-Energy Mid-Infrared Sub-Cycle Pulse Synthesis from a Parametric Amplifier. *Nat. Commun.* **2017**, *8*, 1–9. https://doi.org/10.1038/s41467-017-00193-4.

(2) Koulouklidis, A. D.; Gollner, C.; Shumakova, V.; Fedorov, V. Y.; Pugžlys, A.; Baltuška, A.; Tzortzakis, S. Observation of Extremely Efficient Terahertz Generation from Mid-Infrared Two-Color Laser Filaments. *Nat. Commun.* **2020**, *11* (292), 1–8. https://doi.org/10.1038/s41467-019-14206-x.

(3) Herink, G.; Solli, D. R.; Gulde, M.; Ropers, C. Field-Driven Photoemission from Nanostructures Quenches the Quiver Motion. *Nature* **2012**, *483*, 190–193. https://doi.org/10.1038/nature10878.

(4) Stingel, A. M.; Petersen, P. B. Couplings Across the Vibrational Spectrum Caused by Strong Hydrogen Bonds : A Continuum 2D IR Study of the 7-Azaindole−Acetic Acid Heterodimer. *J. Phys. Chem. B* **2016**, *120*, 10768–10779. https://doi.org/10.1021/acs.jpcb.6b05049.

(5) Tian, K.; He, L.; Yang, X.; Liang, H. Mid-Infrared Few-Cycle Pulse Generation and Amplification. *Photonics* **2021**, *8* (290), 1–24. https://doi.org/10.3390/PHOTONICS8080290.

(6) Hamm, P.; Zanni, M. *Concepts and Methods of 2D Infrared Spectroscopy*; Cambridge University Press: Cambridge, UK and New York, NY, USA, 2011.

(7) Kaindl, R. A.; Wurm, M.; Reimann, K.; Hamm, P.; Weiner, A. M.; Woerner, M. Generation, Shaping, and Characterization of Intense Femtosecond Pulses Tunable from 3 to 20 Mm. *J. Opt. Soc. Am. B* **2000**, *17* (12), 2086. https://doi.org/10.1364/JOSAB.17.002086.

(8) Fecko, C. J.; Loparo, J. J.; Tokmakoff, A. Generation of 45 Femtosecond Pulses at 3 Mm with a KNbO3 Optical Parametric Amplifier. *Opt. Commun.* **2004**, *241*, 521–528. https://doi.org/10.1016/j.optcom.2004.07.038.

(9) Fournier, J. A.; Carpenter, W. B.; Lewis, N. H. C.; Tokmakoff, A. Broadband 2D IR Spectroscopy Reveals Dominant Asymmetric H5O2+ Proton Hydration Structures in Acid Solutions. *Nat. Chem.* **2018**, *10* (September), 932–937. https://doi.org/10.1038/s41557-018-0091-y.

(10) Fuji, T.; Nomura, Y. Generation of Phase-Stable Sub-Cycle Mid-Infrared Pulses from Filamentation in Nitrogen. *Appl. Sci.* **2013**, *3* (1), 122–138. https://doi.org/10.3390/app3010122.

(11) Petersen, P. B.; Tokmakoff, A. Source for Ultrafast Continuum Infrared and Terahertz Radiation. *Opt. Lett.* **2010**, *35* (12), 1962. https://doi.org/10.1364/OL.35.001962.

(12) von Grafenstein, L.; Bock, M.; Ueberschaer, D.; Zawilski, K.; Schunemann, P.; Griebner, U.; Elsaesser, T. 5 Mm Few-Cycle Pulses with Multi-Gigawatt Peak Power at a 1 KHz Repetition Rate. *Opt. Lett.* **2017**, *42* (19), 3796–3799.

(13) Liu, K.; Liang, H.; Wang, L.; Qu, S.; Lang, T.; Li, H.; Wang, Q. J.; Zhang, Y. Multimicrojoule GaSe-Based Midinfrared Optical Parametric Amplifier with an Ultrabroad Idler Spectrum Covering 42–16 Mm. *Opt. Lett.* **2019**, *44* (4), 1003–1006. https://doi.org/10.1364/ol.44.001003.

(14) Budriūnas, R.; Jurkus, K.; Vengris, M.; Varanavičius, A. Long Seed, Short Pump: Converting Yb-Doped Laser Radiation to Multi-MJ Few-Cycle Pulses Tunable through 2.5–15 Mm. *Opt. Express* **2022**, *30* (8), 13009. https://doi.org/10.1364/oe.455180.

(15) Gaida, C.; Gebhardt, M.; Heuermann, T.; Stutzki, F.; Jauregui, C.; Antonio-Lopez, J.; Schülzgen, A.; Amezcua-Correa, R.; Tünnermann, A.; Pupeza, I.; Limpert, J. Watt-Scale Super-Octave Mid-Infrared Intrapulse Difference Frequency Generation. *Light Sci. Appl.* **2018**, *7* (1). https://doi.org/10.1038/s41377-018-0099-5.

(16) Vasilyev, S.; Moskalev, I. S.; Smolski, V. O.; Peppers, J. M.; Mirov, M.; Muraviev, A. V.; Zawilski, K.; Schunemann, P. G.; Mirov, S. B.; Vodopyanov, K. L.; Gapontsev, V. P. Super-Octave Longwave Mid-Infrared Coherent Transients Produced by Optical Rectification of Few-Cycle 2.5-Mm Pulses. *Optica* **2019**, *6* (1), 111–114. https://doi.org/10.1364/optica.6.000111.

(17) Demirdöven, N.; Khalil, M.; Golonzka, O.; Tokmakoff, A. Dispersion Compensation with Optical Materials for Compression of Intense Sub-100-Fs Mid-Infrared Pulses. *Opt. Lett.* **2002**, *27* (6), 433–435. https://doi.org/10.1364/ol.27.000433.

(18) Mayerhofer, T. G.; Pahlow, S.; Hubner, U.; Popp, J. CaF2: An Ideal Substrate Material for Infrared Spectroscopy? *Anal. Chem.* **2020**, *92*, 9024–9031.

(19) Trebino, R.; DeLong, K. W.; Fittinghoff, D. N.; Sweetser, J. N.; Krumbügel, M. A.; Richman, B. A.; Kane, D. J. Measuring Ultrashort Laser Pulses in the Time-Frequency Domain Using Frequency-Resolved Optical Gating. *Rev. Sci. Instrum.* **1997**, *68* (9), 3277–3295. https://doi.org/10.1063/1.1148286.

(20) Joo, T.; Jia, Y.; Yu, J. Y.; Lang, M. J.; Fleming, G. R. Third-Order Nonlinear Time Domain Probes of Solvation Dynamics. *J. Chem. Phys.* **1996**, *104*, 6089–6108. https://doi.org/10.1063/1.471276.

(21) Gardecki, J. A.; Constantine, S.; Zhou, Y.; Ziegler, L. D. Optical Heterodyne Detected Spectrograms of Ultrafast Nonresonant Electronic Responses. *J. Opt. Soc. Am. B* **2000**, *17* (4), 652. https://doi.org/10.1364/josab.17.000652.

(22) Tropf, W. J.; Thomas, M. E.; Harris, T. J. *Handbook of Optics*, 2nd ed.; M. Bass, Ed.; McGraw-Hill: New York, 1995.

(23) Kundu, A.; Dahms, F.; Fingerhut, B. P.; Nibbering, E. T. J.; Pines, E.; Elsaesser, T. Hydrated Excess Protons in Acetonitrile/Water Mixtures: Solvation Species and Ultrafast Proton Motions. *J. Phys. Chem. Lett.* **2019**, *10* (9), 2287–2294. https://doi.org/10.1021/acs.jpclett.9b00756.

(24) DeFlores, L. P.; Nicodemus, R. A.; Tokmakoff, A. Two-Dimensional Fourier Transform Spectroscopy in the Pump-Probe Geometry. *Opt. Lett.* **2007**, *32* (20), 2966. https://doi.org/10.1364/ol.32.002966.

(25) De Marco, L. The Molecular Dynamics of Hydrogen-Bonding Explored with Broadband

Two Dimensional Infrared Spectroscopy, Massachusetts Institute of Technology, 2016.

(26) De Marco, L.; Ramasesha, K.; Tokmakoff, A. Experimental Evidence of Fermi Resonances in Isotopically Dilute Water from Ultrafast Broadband IR Spectroscopy. *J. Phys. Chem. B* **2013**, *117* (49), 15319–15327. https://doi.org/10.1021/jp4034613.

(27) Auer, B.; Kumar, R.; Schmidt, J. R.; Skinner, J. L. Hydrogen Bonding and Raman, IR, and 2D-IR Spectroscopy of Dilute HOD in Liquid D2O. *Proc. Natl. Acad. Sci. U. S. A.* **2007**, *104* (36), 14215–14220. https://doi.org/10.1073/pnas.0701482104.

(28) De Marco, L.; Thämer, M.; Reppert, M.; Tokmakoff, A. Direct Observation of Intermolecular Interactions Mediated by Hydrogen Bonding. *J. Chem. Phys.* **2014**, *141*, 034502. https://doi.org/10.1063/1.4885145.

(29) Markovitch, O.; Chen, H.; Izvekov, S.; Paesani, F.; Voth, G. A.; Agmon, N. Special Pair Dance and Partner Selection: Elementary Steps in Proton Transport in Liquid Water. *J. Phys. Chem. B* **2008**, *112* (31), 9456–9466. https://doi.org/10.1021/jp804018y.

(30) Agmon, N.; Bakker, H. J.; Campen, R. K.; Henchman, R. H.; Pohl, P.; Roke, S.; Thämer, M.; Hassanali, A. Protons and Hydroxide Ions in Aqueous Systems. *Chem. Rev.* **2016**, *116* (13), 7642–7672. https://doi.org/10.1021/acs.chemrev.5b00736.

(31) Vjunov, A.; Wang, M.; Govind, N.; Huthwelker, T.; Shi, H.; Mei, D.; Fulton, J. L.; Lercher, J. A. Tracking the Chemical Transformations at the Brønsted Acid Site upon Water-Induced Deprotonation in a Zeolite Pore. *Chem. Mater.* **2017**, *29* (21), 9030–9042. https://doi.org/10.1021/acs.chemmater.7b02133.

(32) Hunter, K. M.; Wagner, J. C.; Kalaj, M.; Cohen, S. M.; Xiong, W.; Paesani, F. Simulation Meets Experiment: Unraveling the Properties of Water in Metal–Organic Frameworks through Vibrational Spectroscopy. *J. Phys. Chem. C* **2021**, *125*, 12451–12460.

(33) Koralek, J. D.; Kim, J. B.; Bruza, P.; Curry, C. B.; Chen, Z.; Bechtel, H. A.; Cordones, A. A.; Sperling, P.; Toleikis, S.; Kern, J. F.; Moeller, S. P.; Glenzer, S. H.; Deponte, D. P. Generation and Characterization of Ultrathin Free-Flowing Liquid Sheets. *Nat. Commun.* **2018**, *9*, 1–8. https://doi.org/10.1038/s41467-018-03696-w.

Appendix 4A. Detailed alignment procedure

Hopefully, you are a student reading this many years in the future, and OPA is still serving you well. If that's the case you may have some practical questions about the alignment, which is somewhat involved. I will do my best to describe how I aligned the OPA and the best practices I've found. A detailed, to-scale diagram of the OPA is shown in Fig. 4A.1 including irises, flipper mirrors, and beam paths for the tracer. Most iris positions use removable irises with a collar, labeled A or B depending on the height of the post holder, so using the correct iris is important.

Seed line

Use the mirror just before the OPA entrance and M1 to align the 800 nm beam onto I1 and the center of CM1. This is feasible because CM1 is a small mirror and the blue 400 nm beam generated in BBO1 is easy to see and collinear with the fundamental. Both IR and some visible (red) are generated in the filament, which are roughly collinear but displaced spatially from the generating beams. Use the generated visible to center the beam on ITO 1-4. Pass the beam as closely by CM1 as possible without clipping.

Flip up FM2, sending the seed to an MCT detector outside the OPA box. This is a good time to optimize seed generation parameters on the total seed power. Outside the box, set two irises on the seed, then use M10 & M11 to position the tracer on those irises. This approach is necessary because the seed is too weak to see on an IR card. Now the tracer is overlapped with the seed, combined at ITO4. Flip down FM2, and align through IB1 & IB2 using M2 & M3 (with Pin1 removed). Then, place Pin1 near the focus with the tracer passing through; the exact position will be optimized later. Next, remove the GaSe crystal and use M4 and Pol. to align through IB3 & IB4. Adjust the position of M4 if large pointing changes are needed.

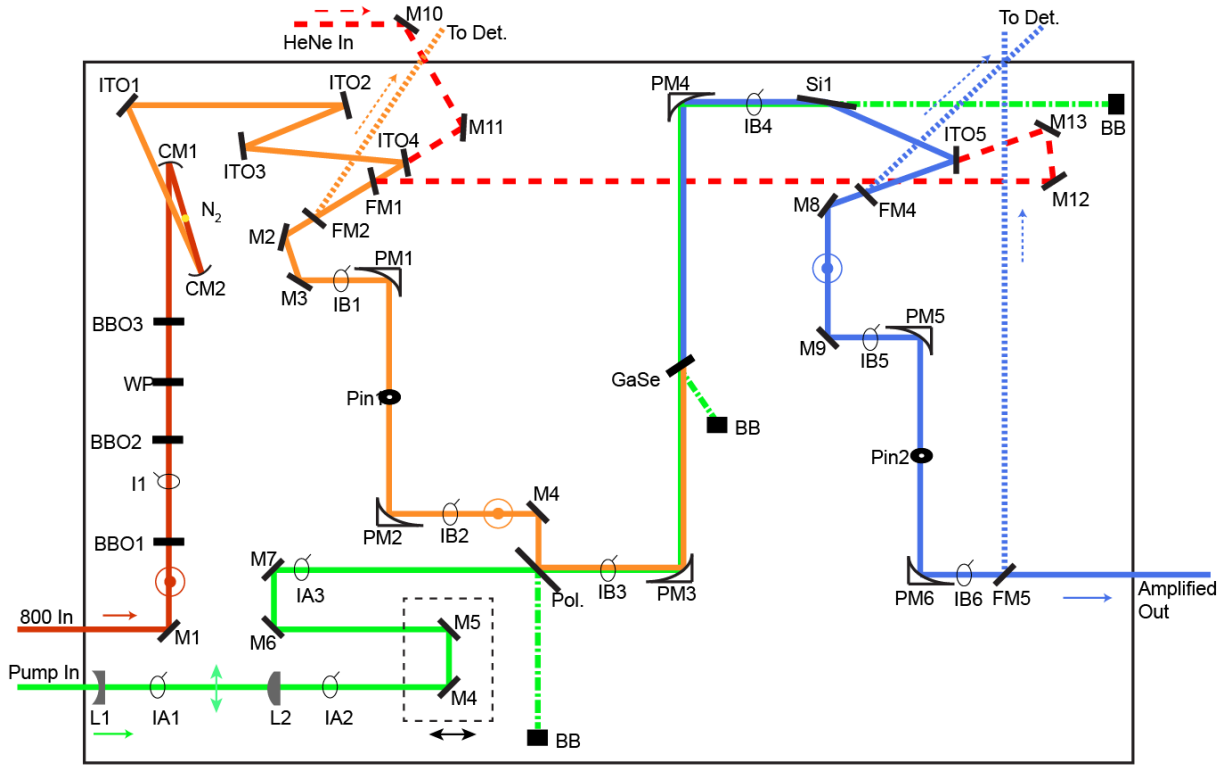

Figure 4A.1. Detailed OPA beam diagram. Box dimensions and optics placements are to scale. BB, beam block; BBO, β-Barium borate; BS, beamsplitter; CM, curved mirror; DP, delay plate; I, permanent iris; IA(B), movable iris in post holder A(B); L, lens; M, plane mirror; Mono., monochromator; Pin, pinhole; PM, parabolic mirror; Pol, polarizer; WP, waveplate. Color scheme: red, Ti:Sapphire fundamental; orange, seed; green, pump; blue, signal; dashed red, visible tracer; dotted lines, alternative beam paths accessed with flipper mirrors.

Pump line

Remove L1 & L2 (make sure they have collars first) and use two pointing mirrors before the OPA box to align the pump through IA1 & IA2. An IR card with sensitivity at 2 μm is the best option for viewing the pump. Replace L1 & L2, using the back reflection to ensure the face is perpendicular to the beam, and check alignment through IA1 & IA2. Use M6 & M7 to align through IA3 & IB3, then check IB4 and adjust alignment through IB3 & IB4 if necessary. With the seed blocked, place an energy meter directly after PM3 (not in the focus!) and optimize pump

generation (TOPAS) parameters on the measured power. Doing so with the energy meter placed here also selects for approximately the correct pump wavelength, since M4-7 are dielectrics coated for 2 μm.

Amplification

Replace the GaSe crystal in its holder and turn the external angle to 32-34º with the back reflection hitting the beam block. Flip up FM4 to send the beam to an MCT detector outside the OPA box. Point the seed onto the MCT detector with the pump blocked. Flip down FM4 and place a 2.4 μm LPF directly in front of the MCT to block the pump. Then, find OPA timing by scanning the stage in the pump line. If you can't find timing with the GaSe crystal, you can replace it with a piece of InSb; using this semiconductor makes timing easier because of the long-lived free carrier response when the seed arrives after the pump. Once timing is found in the OPA crystal, select for either the signal or idler by placing a filter directly in front of the MCT detector. For idler, a 2222 cm^{-1} LPF works well; for signal, a glass slide can function as a ~2500 cm^{-1} SPF. This is an important step because the signal and idler are not perfectly collinear. Re-optimize pointing onto the MCT detector with the filter inserted. Next, optimize all generation parameters on the energy of the selected beam (including OPA timing, pump pointing into GaSe, phase-matching angle, seed spatial filter, etc.).

Set two irises on the amplified IR. Then, flip down FM1 and use M13 & M14 to overlap the tracer with the IR beam. Use a long pathlength (several meters) between irises for an accurate overlap. Then, flip down FM4 and align the beam through IB5 & IB6. Flip up FM5 and again send the beam to an external MCT. Re-do the tracer overlap using M12 & M13, which is likely imperfect after passing through PM5 & PM6. Iterate between fixing the tracer overlap and pointing

through IB5 & IB6. It may take several iterations, but I found this step is important to achieve a good spatial mode, tracer overlap, and signal/idler spectral separation. Once complete, insert Pin2 and set its position using the transmitted beam using the filter just before the MCT (selecting for signal or idler). Finally, send the OPA output to an interferometer or spectrometer to measure the pulse spectrum. Check that only the selected signal or idler is passing through Pin2. This may require some iteration between the desired spectrum and transmitted pulse energy by adjusting the position of Pin2. Once complete, the amplified beam exits the OPA overlapped with the tracer with the desired spectrum and pulse energy and the alignment is finished.

Operation

The spectrum can be moderately tuned by adjusting both phase-matching angle and OPA timing together. My preferred method was to use a band pass filter to select for the desired center frequency, optimizing OPA parameters on the transmitted power at that frequency. It is important to periodically measure the spectrum and pulse energy while tuning OPA parameters to make sure you are tuning towards the desired spectrum. With all flipper mirrors down, the amplified beam exits the OPA box for use in spectroscopy. Flipping up FM1 sends the tracer in the same direction as the OPA output for alignment downstream.

Chapter 5

Protonated water clusters in highly hydrated HZSM-5 zeolite

The work presented in this chapter has been published and is adapted with permission from:

Hack, J. H., Dombrowski, J. P., Ma, X., Chen, Y., Lewis, N. H. C., Carpenter, W. B., Li, C., Voth, G. A., Kung, H. H., Tokmakoff, A. Structural characterization of protonated water clusters confined in HZSM-5 zeolites. *Journal of the American Chemical Society*, **143**, 10203-10213 (2021).

5.1. Introduction

Zeolites are a class of nanoporous, crystalline silicate materials with applications for ion transport and separations,[1–3] as desiccants,[4,5] and as catalysts,[6–11] as described in Chapter 1. They display tunable behavior depending on framework type, pore structure, framework dopant atoms, and charge-compensating cations. Of special note are aluminosilicate zeolites with Al^{3+} and charge-compensating protons substituted for Si^{4+}, which contain strong Brønsted acid sites. The interactions between water and protonated zeolites play a role in many established and emerging applications including acid-catalyzed dehydration reactions,[12–15] aqueous biofuel synthesis,[8] and

proton-selective ion separations.[16] As such, understanding the hydration behavior of zeolites[17–20] is crucial for a mechanistic description of these processes. Recent investigations have led to discoveries regarding the speciation of water, its effect on framework sites, and its involvement in zeolite-mediated chemical processes.[16,21–23]

In the low-hydration limit, vibrational and NMR spectroscopic studies have uncovered distinct hydration structures in aluminosilicate zeolites,[24,25] while detailed structural characterization has remained elusive for higher hydration states. Fourier-transform infrared (FTIR) Spectroscopy is a particularly common and valuable method for investigating water structure as the O-H stretching frequency is sensitive to the local H-bonding environment.[26] Zeolite HZSM-5 is a well-studied example.[21,27–32] At one equivalent H_2O per aluminum site, a surface-bound water molecule H-bonding to the Brønsted acid site is reported.[30,33–37] At two H_2O equivalents, a pair of water molecules is reported as forming either a dimer that H-bonds to the surface-bound proton or forming a protonated $H_5O_2^+$ species with the acidic proton located between oxygen atoms of both water molecules.[36,38–40] Deprotonation of acidic aluminosilicate zeolites to form protonated water clusters has been well-established to occur once a critical level of hydration is obtained,[18,40–46] which is 2-3 water molecules per aluminum site for HZSM-5.[14,15,19,21,27,28,32,33,39,42,46–52] Beyond two H_2O equivalents the water speciation in HZSM-5 is far less established, in part due to the appearance of broad, overlapping hydroxyl stretching features in the IR spectrum. As a result, proposed water speciation in the experimental literature is often based on bulk measurements of water uptake in zeolite pores.[9,27,53] Microcalorimetric uptake measurements demonstrate that, in the limit of isolated aluminum centers, the heats of water adsorption approach that of water condensation at around 8 equivalents (equiv.) water added per Al site.[27,51,53] These studies,

combined with recent NMR spectroscopic investigations,[47] provide experimental evidence for proposed speciation at high levels of hydration in HZSM-5.

While the available evidence points to the formation of protonated clusters of ~8 water molecules in zeolite pores under high hydration, little is understood about the molecular structures of these clusters. How do the water molecules arrange themselves relative to each other, the zeolite framework, and the deprotonated Brønsted acid site? What H-bonding configurations do the water molecules find themselves in, and in what proportions?

To address these questions, we investigated water clusters at high hydration in HZSM-5 zeolites (~13 equiv. and ~6 equiv. H_2O per Al atom) through the combination of FTIR, two-dimensional infrared (2D IR) spectroscopy, and *ab initio* molecular dynamics (AIMD) simulations. 2D IR spectroscopy provides additional structural insight over FTIR spectroscopy by spreading spectral information over two frequency axes that monitor the change in absorption at detection frequency ω_{det} following excitation at frequency ω_{exc}, as described in Chapter 2. Beyond the features observed in FTIR, cross-peaks between resonances in 2D IR spectra encode vibrational couplings and transition dipole orientations that can be translated into bond-oriented structural details, and 2D IR lineshapes characterize the variation of H-bond strength in the sample. AIMD provides an atomistic description of the structure and dynamics of this system that allows us to interpret the structural content encoded in the IR spectrum.

2D IR spectroscopy has been used effectively to study water H-bonding structure and dynamics in numerous contexts, including hydrated protons in bulk aqueous solution[54,55] and water under nano-scale confinement.[56,57] However, its application has not yet been extended to the exploration of solid acids with sub-nanopore confinement. This is due in part to the experimental challenges

of applying 2D IR techniques to highly scattering samples such as zeolites. Recent technical advances have enabled the use of 2D IR methods for select highly scattering samples.[58–60] We combined some of these methods with new sample preparation protocols to investigate hydrated protons confined in HZSM-5 zeolites with 2D IR spectroscopy.

From 2D IR correlations between the continuum absorption of the excess proton and vibrations of both terminal and H-bonded O-H groups, we provide direct evidence for the formation of protonated water clusters in HZSM-5 pores. We also quantify H-bond speciation within the cluster, finding good agreement with the statistics calculated from a AIMD simulations of protonated $H^+(H_2O)_8$ clusters in HZSM-5. These simulations, together with DFT spectral calculations, validate our IR spectral assignments and reveal that the excess charge resides near the more highly coordinated water molecules in the cluster. These results support previous literature findings[18,40–46] that small, protonated water clusters form the dominant species in HZSM-5 under high hydration, and provide a new level of quantitative molecular insight. 2D IR spectroscopy provides the information necessary to dissect and assign the complex, overlapping IR spectrum of high hydration HZSM-5, providing molecular-level details about the topology of water's hydrogen bonding network under tight confinement.

5.2. Experimental and Theoretical Methods

To prepare the samples, HZSM-5(Si:Al = 40) zeolite samples (Johnson Matthey) were calcined in an oxygenated atmosphere and then subjected to three ammonium nitrate ion-exchange cycles. To reduce scatter from the largest particles, zeolite samples were filtered using 5 μm Nylon net

membranes. The filtered samples were then calcined again to convert the ammonium-form zeolite into the desired proton-form. Next, samples were dehydrated using Schlenk-line vacuum dehydration under heating,[43] and stored in a glovebox prior to rehydration. Dehydration of samples was confirmed via FTIR spectroscopy. The Si:Al ratio was measured to be 45:1 by inductively coupled plasma – optical emission spectroscopy.

Zeolites were rehydrated in a nitrogen-filled glovebox with small, targeted quantities of water before sealing in a Parr acid digestion vessel with a Teflon liner. Water was added directly to the zeolite powder, which was then thermally equilibrated at 150 ^{o}C without significant evaporative loss. Following hydration, zeolite samples were suspended in a refractive index-matching oil as a mull before being pressed between two 1 mm thick CaF_2 windows for IR spectroscopy measurements. The mull was composed of a mixture of Fluorolube-brand polychlorotrifluoroethylene (PCTFE, $n = 1.38$),[61,62] and perfluoro(tetradecahydro-phenanthrene)[63] ($n = 1.33$). The mixture of these oils was tuned to match the refractive index of the sample ($n = 1.40$ for HZSM-5), which varied slightly with the hydration level.

Two H_2O/HZSM-5 samples were used in this study. The first was prepared with ~13 equiv. H_2O/Al site and the second with ~6 equiv. H_2O/Al site. From prior studies, it is expected that the 13 equiv. sample contains both fully hydrated Al sites and some degree of surface water or internal silanol hydration.[47] Since O-H vibrations in water clusters tend to delocalize across several bonds, a third sample was prepared using isotopically dilute 5% HOD in D_2O to study more isolated O-H stretch vibrations. The third sample had a hydration level of ~6 equiv. per Al site, referred to as HOD/HZSM-5. The HZSM-5 substrate used in all three samples was ~98% proton exchanged (~2% Na^+ remaining), with a surface area of ~300 m^2/g measured by N_2 isothermal adsorption.

Polarization-dependent 2D IR spectra were collected in the pump-probe geometry using a spectrometer which has been described in detail previously[64–66] and in Chapter 3. Parallel and perpendicular spectral components were collected simultaneously, allowing for the construction of the isotropic component of the spectrum $S_{Iso} = S_{||} + 2S_{\perp}$ and anisotropy $r = (S_{||} - S_{\perp}) / (S_{||} + 2S_{\perp})$.

Even after the steps taken during sample preparation, additional measures were required to collect high-quality 2D IR spectra from highly scattering zeolite samples. Suppression of scattering artifacts from all three incident pulses was accomplished by chopping both the stationary pump pulse and the probe, quasi-phase cycling[67] by oscillating the pulse 2 delay stage, and negative-time subtraction, with details described in Chapter 3.

The dynamics and vibrational spectra of water clusters in the HZSM-5 zeolite were calculated with AIMD simulations[68,69] at 298 K using density functional theory (DFT) at the revPBE/DZVP level of theory,[70] together with the D3 dispersion correction.[71] The CP2K (version 4.1) software[72] was used for AIMD simulations and harmonic vibrational spectrum calculations. Two unit cells were rendered with 8 water molecules, an excess proton, and one Al T-site located in a channel intersection or S-channel. In a separate simulation, water-packed zeolite channels were filled with 80 water molecules and an excess proton near the Al T-center at a channel intersection (T1 site). These – and all other AIMD simulations reported in this thesis – were performed by our collaborator Xinyou Ma in the research group of Greg Voth.

For spectral assignments, a protonated water cluster configuration – including the zeolite framework – was optimized from a snapshot of the AIMD trajectory and used to calculate the

harmonic vibrational spectra using DFT. To isolate the spectral contribution from each normal mode Q_i arising from a particular O-H bond, each O-H stretch local mode is represented as a linear combination of all normal modes weighted by the eigenvector *L* that diagonalizes the Hessian matrix.[73] Then, the intensity weighted spectral density of an O-H local mode is:

$$\rho_{O-H}(\omega) = \sum_i |L_i| \left| \frac{\partial \mu}{\partial Q_i} \right| \delta(\omega - \omega_i) \tag{5.1}$$

where $|L_i|$ is the norm of the Cartesian component of the H atom and μ is the dipole moment.

For each snapshot of the trajectory, the water bonding topology was identified by assigning each oxygen atom to its two nearest H atoms. The remaining H atom was then assigned to the closest water molecule with the shortest O-H distance to form one H_3O^+ ion. Next, four geometric criteria were used to assign a H-bond: $r(O_1 - O_2) < 3.0$ Å, $r(O_1 - H_2) < 2.5$ Å, $\theta(O_1 - H_1 - H_2) < 30°$, and $\theta(O_1 - H_2 - H_1) < 30°$, where the subscripts 1 and 2 label atoms in the acceptor and donor, respectively. Interfacial H-bonds were assigned using the criterion $r(O_1 - O_2) < 3.0$ Å. The center of the excess positive charge (CEC) from the proton was calculated using the rCEC approach by Li and Swanson,[74] which is described in more detail in Chapter 6.

5.3. Results and discussion

5.3.1. FTIR Spectrum of H_2O in highly hydrated HZSM-5.

The linear IR spectra of H_2O/HZSM-5 and HOD/HZSM-5 are displayed in Fig. 5.1, along with bulk liquid HOD, H_2O and 6M HCl. The spectrum of H_2O/HZSM-5 is extremely broad, with an asymmetric low-frequency wing and three features peaked at 3650 cm^{-1} with a shoulder at 3600

cm^{-1}, 3400 cm^{-1}, and 3200 cm^{-1}. The local maximum at 3400 cm^{-1} appearing in the H_2O/HZSM-5 and HOD/HZSM-5 spectra is at the same frequency as the vibration in bulk H_2O, indicative of water H-bonded O-H stretch.

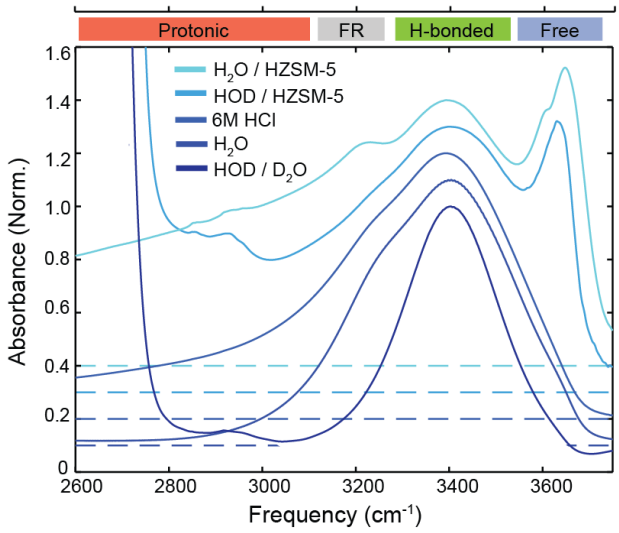

Figure 5.1. Distinct IR spectrum of H_2O in HZSM-5. FTIR spectrum of 13 equiv. H_2O in HZSM-5; FTIR spectra of 2% HOD/D_2O, H_2O, 6M HCl, and 6 equiv. 5% HOD/D_2O in HZSM-5 are included for comparison. Spectra were collected against a nitrogen background, normalized to their local maxima near 3400 $cm^{-1,}$ and displaced for clarity. Dashed lines mark the baselines for the spectra of corresponding color. Colored bars denote spectral band assignments for H_2O/HZSM-5.

Perhaps the most striking feature is the intense peak near 3650 cm^{-1} seen in both spectra of H_2O/HZSM-5 and HOD/HZSM-5. The frequency and linewidth of this transition are similar to the O-H stretch vibrations of water monomers in polar solvents,[75] indicating that these correspond terminal (free) O-H stretch vibrations. The intensity of this feature indicates a large population of free O-H stretches in this system, particularly because the transition dipole moment of the free O-H stretch in water is about half that of the H-bonded water O-H stretch.[76] A weak shoulder is located near 3600 cm^{-1}, which is characteristic of the splitting between symmetric and asymmetric

O-H stretches for water molecules that donate zero H-bonds. The shoulder vanishes when H_2O is replaced by dilute HOD in D_2O, suggesting that this feature arises from HOH vibrational splitting.

The feature at 3200 cm^{-1} observed in H_2O/HZSM-5 is close in frequency to a weak feature in bulk H_2O that originates from the Fermi resonance (FR) between the water O-H stretch and HOH bend overtone.[77–79] The decreased intensity of this feature in the HOD/HZSM-5 sample indicates that the 3200 cm^{-1} feature in H_2O/HZSM-5 is also due to the FR, although we note that this is also where the flanking water stretching vibrations to protonated water are expected.[54,80] The increased intensity of this band in H_2O/HZSM-5 relative to bulk H_2O may be caused in part by a shift in the HOH bend frequency for interfacial water. A similarly enhanced FR feature has been observed in H_2O confined in carbon nanotubes[81] and at the air-water interface.[82,83]

The long tail extending below 3200 cm^{-1} is characteristic of the continuum band of the hydrated excess proton,[80,84] and a similar feature is observed for bulk 6M HCl in H_2O, as seen in Fig. 5.1. The prominence of this tail in the H_2O/HZSM-5 sample is consistent with an effective proton concentration of approximately 6M (or H^+/H_2O ratio of 1/8), estimated from the integrated areas of water and proton features.

Comparing spectra of samples prepared with ~13 and ~6 H_2O equiv./Al site, we find that they display very similar FTIR and 2D IR spectra (Fig. 5.2) indicating a similar distribution of terminal and H-bonding O-H groups. Subtle preferences for free O-H bonds in the 13 equiv. sample are small enough that any quantitative differences in O-H bond speciation is smaller than our error bars. Therefore, the 13 equiv. sample is presented here as an appropriate representative of the HZSM-5 spectrum in the high-hydration limit.

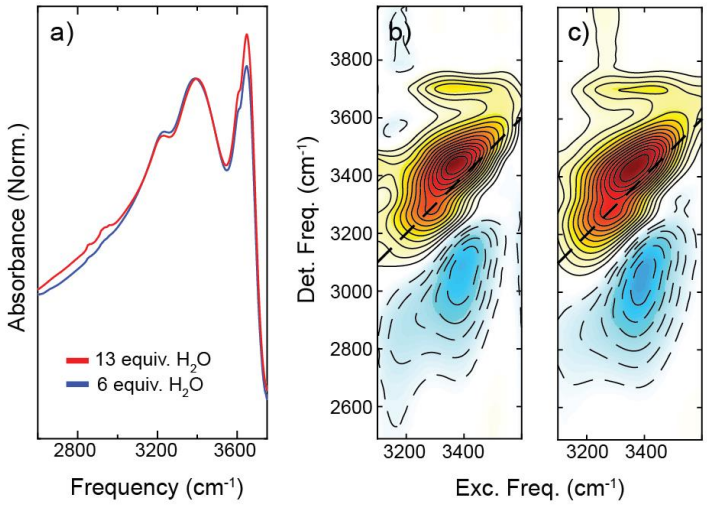

Figure 5.2. Comparison between (a) FTIR spectra and 2D IR spectra of (b) 13 equiv. and (c) 6 equiv. H_2O / HZSM-5. 2D IR spectra are isotropic, taken at 100 fs waiting time, and are not pump corrected.

5.3.2. Computed spectra arising from local O-H environments.

The connection between local structure and vibrational frequency for water O-H stretches in H_2O/HZSM-5 was investigated using density functional theory (DFT) on optimized clusters of $H^+(H_2O)_8$ in HZSM-5 pores. Two ZSM-5 unit cells were rendered with one Al T-site placed either in the straight channel (T11 site) or at the channel intersection (T1 site), yielding a Al:Si ratio of 1:191. While this is quite different from the experimental ratio, the behavior of each site is independent of the Al:Si ratio assuming isolated sites.

Connections between harmonic frequency and local molecular environment were determined by decomposing the calculated spectrum from the normal modes to individual local mode O-H stretches. These local mode spectra are presented for ten representative hydrogen positions within a cluster in Fig. 5.3. Based on the molecular structure, the O-H stretches in each protonated water

octamer were sorted into four categories: free, H-bonded, protonic, and interfacial. Here interfacial refers to O-H stretches directly adjacent to the deprotonated Brønsted acid site. The H-bonded and interfacial O-H stretches were further distinguished by interaction strength.

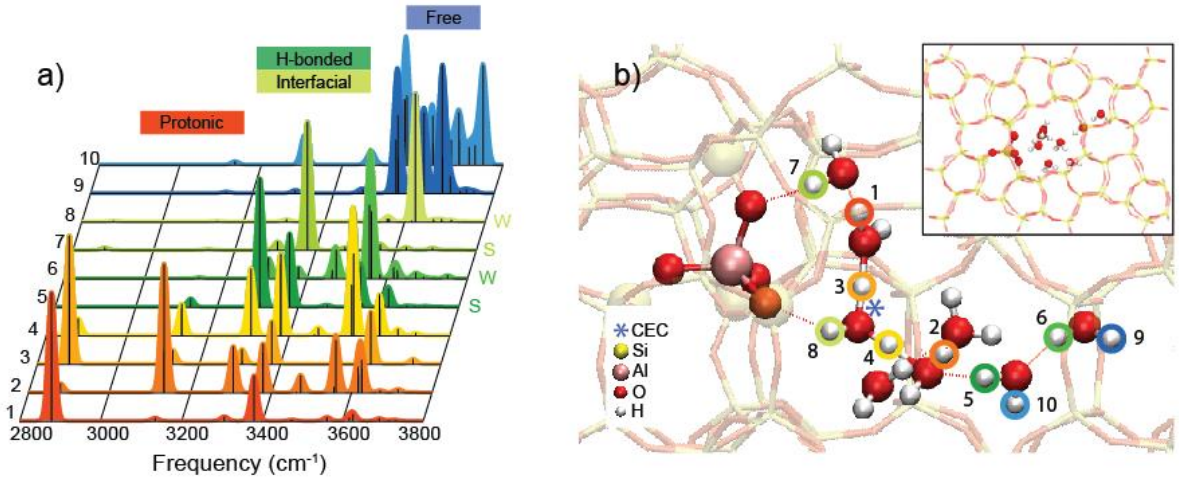

Figure 5.3. DFT calculations connect spectral signatures to local O-H environments. a) Harmonic spectral components of local mode O-H bonds in the b) optimized protonated water cluster configuration with one Al T-site located in the S-channel (T11 site). Inset: cluster visualized along the S-channel. The center of excess charge (CEC) is denoted by a blue asterisk. Each spectrum corresponds to an individual hydrogen atom, labeled by color and number. Two representative spectra are displayed of O-H bonds in free environments. Stick spectra (black) were convolved with a Gaussian lineshape for clarity. For H-bonded and interfacial O-H stretches, strong (s) and weak (w) association with the acceptor were distinguished based on geometry.

The free, H-bonded, and protonic environments display spectral trends that corroborate the proposed spectral assignments in Section 5.3.1. In the harmonic decomposition, free O-H stretches display a doublet or multiplet around 3700 cm^{-1}. The H-bonded stretches display frequencies in the range of ~3300-3600 cm^{-1}, with stronger H-bonds contributing more prominently in the lower end of that range. Protonic O-H stretch vibrations are delocalized over multiple hydrogen atoms and display intense features over the spectral range displayed. We label the 2800-3200 cm^{-1}

spectral range protonic as these are the most prominent O-H stretch modes with significant intensity in that region under the harmonic approximation. Interestingly, the interfacial O-H stretches, which donate H-bonds to the oxygen atoms of the deprotonated Brønsted site, can contribute to different spectral regions depending on interaction strength. More strongly interacting interfacial H-bonds appear in the ~3200-3400 cm^{-1} region, while more weakly interacting bonds appear near 3650 cm^{-1}. This is valuable information for interpreting the experimental spectrum: the feature peaked at 3400 cm^{-1} includes both H-bonds donated to water and to the deprotonated Brønsted site, while the peak at 3650 cm^{-1} includes both free and weakly-interacting O-H stretches. As an anharmonic feature, the Fermi resonance observed in the FTIR spectrum is absent from these calculations.

Our analysis of IR spectra of protonated water in zeolites shows both similarities and differences when compared to the IR spectra of cold, gas-phase protonated water clusters.[85–87] In isolation, $H^+(H_2O)_n$ clusters with $n \gtrsim 6$ minimize their energy though internal H-bonding and thus preferentially form compact ringed clusters. With the strong confinement effects of the zeolite channels, the most likely configurations involve extended or branched chains, although these changes do not result in a large change in the fraction of free O-H bonds relative to gas phase clusters. Acknowledging the differences in H-bond topology and temperature – which influences intensities and linewidths – the O-H stretching frequencies in computed and experimental spectra of cold gas phase clusters are assigned in a similar manner. Free O-H stretches are observed >3650 cm^{-1} and are typically split bands consistent with the features we observe in our broadened spectra. O-H stretches of water bound with the excess proton are observed <3200 cm^{-1}, and O-H stretches for H-bonded water molecules display intermediate frequencies.

5.3.3. 2D IR spectroscopy of water in HZSM-5.

To further investigate the structural details of this system, we collected the 2D IR spectrum across a broad range of excitation and detection frequencies (Fig. 5.4a). Because the vibrational transitions are so spectrally broad, they are limited by the bandwidth of the excitation pulse in the 2D IR spectrum, artificially narrowing the measured features. This was partially remedied by collecting the spectrum with multiple excitation pulses that overlap spectrally. In Fig. 5.4a the 2D IR spectra were additionally normalized by the spectrum of the excitation pulses, and intensities were scaled to match approximately at the boundaries of 3000 cm^{-1} and 3250 cm^{-1}.

Characteristic peaks are observed along the diagonal axis that correspond to the features in Fig. 5.1, although the relative intensities differ due to the 4^{th} power scaling in transition dipole moment in the 2D IR spectrum. Strikingly, cross peaks are present between features at 100 fs waiting time, revealing that all features originate from the coupled vibrations of a common molecular species containing both free O-H bonds and O-H bonds of varying H-bond strength.

The H-bonded O-H stretch at 3400 cm^{-1} (peak 1) displays diagonal elongation, indicating increased inhomogeneous broadening relative to bulk water. This is more clearly observed by comparing the slope of the 2D lineshape for HOD/HZSM-5 and liquid HOD/D_2O samples (Fig 5.3b-c), where the center line slope is 0.70 for HOD/HZSM-5 compared to 0.41 for HOD/D_2O. This inhomogeneous broadening reflects a distribution of both molecular environments and interactions. As shown in Fig. 5.3, both H-bonded and interfacial water molecules contribute to the spectrum at 3400 cm^{-1}, in addition to the fact that the O-H stretch frequency depends strongly on the H-bonding strength.[26] Furthermore, the H-bonding configurations likely play a role in

inhomogeneous broadening as well, as the local O-H stretch frequency depends modestly on the number of other H-bond donors and acceptors for the water molecule.[88]

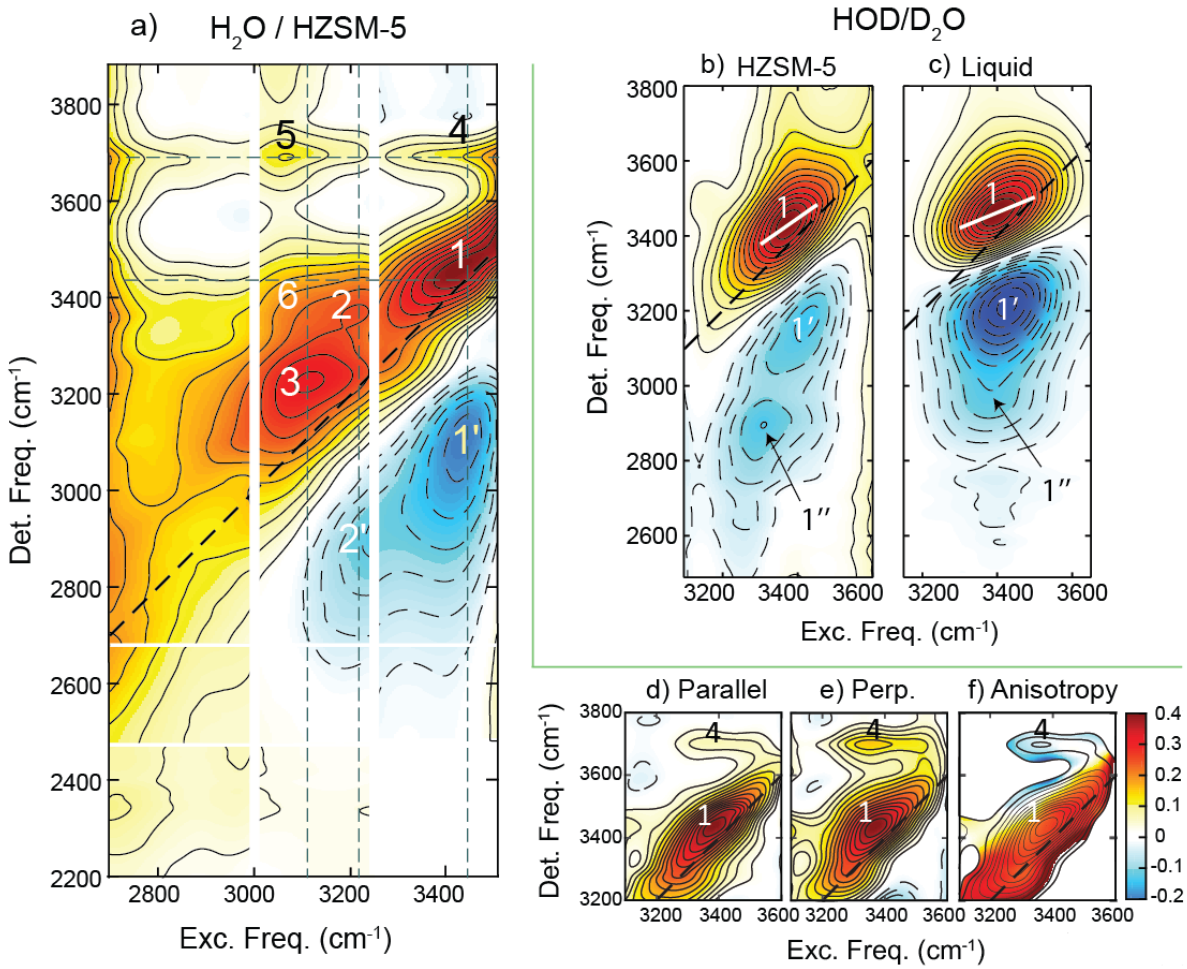

Figure 5.4. Broadband 2D IR spectroscopy of water in HZSM-5. a) Isotropic 2D IR spectrum of 13 equiv. H_2O in HZSM-5 at 100 fs waiting time. The three panels show the system excited with three different center frequencies: 2850 cm^{-1}, 3100 cm^{-1}, and 3350 cm^{-1}. Panels have been normalized to the excitation pulse and scaled to allow comparison of different spectral intensities. Peak numbers are described in the text. b) Isotropic 2D IR spectrum for isotopically dilute 6 equiv. 5% HOD/D_2O in HZSM-5 and c) isotopically dilute 2% HOD/D_2O in bulk liquid. White lines in b) & c) are fitted center lines. d-f) Polarization dependent 2D IR spectrum for 13 equiv. H_2O/HZSM-5 at 100 fs waiting time: d) parallel, e) perpendicular, and f) 2D anisotropy spectra.

Although our excitation source was not able to directly pump the free O-H stretch, this vibration is observed through cross peaks to the H-bonded O-H (peak 4) and proton flanking water stretch (peak 5). Peak 4 provides a unique marker to quantify single-donor H_2O molecules – those with one free and one H-bonded O-H. The asymmetric environment of such molecules results in two local O-H bond vibrations with very different frequencies, rather than the more common symmetric and asymmetric vibrations of H_2O. This assignment can be confirmed with 2D spectra measured with varying polarization (Fig. 5.4d-f). Peak 4 is more intense in the perpendicular 2D spectrum (Fig. 5.4e) compared to the parallel component (Fig. 5.4d). The resulting anisotropy in the range of approximately -0.05 to -0.15 (Fig. 5.4f) corresponds to a transition dipole angle in the range of 120° to 106°, consistent with the ~109° intramolecular H-O-H bond angle in H_2O.

The Fermi resonance at 3200 cm^{-1} is not cleanly observed, partially due to overlap with another strong peak (3) at 3100 cm^{-1}, but it is identified through a cross-peak (2) and induced absorption (2') in Fig. 5.4a. For comparison, the Fermi resonance for HOD/D_2O is observed in 2D IR through the induced absorption to the stretch + bend overtone combination band at 2900 cm^{-1} (Fig. 5.4c peak 1"),[78] which is significantly redshifted and skewed in HZSM-5 (Fig. 5.4b).

Peak 3 spans frequencies expected for O-H stretching vibrations of flanking water molecules to the excess proton,[84,89] and merges smoothly into the continuum absorption red of 3200 cm^{-1}. Cross-peaks 5 and 6 to the free and H-bonded water vibrations indicate that the hydrated proton is strongly coupled to other water molecules in the cluster, including on the periphery.

Excitation at 2850 cm^{-1} causes spectral response at all measured frequencies from 2200-3700 cm^{-1}. This shows that the proton continuum couples to the other features, indicating strong interactions between water O-H vibrations of the cluster. These cross-peaks following excitation

of the proton continuum confirm that the proton is detached from the Brønsted acid site and present as an excess proton in the water cluster.

5.3.4. AIMD simulation of $H^+(H_2O)_8$ in HZSM-5.

AIMD simulations of $H^+(H_2O)_8$ confined in HZSM-5 were performed with the Al T-site placed either in the straight (S) channel (T11 site) or at the intersection between S and zig-zag (Z) channels (T1 site), collecting ~36,000 snapshots from each trajectory. The clusters are confined by the solid phase framework and thus the structures reflect the 3D topology of the nanopores. In both cases, the water molecules are drawn towards the channel intersection where the available volume is largest. When the Al T-site is in the S-channel (Fig. 5.5a), this results in an elongated shape of the water cluster, with 2-3 water molecules connecting the deprotonated Brønsted site to the water molecules clustered at the intersection. When the Al T-site is placed at the channel intersection (Fig. 5.5b), the cluster shape is more compact with 3-4 water molecules reaching into the nearby S- and Z-channels. Some H-bond rearrangement was observed over the course of the trajectory, though no H_2O molecules became detached from the cluster.

For comparison, multistate empirical valence-bond (MSEVB)[90] simulations of the protonated water octamer in vacuum found a total of 18 potential minimum configurations, including 3 cubic-like, 5 fused-ring, 5 single-ring, and 5 branched configurations.[91] At room temperature, only the branched configurations (with 3-5 branches) had a prominent population.[91] Similarly, in the zeolite pores the dominant species was Y-shaped configuration with branches into 3 nearby channels, where the excess proton is flanked by a few highly coordinated water molecules. However, in contrast to the gas-phase results, configurations with more than 3 branches are rare in the zeolite channels, reflecting confinement from the rigid framework.

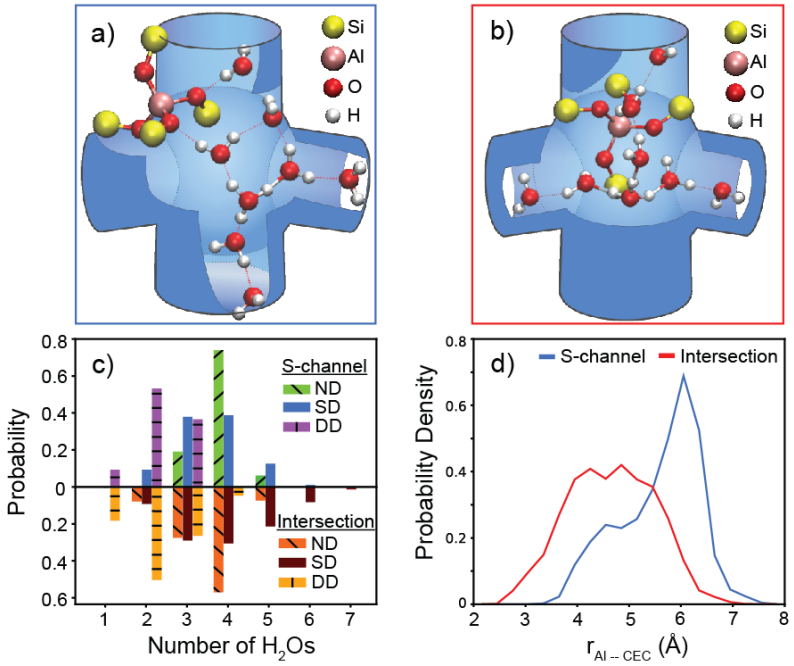

Figure 5.5. AIMD simulation of water in HZSM-5. Representative trajectory snapshots of the protonated water cluster configurations with the Al T-site located at a) the S-channel, and b) the intersection with the zig-zag channel. The statistics of c) water molecule H-bonding configurations – double donor (DD), single donor (SD), and no donor (ND) – and d) the distance between the Al atom and center of positive excess charge (CEC) were calculated from AIMD trajectories. Dashed red lines in a) and b) depict H-bonds.

To further describe the H-bonding configurations of water molecules in the cluster, we collected statistics to classify water molecules based on the number of donated H-bonds: double donors (DD), single donors (SD), and no donors (ND) (Fig. 5.5c). The mean of each distribution $\left(P_{ND}, P_{SD}, P_{DD}\right)$ is shown in Fig. 5.6. These H-bonding statistics are related to the size and structure of the water cluster. For example, an infinite 1D chain would be composed of all SD water molecules. The observed H-bonding distributions for simulations at the S-channel and intersection are quite similar to each other, with roughly 40% of water molecules in each ND and SD configurations, and roughly 20% in DD configurations. At the intersection, there is a slightly

greater fraction of SD water molecules, while in the S-channel the fraction of ND water molecules is slightly greater. The tighter water cluster at the intersection can accommodate a higher degree of connectivity, yielding the higher probability of SD water molecules.

The excess proton is solvated near the center of the water cluster, with the distance between the Al atom in the zeolite lattice and the center of excess charge (CEC) is shown statistically in Fig. 5.5d. The CEC position represents the mean location of the excess proton charge defect.[74] The probability distribution is peaked at ~4.5 Å (intersection) and ~6 Å (S-channel), with zero probability for $r(\mathrm{Al}-\mathrm{CEC}) < 2.5$ Å, indicating that the excess charge resides on average multiple molecules away from the deprotonated BAS.

For each cluster configuration, the excess proton together with the closest water molecule was assigned as hydronium, and the H-bonding topology of the 2-3 water molecules in its first solvation shell were characterized. On average, the O-H groups of these water molecules were ~1/3 free and ~2/3 H-bonded. This indicates that the excess proton resides preferentially near the more highly coordinated SD and DD water molecules in the cluster, and that a second solvation shell is not fully formed. Moreover, the proximity of the excess proton to free O-H in the first solvation shell is consistent with the cross peak observed between free and proton-associated O-H stretches.

5.3.5. Speciation of water H-bonding configurations.

To experimentally quantify H-bonding configurations within the cluster, we used FTIR and 2D IR spectra to determine the presence of the three types of water molecules considered in the previous section: DD, SD, and ND. These water types can be deduced by quantifying the different types of O-H bonds—those that are H-bonded (HB) or free (F) corresponding to peaks at 3400 cm^{-1} and 3650 cm^{-1}, respectively. Additionally, we can quantify the fraction of SD water molecules

from the cross peak 4 in the 2D IR spectrum at ($\omega_{Exc} = 3400\,\mathrm{cm}^{-1}$, $\omega_{Det} = 3700\,\mathrm{cm}^{-1}$). This gives a measure of the free O-H bonds which share a molecule with a H-bonded O-H, denoted F/HB. Populations for O-H bonds in these different environments were obtained from a self-consistent analysis of FTIR peak areas and 2D IR peak volumes, described in Appendix 5A. We accounted for the μ^2 and μ^4 peak intensity scaling in transition dipole moment μ in FTIR and 2D IR using the empirical relationship from Loparo et al.[76] After extracting the relative O-H stretch populations (χ_1 where *i* = F, HB, or F/HB) from the spectra, the populations were related to the H_2O H-bonding configurations (P_j where *j* = ND, SD, or DD) using the relations: $\chi_{HB} = 2P_{DD} + P_{SD}$, $\chi_F = 2P_{ND} + P_{SD}$, and $\chi_{F/HB} = P_{SD}$. The results of this fitting analysis are shown in Fig. 5.6.

Compared to the simulated water octamer in HZSM-5, the experimental spectral fitting yields a very similar SD fraction, with a lower fraction of ND and a higher fraction of DD water molecules, deviating by about 5-10% from the $H^+(H_2O)_8$ simulation. This is a reasonable agreement, given the simplicity of this model and the assumptions made in fitting, We note that the hydration level is higher in the measured 13 equiv. sample relative to simulations, which may lead to the formation of larger water clusters with a higher fraction of DD water molecules.

For another point of comparison, we performed a similar AIMD analysis on a water-packed state – a collection of 80 water molecules in two HZSM-5 unit cells (Fig. 5.7a). This produced a structure with extensive H-bonding connectivity, largely in the form of single-file water wires extending through the channels. This structure has a much higher fraction of SD water molecules (0.66) compared to either the measured sample or the $H^+(H2O)_8$ in HZSM-5 model. Therefore, we can rule out extensive water-wire formation through the zeolite channels, even at high hydration.

This result is consistent with expectations, as the pores of HZSM-5 are hydrophobic in the absence of Al substitutions or a large number of internal defects.[92–98]

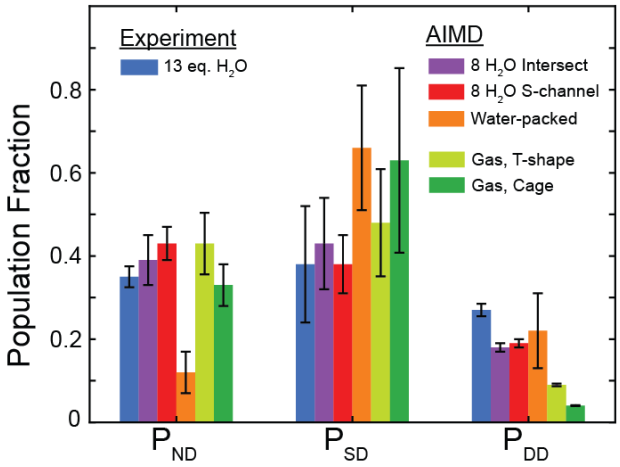

Figure 5.6. Speciation of H-bonding configurations in H_2O/HZSM-5. Distributions of ND, SD, and DD water molecules are compared between fits of IR spectra and AIMD simulations. Three HZSM-5 simulations and two gas phase simulations were performed, as described in the text. In the water-packed simulation, HZSM-5 pores were filled with water wires, yielding extended H-bonding not consistent with experiment. Error bars are the variance of the O-H configuration probability distributions (AIMD), and values at which the coefficient of determination R^2 for the fit is reduced to 0.95 by adjusting a single population parameter (Experiment).

Finally, to investigate the effect of channel confinement, water H-bonding statistics were calculated for two gas phase protonated water octamer clusters at room temperature using AIMD simulations – one starting from a T-shape (Fig. 5.7b) and one starting from a cage structure (Fig. 5.7c). A variety of gas phase configurations[91] were sampled with the two ~10 ps trajectories. Compared to experiment and simulated water octamer clusters in HZSM-5, the initial T-shaped gas phase cluster has a significantly lower DD fraction, with larger ND and SD fractions within the error bars (Fig. 5.6). While the initial T-shape configuration is similar to the cluster shape under confinement, the gas phase cluster can occupy a larger volume yielding a lower DD fraction. On

the other hand, when starting from a cage structure the gas phase cluster samples a collection of ring configurations, displaying a larger SD fraction and smaller DD fraction (Fig. 5.6), inconsistent with the experimental values. This comparison further supports the finding that water clusters in HZSM-5 primarily form branched configurations, in contrast to the gas phase where cage and ring configurations are also stable.[91]

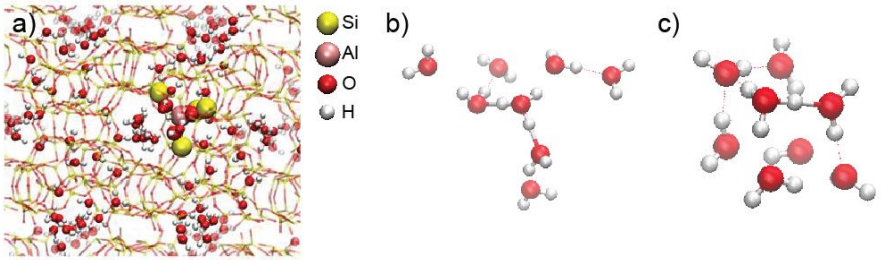

Figure 5.7. Additional water configurations considered in Fig. 5.6: (a) water-packed HZSM-5, (b) gas phase T-shape protonated water octamer, (c) gas phase cage protonated water octamer.

5.4. Conclusions

A combined 2D IR and AIMD approach showed that small, protonated water clusters form the dominant structural motif for H_2O in HZSM-5 pores under high hydration conditions. The clusters remain tethered to the deprotonated Brønsted acid site through H-bonding interactions of varying strengths, and extended water wires are not formed due to the hydrophobicity of the pores. The overall structure of the cluster conforms to the zeolite lattice, favoring a Y-shaped cluster at channel intersections and an elongated configuration inside S-channels. Individual water molecules populate a distribution of H-bonding configurations with a large inhomogeneous distribution of H-bonding strengths. The experimentally measured water speciation statistics show a large population of water molecules donating one or zero H-bonds, consistent with a short-range

branched H-bonding network terminating after 2-4 water molecules. The excess charge resides, on average, near the more highly-coordinated water molecules in the cluster, though remains in close proximity to free O-H bonds due to the cluster geometry. The excess charge remains delocalized over the water cluster and not on the zeolite lattice, as evidenced by correlations in the 2D IR spectrum and the spatial distribution function calculated from the AIMD simulation.

5.5. References

(1) Bernardo, P.; Drioli, E.; Golemme, G. Membrane Gas Separation: A Review/State of the Art. *Ind. Eng. Chem. Res.* **2009**, *48* (10), 4638–4663. https://doi.org/10.1021/ie8019032.

(2) Khulbe, K. C.; Matsuura, T.; Feng, C. Y.; Ismail, A. F. Recent Development on the Effect of Water/Moisture on the Performance of Zeolite Membrane and MMMs Containing Zeolite for Gas Separation; Review. *RSC Adv.* **2016**, *6* (49), 42943–42961. https://doi.org/10.1039/c6ra03007f.

(3) Kosinov, N.; Gascon, J.; Kapteijn, F.; Hensen, E. J. M. Recent Developments in Zeolite Membranes for Gas Separation. *J. Memb. Sci.* **2016**, *499*, 65–79. https://doi.org/10.1016/j.memsci.2015.10.049.

(4) Masters, A. F.; Maschmeyer, T. Zeolites - From Curiosity to Cornerstone. *Microporous Mesoporous Mater.* **2011**, *142* (2–3), 423–438. https://doi.org/10.1016/j.micromeso.2010.12.026.

(5) Sherman, J. D. Synthetic Zeolites and Other Microporous Oxide Molecular Sieves. *Proc. Natl. Acad. Sci.* **1999**, *96* (11), 3471–3478.

(6) Tanabe, K.; Hölderich, W. F. Industrial Application of Solid Acid-Base Catalysts. *Appl. Catal. A Gen.* **1999**, *181* (2), 399–434. https://doi.org/10.1016/S0926-860X(98)00397-4.

(7) Li, G.; Wang, B.; Resasco, D. E. Water-Mediated Heterogeneously Catalyzed Reactions. *ACS Catal.* **2020**, *10* (2), 1294–1309. https://doi.org/10.1021/acscatal.9b04637.

(8) Resasco, D. E.; Wang, B.; Crossley, S. Zeolite-Catalysed C-C Bond Forming Reactions for Biomass Conversion to Fuels and Chemicals. *Catal. Sci. Technol.* **2016**, *6* (8), 2543–2559. https://doi.org/10.1039/c5cy02271a.

(9) Chen, K.; Kelsey, J.; White, J. L.; Zhang, L.; Resasco, D. Water Interactions in Zeolite Catalysts and Their Hydrophobically Modified Analogues. *ACS Catal.* **2015**, *5* (12), 7480–7487. https://doi.org/10.1021/acscatal.5b02040.

(10) Galadima, A.; Muraza, O. Stability Improvement of Zeolite Catalysts under Hydrothermal Conditions for Their Potential Applications in Biomass Valorization and Crude Oil Upgrading. *Microporous Mesoporous Mater.* **2017**, *249*, 42–54. https://doi.org/10.1016/j.micromeso.2017.04.023.

(11) Davis, M. E. Zeolite-Based Catalysts for Chemicals Synthesis. *Microporous Mesoporous Mater.* **1998**, *21* (4–6), 173–182. https://doi.org/10.1016/S1387-1811(98)00007-9.

(12) Bates, J. S.; Gounder, R. Influence of Confining Environment Polarity on Ethanol Dehydration Catalysis by Lewis Acid Zeolites. *J. Catal.* **2018**, *365*, 213–226. https://doi.org/10.1016/j.jcat.2018.05.009.

(13) Mei, D.; Lercher, J. A. Effects of Local Water Concentrations on Cyclohexanol Dehydration in H-BEA Zeolites. *J. Phys. Chem. C* **2019**, *123* (41), 25255–25266. https://doi.org/10.1021/acs.jpcc.9b07738.

(14) Mei, D.; Lercher, J. A. Mechanistic Insights into Aqueous Phase Propanol Dehydration in H-ZSM-5 Zeolite. *AIChE J.* **2017**, *63* (1), 172–184. https://doi.org/10.1002/aic.15517.

(15) Zhi, Y.; Shi, H.; Mu, L.; Liu, Y.; Mei, D.; Camaioni, D. M.; Lercher, J. A. Dehydration Pathways of 1-Propanol on HZSM-5 in the Presence and Absence of Water. *J. Am. Chem. Soc.* **2015**, *137* (50), 15781–15794. https://doi.org/10.1021/jacs.5b09107.

(16) Xu, Z.; Michos, I.; Cao, Z.; Jing, W.; Gu, X.; Hinkle, K.; Murad, S.; Dong, J. Proton-Selective Ion Transport in ZSM-5 Zeolite Membrane. *J. Phys. Chem. C* **2016**, *120* (46), 26386–26392. https://doi.org/10.1021/acs.jpcc.6b09383.

(17) Termath, V.; Haase, F.; Sauer, J.; Parrinello, M. Understanding the Nature of Water Bound to Solid Acid Surfaces. Ab Initio Simulation on HSAPO-34. *J. Am. Chem. Soc.* **1998**, *120*, 8512–8516.

(18) Vener, M. V.; Rozanska, X.; Sauer, J. Protonation of Water Clusters in the Cavities of Acidic Zeolites: (H 2O)N·H-Chabazite, n = 1-4. *Phys. Chem. Chem. Phys.* **2009**, *11* (11), 1702–1712. https://doi.org/10.1039/b817905k.

(19) Liu, P.; Mei, D. Identifying Free Energy Landscapes of Proton-Transfer Processes between Brønsted Acid Sites and Water Clusters Inside the Zeolite Pores. *J. Phys. Chem. C* **2020**, *124* (41), 22568–22576. https://doi.org/10.1021/acs.jpcc.0c07033.

(20) Grifoni, E.; Piccini, G. M.; Lercher, J. A.; Glezakou, V. A.; Rousseau, R.; Parrinello, M. Confinement Effects and Acid Strength in Zeolites. *Nat. Commun.* **2021**, *12*. https://doi.org/10.1038/s41467-021-22936-0.

(21) Losch, P.; Joshi, H. R.; Vozniuk, O.; Grünert, A.; Ochoa-Hernández, C.; Jabraoui, H.; Badawi, M.; Schmidt, W. Proton Mobility, Intrinsic Acid Strength, and Acid Site Location in Zeolites Revealed by Varying Temperature Infrared Spectroscopy and Density Functional Theory Studies. *J. Am. Chem. Soc.* **2018**, *140* (50), 17790–17799. https://doi.org/10.1021/jacs.8b11588.

(22) Chen, K.; Horstmeier, S.; Nguyen, V. T.; Wang, B.; Crossley, S. P.; Pham, T.; Gan, Z.; Hung, I.; White, J. L. Structure and Catalytic Characterization of a Second Framework Al(IV) Site in Zeolite Catalysts Revealed by NMR at 35.2 T. *J. Am. Chem. Soc.* **2020**, *142* (16), 7514–7523. https://doi.org/10.1021/jacs.0c00590.

(23) Bai, P.; Neurock, M.; Siepmann, J. I. First-Principles Grand-Canonical Simulations of Water Adsorption in Proton-Exchanged Zeolites. *J. Phys. Chem. C* **2021**, Article ASAP. DOI: 10.1021/acs.jpcc.0c10104. https://doi.org/10.1021/acs.jpcc.0c10104.

(24) Bordiga, S.; Lamberti, C.; Bonino, F.; Travert, A.; Thibault-Starzyk, F. Probing Zeolites by Vibrational Spectroscopies. *Chem. Soc. Rev.* **2015**, *44* (20), 7262–7341. https://doi.org/10.1039/c5cs00396b.

(25) Gedeon, A.; Fernandez, C. Solid-State NMR Spectroscopy in Zeolite Science. *Stud. Surf. Sci. Catal.* **2007**, *168*, 403–XII. https://doi.org/https://doi.org/10.1016/S0167-2991(07)80800-7.

(26) Eaves, J. D.; Tokmakoff, A.; Geissler, P. L. Electric Field Fluctuations Drive Vibrational Dephasing in Water. *J. Phys. Chem. A* **2005**, *109* (42), 9424–9436. https://doi.org/10.1021/jp051364m.

(27) Eckstein, S.; Hintermeier, P. H.; Zhao, R.; Baráth, E.; Shi, H.; Liu, Y.; Lercher, J. A. Influence of Hydronium Ions in Zeolites on Sorption. *Angew. Chemie - Int. Ed.* **2019**, *58* (11), 3450–3455. https://doi.org/10.1002/anie.201812184.

(28) Jentys, A.; Warecka, G.; Derewinski, M.; Lercher, J. A. Adsorption of Water on ZSM5 Zeolites. *J. Phys. Chem.* **1989**, *93* (12), 4837–4843. https://doi.org/10.1021/j100349a032.

(29) Hunger, B.; Heuchel, M.; Matysik, S.; Beck, K.; Einicke, W. D. Adsorption of Water on ZSM-5 Zeolites. *Thermochim. Acta* **1995**, *269/270* (C), 599–611. https://doi.org/10.1016/0040-6031(95)02541-3.

(30) Sárkány, J. Effects of Water and Ion-Exchanged Counterion on the FTIR Spectra of ZSM-5. I. NaH-ZSM-5: *Appl. Catal. A Gen.* **1999**, *188* (1–2), 369–379. https://doi.org/10.1016/s0926-860x(99)00257-4.

(31) Wakabayashi, F.; Kondo, J. N.; Domen, K.; Hirose, C. FT-IR Study of H218O Adsorption on H-ZSM-5: Direct Evidence for the Hydrogen-Bonded Adsorption of Water. *J. Phys. Chem.* **1996**, *100* (5), 1442–1444. https://doi.org/10.1021/jp953089h.

(32) Kondo, J. N.; Iizuka, M.; Domen, K.; Wakabayashi, F. IR Study of H2O Adsorbed on H-ZSM-5. *Langmuir* **1997**, *13* (4), 747–749. https://doi.org/10.1021/la9607565.

(33) Vjunov, A.; Wang, M.; Govind, N.; Huthwelker, T.; Shi, H.; Mei, D.; Fulton, J. L.; Lercher, J. A. Tracking the Chemical Transformations at the Brønsted Acid Site upon Water-Induced Deprotonation in a Zeolite Pore. *Chem. Mater.* **2017**, *29* (21), 9030–9042. https://doi.org/10.1021/acs.chemmater.7b02133.

(34) Pelmenschikov, A. G.; Van Santen, R. A. Water Adsorption on Zeolites: Ab-Initio Interpretation of IR Data. *J. Phys. Chem.* **1993**, *97* (41), 10678–10680. https://doi.org/10.1021/j100143a025.

(35) Pelmenschikov, A. G.; van Wolput, J. H. M. C.; Jaenchen, J.; van Santen, R. A. (A,B,C) Triplet of Infrared OH Bands of Zeolitic H-Complexes. *J. Phys. Chem.* **1995**, *99* (11), 3612–3617. https://doi.org/10.1021/j100011a031.

(36) Sazama, P.; Tvaruzkova, Z.; Jirglova, H.; Sobalik, Z. Water Adsorption on High Silica Zeolites. Formation of Hydroxonium Ions and Hydrogen-Bonded Adducts. *Elsevier* **2008**, *174*, 821–824. https://doi.org/https://doi.org/10.1016/S0167-2991(08)80014-6.

(37) Parker, L. M.; Bibby, D. M.; Burns, G. R. An Infrared Study of H2O and D2O on HZSM-5 and DZSM-5. *Zeolites* **1993**, *13* (2), 107–112. https://doi.org/10.1016/0144-2449(93)90069-F.

(38) Krossner, M.; Sauer, J. Interaction of Water with Brønsted Acidic Sites of Zeolite Catalysts. Ab Initio Study of 1:1 and 2:1 Surface Complexes. *J. Phys. Chem.* **1996**, *100* (15), 6199–6211. https://doi.org/10.1021/jp952775d.

(39) Olson, D. H.; Zygmunt, S. A.; Erhardt, M. K.; Curtiss, L. A.; Iton, L. E. Evidence for Dimeric and Tetrameric Water Clusters in HZSM-5. *Zeolites* **1997**, *18*, 347–349. https://doi.org/10.1016/S0144-2449(97)00024-9.

(40) Zygmunt, S. A.; Curtiss, L. A.; Iton, L. E. Protonation of an H2O Dimer by a Zeolitic Brønsted Acid Site. *J. Phys. Chem. B* **2001**, *105* (15), 3034–3038.

https://doi.org/10.1021/jp003469p.

(41) Jiménez-Ruiz, M.; Gahle, D. S.; Lemishko, T.; Valencia, S.; Sastre, G.; Rey, F. Evidence of Hydronium Formation in Water-Chabazite Zeolite Using Inelastic Neutron Scattering Experiments and Ab Initio Molecular Dynamics Simulations. *J. Phys. Chem. C* **2020**, *124* (9), 5436–5443. https://doi.org/10.1021/acs.jpcc.9b11081.

(42) Olson, D. H.; Haag, W. O.; Borghard, W. S. Use of Water as a Probe of Zeolitic Properties: Interaction of Water with HZSM-5. *Microporous Mesoporous Mater.* **2000**, *35–36*, 435–446. https://doi.org/10.1016/S1387-1811(99)00240-1.

(43) Beta, I. A.; Böhlig, H.; Hunger, B. Structure of Adsorption Complexes of Water in Zeolites of Different Types Studied by Infrared Spectroscopy and Inelastic Neutron Scattering. *Phys. Chem. Chem. Phys.* **2004**, *6* (8), 1975–1981. https://doi.org/10.1039/b313234j.

(44) Liu, Y.; Vjunov, A.; Shi, H.; Eckstein, S.; Camaioni, D. M.; Mei, D.; Baráth, E.; Lercher, J. A. Enhancing the Catalytic Activity of Hydronium Ions through Constrained Environments. *Nat. Commun.* **2017**, *8* (March), 2–9. https://doi.org/10.1038/ncomms14113.

(45) Bordiga, S.; Regli, L.; Lamberti, C.; Zecchina, A.; Bjorgen, M.; Lillerud, K. P. FTIR Adsorption Studies of H2O and CH3OH in the Isostructural H-SSZ-13 and H-SAPO-34: Formation of H-Bonded Adducts and Protonated Clusters. *J. Phys. Chem. B* **2005**, *109*, 7724–7732. https://doi.org/10.1021/jp04432b.

(46) Zecchina, A.; Geobaldo, F.; Spoto, G.; Bordiga, S.; Ricchiardi, G.; Buzzoni, R.; Petrini, G. FTIR Investigation of the Formation of Neutral and Ionic Hydrogen-Bonded Complexes by Interaction of H-ZSM-5 and H-Mordenite with CH3CN and H2O: Comparison with the H-NAFION Superacidic System. *J. Phys. Chem.* **1996**, *100* (41), 16584–16599. https://doi.org/10.1021/jp960433h.

(47) Wang, M.; Jaegers, N. R.; Lee, M. S.; Wan, C.; Hu, J. Z.; Shi, H.; Mei, D.; Burton, S. D.; Camaioni, D. M.; Gutiérrez, O. Y.; Glezakou, V. A.; Rousseau, R.; Wang, Y.; Lercher, J. A. Genesis and Stability of Hydronium Ions in Zeolite Channels. *J. Am. Chem. Soc.* **2019**, *141* (8), 3444–3455. https://doi.org/10.1021/jacs.8b07969.

(48) Zygmunt, S. A.; Curtiss, L. A.; Iton, L. E.; Erhardt, M. K. Computational Studies of Water Adsorption in the Zeolite H-ZSM-5. *J. Phys. Chem.* **1996**, *100*, 6663–6671.

(49) Harris, K. D. M.; Xu, M.; Thomas, J. M. Probing the Evolution of Water Clusters during Hydration of the Solid Acid Catalyst H-ZSM-5. *Philos. Mag.* **2009**, *89* (33), 3001–3012. https://doi.org/10.1080/14786430903164606.

(50) Joshi, K. L.; Psofogiannakis, G.; Van Duin, A. C. T.; Raman, S. Reactive Molecular Simulations of Protonation of Water Clusters and Depletion of Acidity in H-ZSM-5 Zeolite. *Phys. Chem. Chem. Phys.* **2014**, *16* (34), 18433–18441. https://doi.org/10.1039/c4cp02612h.

(51) Jungsuttiwong, S.; Limtrakul, J.; Truong, T. N. Theoretical Study of Modes of Adsorption of Water Dimer on H-ZSM-5 and H-Faujasite Zeolites. *J. Phys. Chem. B* **2005**, *109* (27), 13342–13351. https://doi.org/10.1021/jp045021k.

(52) Ohlin, L.; Bazin, P.; Thibault-Starzyk, F.; Hedlund, J.; Grahn, M. Adsorption of CO2, CH4, and H2O in Zeolite Zsm-5 Studied Using in Situ ATR-FTIR Spectroscopy. *J. Phys. Chem. C* **2013**, *117*, 16972–16982.

(53) Bolis, V.; Busco, C.; Ugliengo, P. Thermodynamic Study of Water Adsorption in High-Silica Zeolites. *J. Phys. Chem. B* **2006**, *110* (30), 14849–14859. https://doi.org/10.1021/jp061078q.

(54) Fournier, J. A.; Carpenter, W. B.; Lewis, N. H. C.; Tokmakoff, A. Broadband 2D IR Spectroscopy Reveals Dominant Asymmetric H5O2+ Proton Hydration Structures in Acid Solutions. *Nat. Chem.* **2018**, *10* (September), 932–937. https://doi.org/10.1038/s41557-018-0091-y.

(55) Dahms, F.; Fingerhut, B. P.; Nibbering, E. T. J.; Pines, E.; Elsaesser, T. Large-Amplitude Transfer Motion of Hydrated Excess Protons Mapped by Ultrafast 2D IR Spectroscopy. *Science* **2017**, *357* (6350), 491–495. https://doi.org/10.1126/science.aan5144.

(56) Moilanen, D. E.; Levinger, N. E.; Spry, D. B.; Fayer, M. D. Confinement or the Nature of the Interface? Dynamics of Nanoscopic Water. *J. Am. Chem. Soc.* **2007**, *129* (8), 14311–14318.

(57) Fenn, E. E.; Wong, D. B.; Fayer, M. D. Water Dynamics at Neutral and Ionic Interfaces. *Proc. Natl. Acad. Sci. U. S. A.* **2009**, *106* (36), 15243–15248. https://doi.org/10.1073/pnas.0907875106.

(58) Yan, C.; Nishida, J.; Yuan, R.; Fayer, M. D. Water of Hydration Dynamics in Minerals Gypsum and Bassanite: Ultrafast 2D IR Spectroscopy of Rocks. *J. Am. Chem. Soc.* **2016**, *138* (30), 9694–9703. https://doi.org/10.1021/jacs.6b05589.

(59) Yamada, S. A.; Shin, J. Y.; Thompson, W. H.; Fayer, M. D. Water Dynamics in Nanoporous Silica: Ultrafast Vibrational Spectroscopy and Molecular Dynamics Simulations. *J. Phys. Chem. C* **2019**, *123* (9), 5790–5803. https://doi.org/10.1021/acs.jpcc.9b00593.

(60) Roget, S. A.; Kramer, P. L.; Thomaz, J. E.; Fayer, M. D. Bulk-like and Interfacial Water Dynamics in Nafion Fuel Cell Membranes Investigated with Ultrafast Nonlinear IR Spectroscopy. *J. Phys. Chem. B* **2019**, *123* (44), 9408–9417. https://doi.org/10.1021/acs.jpcb.9b07592.

(61) Janićijević, D.; Uskoković-Marković, S.; Ranković, D.; Milenković, M.; Jevremović, A.; Nedić Vasiljević, B.; Milojević-Rakić, M.; Bajuk-Bogdanović, D. Double Active BEA Zeolite/Silver Tungstophosphates – Antimicrobial Effects and Pesticide Removal. *Sci. Total Environ.* **2020**, *735*, 139530. https://doi.org/10.1016/j.scitotenv.2020.139530.

(62) Raja, R.; Ratnasamy, P. Selective Oxidation with Copper Coplexes Incorporated in Molecular Sieves. *Stud. Surf. Sci. Catal.* **1996**, *101*, 181–190.

(63) *Alfa Aesar Perfluoro(tetradecahydrophenanthrene), mixture of isomers | Fisher Scientific*. https://www.fishersci.com/shop/products/perfluoro-tetradecahydrophenanthrene-mixture-isomers/AAA1889814 (accessed 2020-09-22).

(64) Carpenter, W. B.; Fournier, J. A.; Biswas, R.; Voth, G. A.; Tokmakoff, A. Delocalization and Stretch-Bend Mixing of the HOH Bend in Liquid Water. *J. Chem. Phys.* **2017**, *147* (8). https://doi.org/10.1063/1.4987153.

(65) Carpenter, W. B.; Fournier, J. A.; Lewis, N. H. C.; Tokmakoff, A. Picosecond Proton Transfer Kinetics in Water Revealed with Ultrafast IR Spectroscopy. *J. Phys. Chem. B* **2018**, *122* (10), 2792–2802. https://doi.org/10.1021/acs.jpcb.8b00118.

(66) De Marco, L.; Fournier, J. A.; Thämer, M.; Carpenter, W.; Tokmakoff, A. Anharmonic Exciton Dynamics and Energy Dissipation in Liquid Water from Two-Dimensional Infrared Spectroscopy. *J. Chem. Phys.* **2016**, *145* (9), 094501. https://doi.org/10.1063/1.4961752.

(67) Bloem, R.; Garrett-roe, S.; Strzalka, H.; Hamm, P.; Donaldson, P. Enhancing Signal Detection and Completely Eliminating Scattering Using Quasi-Phase-Cycling in 2D IR Experiments. *Opt. Express* **2010**, *18* (26), 1747–1756.

(68) Knight, C.; Voth, G. A. The Curious Case of the Hydrated Proton. *Acc. Chem. Res.* **2012**, *45* (1), 101–109. https://doi.org/10.1021/ar200140h.

(69) Tse, Y. L. S.; Knight, C.; Voth, G. A. An Analysis of Hydrated Proton Diffusion in Ab Initio Molecular Dynamics. *J. Chem. Phys.* **2015**, *142* (142), 014104. https://doi.org/10.1063/1.4905077.

(70) Zhang, Y.; Yang, W. Comment on " Generalized Gradient Approximation Made Simple ." *Phys. Rev. Lett.* **1998**, *80* (1998), 890.

(71) Grimme, S.; Antony, J.; Ehrlich, S.; Krieg, H. A Consistent and Accurate Ab Initio Parameterization of Density Functional Dispersion Correctin (DFT-D) for the 94 Elements of H-Pu. *J. Chem. Phys.* **2010**, *132*, 154104. https://doi.org/10.1063/1.3382344.

(72) Kühne, T. D.; Laino, T.; Iannuzzi, M.; Ben, M. Del; Khaliullin, R. Z.; Schütt, O.; Rybkin, V. V; Seewald, P.; Schiffmann, F.; Golze, D.; Schade, R.; Mundy, C. J.; Chulkov, S. CP2K : An Electronic Structure and Molecular Dynamics Software Package - Quickstep : Efficient and Accurate Electronic Structure Calculations. *J. Chem. Phys.* **2020**, *152*, 194103. https://doi.org/10.1063/5.0007045.

(73) Baer, T.; Hase, W. L. *Unimolecular Reaction Dynamics: Theory and Experiments*; Oxford University Press, 1996.

(74) Li, C.; Swanson, J. M. J. Understanding and Tracking the Excess Proton in Ab Initio Simulations; Insights from IR Spectra. *J. Phys. Chem. B* **2020**, *124*, 5696–5708. https://doi.org/10.1021/acs.jpcb.0c03615.

(75) Cringus, D.; Jansen, T. I. C. L. C.; Pshenichnikov, M. S.; Wiersma, D. A. Ultrafast Anisotropy Dynamics of Water Molecules Dissolved in Acetonitrile. *J. Chem. Phys.* **2007**, *127* (8), 084507. https://doi.org/10.1063/1.2771178.

(76) Loparo, J. J.; Roberts, S. T.; Nicodemus, R. A.; Tokmakoff, A. Variation of the Transition Dipole Moment across the OH Stretching Band of Water. *Chem. Phys.* **2007**, *341* (1–3), 218–229. https://doi.org/10.1016/j.chemphys.2007.06.056.

(77) De Marco, L.; Carpenter, W.; Liu, H.; Biswas, R.; Bowman, J. M.; Tokmakoff, A. Differences in the Vibrational Dynamics of H2O and D2O: Observation of Symmetric and Antisymmetric Stretching Vibrations in Heavy Water. *J. Phys. Chem. Lett.* **2016**, *7* (10), 1769–1774. https://doi.org/10.1021/acs.jpclett.6b00668.

(78) De Marco, L.; Ramasesha, K.; Tokmakoff, A. Experimental Evidence of Fermi Resonances in Isotopically Dilute Water from Ultrafast Broadband IR Spectroscopy. *J. Phys. Chem. B* **2013**, *117* (49), 15319–15327. https://doi.org/10.1021/jp4034613.

(79) Kananenka, A. A.; Skinner, J. L. Fermi Resonance in OH-Stretch Vibrational Spectroscopy of Liquid Water and the Water Hexamer. *J. Chem. Phys.* **2018**, *148* (24). https://doi.org/10.1063/1.5037113.

(80) Kim, J.; Schmitt, U. W.; Gruetzmacher, J. A.; Voth, G. A.; Scherer, N. E. The Vibrational Spectrum of the Hydrated Proton: Comparison of Experiment, Simulation, and Normal Mode Analysis. *J. Chem. Phys.* **2002**, *116* (2), 737–746. https://doi.org/10.1063/1.1423327.

(81) Dalla Bernardina, S.; Paineau, E.; Brubach, J. B.; Judeinstein, P.; Rouzière, S.; Launois, P.; Roy, P. Water in Carbon Nanotubes: The Peculiar Hydrogen Bond Network Revealed by Infrared Spectroscopy. *J. Am. Chem. Soc.* **2016**, *138* (33), 10437–10443. https://doi.org/10.1021/jacs.6b02635.

(82) Schaefer, J.; Backus, E. H. G.; Nagata, Y.; Bonn, M. Both Inter- and Intramolecular Coupling of O-H Groups Determine the Vibrational Response of the Water/Air Interface. *J. Phys. Chem. Lett.* **2016**, *7* (22), 4591–4595. https://doi.org/10.1021/acs.jpclett.6b02513.

(83) Das, S.; Imoto, S.; Sun, S.; Nagata, Y.; Backus, E. H. G.; Bonn, M. Nature of Excess Hydrated Proton at the Water-Air Interface. *J. Am. Chem. Soc.* **2020**, *142* (2), 945–952. https://doi.org/10.1021/jacs.9b10807.

(84) Yu, Q.; Carpenter, W. B.; Lewis, N. H. C.; Tokmakoff, A.; Bowman, J. M. High-Level VSCF/VCI Calculations Decode the Vibrational Spectrum of the Aqueous Proton. *J. Phys. Chem. B* **2019**, *123* (33), 7214–7224. https://doi.org/10.1021/acs.jpcb.9b05723.

(85) Fournier, J. A.; Wolke, C. T.; Johnson, M. A.; Odbadrakh, T. T.; Jordan, K. D.; Kathmann, S. M.; Xantheas, S. S. Snapshots of Proton Accommodation at a Microscopic Water Surface: Understanding the Vibrational Spectral Signatures of the Charge Defect in Cryogenically Cooled H+(H2O)N=2-28 Clusters. *J. Phys. Chem. A* **2015**, *119*, 9425–9440. https://doi.org/10.1021/acs.jpca.5b04355.

(86) Headrick, J. M.; Diken, E. G.; Walters, R. S.; Hammer, N. I.; Christie, R. A.; Cui, J.; Myshakin, E. M.; Duncan, M. A.; Johnson, M. A.; Jordan, K. D. Spectral Signatures of Hydrated Proton Vibrations in Water Clusters. *Science* **2005**, *308*, 1765–1769. https://doi.org/10.1126/science.1113094.

(87) Shin, J.; Hammer, N. I.; Diken, E. G.; Johnson, M. A.; Walters, R. S.; Jaeger, T. D.; Duncan, M. A.; Christie, R. A.; Jordan, K. D. Infrared Signature of Structures Associated with the H+(H2O)n (N= 6 to 27) Clusters. *Science* **2004**, *304* (May), 1137–1141.

(88) Auer, B.; Kumar, R.; Schmidt, J. R.; Skinner, J. L. Hydrogen Bonding and Raman, IR, and 2D-IR Spectroscopy of Dilute HOD in Liquid D2O. *Proc. Natl. Acad. Sci. U. S. A.* **2007**, *104* (36), 14215–14220. https://doi.org/10.1073/pnas.0701482104.

(89) Carpenter, W. B.; Yu, Q.; Hack, J. H.; Dereka, B.; Bowman, J. M.; Tokmakoff, A. Decoding the 2D IR Spectrum of the Aqueous Proton with High-Level VSCF/VCI Calculations. *J. Chem. Phys.* **2020**, *153* (12), 124506. https://doi.org/10.1063/5.0020279.

(90) Schmitt, U. W.; Voth, G. A. The Computer Simulation of Proton Transport in Water. *J. Chem. Phys.* **1999**, *111* (20), 9361–9381. https://doi.org/10.1063/1.480032.

(91) Christie, R. A.; Jordan, K. D. Finite Temperature Behavior of H+(H2O)6 and H+(H2O)8†. *J. Phys. Chem. B* **2002**, *106*, 8376–8381.

(92) Farzaneh, A.; Zhou, M.; Potapova, E.; Bacsik, Z.; Ohlin, L.; Holmgren, A.; Hedlund, J.; Grahn, M. Adsorption of Water and Butanol in Silicalite-1 Film Studied with in Situ Attenuated Total Reflectance-Fourier Transform Infrared Spectroscopy. *Langmuir* **2015**, *31* (17), 4887–4894. https://doi.org/10.1021/acs.langmuir.5b00489.

(93) Smirnov, K. S. A Molecular Dynamics Study of the Interaction of Water with the External Surface of Silicalite-1. *Phys. Chem. Chem. Phys.* **2017**, *19* (4), 2950–2960. https://doi.org/10.1039/c6cp06770k.

(94) Cailliez, F.; Stirnemann, G.; Boutin, A.; Demachy, I.; Fuchs, A. H. Does Water Condense in Hydrophobic Cavities? A Molecular Simulation Study of Hydration in Heterogeneous Nanopores. *J. Phys. Chem. C* **2008**, *112* (28), 10435–10445. https://doi.org/10.1021/jp710746b.

(95) Trzpit, M.; Soulard, M.; Patarin, J.; Desbiens, N.; Cailliez, F.; Boutin, A.; Demachy, I.; Fuchs, A. H. The Effect of Local Defects on Water Adsorption in Silicalite-1 Zeolite: A Joint Experimental and Molecular Simulation Study. *Langmuir* **2007**, *23* (20), 10131–10139. https://doi.org/10.1021/la7011205.

(96) Özgür Yazaydin, A.; Thompson, R. W. Molecular Simulation of Water Adsorption in Silicalite: Effect of Silanol Groups and Different Cations. *Microporous Mesoporous Mater.* **2009**, *123* (1–3), 169–176. https://doi.org/10.1016/j.micromeso.2009.03.045.

(97) Pellenq, R. J. M.; Roussel, T.; Puibasset, J. Molecular Simulations of Water in Hydrophobic Microporous Solids. *Adsorption* **2008**, *14* (4–5), 733–742. https://doi.org/10.1007/s10450-008-9135-8.

(98) Ahunbay, M. G. Monte Carlo Simulation of Water Adsorption in Hydrophobic MFI Zeolites with Hydrophilic Sites. *Langmuir* **2011**, *27* (23), 14703. https://doi.org/10.1021/la2039174.

Appendix 5A. Self-consistent fitting of 2D IR and FTIR spectra

The FTIR and 2D IR spectra of H_2O / HZSM-5 were fit to a sum of Gaussian functions (FTIR) and 2D Gaussian and Gaussian-Stochastic functions (2D IR) to estimate the relative populations of H_2O hydrogen-bonding configurations. The models used for this fitting are described below.

FTIR Model

$$\begin{aligned} S_{FTIR} = & \frac{A_1 |\mu_1|^2 \chi_{HB}}{\sigma_1\sqrt{2\pi}} \exp\left(\frac{(\omega-\omega_1)^2}{2\sigma_1^{\,2}}\right) + \frac{A_2}{\sigma_2\sqrt{2\pi}} \exp\left(\frac{(\omega-\omega_2)^2}{2\sigma_2^{\,2}}\right) \\ & + \frac{A_3}{\sigma_3\sqrt{2\pi}} \exp\left(\frac{(\omega-\omega_3)^2}{2\sigma_3^{\,2}}\right) + \frac{A_4}{\sigma_4\sqrt{2\pi}} \exp\left(\frac{(\omega-\omega_4)^2}{2\sigma_4^{\,2}}\right) \\ & + \frac{A_1 |\mu_5|^2 \chi_F}{\sigma_5\sqrt{2\pi}} \exp\left(\frac{(\omega-\omega_5)^2}{2\sigma_5^{\,2}}\right) \end{aligned} \tag{5.2}$$

2D IR Model

$$\begin{aligned} S_{2DIR} = & A_1 |\mu_1|^4 \chi_{HB} GS(\omega_1, \omega_3, \omega_{11}, \omega_{13}, \tau_{c1}, \Delta_1, t_2) \\ & + A_2 G(\omega_1, \omega_3, \omega_{21}, \omega_{23}, \Delta_{21}, \Delta_{23}) \\ & + A_3 G(\omega_1, \omega_3, \omega_{31}, \omega_{33}, \Delta_{31}, \Delta_{33}) \\ & + A_4 GS(\omega_1, \omega_3, \omega_{41}, \omega_{43}, \tau_{c4}, \Delta_4, t_2) \\ & + A_1 |\mu_1|^2 |\mu_5|^2 \chi_{FHB} G(\omega_1, \omega_3, \omega_{51}, \omega_{53}, \Delta_{51}, \Delta_{53}) \\ & + A_6 G(\omega_1, \omega_3, \omega_{61}, \omega_{63}, \Delta_{61}, \Delta_{63}) \\ & - A_7 G^{(rot)}(\omega_1, \omega_3, \omega_{71}, \omega_{73}, \Delta_{7d}, \Delta_{7ad}, \theta_7) \\ & - A_8 G(\omega_1, \omega_3, \omega_{81}, \omega_{83}, \Delta_{81}, \Delta_{83}) \\ & + A_9 G(\omega_1, \omega_3, \omega_{91}, \omega_{93}, \Delta_{91}, \Delta_{93}) \\ & + A_{10} G(\omega_1, \omega_3, \omega_{101}, \omega_{103}, \Delta_{101}, \Delta_{103}) \end{aligned} \tag{5.3}$$

The FTIR model is a simple Gaussian decomposition. In the 2D IR model, $S_{2D\,IR}$ is the isotropic 2D IR signal, A_i is the amplitude of peak *i*, ω_1 and ω_3 are the excitation and detection frequencies respectively, μ_j is the transition dipole moment of transition *j*, calculated using the relation in

Loparo *et* al.[76] The functions *G*, $G^{(rot)}$, and *GS* are normalized 2D Gaussians, rotated Gaussians, and Gaussian-Stochastic lineshape functions defined below. In Eq. (5.6) FT is the normalized Fourier transform over t_1 and t_3, and * represents the complex conjugate.

$$G(\omega_1,\omega_3,\omega_{i1},\omega_{i3},\Delta_{i1},\Delta_{i3}) = \frac{1}{2\pi\Delta_{i1}\Delta_{i3}}\exp\left(\frac{(\omega_1-\omega_{i1})^2}{2\Delta_{i1}{}^2}\right)\exp\left(\frac{(\omega_3-\omega_{i3})^2}{2\Delta_{i3}{}^2}\right) \tag{5.4}$$

$$\begin{aligned} G^{(rot)}(\omega_1,\omega_3,\omega_{i1},\omega_{i3},\Delta_{id},\Delta_{iad},\theta_i) = \\ \frac{1}{2\pi\Delta_{i1}\Delta_{i3}}\exp\left(\frac{\left[(\cos(\theta_i)\omega_1+\sin(\theta_i)\omega_3)-(\cos(\theta_i)\omega_{i1}+\sin(\theta_i)\omega_{i3})\right]^2}{2\Delta_{id}{}^2}\right) \\ \times\exp\left(\frac{\left[(\sin(\theta_i)\omega_1-\cos(\theta_i)\omega_3)-(\sin(\theta_i)\omega_{i1}+\cos(\theta_i)\omega_{i3})\right]^2}{2\Delta_{iad}{}^2}\right) \end{aligned} \tag{5.5}$$

$$\begin{aligned} &GS(\omega_1,\omega_3,\omega_{i1},\omega_{i3},\tau_{ci},\Delta_i,t_2) = \mathrm{Re}[FT(P_R)+FT(P_{NR})] \\ &P_R = \exp\left(-i\omega_{eg}(t_3+t_1)\right)\exp(f_1) \\ &P_{NR} = \exp\left(-i\omega_{eg}(t_1-t_3)\right)\exp(f_2) \\ &f_1 = -g^*(t_3,\tau_{ci},\Delta_i)-g(t_1,\tau_{ci},\Delta_i)-g^*(t_2,\tau_{ci},\Delta_i) \\ &\quad +g(t_1+t_2,\tau_{ci},\Delta_i)+g^*(t_3+t_2,\tau_{ci},\Delta_i)-g(t_3+t_2+t_1,\tau_{ci},\Delta_i) \\ &f_2 = -g^*(t_3,\tau_{ci},\Delta_i)-g^*(t_1,\tau_{ci},\Delta_i)+g(t_2,\tau_{ci},\Delta_i) \\ &\quad -g^*(t_1+t_2,\tau_{ci},\Delta_i)-g(t_3+t_2,\tau_{ci},\Delta_i)+g^*(t_3+t_2+t_1,\tau_{ci},\Delta_i) \\ &g(t,\tau_{ci},\Delta_i) = \Delta_i{}^2\tau_{ci}{}^2\left[\exp(-t/\tau_{ci})+t/\tau_{ci}-1\right] \end{aligned} \tag{5.6}$$

In this analysis, ω_{eg} was set to zero and the lineshape function was centered at the coordinates $(\omega_{i1},\omega_{i3})$ after the Fourier transform. To reduce the number of fit parameters, frequency and linewidth parameters were first fit to portions of the spectra. Then, population parameters P_{ND}, P_{SD}, and P_{DD} were fit to FTIR and 2D IR spectra, using the relations $\chi_{HB} = 2P_{DD}+P_{SD}$, $\chi_F = 2P_{ND}+P_{SD}$, and $\chi_{F/HB} = P_{SD}$ to relate water population and H-bond environment parameters.

This model was fit to both H_2O/HZSM-5 and HOD/HZSM-5 data sets, with the results presented in Fig. 5A.1.

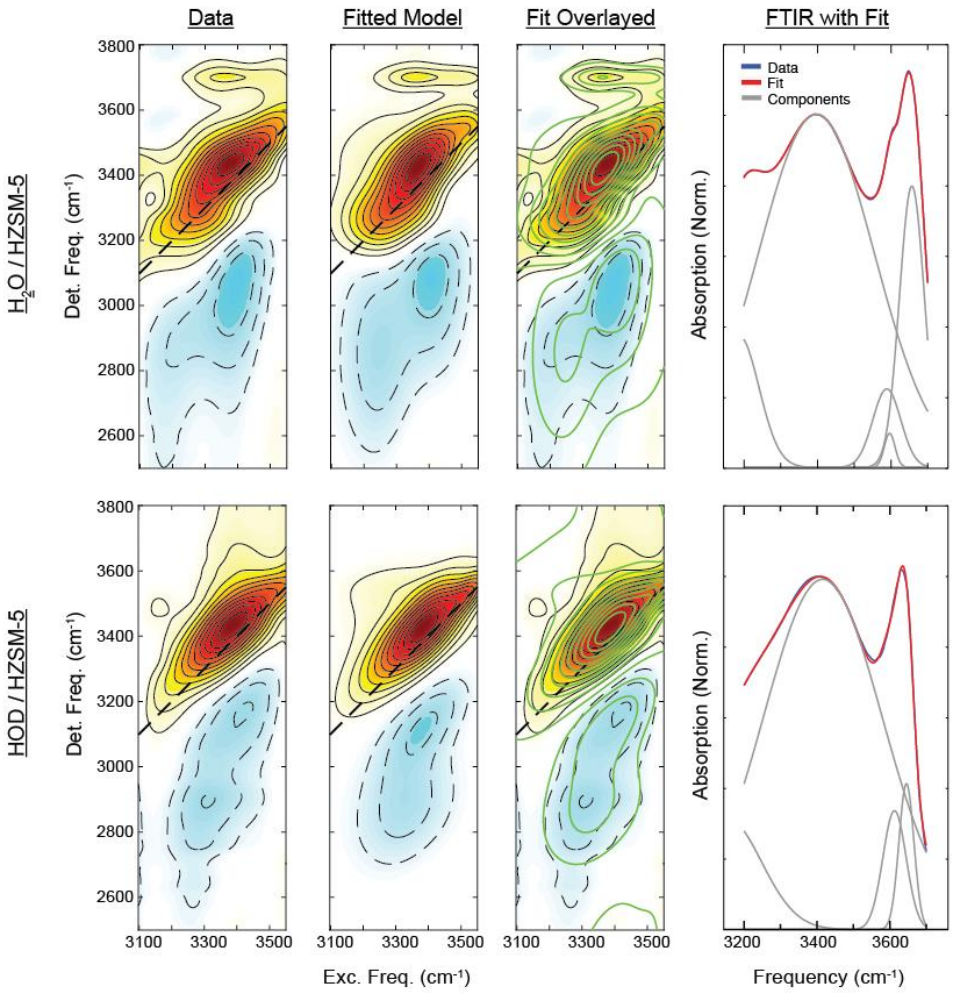

Figure 5A.1. Results for self-consistent fitting to isotropic 2D IR spectra and FTIR spectra of 13 equiv. H_2O/HZSM-5 (top row) and 6 equiv. HOD/HZSM-5 (bottom row). 2D IR spectra (first column) are shown next to the fitted model (second column) and overlayed (third column) with the fitted model contours shown in green. The FTIR spectra and fit result are shown overlayed in the fourth column.

Chapter 6

Proton dissociation and delocalization under stepwise hydration of zeolite

The work presented in this chapter has been submitted for publication:

Hack, J. H., Ma, X., Chen, Y., Dombrowski, J. P., Lewis, N. H. C., Li, C., Voth, Kung, H. H., G. A., Tokmakoff, A. Proton dissociation and delocalization under stepwise hydration of zeolite HZSM-5. (*Under review*)

6.1. Introduction

Acidic zeolites are among the most widely-used heterogeneous catalysts in industrial processes, catalyzing alkylation, isomerization, cracking, and other reactions in oil refining and petrochemistry, as described in Chapter 1.[1–4] With the growing necessity for divestment from fossil fuels,[5] zeolites have emerged as promising catalysts for the production of fuels and chemicals derived from biomass.[6–8] Water is often present as a reaction product or solvent in the conversion of oxygen-rich biomass feedstocks,[9] and has been shown to influence catalytic activity in several zeolite-catalyzed reactions.[10–15] A comprehensive understanding of the interactions between water and zeolite acid sites is an important component for gaining deeper mechanistic insight into these processes.

The protonation state of the zeolite Brønsted acid site (BAS) and adsorbed water clusters depends on the number of adsorbed water molecules. At 1 H_2O / BAS the proton resides on the BAS, which forms a hydrogen bond to the water molecule.[16–23] The proton affinity of the water cluster increases with size,[24–27] deprotonating the BAS above a critical hydration number, which is a topic of ongoing study and debate. While most investigations place the critical size at 2-3 H_2O for HZSM-5, theoretical studies are divided on the nature of the adsorbed water dimer. Depending on the choice of method, basis set, and treatment of zero-point energy, different calculations have concluded that protonated BAS,[20] protonated water cluster,[28] or both[17–19,22,23] are stable in the presence of two H_2O molecules. The details of the proton position and charge delocalization in larger clusters are also of interest. A recent metadynamics study suggested that the proton resides primarily on the water molecule adjacent to the BAS up to 4 H_2O, but becomes fully solvated and detached from the BAS at higher hydration.[23] An accurate description of the protonation state is complicated by charge delocalization[23,29] and dynamics such as proton hopping and shuttling.[22]

Experiments are needed which can access molecular-level details about the protonation state as a function of zeolite hydration. Hydration-dependent ^{1}H NMR spectroscopy was used to identify a signature of hydronium ions which appeared at water loadings between 1.6-9.1 H_2O/BAS.[21] Infrared (IR) spectroscopy is a complementary technique which is sensitive to the molecular environment of O–H bonds and can support sub-picosecond light pulses to probe the timescales of water's structural dynamics.[30,31] Most IR spectroscopic studies of hydrated zeolite used steady-state Fourier-transform IR (FTIR) spectroscopy and focused primarily on the characterization of $\leq$ 1 H_2O / BAS,[16,32–34] where the most prominent spectroscopic feature is a broad doublet arising from the H-bonded BAS O–H stretch.[16,17,35,36] Higher hydration levels have

been accessed by *in-situ* hydration studies using temperature to vary the amount of water adsorbed.[20] At higher hydration additional broad, overlapping features appear which are not straightforward to deconvolve in FTIR spectra,[20] making a quantitative determination of the critical water cluster size difficult. Additional experimental challenges include achieving precise control of the hydration level and deconvoluting the distribution of microscopic H_2O cluster sizes at a given macroscopic hydration level.

Time-resolved IR spectroscopy can provide additional information about the structure and dynamics of water molecules and protons in zeolite. Picosecond transient absorption studies have been used to measure vibrational energy relaxation of zeolite hydroxyls and adsorbed molecules including water.[37,38] Recently, two-dimensional infrared (2D IR) spectroscopy was used to study the structure of protonated water clusters in highly-hydrated HZSM-5.[29]

In this chapter we present a quantitative measurement of proton dissociation from protonated zeolite BAS to hydrated excess proton using FTIR and 2D IR spectroscopy and *ab initio* molecular dynamics (AIMD) simulations. Quantitative spectroscopic analysis was enabled by sample preparation at controlled hydration level (equivalents or equiv. H_2O/Al atom). IR spectral signatures of distinct protonation states were identified using spectral decomposition, consistent with hydration-dependent 2D IR spectra. The hydration trends of those signatures were used to infer that the proton is dissociated from the BAS in clusters of 2 or more adsorbed water molecules, with an estimated deprotonation energy of 1.6 kcal/mol. AIMD simulations of 1-8 H_2O clusters in HZSM-5 were used to reveal connections between molecular structure, excess charge position, and vibrational spectral density. Calculations including the position and delocalization of excess proton defect charge, statistics of atomic positions, and power spectra are presented with atomic

specificity across several hydration levels. Together, these results track the evolution of the protonation state with stepwise hydration, showing a transition from zeolite-bound proton in the presence of one H_2O molecule to an excess proton when two or more water molecules are adsorbed.

6.2. Sample preparation, experimental, and theoretical methods

Sample preparation was a crucial component for hydration-dependent IR spectroscopy, which required quantitative control of the hydration level. The methodology was based on previously-published work[29] also described in Chapter 5. HZSM-5 samples (received from Johnson Matthey) were calcined in air, dehydrated on a Schlenk-line with vacuum, then rehydrated *ex-situ* at 150 ^{o}C to a fixed level in a sealed Parr acid digestion chamber. Hydrated zeolites were suspended in a mixture of oils (Flurolube polychlorotrifluoroethylene and perfluoro(tetradecahydrophenanthrene)) which prevented exchange of water with the atmosphere. The mean hydration level of each sample, $\bar{h}$, is the ratio of adsorbed water to Al content, measured by methanol titration and inductively coupled plasma – optical emission spectroscopy (ICP-OES) respectively. As a simple ratio between two directly-measured quantities, this measurement of the hydration level does not require calibration to a second experiment such as thermogravimetric analysis or isothermal adsorption. In addition, *ex-situ* hydration has the advantage of enabling suspension in index-matching oils, which significantly reduces scatter in nonlinear IR spectroscopy.[29,39] A Si:Al ratio of 17:1 was used to reach a sufficient signal / scatter level in nonlinear experiments. This lower Si:Al ratio, compared to that in Chapter 5, was necessary to increase the H_2O concentration (per volume of sample) at low hydration (per Al site) for nonlinear

experiments. The linear IR spectra were unchanged compared to Si:Al = 45, suggesting that the Al sites and water clusters can still be considered largely independent at this ratio.

IR spectra were collected with samples suspended between two 1-mm CaF_2 windows. Spectral decomposition used maximum entropy reweighting of SVD components based on the method of Widjaja and Garland.[40] 2D IR and transient absorption spectra were collected with polarization control using a spectrometer that has been described previously[41,42] and in Chapter 3. Scatter artifacts were suppressed with a combination of chopping both pump and probe beams, quasi-phase cycling[43] by oscillating the probe delay stage, and negative time subtraction, as detailed in our previous work[29] and in Chapter 3.

The atomistic modeling of the protonated water cluster includes a BAS residing in a two-unit cell ZSM-5 zeolite framework (l_a = 20.090 Å, l_b = 19.736Å, l_c = 26.284 Å),[44] an excess proton to balance the negative charge at the Aluminum T11 site, and a water molecular cluster $(H_2O)_n$ consisted of 1, 2, 3, 4, 6, or 8 water molecules near the BAS. To capture proton shuttling within the cluster and at the interface, as well as the dynamics and statistical distributions of the protonated water cluster at each hydration level, the zeolite framework and the protonated water cluster were treated explicitly with quantum mechanical calculations at the DFT/revPBE/DZVP level of theory.[45] The CP2K package[46] was used to carry out the AIMD simulation using the Quickstep code[47] and the hybrid Gaussian and plane waves (GPW) method.[48] with the Goedecker-Teter-Hutter pseudo potential parameterized for the PBE functional.[49] Grimme's D3 dispersion correction was applied to the long range interactions using a cut-off distance of 40 Å.[50] All AIMD simulations of protonated water clusters are integrated with an MD time step of 0.5 fs at 298 K to sample configurations in the constant NVT ensemble with a Nose-Hoover thermostat

and a time constant of 1 ps. For each protonated cluster, the AIMD simulation was first equilibrated for ~4 ps prior to a production run of ~20 ps.

The power spectra of protonated water clusters were calculated from Fourier transform of the velocity-velocity autocorrelation function of each H atom. Since the protonic excess charge is delocalized in the hydrogen bond network, the protonic charge is described by the CEC position rather than a localized atomic position. The rCEC approach[51,52] was used to assign the CEC positions in the AIMD trajectories of protonated water clusters at BAS. The rCEC analysis also provides the distribution of the excess charge in the BAS oxygen atoms and all water molecules. Further details of the AIMD methodology were reported previously.[29]

6.3. Results and Discussion

6.3.1. Hydration dependent IR spectroscopy and spectral decomposition

FTIR spectra of H_2O in HZSM-5(17) zeolites were measured as a function of hydration level from 0.5-8.0 equiv. H_2O per Al (Fig. 6.1). Fig. 6.1b shows the hydration series with the dehydrated zeolite subtracted; the series without subtraction is shown in Fig. 6.1a. At low hydration, 0.5-1.0 equiv. H_2O, the most prominent spectroscopic feature is a broad doublet peaked near 2500 cm^{-1} and 2850 cm^{-1}. The depletion at 3610 cm^{-1} arises from the subtraction of the O–H stretch of dehydrated BAS, and adsorbed water free O–H appears at 3700 cm^{-1}. The doublet is often assigned to Fermi resonance between red-shifted zeolitic bridging O–H stretch and O–H–O bend overtone.[16,17,20,34–36] While the character of the band can be debated, it is unambiguous that the doublet arises from the H-bonded zeolite BAS O–H stretch, as the same feature appears for a range of H-bond acceptors including dimethyl ether and THF which lack intramolecular O–H bonds.[16,34]

Therefore, in the hydrated zeolite system this feature is a signature of protonated zeolite BAS donating a H-bond to adsorbed H_2O.

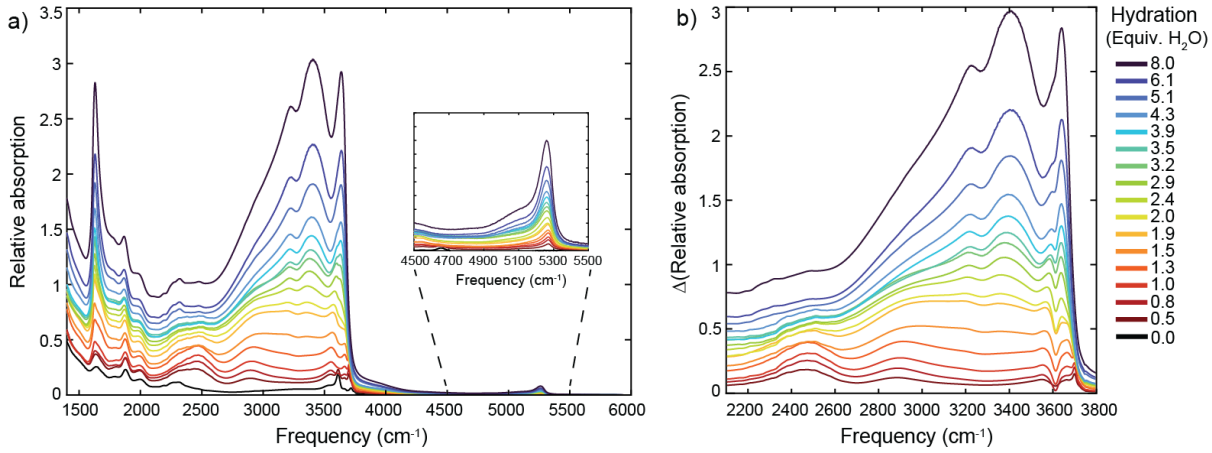

Figure 6.1. FTIR hydration series. (a) FTIR spectra of HZSM-5 from 0.5-8.0 equiv. H_2O/Al. Spectra were normalized to the water stretch-bend combination band at 5260 cm^{-1} (a, inset) and scaled to the measured hydration level. (b) Spectra after subtraction of the dehydrated spectrum.

The IR spectrum changes dramatically with increasing hydration, gaining intensity across the O-H stretch frequency range. At high hydration, 4-8 equiv. H_2O, a prominent set of features arise centered at high frequencies, with a broad tail extending across the observed spectral region. On the basis of 2D IR spectroscopy, AIMD simulations, and spectral calculations, in Chapter 5 we assigned the features at 3220 cm^{-1}, 3400 cm^{-1}, and 3640 cm^{-1} to the water stretch-bend Fermi resonance (FR), H-bonded O–H stretch, and free O–H stretch, respectively.[29] We assigned the broad continuum absorption as a signature of the hydrated proton, as a qualitatively similar feature is observed in the liquid[53,54] and protonated gas phase water clusters.[55] At lower frequencies, below 2100 cm^{-1}, water and proton features are obscured by zeolite framework modes (Fig. 6.1a).

While variations in the IR spectrum represent changes in the populations of water molecules experiencing different environments and protonation states, a quantitative analysis is complicated

by the broad and overlapping spectral signatures. Furthermore, due to non-Condon effects in vibrational O-H stretch spectroscopy,[56] the absorption cross-section is expected to vary for water molecules in different environments.

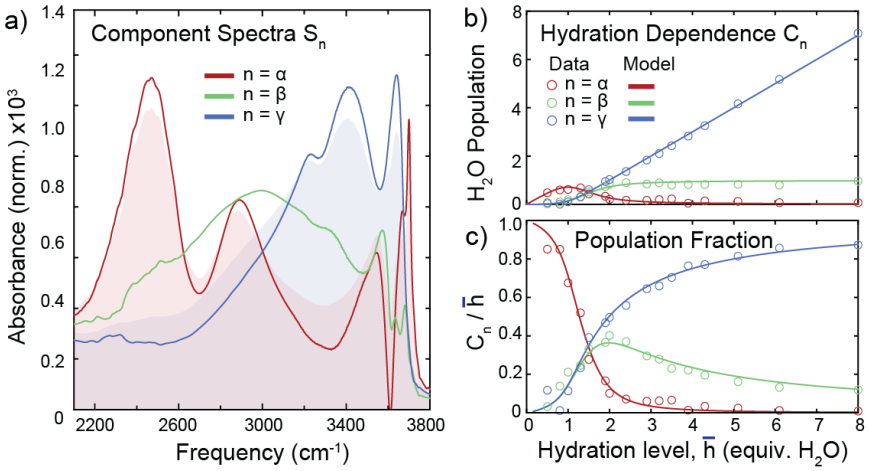

Figure 6.2. Spectral decomposition using constrained SVD analysis. (a) Area-normalized spectral components with hydration dependence presented as (b) distribution of all H_2O molecules among α, β, and γ environments and (c) the corresponding population fractions. The components correspond to water and protons in different environments. Components α and β report on the protonation state, with component α representing protonated zeolite BAS donating a H-bond and component β representing excess proton. Component γ is the signature of additional water molecules that are not strongly perturbed by the excess proton. Shaded curves in (a) are area-normalized spectra at 0.5 equiv. (red) and 8.0 equiv. (blue). Solid lines in (b-c) are the fit to a modified BET model described in the text.

We sought a quantitative relationship between changes in the IR spectrum to populations of water molecules in specific environments with distinct spectral signatures $S_n(\omega)$ and the hydration-dependent populations in those environments $C_n(\bar{h})$. To deconvolve the features, we assumed that the hydration series absorbance (after subtraction of the dehydrated spectrum) $A(\bar{h},\omega)$ can be expressed as a linear combination of three components labeled α, β, and γ.

$$A\left(\bar{h},\omega\right)=\sum_{n=\alpha,\beta,\gamma} C_n\left(\bar{h}\right)\varepsilon_n\, S_n\left(\omega\right) \tag{6.1}$$

Component spectra and amplitudes were computed using singular value decomposition (SVD) with reweighted components subject to maximum-entropy, positivity, and dissimilarity constraints,[40] described in Appendix 6A. The resulting area-normalized component spectra are displayed in Fig. 6.2a. To account for differences in absorption cross-sections between spectral components, the component populations were constrained to sum to the hydration level.

$$\bar{h}=\sum_{n} C_n\left(\bar{h}\right) \tag{6.2}$$

The relative absorption cross-sections – integrated over the frequency axis – are contained in the fitted values ε_n, yielding $\varepsilon_\beta/\varepsilon_\gamma=2.6$ and $\varepsilon_\alpha/\varepsilon_\gamma=0.96.$ Then, the hydration-dependent amplitude $C_n(\bar{h})$ of component *n* is proportional to the population of water molecules with spectrum $S_n(\omega)$ at mean hydration level $\bar{h},$ shown in Fig. 6.2b. Fig. 6.2c shows the populations of the three components as fractions of the total water adsorbed, $C_n/\bar{h}.$

Next, we assigned the components to their respective molecular environments using their spectral signatures. S_α strongly resembles the spectrum at low hydration, capturing the broad doublet, water free O–H stretch, and subtraction of the dry zeolite bridging O–H stretch. Therefore, we assigned component α to the zeolite-bound proton donating a H-bond to adsorbed water. S_γ strongly resembles the spectrum at high hydration, capturing the prominent water stretch-bend FR, water-water H-bond, and free O–H features. Therefore, we assigned component γ to the addition of water molecules to a water cluster. Comparing S_γ to the high-hydration spectrum, intensity is

missing in the broad low-frequency shoulder, which we previously assigned to the excess proton.[29] This broad feature is captured by S_β, which spans the entire spectral range in Fig. 6.1b.

The hydration-dependent populations of the components (Fig. 6.2b-c) are consistent with these assignments. At low hydration C_α accounts for the majority the adsorbed water molecules, but it falls off steeply accounting for only 10% of the population by 2 equiv. H_2O. This is the expected behavior of a protonated zeolite component, since the BAS becomes deprotonated at higher hydration.[17,21,23] C_β rises steeply from 0.5-2.0 equiv. H_2O, then plateaus at higher hydration. This is the expected behavior of an excess proton component, which grows in as the zeolite is deprotonated and reaches a constant value once deprotonation is complete. C_γ grows slowly at low hydration, then linearly with hydration above 2.0 equiv. H_2O, consistent with a component capturing the addition of water not strongly influenced by the excess proton.

Therefore, the spectral decomposition allows us to extract quantitative trends describing the changes in protonation state and water environments as a function of hydration level. However, the linear decomposition is a simplifying assumption which does not account for changes in the individual component spectra with hydration. This could be an issue if the excess proton spectrum varies dramatically between clusters of 2-8 H_2O, as is the case in cold gas-phase protonated water clusters.[55] We found that the reconstruction with three components has excellent agreement with the measurement, with coefficient of determination $R^2 > 0.99$ and without systematic errors indicative of spectral shifts. Most likely the excess proton spectrum varies somewhat with cluster size, but the linewidth of the feature is so broad at room temperature that those shifts are relatively small and can be neglected to a good approximation.

6.3.2. 2D IR spectroscopy with variable hydration

To further validate the spectral decomposition, we investigated the persistence of the doublet feature S_α by collecting 2D IR spectra as a function of hydration. 2D IR spectroscopy can more selectively probe this feature, without the use of spectral decomposition, by exciting the lower-frequency band at 2500 cm^{-1} where spectral overlap with other features is minimized.

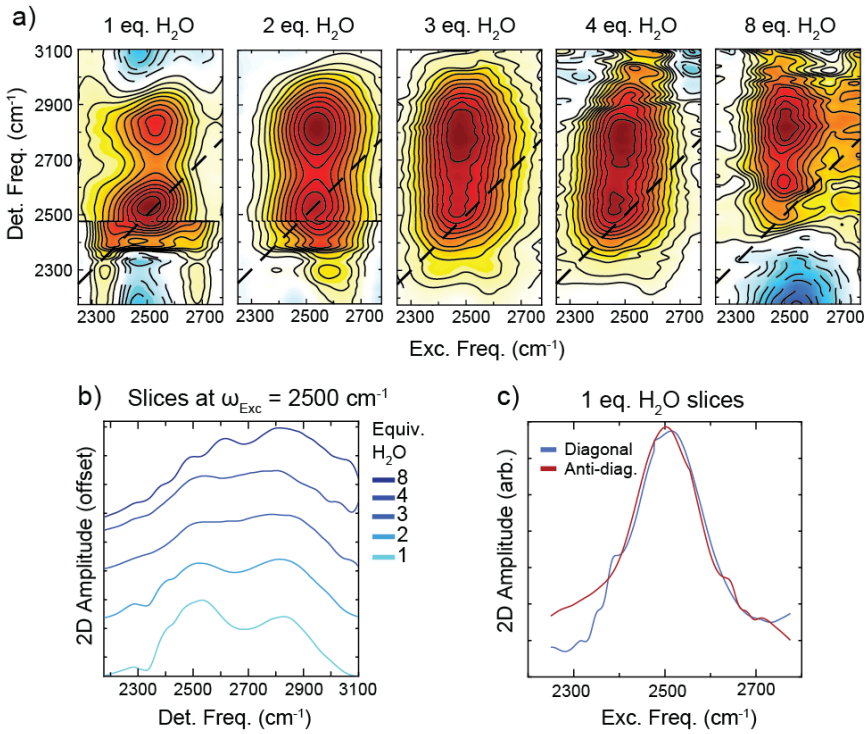

Figure 6.3. 2D IR hydration series. (a) 2D IR hydration series of HZSM-5 at 100 fs waiting time and perpendicular polarization, excited with pulses centered at 2500 cm^{-1}. Slices of the spectra at excitation frequency 2500 cm^{-1} are displayed in (b). The relative intensities of major features do not have a strong polarization dependence, as shown in Fig. S12; perpendicular (ZZYY) components are displayed to minimize scatter artifacts. Diagonal and anti-diagonal slices of the 1 equiv. H_2O spectrum are displayed in (c).

Fig. 6.3 shows the 2D IR hydration series with excitation centered at 2500 cm^{-1}, measured at 100 fs waiting time. At 1 equiv. H_2O, a diagonal feature at 2500 cm^{-1} is observed alongside a

prominent cross peak to the higher frequency band of the doublet at 2850 cm^{-1}. This is the 2D IR signature of the doublet corresponding to protonated zeolite BAS donating a H-bond. The lineshape displays homogeneous broadening, with equal diagonal and antidiagonal linewidths of 170 cm^{-1} FWHM in the isotropic spectrum (Fig. 6.3c). The transient absorption spectrum (Fig. 6.4) shows the feature is short-lived with a population relaxation timescale of ≤190 fs. Using that timescale, we estimate a lifetime-broadening of ~175 cm^{-1}, which accounts entirely for the 2D IR linewidth. The fast population relaxation is consistent with previous suggestions that the zeolitic H-bonded O–H stretch is strongly coupled to O–O stretching[16,35] and other low-frequency modes, providing a route for rapid non-radiative relaxation.

The predominant signature of a homogeneously rounded diagonal and cross peak persists from 1-4 equiv. H_2O in the early-time 2D IR spectrum. The relative intensity of the cross-peak appears to increase with hydration, which is likely caused by overlap with the growing excess proton continuum. These data confirm the presence of the doublet feature at 2-4 equiv. H_2O, as captured by the decomposition of the FTIR series.

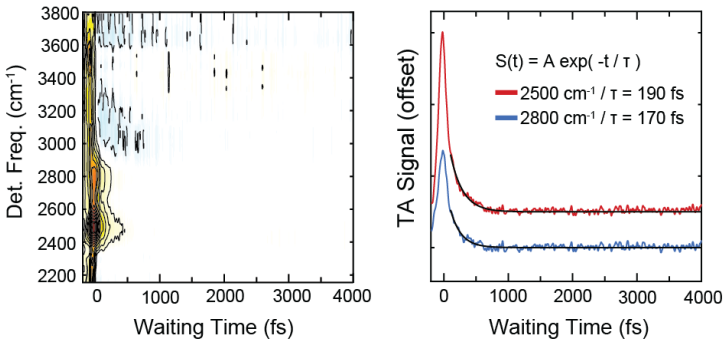

Figure 6.4. Isotropic transient absorption spectrum of 1.0 equiv. H_2O. Time traces at 2500 cm^{-1} and 2800 cm^{-1}, past 100 fs, were fit to a single exponential function with time constants ≤ 190 fs, shown in black.

The 2D IR spectrum of the low hydration doublet is unusual due to the lack of clear, high-intensity induced absorption resonances. While the assignment of the doublet to the protonated BAS donating a H-bond to water is firmly rooted in experimental evidence,[16,57] the 2D IR spectrum could provide further information about the assignment of the bands. The traditional explanation for the splitting has been stretch-bend Fermi resonance,[34–36,58] though that assignment does not explain the missing induced absorption intensity in the 2D IR spectrum.[59] Further 2D IR experiments and analysis of this feature are explored in Chapter 7 to address this topic. For now, we treat the doublet merely as a fingerprint of the protonated BAS state.

6.3.3. Modified BET model for hydration dependence

The spectra in Figs. 6.1-6.3 are ensemble measurements at macroscopic hydration level $\bar{h}$, which is an average over the distribution of microscopic hydration numbers $h = 0,1,2...$ Therefore, there are two possible explanations for the presence of the protonated BAS signature α at $\bar{h} = 2$: (a) both protonated BAS and excess proton are stable species in adsorbed water dimer clusters or (b) protonated BAS is only stable in the adsorbed water monomer, but there is a substantial fraction of clusters with $h = 1$ at mean hydration level $\bar{h} = 2.$ To distinguish between these possibilities, a model is needed which can relate the mean water adsorbed per site $\bar{h}$ to the distribution of adsorbed cluster sizes $\{\theta_h\}$, where θ_h is the fraction of sites occupied by clusters of size *h*.

To do so, we considered the preparation of our samples, where zeolites were equilibrated with water vapor in a sealed container at 150 ºC. We modeled this equilibrium using a modification of Brunauer-Emmett-Teller (BET) theory.[60] In this model, equilibrium is reached between water adsorbed on the zeolite sites and water in the gas phase at partial pressure P_{H2O} according to a system of equations for sequential adsorption events.

$$\theta_h + H_2O \rightleftharpoons \theta_{h+1},\ K_{h+1} \tag{6.3}$$

The adsorption of the first and second water molecule at BAS have distinct equilibrium constants K_1 and K_2, and all subsequent steps are described by $K_L = 1/P_0$, the equilibrium constant for liquefaction. P_0 is the saturation partial pressure and equilibrium constants are related to heats of adsorption q_h by $K_h = \exp\left(q_h / k_B T\right)$. In the typical BET model only K_1 is distinct, and otherwise our model is identical. This treatment of K_h for subsequent adsorption steps is a reasonable approximation, based on adsorption studies showing that the heat of adsorption decreases with hydration and varies gradually at hydration levels greater than 2.[61–63] Rearranging Eq. (6.3) yields a recursive formula for all fractional coverages in terms of $x = P_{H2O} / P_0$ and two BET constants $b_1 = K_1 / K_L$ and $b_2 = K_2 / K_L$.

$$\begin{aligned} \theta_1 &= b_1 \theta_0 x \\ \theta_h &= b_1 b_2 \theta_0 x^h,\ h > 1 \end{aligned} \tag{6.4}$$

The fractional coverages are constrained by the conservation of adsorption sites. In the context of our system, this constraint implies that adsorption sites are independent, and there is exactly one proton per site, which is reasonable because zeolite channels are highly hydrophobic in the absence of acid sites.[62]

$$1 = \sum_{h=0}^{\infty} \theta_h \tag{6.5}$$

Equations (6.4) and (6.5) were solved together to find a closed-form solution for θ_0, using the solution to the converging harmonic series $\sum_h x^h = 1/(1-x),\ x < 1$. Then, all θ_h were calculated according to eqn. (6.4).

$$\theta_0 = \frac{1-x}{(1-x)(1+b_1x)+b_1b_2x^2} \tag{6.6}$$

Next, the total number of adsorbed molecules per site $\bar{h}$ and number of adsorbed molecules per site in a cluster of size *h*, N_h, can be calculated as follows. To find the analytical solution we made use of $\sum_h hx^h = x/(1-x)^2,\ x<1.$

$$N_h = h\theta_h \tag{6.7}$$

$$\bar{h} = \sum_{h=0}^{\infty} h\theta_h = \theta_0\left(b_1x(1-b_2) + \frac{b_1b_2x}{(1-x)^2}\right) \tag{6.8}$$

By treating *x* as an implicit variable – which was not measured during sample preparation – we then expressed θ_h, from Eq. (6.4), as a function of $\bar{h}$, from Eq. (6.8), subject to two parameters b_1 and b_2. Finally, we related the derived expressions for the distribution of adsorbed molecules in clusters of size *h* to the populations, or number of molecules, displaying spectral signatures α, β, and γ (representing protonated BAS, excess proton, and additional adsorbed water molecules respectively). We assumed that S_α arises only from singly-hydrated sites, therefore C_α is given by the fraction of sites with $h=1$.

$$C_\alpha = \theta_1 \tag{6.9}$$

Since a hydrated site can either be protonated with signature S_α or deprotonated with signature S_β, C_β is the fraction of sites hydrated by two or more molecules.

$$C_\beta = \sum_{h\geq 2}\theta_h \tag{6.10}$$

Then, in clusters of size two or more one water molecule is accounted for by C_β and the rest are accounted for by C_γ. The number of subsequent water molecules is given by the total molecules adsorbed in clusters of two or more subtracting the first molecule in those clusters.

$$C_\gamma = \sum_{h\geq 2} (h-1)\,\theta_h \tag{6.11}$$

Equations (6.9)-(6.11) comprise a model of $C_n(\bar{h})$ with fit parameters b_1 and b_2. Fitting that model to the data yielded $b_1 = 180$ and $b_2 = 7$ with the resulting curves plotted in Fig. 2b-c and coefficient of determination $R^2 > 0.99$. Using the preparation temperature of 150 ºC, this corresponds to relative heats of adsorption for the first two water molecules $\Delta q_1 = q_1 - q_L = 4.4$ kcal/mol and $\Delta q_2 = 1.6$ kcal/mol. Using the heat of liquefaction,[64] $q_L = 9.1$ kcal/mol at 150 ºC results in $q_1 = 13.5$ kcal/mol and $q_2 = 10.7$ kcal/mol, both falling within the range of previous measurements.[32,61–63]

Setting $b_2 = 1$ returns the model to the typical BET theory, where only the first adsorption has a distinct equilibrium constant. Under that assumption, the data is well-fit except for the region near $\bar{h} = 2$, where the model then under-estimates C_β (Fig. 6.5). Increasing $b_2 > 1$ accounts for an additional stabilization energy for adsorption of the second water molecule, attributed to the stabilization from proton dissociation which we estimate as $\Delta q_2 = 1.6$ kcal/mol.

Therefore, the hydration-dependent IR spectra of HZSM-5 can be captured quantitatively by treating the proton as dissociated from the BAS when 2 or more molecules are adsorbed; the presence of protonated BAS states in adsorbed water dimers is not necessary. The persistence of

the signature C_α until ~4 equiv. H_2O is accounted for by the distribution of microscopic hydration environments, which includes a fraction of singly-hydrated sites at higher hydration levels.

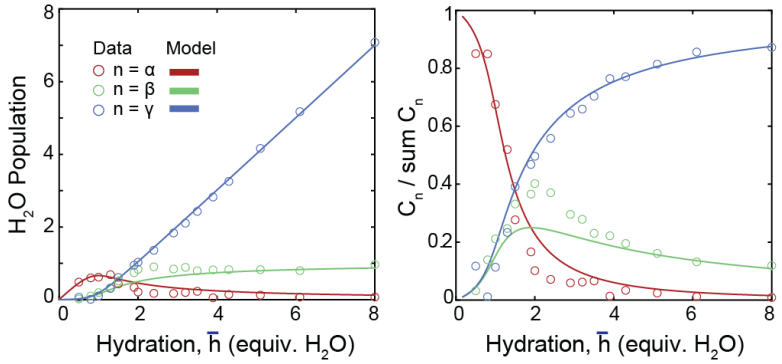

Figure 6.5. BET model with a single fit parameter b_1 = 20 (b_2 = 1) plotted against the data reported in Fig. 6.2.

6.3.4. AIMD simulations of 1–8 H_2O molecules at the Brønsted acid site

To understand the spectroscopic components at atomistic detail and to further investigate the evolution of the protonation state as a function of adsorbed water cluster size, AIMD simulations were performed with 1-8 H_2O molecules equilibrated in HZSM-5 at 298 K. Six independent trajectories were analyzed, revealing connections between calculated atomic positions, charge location and delocalization, and vibrational spectra.

The H-bond network is relatively simple at lower hydration numbers (1-3 H_2O) and becomes complicated with increasing cluster size. Beyond 2 H_2O molecules, numerous potential energy minimum structures can be located through geometry optimization at 0 K, but only a few are statistically meaningful at room temperature. The most representative configurations of protonated water clusters at the BAS are shown in Fig. 6.6.

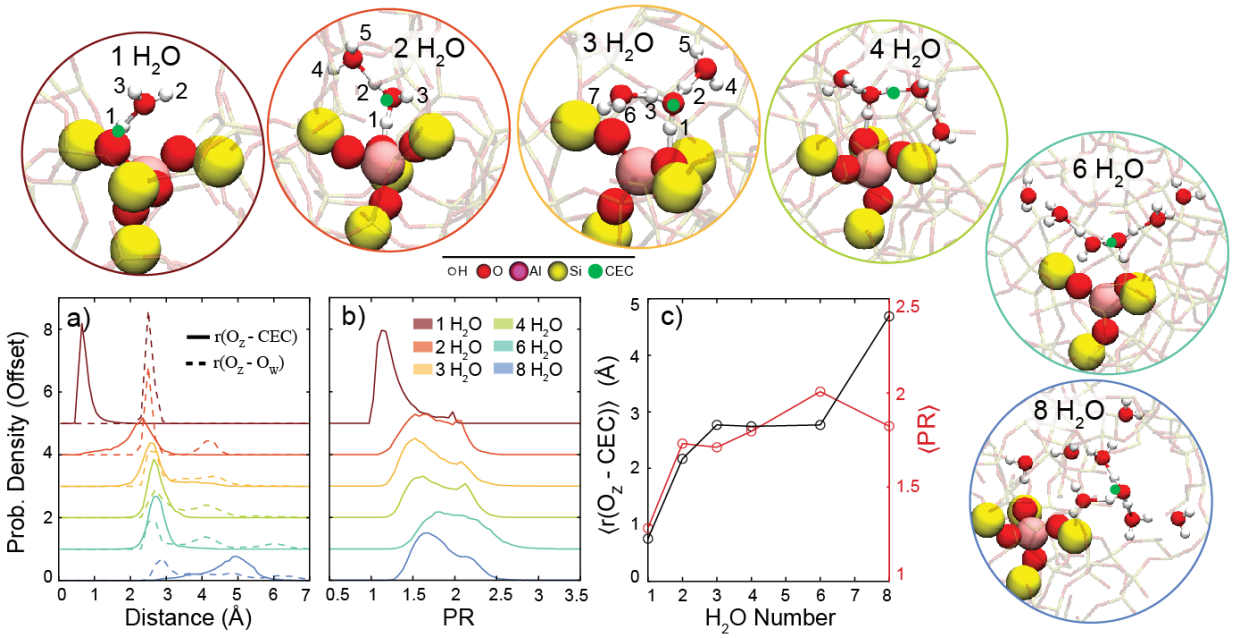

Figure 6.6. AIMD trajectory statistics of CEC position and delocalization. (a) The distribution of distances between the zeolite oxygen atom (O_Z) and center of excess charge (CEC, solid lines), overlaid with the distribution of water oxygen (O_W) atoms (dashed lines). (b) Proton charge delocalization, represented by the distribution of participation ratios (PR).[69,70] Probability distributions are offset by 1 unit for clarity. (c) Expectation values of r(O_Z-CEC) and PR as a function of water cluster size. Representative trajectory snapshots from AIMD simulations of 1-8 H_2O molecules in HZSM-5 are displayed above and labeled by the number of H_2O molecules. The CEC, which represents the excess proton charge location, is displayed in each configuration as a green dot. Hydrogen atoms in snapshots of 1-3 H_2O molecules are numbered for reference.

H-bond formation was observed between water molecules and one or more oxygen atoms in the BAS (the 4 nearest-neighbor oxygens to Al), which we will refer to as interfacial H-bonds. H-bonding was not observed to any other framework oxygen atoms. At an equilibrated state, the hydrogen bond configuration within the protonated water cluster is relatively stable, and at least one interfacial H-bond remained intact during each simulation. When two or more interfacial

H-bonds were present, the bond with shortest O-O distance was identified and the participating zeolite and water oxygens labeled O_Z and O_{W1}.

The distributions of $O_Z - O_W$ distances are displayed as dashed lines in Fig. 6.6a. The most probable distance from O_Z to the first water oxygen is 2.5 Å when one water is present and increases with cluster size to 2.9 Å in the 8-water cluster. The second and third adsorbed water molecules form H-bonds to the first with $O_Z - O_W$ distances of ~4 Å. In larger clusters the constrained geometry of the zeolite channels influences the H-bonding network, causing some branching into the pores and not necessarily maximizing water-water H-bonds. For example, in the representative snapshot for 6 H_2O, the only triply-coordinated water molecules are coordinated to a zeolite oxygen, while the 8-water cluster supports triple-coordination to three other water molecules.

The charge distribution associated with the excess proton and its hydration dependence was quantified using the rCEC approach adopted from Li *et* al.[51,52] Based on the multi-state empirical valence bond (MS-EVB) method developed by the Voth group,[65–67] r^{CEC} is a collective variable which describes the location of the center of excess charge (CEC) associated with the net positive charge defect from the excess proton. In this method, the adiabatic ground state of a configuration as a function of the nuclear coordinates is expressed in a basis of diabatic states determined by the H-bonding topology.

$$\left|\psi^{adi}\right\rangle = \sum_i c_i \left|\psi_i^{dia}\right\rangle \tag{6.12}$$

Each diabatic state represents a localized excess charge near a single oxygen atom, defined by its center-of-charge (COC) position $\mathbf{r}^{\mathrm{COC}}$. For a molecular cluster with h H_2O molecules at the

BAS there are h+4 basis states, one for each H_2O oxygen atom plus the four zeolitic oxygen atoms bonded to Al. The squared expansion coefficient c_i^2 represents the distribution of proton excess charge in the i^{th} diabatic state. In the rCEC method, the weights of adjacent diabatic states are parameterized based on the interatomic O-H-O distances using constrained DFT calculations.[68] The CEC position $\mathbf{r}^{\mathrm{CEC}}$ is the weighted average of the COC positions.

$$\mathrm{r}^{CEC} = \sum_i c_i^2 \mathrm{r}_i^{COC} \tag{6.13}$$

Figure 6.6a displays trajectory statistics of the CEC position with respect to O_Z, $r(O_Z - CEC)$ next to the $r(O_Z - O_W)$ distributions. The distribution of $r(O_Z - CEC)$ shifts dramatically from 1 H_2O, where the CEC is much closer to O_Z, to 2 H_2O where the CEC distribution overlaps with O_W. From 2 to 4 H_2O molecules the center of the $r(O_Z - CEC)$ distribution displays a much smaller positive shift, while the tails have different behavior. The distribution for 2 H_2O has a tail to smaller distances, indicating charge sharing between O_{W1} and O_Z. While there is little change in the CEC position from 3 to 6 H_2O, there is an increase by about 2 Å from 6 to 8 H_2O.

In the 8 H_2O cluster the proton charge is statistically located on the periphery of the cluster, shared between water molecules that are not coordinated to a zeolitic oxygen. This shifting of the excess proton position away from the deprotonated BAS at high hydration numbers was also captured in metadynamics simulations by Grifoni *et* al.[23] This observation can be neither verified nor disputed on the basis of FTIR spectroscopy experiments, as we do not resolve any changes in the measured excess proton IR spectrum from 6 to 8 equiv. H_2O.

The delocalization of the protonic charge defect was quantified using the participation ratio (*PR*) at each hydration number. The *PR*, shown in Fig. 6.6b, is a measure of the number of diabatic states that contribute effectively to the state of the excess proton.[69,70]

$$PR = \left(\sum_i c_i^4 \right)^{-1} \tag{6.14}$$

The participation ratio ranges from $PR = 1$ for a localized state to *N* for full delocalization over *N* basis states. The participation ratio distribution displays a large shift from 1 H_2O to 2 H_2O, and relatively minor changes at higher hydration. At 1 H_2O, the excess charge is largely localized in a single state (mean value $PR = 1.2$ corresponds to approximately $c_1^2 = 0.9$ and $c_2^2 = 0.1$), with a tail to larger values indicating a small fraction of configurations where there is increased charge sharing with the adsorbed H_2O molecule. For 2-8 H_2O, the *PR* assumes a roughly bimodal distribution peaked near *PR* = 1.5 & 2. This indicates that the protonic charge is largely shared unequally between two states. Interestingly, while the number of diabatic states grows linearly with the number of water molecules, the *PR* does not. The *PR* never approaches a value of 3, indicating that most of the protonic charge remains relatively localized along a single O-H-O axis.

6.3.5. Hydrogen atomic positions

In addition to the charge distribution, the protonation state is related to the atomic positions of hydrogen atoms. To investigate the proton dissociation from BAS to water cluster, we consider the statistics of hydrogen atom locations along selected O-H-O axes for 1-3 H_2O molecules. Trajectory statistics were used to calculate the potential of mean force (PMF) between O_Z and the adsorbed water oxygen O_{W1} as a function of $\delta r(O_Z - H - O_{W1}) = r(O_Z - H) - r(O_{W1} - H)$, shown in Fig. 6.7a. The PMF minimum shifts from $\delta r = -0.5$ Å at 1 H_2O to +0.3 Å at 2 H_2O and +0.5 Å

at 3 H_2O, showing that the most probable proton position switches from the O_Z side of the axis to the O_{W1} side between 1 and 2 H_2O, and moves even closer to O_{W1} at 3 H_2O.

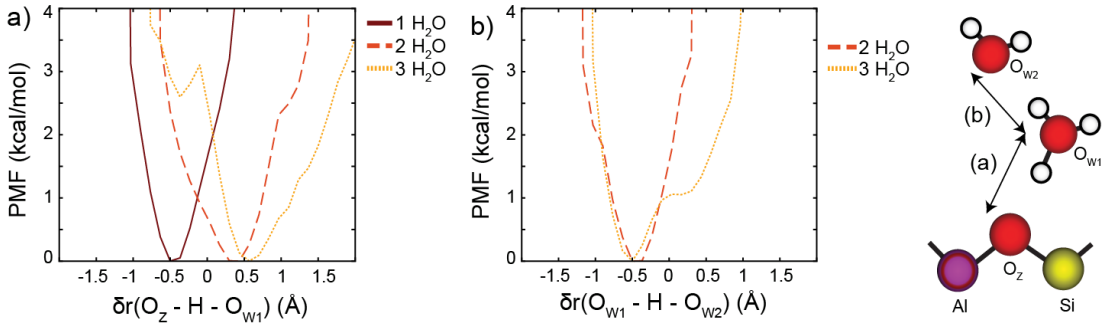

Figure 6.7. Potential of mean force (PMF) at 298 K across (a) the O_Z – H – O_{W1} axis between the zeolite oxygen and nearest water oxygen and (b) the O_{W1}–H–O_{W2} axis between the first two water oxygen atoms. The hydrogen atom position is described by the difference between O-H distances, $\delta r(O_A–H–O_B) = r(O_A–H) – r(O_B–H)$. The cartoon on the right depicts an adsorbed water dimer labeling the O–H–O axes considered in (a-b).

Proton sharing between water molecules is visualized by the PMF along the $O_{W1} - H - O_{W2}$ axis (Fig. 6.7b), where O_{W2} is defined as the water oxygen closest to O_{W1} at a given trajectory snapshot. When 2 H_2O molecules are present, the PMF across the $O_{W1} - H - O_{W2}$ axis favors O_{W1} with a minimum at $\delta r = –0.5$ Å. At 3 H_2O, the PMF retains that global minimum and gains an additional local minimum at $\delta r = +0.3$ Å. The shape of this PMF is a result of water trimer configurations such as the one pictured in Fig. 4 where the first H_2O molecule is H-bonded to two other water molecules, and thus has two potential partners for proton sharing. When the excess proton is not shared with O_{W2}, then the hydrogen atom along that axis is bound to O_{W1} with PMF minimum at $\delta r = –0.5$ Å, while states with asymmetric proton sharing between O_{W1} and O_{W2} accounts for the additional local minimum at $\delta r = +0.3$ Å. Together, the results in Fig. 6.7 show

that atomic hydrogen positions follow a similar trend as the charge distribution, consistent with the assignment of a shared proton in clusters of 2-3 H_2O molecules and proton sharing between O_Z and O_W in the adsorbed dimer.

6.3.6. Spectral analysis

To draw connections between hydration, molecular structure, and vibrational spectra, both harmonic normal mode spectra and anharmonic power spectra were calculated. We found that O-H stretch normal modes in harmonic spectra of optimized clusters fell broadly in the expected frequency ranges, but that treatment was limited for describing the highly anharmonic vibrations of water and protons.[54] Instead, we considered power spectra of individual hydrogen atoms in clusters of 1-3 H_2O, which each correspond to the motions of the selected atom. Power spectra are shown in Fig. 6.8 following the hydrogen atom numbering in Fig. 6.6. This approach better reflects the anharmonicity of the vibrations, and relates calculated frequencies to molecular environments with atomic specificity.

The power spectra in Fig. 6.8 display either a broad proton feature spanning ~2000-3000 cm^{-1} or narrow free O-H features >3500 cm^{-1}. The proton feature is most prominent in the spectra of H_1 (1 H_2O), H_1 & H_2 (2 H_2O), and H_2 & H_3 (3 H_2O). The evolution of that feature correlates well to the movement of the CEC and atomic hydrogen positions in Figs. 6.4-6.5. The spectra of H_1 & H_7 in the 3 H_2O cluster – both located along a $O_Z - H - O_W$ axis – display some spectral density between ~3000-3500 cm^{-1}, reflecting interfacial H-bond formation. Broadening of the free O-H features and growth in the H-bonded O-H region with increasing hydration agrees qualitatively with trends in the experimental IR spectrum.

While power spectra show reasonable agreement with the frequencies and linewidths of experimental excess proton and free O-H features, they notably do not capture the broad doublet feature at 1 H_2O. This may be a result of relatively large-amplitude motions of H_1 (1 H_2O) combined with the ~20 ps trajectory length which is feasible for AIMD simulations. As a result, modulations in the broad H_1 feature are on the order of the noise level, which could be improved with longer simulation time. Therefore, these spectral calculations are useful for identifying hydrogen atoms that carry some protonic charge – leading to broad low-frequency spectra – but not for discriminating between bound and excess proton states.

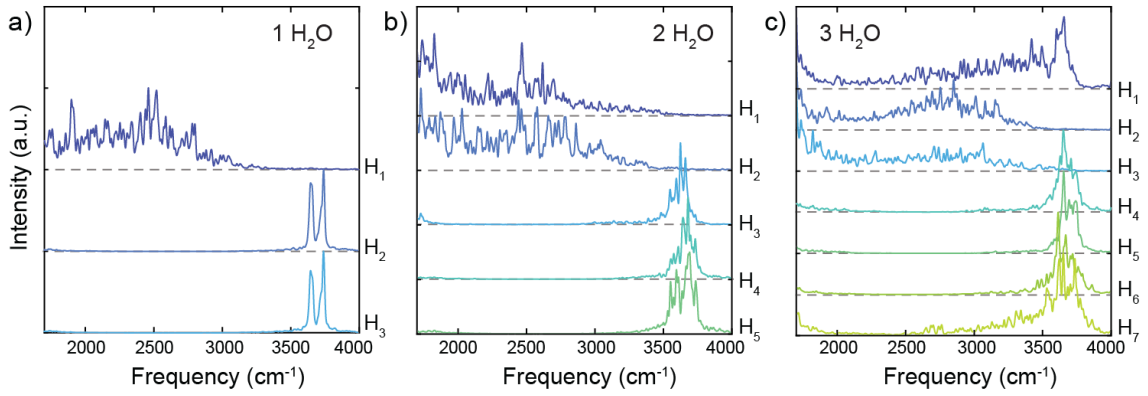

Figure 6.8: Power spectra of individual hydrogen atoms in optimized clusters of (a) 1 H_2O, (b) 2 H_2O and (c) 3 H_2O. Hydrogen atoms are labeled by number, corresponding to the labels in Fig. 4. Spectra are offset for clarity; dashed lines are baselines.

6.3.7. Protonation state and H-bonding network

Taken together, the trends in the AIMD simulations support the model of hydration-dependent protonation state that was used to capture the experimental IR spectra. The proton can be described as zeolite-bound in the presence of one H_2O molecule, and shared excess proton when two or more H_2O molecules are present. The clear transition between these two states can be observed in the

CEC position, *PR*, and PMF minimum between O_Z and O_{W1}, and is consistent with trends in the power spectra of hydrogen atoms.

The AIMD simulations reveal further atomistic details and connections between the protonation state and H-bonding network. The *PR* distribution between ~1.5-2 for clusters of 2-8 water molecules suggests delocalization over 2 oxygen atoms, leading to the language of a shared proton. While the water dimer is described well by this picture, the proton can be shared either between O_Z and O_{W1} or O_{W1} and O_{W2}, with roughly equal probability. This is distinct from larger clusters, where the proton is more prominently shared between two water molecules, as seen in the shift in $r(O_Z - CEC)$, PMF, and hydrogen power spectra. This distinction may account for some of the debate over the description of the water dimer.

Furthermore, the simulation results suggest that the location of the excess proton is strongly influenced by the connectivity of the H-bonding network, which extends to the zeolitic oxygen atoms. The trends in H-bond connectivity and CEC location suggest that the proton charge is located preferentially near the most highly-coordinated water molecules. For the small clusters present in confined HZSM-5 pores, the largest coordination number is often 3, and a triply-coordinated water molecule is an important structural motif for stabilizing the proton. The adsorbed water trimer is the smallest cluster where a water molecule is triply-coordinated, and also the smallest cluster where the proton is shared primarily between water molecules and not with O_Z. At higher hydration, the excess proton charge defect position r^{CEC} moves further from the deprotonated BAS only when water molecules triply-coordinated to three O_W become available in the water octamer. Therefore, we suggest a simple scheme for locating the most probable proton location in adsorbed water clusters: (1) in the adsorbed water monomer, the zeolite BAS is

protonated, (2) in the adsorbed water dimer the proton is shared either between O_Z and O_{W1} or O_{W1} and O_{W2}, and (3) at higher hydration the proton is shared preferentially between the most highly-coordinated water molecules.

6.4. Conclusions

We have presented experimental IR spectroscopic evidence identifying the crossover point from protonated zeolite BAS to shared proton. Using a spectral decomposition, we extracted quantitative information from the hydration series of HZSM-5 zeolite prepared at controlled hydration levels. At 1 H_2O, the proton is stabilized on the zeolite BAS. From 2-8 H_2O, the proton is instead shared between two oxygen atoms, placing the critical water number at 2 H_2O. These findings were supported by a series of AIMD simulations with varying H_2O number interacting with the zeolite BAS. An analysis of excess charge position, atomic potential of mean force, and local mode power spectra further revealed that the excess protonic charge is shared asymmetrically between two oxygen atoms. The case of the water dimer is distinct because significant sharing occurs between water and the deprotonated BAS, while proton sharing in larger clusters occurs primarily between two water molecules. H-bonding connectivity is important for determining protonation state and location, as the excess proton preferentially occupies locations resembling a triply-coordinated hydronium ion. Taken together, these experimental and theoretical results provide a consistent description of the protonation state of the HZSM-5 BAS and its evolution across the hydration range of 1-8 H_2O per acid site.

6.5. References

(1) Davis, M. E. Zeolite-Based Catalysts for Chemicals Synthesis. *Microporous Mesoporous Mater.* **1998**, *21* (4–6), 173–182. https://doi.org/10.1016/S1387-1811(98)00007-9.

(2) Tanabe, K.; Hölderich, W. F. Industrial Application of Solid Acid-Base Catalysts. *Appl. Catal. A Gen.* **1999**, *181* (2), 399–434. https://doi.org/10.1016/S0926-860X(98)00397-4.

(3) Corma, A. State of the Art and Future Challenges of Zeolites as Catalysts. *J. Catal.* **2003**, *216* (1–2), 298–312. https://doi.org/10.1016/S0021-9517(02)00132-X.

(4) Martínez, C.; Corma, A. Inorganic Molecular Sieves: Preparation, Modification and Industrial Application in Catalytic Processes. *Coord. Chem. Rev.* **2011**, *255* (13–14), 1558–1580. https://doi.org/10.1016/j.ccr.2011.03.014.

(5) IPCC; 2022. *Climate Change 2022: Mitigation of Climate Change. Contribution of Working Group III to the Sixth Assessment Report of the Intergovernmental Panel on Climate Change*; Shukla, P. R., Skea, J., Slade, R., Al Khourdajie, A., Diemen, R. van, McCollum, D., Pathak, M., Some, S., Vyas, P., Fradera, R., Belkacemi, M., Hasija, A., Lisboa, G., Luz, S., Malley, J., Eds.; Cambridge University Press: Cambridge, UK and New York, NY, USA, 2022. https://doi.org/10.1017/9781009157926.

(6) Taarning, E.; Osmundsen, C. M.; Yang, X.; Voss, B.; Andersen, S. I.; Christensen, C. H. Zeolite-Catalyzed Biomass Conversion to Fuels and Chemicals. *Energy Environ. Sci.* **2011**, *4*, 793–804. https://doi.org/10.1039/c004518g.

(7) Mardiana, S.; Azhari, N. J.; Ilmi, T.; Kadja, G. T. M. Hierarchical Zeolite for Biomass Conversion to Biofuel: A Review. *Fuel* **2022**, *309*, 122119. https://doi.org/10.1016/J.FUEL.2021.122119.

(8) Ennaert, T.; Van Aelst, J.; Dijkmans, J.; De Clercq, R.; Schutyser, W.; Dusselier, M.; Verboekend, D.; Sels, B. F. Potential and Challenges of Zeolite Chemistry in the Catalytic Conversion of Biomass. *Chem. Soc. Rev.* **2016**, *45* (3), 584–611. https://doi.org/10.1039/c5cs00859j.

(9) Stanciakova, K.; Weckhuysen, B. M. Water–Active Site Interactions in Zeolites and Their Relevance in Catalysis. *Trends Chem.* **2021**, *3* (6), 456–468. https://doi.org/10.1016/J.TRECHM.2021.03.004.

(10) Mei, D.; Lercher, J. A. Mechanistic Insights into Aqueous Phase Propanol Dehydration in H-ZSM-5 Zeolite. *AIChE J.* **2017**, *63* (1), 172–184. https://doi.org/10.1002/aic.15517.

(11) Mei, D.; Lercher, J. A. Effects of Local Water Concentrations on Cyclohexanol Dehydration in H-BEA Zeolites. *J. Phys. Chem. C* **2019**, *123* (41), 25255–25266.

https://doi.org/10.1021/acs.jpcc.9b07738.

(12) Zhi, Y.; Shi, H.; Mu, L.; Liu, Y.; Mei, D.; Camaioni, D. M.; Lercher, J. A. Dehydration Pathways of 1-Propanol on HZSM-5 in the Presence and Absence of Water. *J. Am. Chem. Soc.* **2015**, *137* (50), 15781–15794. https://doi.org/10.1021/jacs.5b09107.

(13) Wang, Q.; Fan, H.; Wu, S.; Zhang, Z.; Zhang, P.; Han, B. Water as an Additive to Enhance the Ring Opening of Naphthalene. *Green Chem.* **2012**, *14* (4), 1152–1158. https://doi.org/10.1039/c2gc16554f.

(14) Chen, K.; Damron, J.; Pearson, C.; Resasco, D.; Zhang, L.; White, J. L. Zeolite Catalysis: Water Can Dramatically Increase or Suppress Alkane C-H Bond Activation. *ACS Catal.* **2014**, *4* (9), 3039–3044. https://doi.org/10.1021/cs500858d.

(15) Li, G.; Wang, B.; Resasco, D. E. Water-Mediated Heterogeneously Catalyzed Reactions. *ACS Catal.* **2020**, *10* (2), 1294–1309. https://doi.org/10.1021/acscatal.9b04637.

(16) Zecchina, A.; Bordiga, S.; Spoto, G.; Scarano, D.; Spanò, G.; Geobaldo, F. IR Spectroscopy of Neutral and Ionic Hydrogen-Bonded Complexes Formed upon Interaction of CH3OH, C2H5OH, (CH3)2O, (C2H5)2O and C4H8O with H-Y, H-ZSM-5 and H-Mordenite: Comparison with Analogous Adducts Formed on the H-Nafion Superacidic Membrane. *J. Chem. Soc. - Faraday Trans.* **1996**, *92* (23), 4863–4875. https://doi.org/10.1039/ft9969204863.

(17) Krossner, M.; Sauer, J. Interaction of Water with Brønsted Acidic Sites of Zeolite Catalysts. Ab Initio Study of 1:1 and 2:1 Surface Complexes. *J. Phys. Chem.* **1996**, *100* (15), 6199–6211. https://doi.org/10.1021/jp952775d.

(18) Zygmunt, S. A.; Curtiss, L. A.; Iton, L. E.; Erhardt, M. K. Computational Studies of Water Adsorption in the Zeolite H-ZSM-5. *J. Phys. Chem.* **1996**, *100*, 6663–6671.

(19) Olson, D. H.; Zygmunt, S. A.; Erhardt, M. K.; Curtiss, L. A.; Iton, L. E. Evidence for Dimeric and Tetrameric Water Clusters in HZSM-5. *Zeolites* **1997**, *18*, 347–349. https://doi.org/10.1016/S0144-2449(97)00024-9.

(20) Vjunov, A.; Wang, M.; Govind, N.; Huthwelker, T.; Shi, H.; Mei, D.; Fulton, J. L.; Lercher, J. A. Tracking the Chemical Transformations at the Brønsted Acid Site upon Water-Induced Deprotonation in a Zeolite Pore. *Chem. Mater.* **2017**, *29* (21), 9030–9042. https://doi.org/10.1021/acs.chemmater.7b02133.

(21) Wang, M.; Jaegers, N. R.; Lee, M. S.; Wan, C.; Hu, J. Z.; Shi, H.; Mei, D.; Burton, S. D.; Camaioni, D. M.; Gutiérrez, O. Y.; Glezakou, V. A.; Rousseau, R.; Wang, Y.; Lercher, J. A. Genesis and Stability of Hydronium Ions in Zeolite Channels. *J. Am. Chem. Soc.* **2019**, *141* (8), 3444–3455. https://doi.org/10.1021/jacs.8b07969.

(22) Liu, P.; Mei, D. Identifying Free Energy Landscapes of Proton-Transfer Processes between Brønsted Acid Sites and Water Clusters Inside the Zeolite Pores. *J. Phys. Chem. C* **2020**, *124* (41), 22568–22576. https://doi.org/10.1021/acs.jpcc.0c07033.

(23) Grifoni, E.; Piccini, G. M.; Lercher, J. A.; Glezakou, V. A.; Rousseau, R.; Parrinello, M. Confinement Effects and Acid Strength in Zeolites. *Nat. Commun.* **2021**, *12*. https://doi.org/10.1038/s41467-021-22936-0.

(24) Kawai, Y.; Yamaguchi, S.; Okada, Y.; Takeuchi, K.; Yamauchi, Y.; Ozawa, S.; Nakai, H. Reactions of Protonated Water Clusters H+(H2O) n (n = 1-6) with Dimethylsulfoxide in a Guided Ion Beam Apparatus. *Chem. Phys. Lett.* **2003**, *377* (1–2), 69–73. https://doi.org/10.1016/S0009-2614(03)01095-9.

(25) Kletnieks, P. W.; Ehresmann, J. O.; Nicholas, J. B.; Haw, J. F. Adsorbate Clustering and Proton Transfer in Zeolites: NMR Spectroscopy and Theory. *ChemPhysChem* **2006**, *7* (1), 114–116. https://doi.org/10.1002/CPHC.200500313.

(26) Cheng, H. P. Water Clusters: Fascinating Hydrogen-Bonding Networks, Solvation Shell Structures, and Proton Motion. *J. Phys. Chem. A* **1998**, *102* (31), 6201–6204. https://doi.org/10.1021/jp981433f.

(27) Wròblewski, T.; Ziemczonek, L.; Karwasz, G. P. Proton Transfer Reactions for Ionized Water Clusters. *Czechoslov. J. Phys.* **2004**, *54* (SUPPL. 3), 747–752. https://doi.org/10.1007/BF03166481.

(28) Zygmunt, S. A.; Curtiss, L. A.; Iton, L. E. Protonation of an H2O Dimer by a Zeolitic Brønsted Acid Site. *J. Phys. Chem. B* **2001**, *105* (15), 3034–3038. https://doi.org/10.1021/jp003469p.

(29) Hack, J. H.; Dombrowski, J. P.; Ma, X.; Chen, Y.; Lewis, N. H. C.; Carpenter, W. B.; Li, C.; Voth, G. A.; Kung, H. H.; Tokmakoff, A. Structural Characterization of Protonated Water Clusters Confined in HZSM-5 Zeolites. *J. Am. Chem. Soc.* **2021**, *143* (27), 10203–10213. https://doi.org/10.1021/jacs.1c03205.

(30) Eaves, J. D.; Tokmakoff, A.; Geissler, P. L. Electric Field Fluctuations Drive Vibrational Dephasing in Water. *J. Phys. Chem. A* **2005**, *109* (42), 9424–9436. https://doi.org/10.1021/jp051364m.

(31) Hamm, P.; Zanni, M. *Concepts and Methods of 2D Infrared Spectroscopy*; Cambridge University Press: Cambridge, UK and New York, NY, USA, 2011.

(32) Ison, A.; Gorte, R. J. The Adsorption of Methanol and Water on H-ZSM-5. *J. Catal.* **1984**, *89* (1), 150–158. https://doi.org/10.1016/0021-9517(84)90289-6.

(33) Jentys, A.; Warecka, G.; Derewinski, M.; Lercher, J. A. Adsorption of Water on ZSM5 Zeolites. *J. Phys. Chem.* **1989**, *93* (12), 4837–4843. https://doi.org/10.1021/j100349a032.

(34) Pelmenschikov, A. G.; van Wolput, J. H. M. C.; Jaenchen, J.; van Santen, R. A. (A,B,C) Triplet of Infrared OH Bands of Zeolitic H-Complexes. *J. Phys. Chem.* **1995**, *99* (11), 3612–3617. https://doi.org/10.1021/j100011a031.

(35) Pelmenschikov, A. G.; Van Santen, R. A. Water Adsorption on Zeolites: Ab-Initio Interpretation of IR Data. *J. Phys. Chem.* **1993**, *97* (41), 10678–10680. https://doi.org/10.1021/j100143a025.

(36) Mihaleva, V. V.; Van Santen, R. A.; Jansen, A. P. J. Quantum Chemical Calculation of Infrared Spectra of Acidic Groups in Chabazite in the Presence of Water. *J. Chem. Phys.* **2004**, *120* (19), 9212–9221. https://doi.org/10.1063/1.1709896.

(37) Bonn, M.; Van Santen, R. A.; Lercher, J. A.; Kleyn, A. W.; Bakker, H. J. Picosecond Infrared Activation of Methanol in Acid Zeolites. *Chem. Phys. Lett.* **1997**, *278* (4–6), 213–219. https://doi.org/10.1016/S0009-2614(97)00982-2.

(38) Bonn, M.; Brugmans, M. J. P.; Kleyn, A. W.; Van Santen, R. A. Fast Energy Delocalization upon Vibrational Relaxation of a Deuterated Zeolite Surface Hydroxyl. *J. Chem. Phys.* **1995**, *102* (5), 2181–2186. https://doi.org/10.1063/1.468740.

(39) Yamada, S. A.; Shin, J. Y.; Thompson, W. H.; Fayer, M. D. Water Dynamics in Nanoporous Silica: Ultrafast Vibrational Spectroscopy and Molecular Dynamics Simulations. *J. Phys. Chem. C* **2019**, *123* (9), 5790–5803. https://doi.org/10.1021/acs.jpcc.9b00593.

(40) Widjaja, E.; Garland, M. Pure Component Spectral Reconstruction from Mixture Data Using SVD, Global Entropy Minimization, and Simulated Annealing. Numerical Investigations of Admissible Objective Functions Using a Synthetic 7-Species Data Set. *J. Comput. Chem.* **2002**, *23*, 911–919. https://doi.org/10.1002/jcc.10080.

(41) Carpenter, W. B.; Fournier, J. A.; Biswas, R.; Voth, G. A.; Tokmakoff, A. Delocalization and Stretch-Bend Mixing of the HOH Bend in Liquid Water. *J. Chem. Phys.* **2017**, *147* (8). https://doi.org/10.1063/1.4987153.

(42) Carpenter, W. B.; Fournier, J. A.; Lewis, N. H. C.; Tokmakoff, A. Picosecond Proton Transfer Kinetics in Water Revealed with Ultrafast IR Spectroscopy. *J. Phys. Chem. B* **2018**, *122* (10), 2792–2802. https://doi.org/10.1021/acs.jpcb.8b00118.

(43) Bloem, R.; Garrett-roe, S.; Strzalka, H.; Hamm, P.; Donaldson, P. Enhancing Signal Detection and Completely Eliminating Scattering Using Quasi-Phase-Cycling in 2D IR Experiments. *Opt. Express* **2010**, *18* (26), 1747–1756.

(44) Olson, D. H.; Khosrovani, N.; Peters, A. W.; Toby, B. H. Crystal Structure of Dehydrated CsZSM-5 (5.8Al): Evidence for Nonrandom Aluminum Distribution. *J. Phys. Chem. B* **2000**, *104*, 4844–4848.

(45) Zhang, Y.; Yang, W. Comment on " Generalized Gradient Approximation Made Simple ." *Phys. Rev. Lett.* **1998**, *80* (1998), 890.

(46) Kühne, T. D.; Laino, T.; Iannuzzi, M.; Ben, M. Del; Khaliullin, R. Z.; Schütt, O.; Rybkin, V. V; Seewald, P.; Schiffmann, F.; Golze, D.; Schade, R.; Mundy, C. J.; Chulkov, S. CP2K : An Electronic Structure and Molecular Dynamics Software Package - Quickstep : Efficient and Accurate Electronic Structure Calculations. *J. Chem. Phys.* **2020**, *152*, 194103. https://doi.org/10.1063/5.0007045.

(47) VandeVondele, J.; Krack, M.; Mohamed, F.; Parrinello, M.; Chassaing, T.; Hutter, J. QUICKSTEP: Fast and Accurate Density Functional Calculations Using a Mixed Gaussian and Plane Waves Approach. *Comp. Phys. Comm.* **2005**, *167*, 103–128. https://doi.org/10.1016/j.cpc.2004.12.014.

(48) Lippert, G.; Hutter, J.; Parrinello, M. The Gaussian and Augmented-Plane-Wave Density Functional Method for Ab Initio Molecular Dynamics Simulations. *Theor. Chem. Acc.* **1999**, *103*, 124–140. https://doi.org/10.1007/s002149900042.

(49) Goedecker, S.; Teter, M.; Hutter, J. Separable Dual-Space Gaussian Pseudopotentials. *Phys. Rev. B* **1996**, *54* (3).

(50) Grimme, S.; Antony, J.; Ehrlich, S.; Krieg, H. A Consistent and Accurate Ab Initio Parameterization of Density Functional Dispersion Correctin (DFT-D) for the 94 Elements of H-Pu. *J. Chem. Phys.* **2010**, *132*, 154104. https://doi.org/10.1063/1.3382344.

(51) Li, C.; Swanson, J. M. J. Understanding and Tracking the Excess Proton in Ab Initio Simulations; Insights from IR Spectra. *J. Phys. Chem. B* **2020**, *124*, 5696–5708. https://doi.org/10.1021/acs.jpcb.0c03615.

(52) Li, C.; Voth, G. A. Using Constrained Density Functional Theory to Track Proton Transfers and to Sample Their Associated Free Energy Surface. *J. Chem. Theory Comput.* **2021**, *17*, 5759–5765. https://doi.org/10.1021/acs.jctc.1c00609.

(53) Kim, J.; Schmitt, U. W.; Gruetzmacher, J. A.; Voth, G. A.; Scherer, N. E. The Vibrational Spectrum of the Hydrated Proton: Comparison of Experiment, Simulation, and Normal Mode Analysis. *J. Chem. Phys.* **2002**, *116* (2), 737–746. https://doi.org/10.1063/1.1423327.

(54) Yu, Q.; Carpenter, W. B.; Lewis, N. H. C.; Tokmakoff, A.; Bowman, J. M. High-Level VSCF/VCI Calculations Decode the Vibrational Spectrum of the Aqueous Proton. *J. Phys. Chem. B* **2019**, *123* (33), 7214–7224. https://doi.org/10.1021/acs.jpcb.9b05723.

(55) Headrick, J. M.; Diken, E. G.; Walters, R. S.; Hammer, N. I.; Christie, R. A.; Cui, J.; Myshakin, E. M.; Duncan, M. A.; Johnson, M. A.; Jordan, K. D. Spectral Signatures of Hydrated Proton Vibrations in Water Clusters. *Science* **2005**, *308*, 1765–1769. https://doi.org/10.1126/science.1113094.

(56) Schmidt, J. R.; Corcelli, S. A.; Skinner, J. L. Pronounced Non-Condon Effects in the Ultrafast Infrared Spectroscopy of Water. *J. Chem. Phys.* **2005**, *123* (4). https://doi.org/10.1063/1.1961472.

(57) Bordiga, S.; Lamberti, C.; Bonino, F.; Travert, A.; Thibault-Starzyk, F. Probing Zeolites by Vibrational Spectroscopies. *Chem. Soc. Rev.* **2015**, *44* (20), 7262–7341. https://doi.org/10.1039/c5cs00396b.

(58) Zecchina, A.; Geobaldo, F.; Spoto, G.; Bordiga, S.; Ricchiardi, G.; Buzzoni, R.; Petrini, G. FTIR Investigation of the Formation of Neutral and Ionic Hydrogen-Bonded Complexes by Interaction of H-ZSM-5 and H-Mordenite with CH3CN and H2O: Comparison with the H-NAFION Superacidic System. *J. Phys. Chem.* **1996**, *100* (41), 16584–16599. https://doi.org/10.1021/jp960433h.

(59) Edler, J.; Hamm, P. Two-Dimensional Vibrational Spectroscopy of the Amide I Band of Crystalline Acetanilide: Fermi Resonance, Conformational Substates, or Vibrational Self-Trapping? *J. Chem. Phys.* **2003**, *119* (5), 2709–2715. https://doi.org/10.1063/1.1586694.

(60) Brunauer, S.; Emmett, P. H.; Teller, E. Adsorption of Gases in Multimolecular Layers. *J. Am. Chem. Soc.* **1938**, *60*, 309–319.

(61) Olson, D. H.; Haag, W. O.; Borghard, W. S. Use of Water as a Probe of Zeolitic Properties: Interaction of Water with HZSM-5. *Microporous Mesoporous Mater.* **2000**, *35–36*, 435–446. https://doi.org/10.1016/S1387-1811(99)00240-1.

(62) Eckstein, S.; Hintermeier, P. H.; Zhao, R.; Baráth, E.; Shi, H.; Liu, Y.; Lercher, J. A. Influence of Hydronium Ions in Zeolites on Sorption. *Angew. Chemie - Int. Ed.* **2019**, *58* (11), 3450–3455. https://doi.org/10.1002/anie.201812184.

(63) Bolis, V.; Busco, C.; Ugliengo, P. Thermodynamic Study of Water Adsorption in High-Silica Zeolites. *J. Phys. Chem. B* **2006**, *110* (30), 14849–14859. https://doi.org/10.1021/jp061078q.

(64) Keenan, J. H.; Keyes, F. G.; Hill, P. G.; Moore, J. G. *Steam Tables*; Wiley: New York, 1969.

(65) Schmitt, U. W.; Voth, G. A. The Computer Simulation of Proton Transport in Water. *J. Chem. Phys.* **1999**, *111* (20), 9361. https://doi.org/10.2741/1213.

(66) Wu, Y.; Chen, H.; Wang, F.; Paesani, F.; Voth, G. A. An Improved Multistate Empirical

Valence Bond Model for Aqueous Proton Solvation and Transport (Journal Physical Chemistry B (2008) 112B (467)). *J. Phys. Chem. B* **2008**, *112*, 476–482. https://doi.org/10.1021/jp8036318.

(67) Biswas, R.; Tse, Y.-L. S.; Tokmakoff, A.; Voth, G. A. Role of Presolvation and Anharmonicity in Aqueous Phase Hydrated Proton Solvation and Transport. *J. Phys. Chem. B* **2016**, *120* (8), 1793–1804. https://doi.org/10.1021/acs.jpcb.5b09466.

(68) Kaduk, B.; Kowalczyk, T.; Van Voorhis, T. Constrained Density Functional Theory. *Chem. Rev.* **2012**, *112* (1), 321–370. https://doi.org/10.1021/cr200148b.

(69) Bell, R. J.; Dean, P. Atomic Vibrations in Vitreous Silica. *Discuss. Faraday Soc.* **1970**, *50*, 55–61. https://doi.org/10.1039/DF9705000055.

(70) Thouless, D. J. Electrons in Disordered Systems and the Theory of Localization. *Phys. Rep.* **1974**, *13* (3), 93–142. https://doi.org/10.1016/0370-1573(74)90029-5.

Appendix 6A. Spectral decomposition of FTIR hydration series

The spectral decomposition into component spectra and hydration dependence was performed by a maximum entropy reweighting of the singular value decomposition (SVD) based on the method of Widjaja and Garland.[40] The final result decomposes the spectral series $A_{k\upsilon}$, with concentration (hydration) index *k* and frequency index υ, into *n* area-normalized component spectra $S_{n\upsilon}$ with hydration dependence C_{kn} and relative frequency-integrated absorption cross-sections ε_n.

$$A_{k\upsilon} = \sum_n C_{kn}\varepsilon_n S_{n\upsilon} \tag{6.15}$$

First, the SVD decomposition was performed with *n* singular values ξ_n.

$$A_{k\upsilon} = \sum_n U_{kn}\xi_n V_{n\upsilon} \tag{6.16}$$

Inserting a transition matrix T_{nn} introduces a reweighting of the component spectra $V_{n\upsilon}$ and concentration dependence U_{kn}:

$$A_{k\upsilon} = \sum_n U_{kn}T_{nn}{}^{-1}T_{nn}\xi_n V_{n\upsilon} \tag{6.17}$$

where the new component spectra $S'_{n\upsilon}$ and concentration dependence c'_{kn} are

$$\begin{aligned} S'_{n\upsilon} &= \sum_n T_{nn}\xi_n V_{n\upsilon} \\ c'_{kn} &= \sum_n U_{kn}T_{nn}{}^{-1} \end{aligned} \tag{6.18}$$

To adjust the reweighting, the transition matrix *T* is optimized with respect to the objective function *F*, given by

$$F = H + \gamma^c P^c + \gamma^\upsilon P^\upsilon + \gamma^D D \tag{6.19}$$

which accounts for information entropy *H*, positivity constraints P^c and P^υ on the concentration dependence and component spectra respectively, and spectral dissimilarity *D*. The relative weighting of these constraints is set by the γ^j terms, where *j* is a superscript. The entropy term penalizes complicated spectral components, given by

$$H = -\sum_n \sum_\upsilon h_{n\upsilon} \ln(h_{n\upsilon})$$
$$h_{n\upsilon} = \frac{S'_{n\upsilon}}{\sum_\upsilon \left| \frac{\partial}{\partial \upsilon} S'_{n\upsilon} \right|} \tag{6.20}$$

The spectral positivity term penalizes spectra with negative absorbance, given by eqn. (6.21). The concentration positivity is given by replacing $S'_{n\upsilon}$ by c'_{kn}.

$$P^\upsilon = \sum_n \sum_\upsilon f(S'_{n\upsilon})(S'_{n\upsilon})^2$$
$$f(x) = \begin{cases} 0, & x \geq 0 \\ 1, & x \leq 0 \end{cases} \tag{6.21}$$

The spectral dissimilarity penalizes similar spectra, calculated by the angle between spectral components when treated as vectors.

$$D = \sum_n \sum_{j>n} D_{nm}$$
$$D_{nm} = \begin{cases} 0, & |\theta_{nm}| \geq \pi/4 \\ 1, & |\theta_{nm}| < \pi/4 \end{cases} \tag{6.22}$$
$$\cos(\theta_{nm}) = \frac{\sum_\upsilon (\hat{S}_{n\upsilon} \bullet \hat{S}_{m\upsilon})}{\sqrt{\sum_\upsilon \hat{S}^2_{n\upsilon} \bullet \sum_\upsilon \hat{S}^2_{m\upsilon}}}$$

After the maximum-entropy reweighting, component spectra are integrated to obtain the area-normalized spectra $S_{n\upsilon}$ and new concentration dependencies c_{kn}. Here, $S'_n(\omega)$ is simply the continuous version of the discrete $S'_{n\upsilon}$, treating frequency as a continuous variable ω.

$$\begin{aligned} N_n &= \int d\omega S'_n(\omega) \\ c_{nk} &= c'_{nk} N_n \\ S_{n\upsilon} &= N_n^{-1} S'_{n\upsilon} \end{aligned} \tag{6.23}$$

This form is sufficient if the transition dipole moment is constant across the component spectra. Then, c_{kn} represent the partition of the system between states with corresponding spectral signatures $S_{n\upsilon}$. Relative values of c_{kn} will report on the relative partitioning, and absolute values carry the same constant factor which includes the pathlength and frequency-integrated, norm-squared transition dipole moment. However, if the transition dipole moment varies across the component spectra, then it is desirable to account for this by further separating c_{kn},

$$c_{kn} = c'_{kn} \varepsilon_n \tag{6.24}$$

where C_{kn} carries only information about the concentration dependence of each component and ε_n carries the relative absorption cross-section. An additional constraint is required to perform this separation. We used the constraint,

$$\sum_n C_{kn} = \bar{h}_k \tag{6.25}$$

where $\bar{h}_k$ is the concentration (mean hydration level) at index *k*. In other words, $C_n\left(\bar{h}\right)$ is defined such that it represents the average number of water molecules in the state with spectral signature $S_n(\omega)$ as a function of hydration level.

Chapter 7

Strong hydrogen bonds in the IR spectrum of hydrated zeolite Brønsted acid sites

7.1. Introduction

Acidic zeolites are widely-used catalysts in a range of chemical transformations, including biomass conversion where water is often present as a reaction product.[1–4] The presence of water in zeolite pores influences the adsorption of reactants[5] and the catalytic activity of acid sites in several chemical reactions.[6–11] As a result, the structure of adsorbed water molecules, the protonation state of the system, and interactions between water and zeolite Brønsted acid sites (BAS) have gained attention as a rich area of investigation.[12–23]

Infrared (IR) spectroscopy, which can access structural information on the length scale of chemical bonds, has been a critical tool for this area of study. Among the most striking and puzzling features in the IR spectrum of hydrated acidic zeolite is a broad doublet which arises at when a single water molecule is adsorbed at the zeolite BAS. Notably, qualitatively similar doublet features have been observed in the spectrum of other systems including some solids and H-bonded dimers.[24–28] Figure 7.1 shows the doublet feature in 1 equivalent (equiv.) H_2O / Al in HZSM-5, also reported in Chapter 6. Experimental IR studies have shown that the feature appears in other zeolites as well.[15,19,20] A longstanding mystery since the first observation in H-bonded solids, the

origin of the doublet feature remains unclear. The feature has been proposed to arise from coupling between the O-H stretch and lower-frequency vibrations,[16,19] or from transitions on a highly-anharmonic O-H potential energy surface.[24,29] Notably, the non-H-bonded (NHB) O-H stretch vibrations ν_{OH}^{NHB} of adsorbed water appear at higher frequencies, with two distinct bands centered near 3550 cm^{-1} and 3700 cm^{-1} in Fig. 7.1.

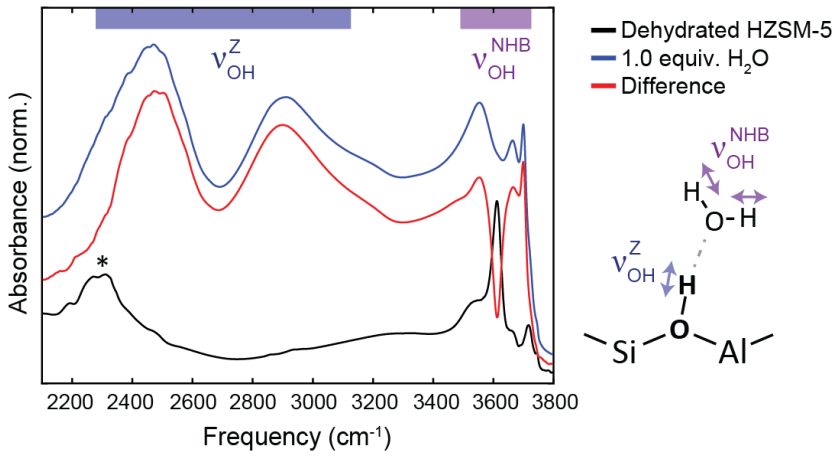

Figure 7.1: FTIR spectra of dehydrated HZSM-5, 1.0 equiv. H_2O / HZSM-5, and the difference. The doublet bands arising from zeolite O-H stretch (ν_{OH}^{Z}) and high-frequency bands from non-H-bonded (NHB) O-H stretch (ν_{OH}^{NHB}) are labeled and depicted schematically to the right. The feature near 2300 cm^{-1} in dry HZSM-5 is a C-F overtone in the halocarbon oil, marked by an asterisk.

In the case of singly-hydrated zeolite BAS, it is well-established that the zeolite is protonated in the ground state and donates a H-bond to the adsorbed water molecule.[17,19] Though early interpretations of the IR spectrum proposed that the water molecule was protonated,[12,30] spectral calculations showed that the water-protonated structure was inconsistent with the experimental spectrum.[17] On the other hand, the calculated H-bonded zeolite O-H stretch (ν_{OH}^{Z}) frequency in the protonated zeolite structure fell in the same region as the experimental doublet bands.[17]

Additionally, several simulation studies found that the protonated water monomer was not a stable species when only a single water molecule is adsorbed.[17,22,23,31] Furthermore, a similar doublet feature was observed in the IR spectrum over a range of different adsorbed H-bond acceptors such as alcohols or ethers, indicating that the doublet arises primarily from ν_{OH}^{Z}, and not from water vibrations.[15,19]

Upon hydrogen bonding, the ν_{OH}^{Z} feature therefore red-shifts by hundreds of wavenumbers from its free O-H frequency of 3610 cm^{-1} in dehydrated HZSM-5 (Fig. 7.1). This red-shifting and broadening is a well-known feature of H-bonds,[32] and the magnitude of the red-shift is correlated with the inter-atomic O-O distance R_{OO}. For example, the H-bonded O-H stretch in liquid water is centered at 3400 cm^{-1} ($R_{OO} = 2.8$ Å) while the O-H stretch of the aqueous excess proton ($R_{OO} \sim 2.45$ Å)[33] is shifted to 1250 cm^{-1}.[33–35] As the H-bonding environment gets stronger and R_{OO} decreases, the shape of the O-H stretch potential energy surface (PES) changes dramatically,[15,19,32,36] from a weakly anharmonic Morse-like potential for conventional H-bonds, to a double-well separated by a barrier, to a broad low-barrier single-well for the shortest H-bonds.[32,36] In the case of ν_{OH}^{Z}, the mean R_{OO} distance[17,31] of 2.5 Å is intermediate between the cases of water and the excess proton complex, consistent with the intermediate frequency range of ~2400-3000 cm^{-1}. Broadening can arise from several sources including a distribution of H-bonding environments and rapid energy relaxation from coupling to O-O stretching and other low-frequency motions.[15,19]

The ν_{OH}^{Z} vibration is split into two distinct broad maxima with approximately equal intensity, peaked near 2500 cm^{-1} and 2850 cm^{-1}. There are multiple interpretations that could explain the

splitting, which have been neither conclusively verified nor disproven. Most commonly, the splitting is assigned to Fermi resonance between ν_{OH}^{Z} and the overtone of the $O_Z - H - O_W$ bend along the axis between zeolite and water oxygen atoms.[15,17,19,22] In that picture, the two doublet bands are quantum-mechanical mixtures of ν_{OH}^{Z} and the bend overtone $2\delta_{OHO}$, with the local minimum between doublet bands at the decoupled $2\delta_{OHO}$ frequency. Alternatively, the overtone transition on a double-well H-bond potential could account for the second peak in the doublet, a possibility which was explored for solids with similar IR spectra.[24,29] In principle, the higher-frequency peak could also a combination band between ν_{OH}^{Z} and a ~350 cm^{-1} vibration.

The origin of the doublet splitting has remained mysterious in part because of the limited information content in the linear IR absorption spectrum. Linear absorption measures transitions from the ground state to excited states, and is therefore sensitive to the lowest-energy region of the potential energy surface. Nonlinear spectroscopy can measure the energies of higher-lying excited states through excited-state absorption (ESA) transitions, providing sensitivity to higher-energy contours of the potential. Two-dimensional IR (2D IR) spectroscopy can be particularly insightful for this purpose, since the frequencies of excitation and detection are recorded simultaneously in a pump-probe measurement. By sensing higher-energy regions of the potential, the frequencies and amplitudes of excited state transitions in 2D IR spectroscopy provide further experimental constraints for interpreting the origin of vibrational transitions.

In this chapter, we used two-dimensional IR (2D IR) spectroscopy to measure fundamental and excited-state transition frequencies and amplitudes in 1 equiv. H_2O / HZSM-5. We compared this data to characteristic 2D peak patterns from four models including Fermi resonance coupling. The Fermi resonance model predicted intense excited-state transitions in frequency ranges which

do not appear in the experiment. By contrast, we found that a double-well ν_{OH}^{Z} potential can reproduce the experimental pattern of peak frequencies and relative amplitudes for all features observed in the experiment. Therefore, the 2D IR spectrum provides experimental evidence which can distinguish between these two models, and is consistent with the assignment of a double-well H-bonding potential.

7.2. Methods

Hydrated zeolite was prepared using a methodology which has been described previously,[37] and in Chapter 6. Briefly, proton-form ZSM-5 zeolites (Johnson Matthey) were dehydrated on a Schlenk-line. The Si:Al ratio was 17:1, measured by inductively coupled plasma – optical emission spectroscopy. Samples were rehydrated in a sealed Parr acid digestion chamber by equilibration with water vapor at 150 °C. The H_2O content of hydrated zeolite was measured by titration with methanol. In a glovebox, hydrated samples were suspended in a mixture of hydrophobic, index-matching oils Fluorolube® PCTFE[38] and perfluoro(tetradecahydrophenanthrene) and pressed between two 1-mm CaF_2 windows. The oils preserved the hydration state for *ex-situ* measurements and reduced scatter in nonlinear IR experiments.

Linear IR spectra were measured with a *Bruker Tensor 27* Fourier-transform IR spectrometer. 2D IR and transient absorption spectra were measured on a spectrometer which has been described previously,[37] and in Chapter 3. Briefly, the output of a 1 kHz Ti:Sapphire (25 fs, 5 mJ, 800 nm, Coherent Legend Elite) is used to generate excitation pulses at 2500 cm^{-1} by down-conversion with an optical parametric amplifier (OPA, TOPAS Prime) followed by difference-frequency generation in $AgGaS_2$. Pulses centered at 2850 cm^{-1} were generated using a home built $KNbO_3$

OPA[39] on the same laser system. Broadband probe pulses were generated by filamentation in N_2 gas.[40] Spectra were collected in the pump-probe geometry[41] and parallel and perpendicular polarization components were measured simultaneously on a 2x64-pixel array (HgCdTe, Infrared Associates). Scatter artifacts were suppressed through a combination of index-matching oils, the addition of a second chopper at 250 Hz in the probe beam, subtraction of a 2D IR surface at -5 ps, and quasi-phase cycling[42] by oscillating the τ_2 stage during data collection.

7.3. 2D IR spectroscopy

Figure 7.2 shows the 2D IR spectrum of 1.0 equiv. H_2O in HZSM-5. Two excitation pulses were used to cover the broad doublet feature, centered at 2500 cm^{-1} (left panel in Fig. 7.2a) and 2850 cm^{-1} (right panel). Green dashed lines plotted at ω_{Exc} = 2700 cm^{-1} show the overlap between the two spectra. While the amplitudes are similar at ω_{Exc} = 2700 cm^{-1}, the panels are not scaled relative to each other, so amplitude comparisons should only be made between features at equal excitation frequency. Along the detection frequency, small discontinuities arise from patching together spectra collected with different grating positions, as discussed in Chapter 3. Diagonal peaks – labeled I and II – appear for both bands of the doublet at 2500 cm^{-1} and 2850 cm^{-1} with prominent cross peaks between them labeled III and IV. Peaks II-IV have round, homogeneously broadened lineshapes. Peak I is inhomogeneously broadened, extending to higher frequencies along the diagonal where strong H-bonds absorb in liquid water.[43]

Curiously, intense excited-state absorption (ESA) features – here in blue – are not observed near either diagonal peak. This is unusual for molecular vibrations. Typically (red) diagonal features at the 0-1 transition frequency are accompanied by an ESA feature at the 1-2 transition

frequency which is roughly equal in intensity and shifted along the detection frequency axis by the anharmonicity $\chi = \omega_{10} - \omega_{21}$.[44] Instead, in Fig. 7.2 the only ESA feature which can be clearly identified near a diagonal peak is the high-frequency tail of the peak labeled II'. While the center frequency of peak II' was not measured due to overlap with zeolite framework vibrations, it is clear that the splitting between peaks II and II' is >300 cm^{-1}, far exceeding the diagonal anharmonic shift typical for molecular vibrations, even in strongly H-bonded systems.[32,34]

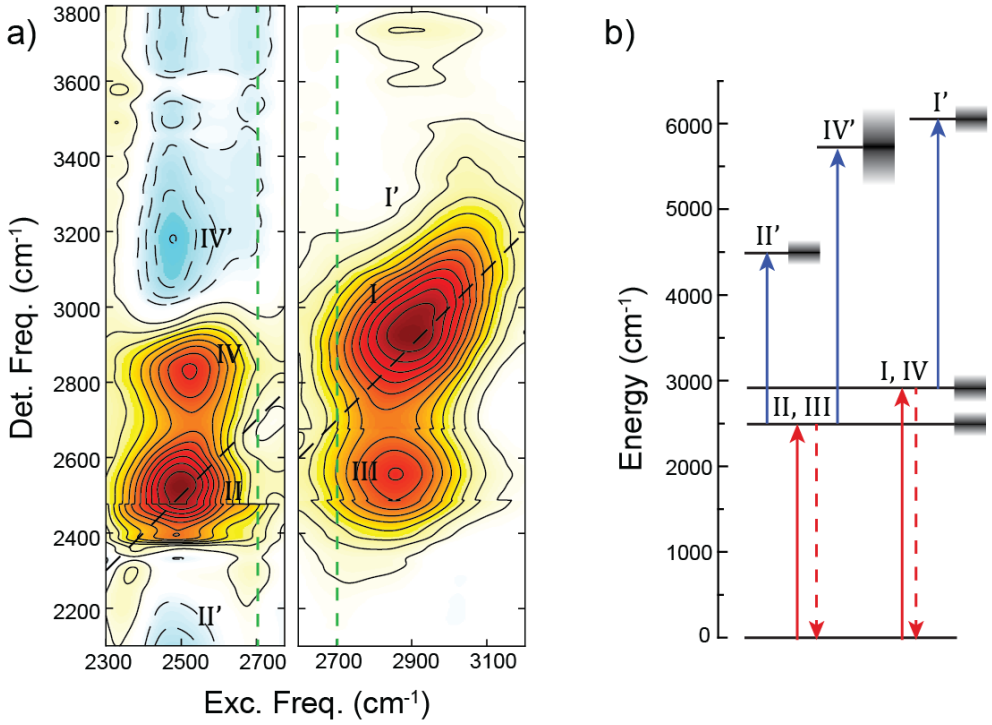

Figure 7.2: 2D IR spectroscopy of 1.0 equiv. H_2O / HZSM-5 at 100 fs waiting time. (a) Isotropic 2D IR spectrum with excitation pulses centered at 2500 cm^{-1} (left) and 2900 cm^{-1} (right). Dashed green lines are plotted at ω_{Exc} = 2700 cm^{-1} in both panels. (b) Energy level diagram recording the measured frequencies of bleach & stimulated emission (red) and excited state absorption (blue) features.

Above peak I, the concave shape of the 2D IR spectrum hints at an ESA feature I' which is observed only through its interference with the more intense peak. Notably, the FTIR spectrum

shows that there is significant intensity in the range of ~3200-3400 cm^{-1}, and the absence of a large signal in this region of the 2D IR spectrum is consistent with overlapping, oppositely-signed features. The most intense ESA feature is the peak labeled IV' which appears above peak IV and extends over a large range of detection frequencies from at least 3000 – 3800 cm^{-1}. Transition frequencies can be inferred from the center positions of the bands in the 2D IR spectrum, with the energy level diagram corresponding to labeled peaks presented in Fig. 7.2b.

In addition to the features associated with ν_{OH}^{Z}, cross peaks to ν_{OH}^{NHB} vibrations are observed near ω_{Det} = 3600 cm^{-1} and 3725 cm^{-1}. Interestingly, these cross peaks appear at ω_{Exc} = 2900 cm^{-1} but not at ω_{Exc} = 2500 cm^{-1}, which may be explained by overlap with the tail of the negatively-signed peak IV'. These two cross peaks reflect the two prominent bands associated with ν_{OH}^{NHB} in the linear absorption spectrum, Fig. 7.1, showing that both are coupled to ν_{OH}^{Z}.

Additional spectroscopic information is contained in the polarization dependence of spectral features, shown in Fig. 7.3. At this early waiting time – assuming molecular reorientation on the timescale of 100 fs is negligible – the orientational intensity in the cross peaks reflects the relative orientation between associated transition dipole moments, as described in Chapter 2. For example, the cross peaks III & IV display more intensity in the parallel (ZZZZ) spectrum, corresponding to positive anisotropy values and indicating that the transition dipole moments of the underlying vibrations have primarily parallel alignment. This result is consistent with the claim that the broad doublet bands, I & II in the 2D IR spectrum, both arise from the same ν_{OH}^{Z} vibration.

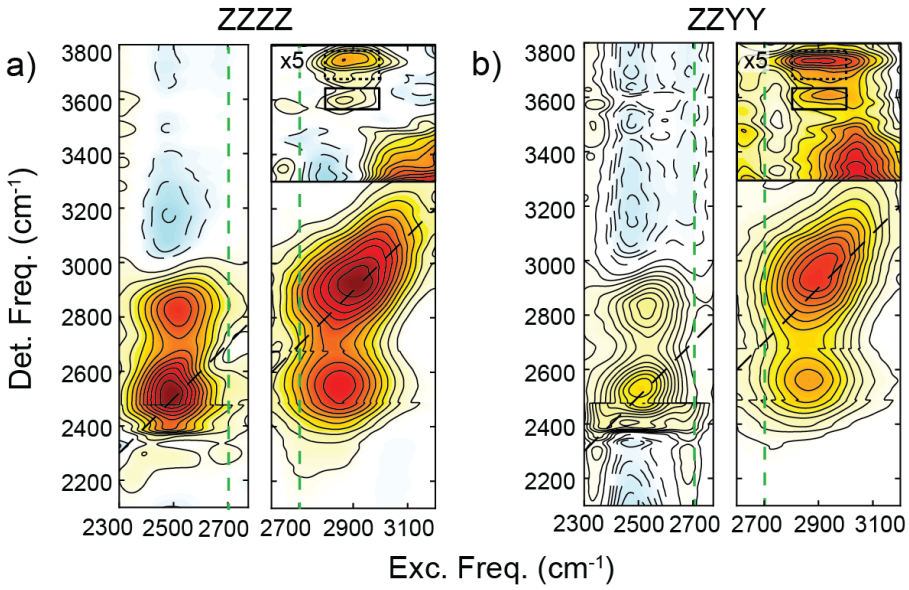

Figure 7.3: Polarization dependent 2D IR spectrum of 1 equiv. H_2O at 100 fs waiting time: (a) parallel and (b) perpendicular components of the spectrum. The colormap is scaled to reflect the correct relative amplitudes between ZZZZ and ZZYY spectra. The upper right-hand corner is enhanced by a factor of 5 to show the cross peaks in that region.

The cross peaks from peak I to ν_{OH}^{NHB} have more intensity in the perpendicular spectrum. Assuming that the ν_{OH}^{Z} transition dipole is oriented primarily along the O-H-O bond, this suggests that both ν_{OH}^{NHB} vibrations are aligned preferentially perpendicular to that axis. Referring to the schematic in Fig. 7.1, this implies that the two ν_{OH}^{NHB} bands are most likely not the symmetric and asymmetric combinations of the two water free O-H stretch vibrations, since the symmetric stretch would have a preferentially parallel alignment with ν_{OH}^{Z}. Instead, the cross-peak anisotropy is consistent with a previous suggestion that the lower frequency band centered near 3550 cm^{-1} is red-shifted by a weak coordination to another oxygen atom in the zeolite lattice, compared to the uncoordinated O-H bond centered near 3700 cm^{-1}.[21,45] Bond angles can be estimated from cross-peak anisotropy values averaged over the features. The anisotropy of the lower-frequency

cross peak was -0.07, averaged over ω_{Exc} = [2800, 3000] cm^{-1} & ω_{Det} = [3550, 3625] cm^{-1} (black box in Fig. 7.3), corresponding to an angle of ~117˚. The anisotropy of the higher-frequency cross peak was -0.17, averaged over ω_{Exc} = [2800, 3000] cm^{-1} & ω_{Det} = [3650, 3750] cm^{-1} (dashed black box in Fig. 7.3), corresponding to an angle of ~103˚.

7.4. Transient absorption

Transient absorption spectra were collected with excitation centered at both 2500 cm^{-1} and 2900 cm^{-1}, shown in Fig. 7.4. When excited at 2500 cm^{-1}, both the feature at ω_{Det} = 2500 cm^{-1} and the uphill cross peak at 2850 cm^{-1} display single-exponential decay with approximately the same lifetime of 150 ± 18 fs (μ ± σ), averaged over ω_{Det} = [2400, 2800] cm^{-1}. The diagonal feature and downhill cross peak excited at 2900 cm^{-1} were better fit to a biexponential, with fitted time constants of 110 ± 27 fs and 540 ± 44 fs averaged over ω_{Det} = [2500, 2900] cm^{-1}. The variations in fitted lifetime with detection frequency are plotted in Fig. 7.4c, showing a small positive trend between both time constants and ω_{Det} for the spectra excited at 2900 cm^{-1}. For comparison, the O-H stretch lifetime in liquid water is 260 fs,[46,47] and the lifetime of the 1250 cm^{-1} O-H stretch of the aqueous excess proton is approximately 100 fs.[34] When fitting the TA traces, only data past 100 fs was considered since nonresonant response from the CaF_2 window appears during pulse overlap. Since the fitted timescale of ~150 fs is only somewhat longer than the instrument response, this places an upper bound on the lifetime of the 2500 cm^{-1} band.

The lifetimes of the doublet features are intermediate between those of liquid water and proton O-H stretch, consistent with an intermediate O-H stretch frequency and H-bonding strength for the

zeolite-water H-bond. While further investigation is required to fully characterize the pathway(s) for vibrational energy relaxation, the ultrafast relaxation timescales are consistent with relatively strong coupling to lower-frequency vibrations such as O-O stretching, which has been suggested previously.[19] A lingering question is the role of the rather bright zeolite framework vibrations in energy relaxation. In ZSM-5 the framework modes have substantial intensity beginning below ~2100 cm^{-1}, and the spectrum in this relatively high-frequency region depends somewhat on the framework type which could provide a route for investigation.[18]

In any case, the longer vibrational lifetime for doublet features excited at 2900 cm^{-1}, compared to those excited at 2500 cm^{-1}, might be rationalized by the greater energy difference – and therefore weaker coupling – between the higher-frequency band of the doublet and the low frequency bath states. Another consideration is the apparent substantial overlap between bleach and SE features excited at 2500 cm^{-1} with the extended ESA features labeled II' and IV' in Fig. 7.2, which could lead to a faster measured decay of those features. However, these differences in the vibrational relaxation timescales are unlikely to provide a means to distinguish the assignment of the doublet bands in terms of a Fermi resonance or tunneling potential model. In the Fermi resonance hypothesis, both doublet bands are quantum-mechanical mixtures of bend overtone and bridging O-H stretch, and approximately equal mixtures if the frequencies are nearly degenerate, $\nu_{OH}^{Z} \approx 2\delta_{HOH}$. While, in the tunneling potential model the two bands both arise from transitions of the same O-H stretch vibration. So, neither model necessarily predicts large differences in the vibrational lifetimes, though in either case differences could be rationalized with the reasoning above. Therefore, the TA results are plausibly consistent with either the tunneling potential or Fermi resonance pictures.

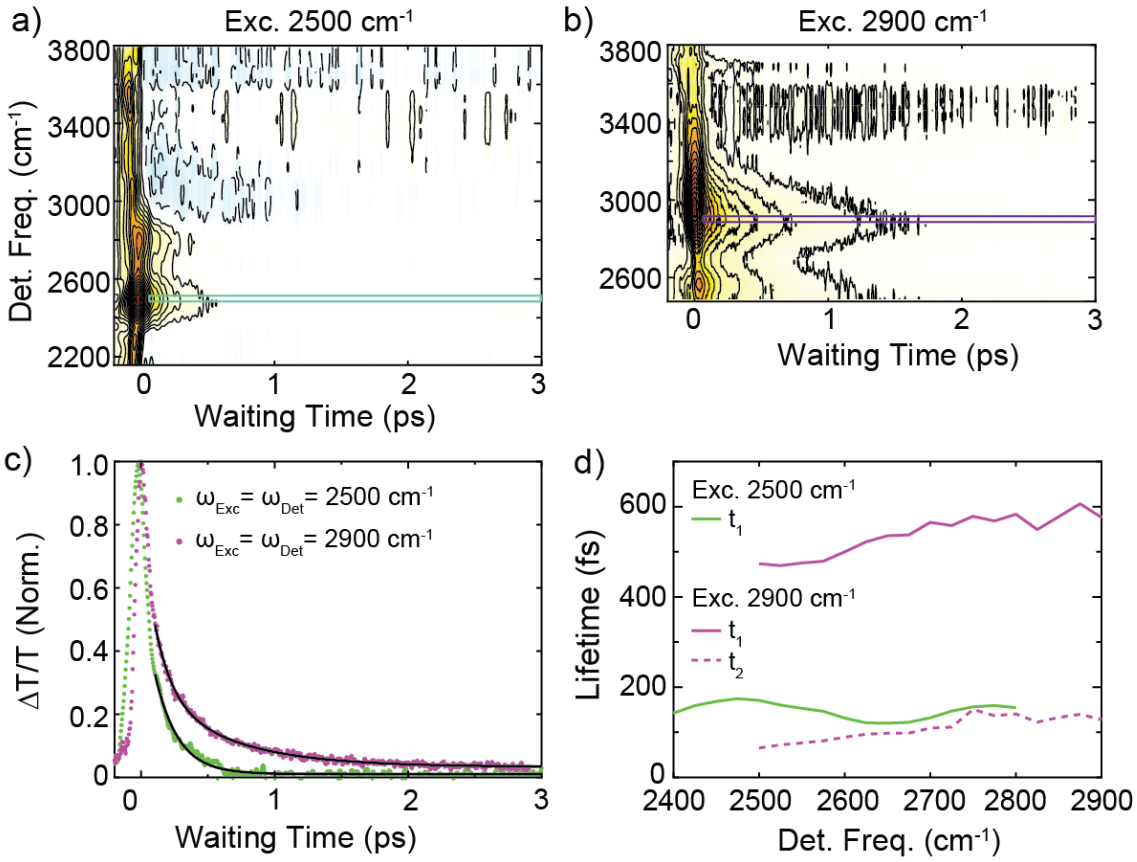

Figure 7.4: (a) Isotropic transient absorption spectrum of 1.0 equiv. H_2O / HZSM-5 with excitation centered at (a) 2500 cm^{-1} and (b) 2900 cm^{-1}. TA spectra at varying ω_{Det} were fit to (a) single exponential $S(\tau_2) = A_1 e^{-\tau_2/t_1} + C$ or (b) biexponential $S(\tau_2) = A_1 e^{-\tau_2/t_1} + A_2 e^{-\tau_2/t_2} + C$. The traces with ω_{Det} at the center frequency of the excitation pulses are displayed in (c), corresponding to the rectangles in (a-b) and fitted curves in black. Fitted time constants are displayed in (d) as a function of ω_{Det}.

7.5. Models for vibrational assignment and comparison to experiment

7.5.1. Model 2D IR spectra approach

The peak positions and relative intensities in the early-time 2D IR spectrum (Fig. 7.2) contain information that can distinguish between Fermi resonance and tunneling potential assignments. To

develop this argument, we compared the experimental result to transition frequencies and amplitudes calculated using model Hamiltonians to describe the vibrational assignments considered. In this approach, neither homogeneous nor inhomogeneous broadening mechanisms were included, so the results are "stick 2D IR" spectra reporting calculated frequencies and amplitudes. Calculated frequencies arise from energy differences in the diagonalized Hamiltonian, and calculated amplitudes arise from the associated transition dipole matrix elements.

Four models were considered for the doublet and corresponding 2D IR peak pattern. The Fermi resonance hypothesis was modeled with a cubic coupling term between the fundamental of a high-frequency vibration and degenerate overtone of a low-frequency vibration. The H-bond tunneling potential hypothesis was modeled with double-well potential energy surface using a quartic function. In addition, two other models were considered which were instructive, but less likely to explain the spectroscopy than the other two: a model for relatively weak coupling between two high-frequency anharmonic oscillators, and a displaced harmonic oscillator model for coupling to a low-frequency vibration. Each model Hamiltonian was diagonalized to generate a set of calculated transition frequencies and corresponding transition dipole matrix elements.

Using the calculated transition frequencies $\{\omega_{ba}\}$ and transition dipole moments $\{\mu_{ba}\}$, the model stick FTIR spectrum was constructed according to Eq. (7.1). The sum is over the peaks in the spectrum *j*, each centered at transition frequency $\omega_{ba,j}$ corresponding to the transition between two states |a⟩ and |b⟩ defined by the model Hamiltonian. The amplitude of each peak is scaled by the corresponding squared transition dipole moment $\left|\mu_{ba,j}\right|^2$. For visualization, the delta function is replaced with a normalized Gaussian function with linewidth $\Delta\omega = 30\,\mathrm{cm}^{-1}$.

$$S_{FTIR}(\omega) = \sum_{peaks\ j} \left|\mu_{ba,j}\right|^2 G(\omega - \omega_{ba,j})$$
$$G(\omega - \omega_j) = \frac{1}{\Delta\omega\sqrt{2\pi}} \exp\left(\frac{-\left(\omega - \omega_j\right)^2}{2(\Delta\omega)^2}\right) \tag{7.1}$$

The stick 2D IR spectrum was constructed in a similar way, according to Eq. (7.2). Each peak *j* in the 2D IR spectrum is distinguished by the combination of center excitation and detection frequencies $\omega_{ba,j}$ and $\omega_{cb,j}$ respectively, where |a⟩, |b⟩, and |c⟩ are states defined by the model Hamiltonian. The peak amplitude is scaled by the corresponding transition dipole moments $\left|\mu_{ba,j}\right|^2 \left|\mu_{cb,j}\right|^2$, which is equal to $\left|\mu_{ba,j}\right|^4$ in the case of a diagonal peak where |a⟩ and |c⟩ are the same state. The amplitude of each peak is further scaled by accounting for the number of Liouville space pathways n_j at a given center excitation and detection frequency pair. The set of pathways considered for each model are enumerated in Appendix 7A. Ignoring coherence pathways – since the two doublet features are not excited simultaneously in the experiment – each pathway can be described as either bleaching (B), stimulated emission (SE), or excited state absorption (ESA).[44,48] The sign of the feature is positive ($\nu_j = 0$) for B & SE pathways, and negative ($\nu_j = 1$) for ESA pathways. Finally, a 2D Gaussian lineshape function G_{2D} was added for visualization, with the same linewidth parameter $\Delta\omega$ used in the FTIR model.

$$S_{2DIR}(\omega_{Exc}, \omega_{Det}) = \sum_{peaks\ j} (-1)^{\nu_j}\, n_j \left|\mu_{ba,j}\right|^2 \left|\mu_{cb,j}\right|^2 G_{2D}(\omega_{Exc} - \omega_{ba,j}, \omega_{Det} - \omega_{cb,j})$$
$$G_{2D}(\omega_{Exc} - \omega_1, \omega_{Det} - \omega_3) = \frac{1}{2\pi(\Delta\omega)^2} e^{-\left(\omega_{Exc} - \omega_1\right)^2/2(\Delta\omega)^2} e^{-\left(\omega_{Det} - \omega_3\right)^2/2(\Delta\omega)^2} \tag{7.2}$$

7.5.2. Two weakly coupled vibrations

For the sake of model development, it is instructive to begin with a model for bilinear coupling between two high-frequency vibrations. Though, we do not expect this model to describe the spectroscopy of the doublet bands in the experiment. In this model the coupling is described by an anharmonic term in the two-dimensional potential energy surface which is linear in both coordinates. The coupling causes mixing between the vibrational states, leading to transitions and characteristic 2D peak patterns summarized in Fig. 7.5. This model is often used to interpret cross peaks in 2D IR spectroscopy, and applies in the case of weak coupling such as between carbonyl stretching vibrations in metal dicarbonyls.[44,49]

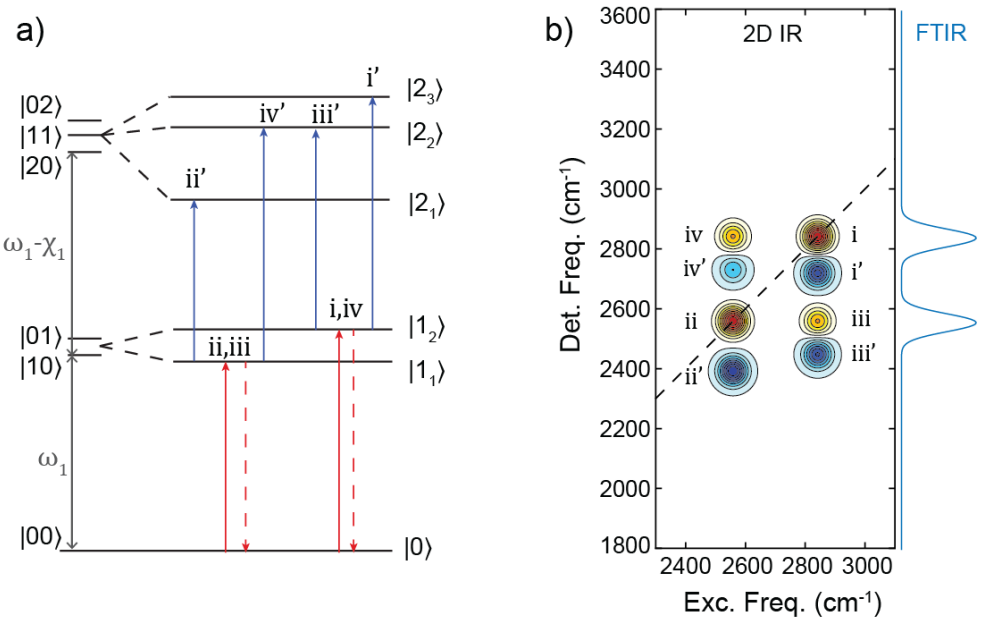

Figure 7.5: Bilinear coupling model. (a) Energy level diagram labeling mixed states and transitions between them. (b) Characteristic stick FTIR and 2D IR spectra calculated using this model, with Gaussian lineshapes added for visualization. Model parameters used in (b) are listed in Table 7.1a.

To write the Hamiltonian, consider the coupling with strength Δ between two vibrations with unmixed frequencies ω_1 and ω_2. Both are anharmonic with anharmonicities χ_1 and χ_2, described by quartic terms in the potential energy surface. The anharmonicity term shifts the site energy of the second excited state from its harmonic value of $2\omega_1$ (or $2\omega_2$) to $2\omega_1 - \chi_1$ (or $2\omega_2 - \chi_2$). For simplicity, $2\pi c\hbar$ is factored out so that ω, Δ, and χ are all in units of cm^{-1}. The resulting Hamiltonian is written in Eq. (7.3) in terms of lowering and raising operators b and $b^\dagger$.

$$H = \omega_1 b_1^\dagger b_1 + \omega_2 b_2^\dagger b_2 + \frac{\Delta}{2}\left(b_2^\dagger b_1 + b_1^\dagger b_2\right) - \frac{\chi_1}{2} b_1^\dagger b_1^\dagger b_1 b_1 - \frac{\chi_2}{2} b_2^\dagger b_2^\dagger b_2 b_2 \tag{7.3}$$

The Hamiltonian can be expressed in matrix form in the basis {00, 10, 01, 20, 11, 02}, where the first label corresponds to ω_1 and the second to ω_2.

$$H = \begin{bmatrix} 0 & 0 & 0 & 0 & 0 & 0 \\ 0 & \omega_1 & \Delta/2 & 0 & 0 & 0 \\ 0 & \Delta/2 & \omega_2 & 0 & 0 & 0 \\ 0 & 0 & 0 & 2\omega_1 - \chi_1 & \Delta/\sqrt{2} & 0 \\ 0 & 0 & 0 & \Delta/\sqrt{2} & \omega_1 + \omega_2 & \Delta/\sqrt{2} \\ 0 & 0 & 0 & 0 & \Delta/\sqrt{2} & 2\omega_2 - \chi_2 \end{bmatrix} \tag{7.4}$$

The dipole matrix **M** is written in the same basis assuming a harmonic dipole surface, with matrix elements $\boldsymbol{\mu}_1$ and $\boldsymbol{\mu}_2$ corresponding to the uncoupled vibrations.

$$\mathbf{M} = \begin{bmatrix} 0 & \boldsymbol{\mu}_1 & \boldsymbol{\mu}_2 & 0 & 0 & 0 \\ \boldsymbol{\mu}_1 & 0 & 0 & \sqrt{2}\boldsymbol{\mu}_1 & \boldsymbol{\mu}_2 & 0 \\ \boldsymbol{\mu}_2 & 0 & 0 & 0 & \boldsymbol{\mu}_1 & \sqrt{2}\boldsymbol{\mu}_2 \\ 0 & \sqrt{2}\boldsymbol{\mu}_1 & 0 & 0 & 0 & 0 \\ 0 & \boldsymbol{\mu}_2 & \boldsymbol{\mu}_1 & 0 & 0 & 0 \\ 0 & 0 & \sqrt{2}\boldsymbol{\mu}_2 & 0 & 0 & 0 \end{bmatrix} \tag{7.5}$$

Diagonalizing *H* returns the eigenvectors $\{\mathbf{v_i}\}$ and eigenvalues $\{\omega_i\}$. Transition frequencies are given by $\omega_{ba} = \omega_b - \omega_a$. Squared transition dipole moments $|\mu_{ba}|^2$ are computed from the matrix elements of **M'**, found by transforming **M** into the basis of eigenvectors $\{\mathbf{v_i}\}$: $\mathbf{M'} = V^{-1}\mathbf{M}V$, where *V* is the change-of-basis matrix. Since **M**, $\boldsymbol{\mu}_1$, and $\boldsymbol{\mu}_2$ are all vector quantities the mixed state transition amplitudes depend on the orientation of unmixed vibrations. For simplicity, we assumed that unmixed transition dipoles are perpendicular, and therefore there is no coupling-induced intensity redistribution in the isotropic spectrum.[44] This simplification does not affect the mixed transition frequencies, only relative amplitudes. Squared transition dipole moments $|\mu_{ba}|^2$ were computed as vector norms. Diagonalized basis states labeled {0, 1_1, 1_2, 2_1, 2_2, 2_3} are displayed schematically in Fig. 7.5. Since *H* is block diagonal, single-excitation states are mixed to form {$|1_1\rangle$, $|1_2\rangle$} and double-excitation states form {$|2_1\rangle$, $|2_2\rangle$, $|2_3\rangle$}.

Peak amplitudes were constructed from the collection of **M'** matrix elements corresponding to the transitions and the number of Liouville pathways contributing to the feature according to Eq. (7.2). The Liouville pathways are enumerated in Fig. 7A.1. The parameters for the model are (ω_1, ω_2, Δ, χ_1, χ_2, μ_1, μ_2). Varying μ_1 and μ_2 only changes the relative peak amplitudes, so for simplicity we used $\mu_1 = \mu_2$.

Figures 7.5b and 7.6a show the typical peak pattern for two bilinearly coupled oscillators with positive site anharmonicities. We chose a combination of ω_1, ω_2, and Δ leading to a mixed state splitting of 400 cm^{-1} to approximately match the experiment, and $\Delta = \omega_1 - \omega_2$. Changing the coupling relative to the unmixed splitting $\omega_1 - \omega_2$ changes the splitting of mixed states, but not the

ordering of the peaks.[44] Peak ordering can be changed by varying the sign of anharmonicity terms. A negative site anharmonicity χ corresponds to an unmixed vibration where $\omega_{21} > \omega_{10}$, which can occur in quantum-confined potentials.[32,34] Figure 7.6 shows the four combinations of positive/negative anharmonicities using the parameters recorded in Table 7.1.

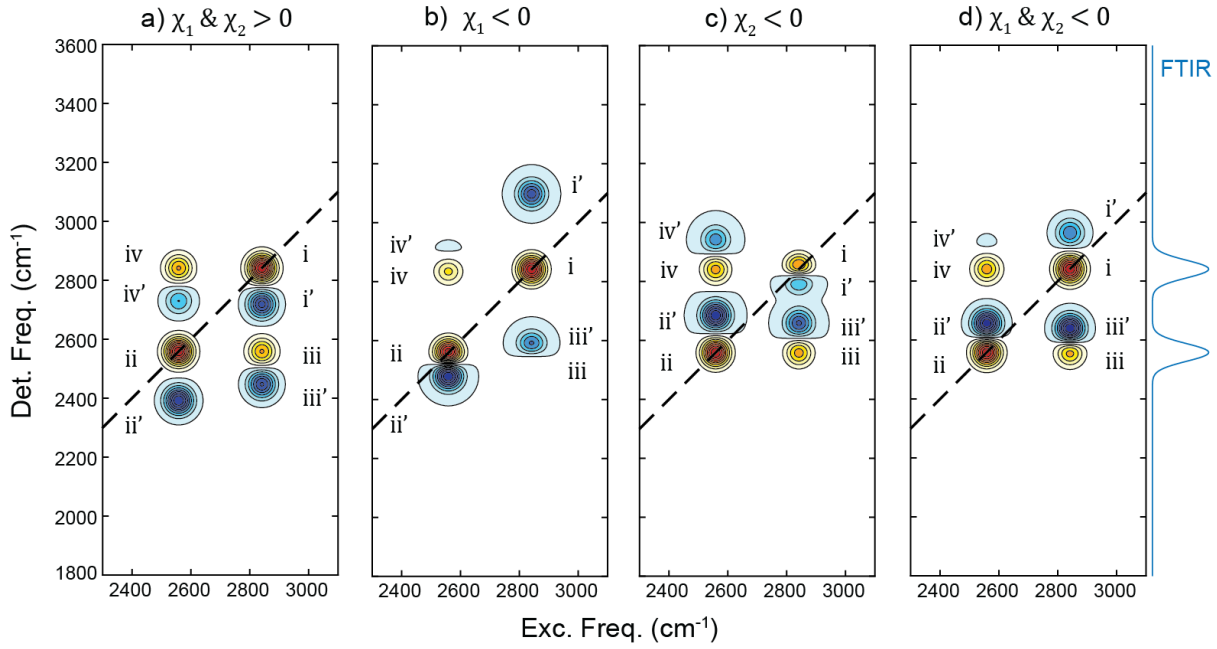

Figure 7.6: Influence of anharmonicity parameters on bilinear coupling model. (a) $\chi_1 > 0$ & $\chi_2 > 0$. (b) $\chi_1 < 0$. (c) $\chi_2 < 0$. (d) $\chi_1 < 0$ & $\chi_2 < 0$. The model FTIR spectrum is unaffected by the anharmonicity parameters. Model parameters are listed in Table 7.1.

The characteristic patterns of 2D IR peak frequencies and relative amplitudes in Figs. 7.5-7.6 can be compared to the experimental result in Fig. 7.2. In the bilinear coupling model, relatively high-amplitude ESA features appear with relatively small splitting from the nearby positive features. The model ESA amplitudes are much larger than the experimental result, and their detection frequencies do not match the experimental peak ordering. For example, in the experiment there are no ESA features observed at detection frequencies between peaks I & III or between II

& IV. In Fig. 7.6a, this is not the case since peak i' falls between i & iii and peak iv' falls between ii & iv. Peak ordering can be changed by flipping the sign of either χ_1 and/or χ_2. For example, in Fig. 7.6b $\chi_1 < 0$ places peaks i' and iv' at detection frequencies above i and iv. But, peak iii' is shifted to a detection frequency between i & iii, so the peak ordering is still different from the experiment. Figure 7.6c-d also show that inverting the sign of χ_2 does not reproduce the peak ordering in the experiment. Therefore, as expected this model cannot produce a set of transition frequencies and relative amplitudes that are consistent with the measured 2D IR spectrum.

Table 7.1: Model parameters used in Figure 7.6

Figure	ω_1 (cm^{-1})	ω_2 (cm^{-1})	Δ (cm^{-1})	χ_1 (cm^{-1})	χ_2 (cm^{-1})
a)	2800	2600	200	200	200
b)	2800	2600	200	-300	100
c)	2800	2600	200	100	-300
d)	2800	2600	200	-150	-150

7.5.3. Fermi resonance model

To model the 2D IR signature of Fermi resonance, we used a model based on the work of Edler & Hamm,[50] where a high-frequency vibration is coupled with strength Δ to the degenerate overtone of a lower-frequency vibration through a cubic term in the Hamiltonian. The higher-frequency vibration has anharmonicity $\chi = \omega_{10} - \omega_{21}$, and the low-frequency vibration is treated as harmonic. In the context of the hydrated zeolite, this describes coupling between the high-frequency O-H stretch and lower-frequency O-H-O bend. The model Hamiltonian is given by Eq. (7.6); coupled states and transitions between them are depicted in Fig. 7.7.

$$H = \omega_1 b_1^\dagger b_1 + \omega_2 b_2^\dagger b_2 + \frac{\Delta}{2}\left(b_1 b_2^\dagger b_2^\dagger + b_2 b_1^\dagger b_1^\dagger\right) - \frac{\chi}{2} b_1^\dagger b_1^\dagger b_1 b_1 \tag{7.6}$$

The relevant basis states are {00, 10, 02, 20, 12, 04}, where the first label corresponds to the high-frequency mode. The Hamiltonian in this basis, Eq. (7.7), has similar block-diagonal structure to the bilinear coupling model.

$$H = \begin{bmatrix} 0 & 0 & 0 & 0 & 0 & 0 \\ 0 & \omega_1 & \frac{\Delta}{2} & 0 & 0 & 0 \\ 0 & \frac{\Delta}{2} & 2\omega_2 & 0 & 0 & 0 \\ 0 & 0 & 0 & 2\omega_1 - \chi & \frac{\Delta}{\sqrt{2}} & 0 \\ 0 & 0 & 0 & \frac{\Delta}{\sqrt{2}} & \omega_1 + 2\omega_2 & \sqrt{\frac{3}{2}}\Delta \\ 0 & 0 & 0 & 0 & \sqrt{\frac{3}{2}}\Delta & 4\omega_2 \end{bmatrix} \tag{7.7}$$

Assuming that the overtone of ω_2 is dark, all intensity comes from the transition dipole of ω_1. Then, the dipole moment matrix is identical to Eq. (7.5) setting $\mu_2 = 0$ and $\mu_1 = \mu$. Unlike the bilinear coupling model, it is not necessary to consider the relative transition dipole orientations since all intensity comes from the dipole moment of the fundamental transition. Any influence of transition dipole orientation is implicitly factored into the coupling strength Δ.

The Hamiltonian was diagonalized and peak amplitudes were constructed in the same way as the bilinear coupling model. The input parameters are (ω_1, ω_2, χ, Δ). The resonance condition between ω_1 and $2\omega_2$ shifts frequencies and relative amplitudes, but does not change the peak ordering, so we choose the case of perfect resonance, $\omega_1 = 2\omega_2$, where $|1_1\rangle$ and $|1_2\rangle$ are equal mixtures of $|01\rangle$ and $|02\rangle$. All splitting between $|1_1\rangle$ and $|1_2\rangle$ comes from the coupling, so a large

value of $\Delta = 400$ cm^{-1} is required to approximately match the experimental peak frequencies in the linear IR spectrum.

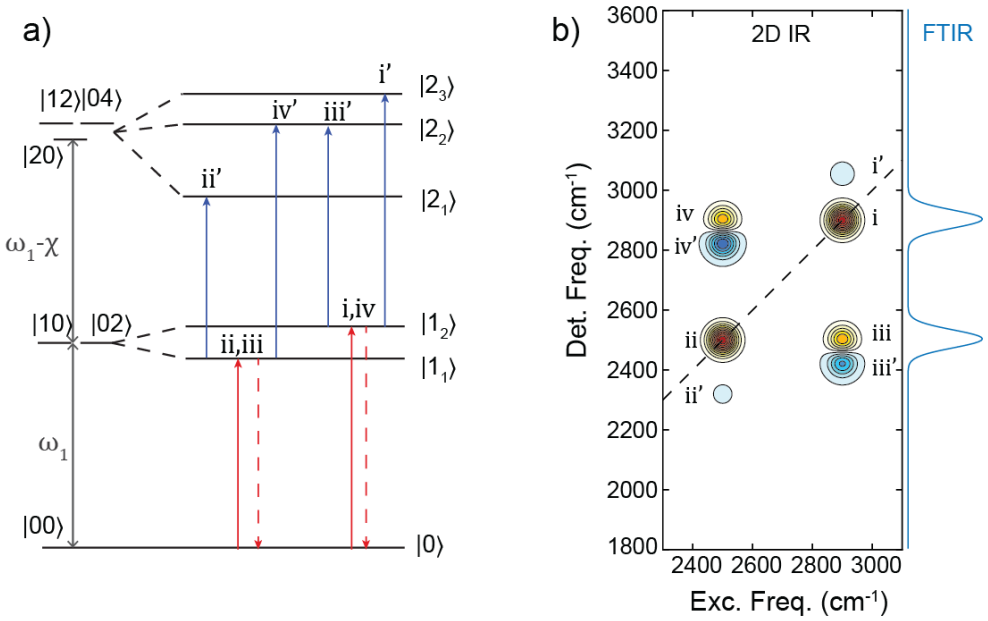

Figure 7.7: Fermi resonance model. (a) Energy level diagram labeling mixed states and transitions between them. (b) Characteristic stick FTIR and 2D IR spectra. Model parameters used in (b) are listed in Table 7.2a.

The model and characteristic 2D peak pattern are displayed in Fig. 7.7, and the corresponding pathways are enumerated in Fig. 7.A1. The peak pattern has similarities to the bilinear coupling result, with high-amplitude ESA peaks iii' and iv' near peaks iii and iv. Though, peaks i' and ii' are lower in amplitude and the detection-frequency ordering of peaks i/i' is flipped compared to Fig. 7.5. While this is a better agreement with the experiment compared to bilinear coupling, the iv/iv' ordering is still incorrect. Changing the sign of the high-frequency mode anharmonicity parameter χ from positive to negative (Fig. 7.8) flips the iii/iii' and iv/iv' ordering simultaneously. So, a high-amplitude ESA peak appears between either ii and iv or between i and iii (where none is observed in the experiment) for all combinations of the model parameters. In addition, the

amplitudes of iii' and iv' are always too large and spaced too closely to peaks iii and iv'. Therefore, the Fermi resonance model does not reproduce the peak ordering or relative amplitudes observed in the 2D IR experiment.

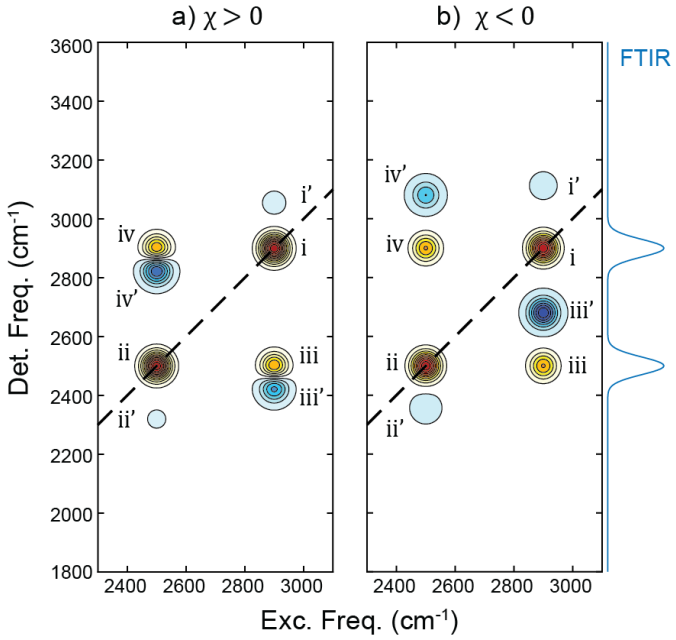

Figure 7.8: Influence of anharmonicity parameters on Fermi resonance model. (a) $\chi > 0$, (b) $\chi < 0$. The model FTIR spectrum is unaffected by the anharmonicity. Model parameters are listed in Table 7.2.

Table 7.2: Model parameters used in Figure 7.8

Figure	ω_1 (cm^{-1})	ω_2 (cm^{-1})	Δ (cm^{-1})	χ (cm^{-1})
a)	2700	1350	400	100
b)	2700	1350	400	-250

7.5.4. Displaced harmonic oscillator model

The models considered so far accounted for coupling between a high-frequency vibration to a second vibration at either comparable or ~1/2 the vibrational frequency. In principle, the

higher-frequency peak could also arise from the combination band with a much lower frequency vibration with frequency similar to the ~350 cm^{-1} splitting of the bands. To model this possibility, we took the linear approximation of Franck-Condon coupling, referred to as the displaced harmonic oscillator (DHO).[48,51] In this model, each level of the higher-frequency vibration is split into sub-bands corresponding to the levels of the lower-frequency vibration, which is modeled as a harmonic oscillator. In the context of the hydrated zeolite system, the higher frequency vibration is the bridging O-H stretch, coupled with a lower-frequency vibration such as O-O stretching. While a model like this is typically used to interpret vibronic coupling, the result is included in this context to gain some intuition about the patterns that might arise from combination bands with a lower-frequency vibration.

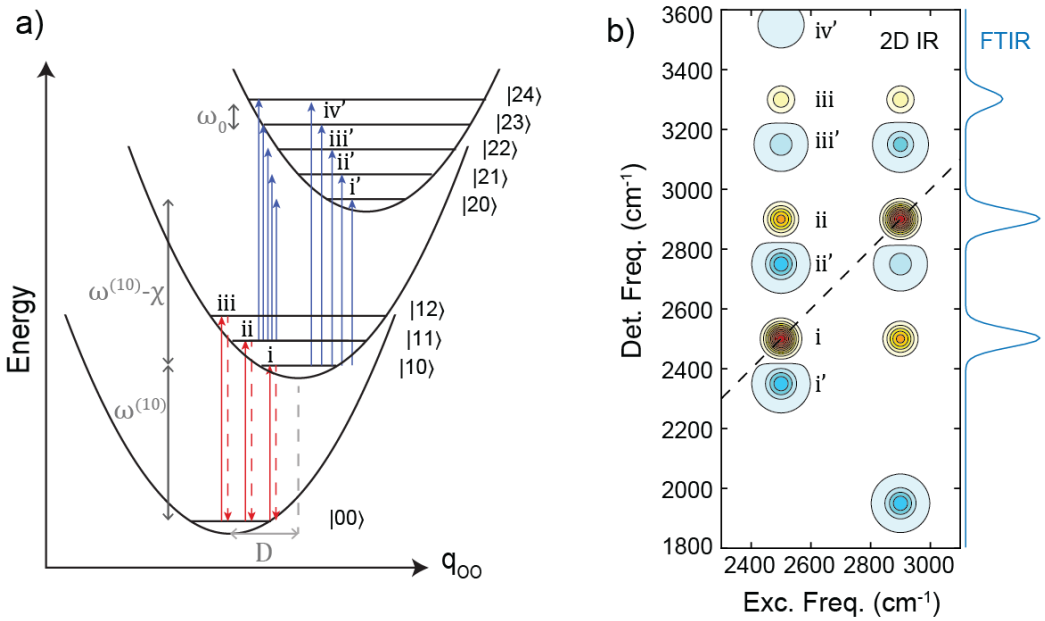

Figure 7.9: Displaced harmonic oscillator model. (a) Energy level diagram labeling mixed states and transitions. (b) Characteristic stick FTIR and 2D IR spectra. Since additional peaks are present, only peaks excited at $\omega_{00}^{(10)}$ are labeled and the labeling convention is different from the other models. Model parameters used in (b) are listed in Table 7.3a.

In this model, we considered three levels of the high-frequency vibration with transition frequencies $\omega^{(10)}$ and $\omega^{(21)} = \omega^{(10)} - \chi$. Each level is split into sub-levels with spacing ω_0, the frequency of the lower-frequency vibration. Treating that vibration as a harmonic oscillator, the sub-bands are all split by the same value ω_0. Coupling is captured by the Huang-Rhys factor *D*. Considering transitions from |0,n⟩ to |1,m⟩, where the first index represents the high-frequency vibration, transition frequencies are given by Eq. (7.8).

$$\omega_{mn}^{(10)} = \omega^{(10)} + (m-n)\omega_0 \tag{7.8}$$

Upper indices correspond to the high-frequency vibration and lower indices correspond to the low-frequency vibration. Assuming the system starts in the ground state, then $n = 0$ in equation (7.8). For transitions from |1,n⟩ to |2,m⟩, frequencies take the same form replacing $\omega^{(21)}$ for $\omega^{(10)}$.

$$\omega_{mn}^{(21)} = \omega^{(21)} + (m-n)\omega_0 \tag{7.9}$$

Under the Franck-Condon approximation the transition dipole moment depends only on the high-frequency vibration, though the amplitude depends on wavefunction overlap between states. If the high-frequency transition dipole moments are $\mu^{(10)}$ and $\mu^{(21)}$, then vibronic transition dipole matrix elements are given for transitions from |0,n⟩ to |1,m⟩.

$$\langle 1m | M | 0n \rangle = \mu^{(10)} \langle m | n \rangle \tag{7.10}$$

For transitions from |1,n⟩ to |2,m⟩ the matrix elements are:

$$\langle 2m | M | 1n \rangle = \mu^{(21)} \langle m | n \rangle \tag{7.11}$$

In general, the wavefunction overlap ⟨m|n⟩ can be computed[52] using associated Laguerre polynomials $L_j^k(x)$.[53]

$$\langle m \mid n \rangle = \begin{cases} \sqrt{\frac{m!}{n!}} D^{(n-m)/2} L_m^{\,n-m}(D^{1/2}) e^{-D}, & n > m \\ \sqrt{\frac{n!}{m!}} D^{(m-n)/2} L_n^{\,m-n}(D^{1/2}) e^{-D}, & m > n \end{cases} \tag{7.12}$$

In the case of $n = 0$ the overlap reduces to the Poisson distribution.

$$|\langle m \mid 0 \rangle|^2 = \frac{D^m e^{-D}}{m!} \tag{7.13}$$

Transition frequencies were calculated using Eqs. (7.8) and (7.9). Transition dipole moments were calculated using Eqs. (7.10) – (7.12), and relative amplitudes are constructed for each 2D feature from the corresponding Liouville pathways, enumerated in Fig. 7A.2. The model parameters are ($\omega^{(10)}$, χ, ω_0, D). We assumed D is the same between all higher-frequency states, and that $\mu^{(21)} = \sqrt{2}\mu^{(10)}$ which simplifies the relative transition amplitudes, but does not change the frequency ordering of the peaks.

The resulting transitions and characteristic 2D peak pattern are displayed in Fig. 7.9. There is a progression of positive peaks extending to higher detection frequencies with equal spacing at ω_0 (set to 400 cm^{-1}). The progression of negative ESA peaks is also equally spaced from each other by ω_0, and shifted relative to the positive peaks by χ. Changing the sign of the anharmonicity shifts all ESA features simultaneously, shown in Fig. 7.10. The model parameters are reported in Table 7.3. The 2D peak pattern clearly does not match the experiment, with ESA features falling between consecutive positive peaks and displaying multiple features at higher detection frequencies which are not observed in the experiment. The amplitudes of higher-frequency bands in the vibrational progression could be reduced by decreasing the Huang-Rhys factor, but this would also decrease the relative amplitude of the combination band at 2900 cm^{-1}.

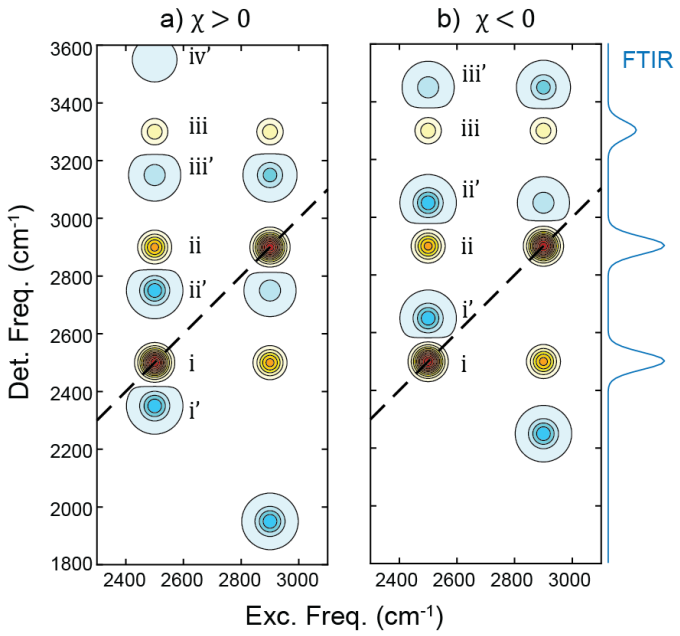

Figure 7.10: Influence of anharmonicity parameter on DHO model. (a) (a) $\chi > 0$, (b) $\chi < 0$. The model FTIR spectrum is unaffected by the anharmonicity. Model parameters are recorded in Table 7.3.

Table 7.3: Model parameters used in Figure 7.10

Figure	$\omega^{(10)}$ (cm^{-1})	ω_0 (cm^{-1})	D	χ (cm^{-1})
a)	2500	400	1	150
b)	2500	400	1	-150

7.5.5. H-bond double well potential with tunneling

In the three models considered thus far, the splitting between doublet bands was the result of coupling between two vibrations. Alternatively, the two bands of the doublet could also arise from transitions on a highly-anharmonic double-well potential of a single vibration.[29] In this case, it is necessary to consider the shape of the potential in more detail. We modeled the potential as a quartic function in the vibrational coordinate *q*:

$$V(q) = \frac{1}{24} v_4 q^4 + \frac{1}{2} v_2 q^2 + v_1 q \tag{7.14}$$

In this model, confinement from steep potential walls is introduced by the quartic term v_4, the barrier between the two local minima arises from the (negative) harmonic term v_2, and the linear term v_1 introduces asymmetry between the wells of the potential. Therefore, the quartic function can be considered the lowest-order expansion of an asymmetric double-well surface in one dimension. In the context of the hydrated zeolite system, the vibrational coordinate of the PES corresponds to the vibrational eigenstate observed in the experiment, which could involve several nuclear motions. Presumably, the largest contribution to that eigenstate is the normal-mode bridging O-H stretch vibration, but it could also include mixing with other normal modes such as O-H-O bending. Such mixing has been reported in other strong H-bonded systems; for example, several broad features in the IR spectrum of the aqueous proton have significantly mixed stretch and bend character.[33,54]

Transition frequencies and amplitudes were calculated on the model potential using the discrete variable representation (DVR).[55] Transition frequencies were calculated from differences between energy eigenstates, and relative transition dipole moments as $\mu_{ba} \propto \langle b | q | a \rangle$. Together with Eq. (7.2), this returned a set of 2D peak frequencies and amplitudes from the set of three model parameters $\{v_1, v_2, v_4\}$; pathways are listed in Fig. 7A.3. For a potential with sufficiently high barrier, the first two excited states $|1\rangle$ and $|2\rangle$ can become close together in energy, leading to two closely-spaced transitions at ω_{10} and ω_{20} separated by only a few hundred wavenumbers. While the 0-2 overtone transition is forbidden under harmonic selection rules, it can have a substantial transition dipole intensity on this highly-anharmonic potential – even exceeding the intensity of the fundamental transition for some configurations of the potential.

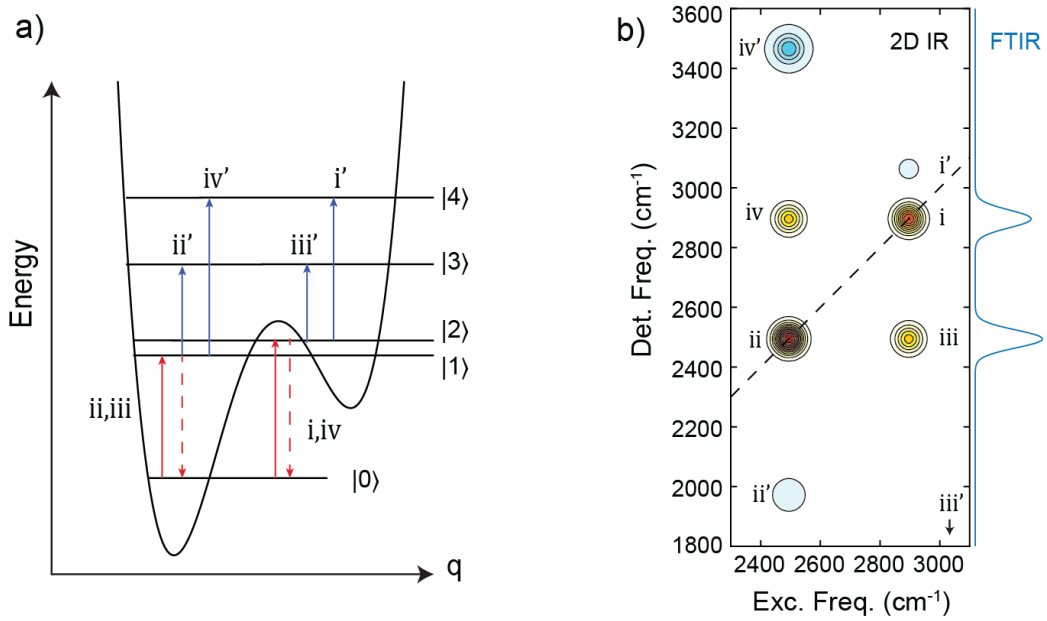

Figure 7.11: H-bond potential model. (a) Energy level diagram labeling mixed states and transitions between them. (b) Characteristic stick FTIR and 2D IR spectra. Model parameters are listed in Table 7.4a.

Figure 7.11b displays the calculated 2D peak pattern for the combination of $\{\nu_1, \nu_2, \nu_4\}$ chosen to best match the peak frequencies observed in the experiment. The positive 4-peak pattern i-iv is reproduced, with similar amplitudes for the diagonal peaks labeled i and ii. No ESA peaks appear between either i & iii or ii & iv. Of the ESA peaks which fall in the experimental frequency range, peak iv' is the most intense, while peaks i' and ii' have relatively low amplitudes. Furthermore, the splitting between peaks ii/ii', iii/iii', and iv/iv' are all large, several hundreds of wavenumbers. Given the relative simplicity of this one-dimensional model, this is a striking agreement with the experimental spectrum in Fig. 7.2, reproducing several trends in relative frequencies and amplitudes that were not captured by the other models considered.

How sensitive is this result to the exact shape of the potential? Starting with the parameter values in Fig. 7.11b and holding all but one parameter constant, Figs. 7.12 – 7.14 show the effect

of varying v_1, v_2, or v_4 respectively. These figures show the trends for modest deviations from the optimized values which retain the qualitative shape of the PES.

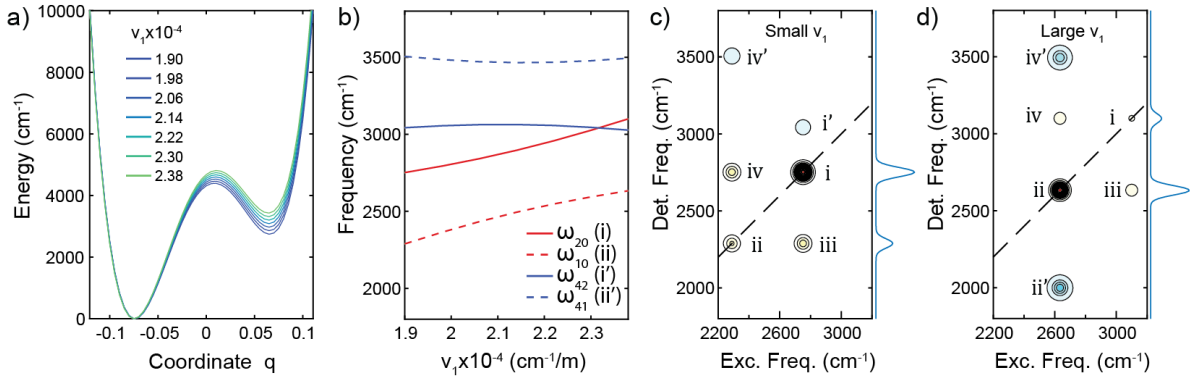

Figure 7.12: Influence of the linear asymmetry parameter v_1 on the PES model. (a) Potential energy surface, and (b) selected transition frequencies are plotted as a function of v_1. Stick FTIR and 2D IR spectra are plotted at the (c) smallest and (d) largest values of v_1 shown in part (a). Parameters are recorded in Table 7.4.

Varying the linear term (Fig. 7.12) changes the asymmetry between the two local minima of the PES. With increasing asymmetry, ω_{10} and ω_{20} blue-shift as the energies of states $|1\rangle$ and $|2\rangle$ increase. The splitting between ω_{10} and ω_{20} changes only slightly, so in the stick 2D spectrum shifts in v_1 cause the positive 4-peak pattern to translate along the diagonal. The excited-state frequencies ω_{41} and ω_{42} are approximately constant, since the higher-lying $|4\rangle$ state is less perturbed by variations in the well depth. The relative amplitudes of peaks i and ii vary more dramatically with asymmetry, where peak ii is more intense for higher asymmetry and peak i is more intense for lower asymmetry.

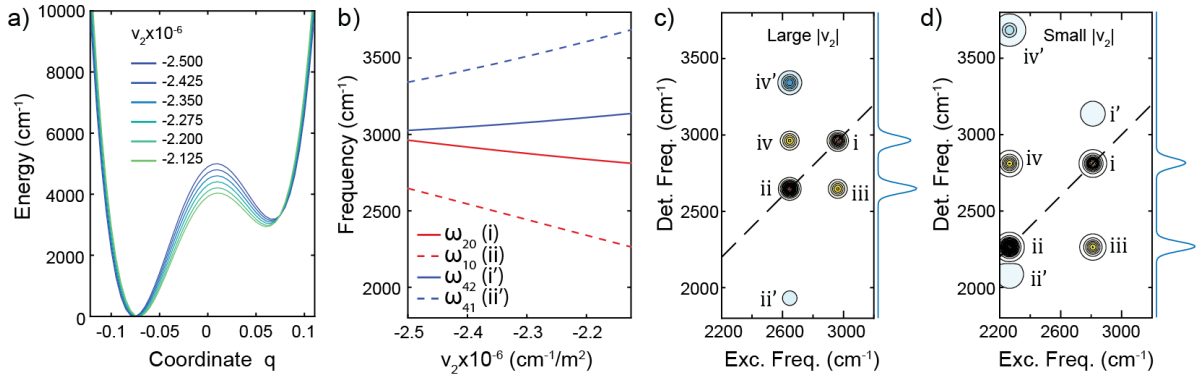

Figure 7.13: Influence of the harmonic barrier parameter v_2 on the PES model. (a) Potential energy surface, and (b) selected transition frequencies are plotted as a function of v_2. Stick FTIR and 2D IR spectra are plotted at the (c) largest and (d) smallest values of $|v_2|$ shown in part (a). Parameters are recorded in Table 7.4.

Varying the harmonic term (Fig. 7.13) changes the barrier between the two local minima of the potential. With decreasing barrier (decreasing $|v_2|$), ω_{10} and ω_{20} both decrease and the splitting between them increases. Excited state frequencies ω_{41} and ω_{42} increase with decreasing barrier, causing peaks ii' and iv' to move further from ii and iv. The relative peaks amplitudes depend only weakly on this parameter.

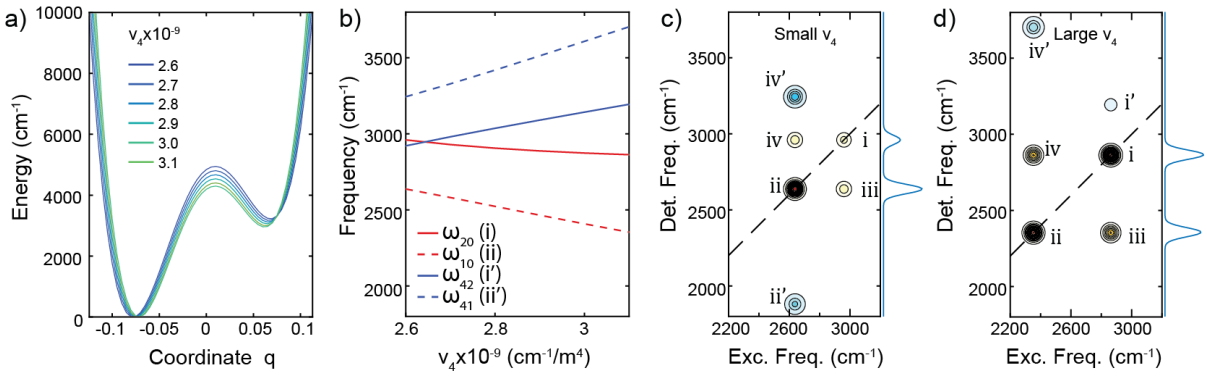

Figure 7.14: Influence of the quartic confinement parameter v_4 on the PES model. (a) Potential energy surface, and (b) selected transition frequencies are plotted as a function of v_4. Stick FTIR and 2D IR spectra are plotted at the (c) smallest and (d) largest values of v_4 shown in part (a). Parameters are recorded in Table 7.4.

Varying the quartic term (Fig. 7.14) changes the confinement of the potential. Increasing the confinement term also decreases the effective barrier (the height of the local maximum near $q = 0$) even though v_2 is held constant. For this reason, the frequency trends with increasing v_4 are similar to the trends with decreasing $|v_2|$: both ω_{10} and ω_{20} decrease but the splitting between them increases. Notably, the relative peak amplitudes depend more strongly on confinement than barrier over the range considered, with larger relative amplitude in peak ii at smaller values of v_4. Table 7.4 shows the model parameters used in the Figures displaying PES model results. Values which differ from the optimized parameters are marked in blue.

Table 7.4: Model parameters used in Figures 7.11 – 7.14

Figure	v_1 x10^{-4} (cm^{-1})	v_2 x10^{-6} (cm^{-1})	v_4 x10^{-9} (cm^{-1})
7.11 b)	2.15	-2.35	2.85
7.12 c)	1.9	-2.35	2.85
7.12 d)	2.38	-2.35	2.85
7.13 c)	2.15	-2.5	2.85
7.13 d)	2.15	-2.125	2.85
7.14 c)	2.15	-2.35	2.6
7.14 d)	2.15	-2.35	3.1

The modeling presented here does not include any treatment of dynamics, and therefore cannot capture the lineshapes of 2D IR features. However, the frequency and amplitude trends with varying potential parameters shown in Figs. 7.12-7.14 provide a starting point for considering the contributions of inhomogeneous broadening. In particular, the two experimental features with the most notable lineshapes are peaks I and IV' (Fig. 7.2). Peak I is elongated along the diagonal, extending to higher frequencies than the peak maximum. Figures 7.12-7.14 show that variations

in all three PES parameters can shift peak i to higher frequencies, but that increasing v_1 or decreasing v_4 also cause the relative amplitude to decrease substantially. Therefore, a distribution of barrier heights, v_2, is the most likely contribution to the inhomogeneous broadening of peak I.

In the case of peak IV', there is substantial broadening along the detection frequency axis. Figure 7.12 shows that the corresponding frequency, ω_{41}, does not depend strongly on the asymmetry parameter. On the other hand, figures 7.13 and 7.14 show that variations in either barrier or confinement can lead to a distribution in the detection frequency of peak iv'. So, broadening from a distribution of barrier or confinement parameters could account in part for the shape of peak IV' in the experimental 2D IR spectrum.

In contrast to the other models considered, certain configurations of the H-bonding potential model can reproduce the peak ordering and relative amplitudes observed in the experimental 2D IR spectrum. Figures 7.12-7.14 show that basic peak pattern is preserved over modest variations in model parameters, with shifts in frequencies that may be consistent with experimental line broadening. Therefore, the H-bond tunneling potential provides a plausible explanation for the origin of the broad doublet IR feature, while the other models considered do not.

7.6. Conclusions

The origin of the broad doublet feature in the IR spectrum of a single water molecule adsorbed at the Brønsted acid site of acidic zeolite has been a longstanding question, and is most often interpreted as splitting due to stretch-bend Fermi resonance. We report the 2D IR spectrum of 1 equiv. H_2O in HZSM-5, which displays a distinct pattern of excited state absorption features with relatively low intensity relative to bleaching and stimulated emission peaks. Fermi resonance

coupling is unable to reproduce the experimental pattern of ESA frequencies and relative amplitudes, showing that this interpretation does not describe the origin of the doublet feature. We propose an alternative model of a strongly H-bonded potential between zeolite and adsorbed water, which has an asymmetric double-well shape and tunneling in the first two vibrationally excited states. In this framework, the two doublet features in the linear IR spectrum arise from the fundamental and overtone transitions, which both have large transition amplitude on the highly-anharmonic potential energy surface. We show that this model can reproduce the relative peak frequencies and amplitudes observed in the 2D IR experiment.

Additionally, the polarization dependence of 2D IR features and the timescale of vibrational relaxation – measured with transient absorption spectroscopy – are reported. These measurements are consistent with the tunneling potential interpretation, but do not necessarily provide a means to distinguish between proposed models for the doublet assignment. The 2D IR spectrum was also used to assign the high-frequency O-H stretch vibrations of adsorbed water. Based on measured transition dipole angles, the cross-peak anisotropy values suggest that the bands at 3550 cm^{-1} and 3700 cm^{-1} arise predominantly from local-mode O-H stretch vibrations of adsorbed water, where the lower-frequency band is weakly coordinated with the zeolite framework.

7.7. References

(1) Taarning, E.; Osmundsen, C. M.; Yang, X.; Voss, B.; Andersen, S. I.; Christensen, C. H. Zeolite-Catalyzed Biomass Conversion to Fuels and Chemicals. *Energy Environ. Sci.* **2011**, *4*, 793–804. https://doi.org/10.1039/c004518g.

(2) Mardiana, S.; Azhari, N. J.; Ilmi, T.; Kadja, G. T. M. Hierarchical Zeolite for Biomass Conversion to Biofuel: A Review. *Fuel* **2022**, *309*, 122119. https://doi.org/10.1016/J.FUEL.2021.122119.

(3) Ennaert, T.; Van Aelst, J.; Dijkmans, J.; De Clercq, R.; Schutyser, W.; Dusselier, M.; Verboekend, D.; Sels, B. F. Potential and Challenges of Zeolite Chemistry in the Catalytic Conversion of Biomass. *Chem. Soc. Rev.* **2016**, *45* (3), 584–611. https://doi.org/10.1039/c5cs00859j.

(4) Stanciakova, K.; Weckhuysen, B. M. Water–Active Site Interactions in Zeolites and Their Relevance in Catalysis. *Trends Chem.* **2021**, *3* (6), 456–468. https://doi.org/10.1016/J.TRECHM.2021.03.004.

(5) Eckstein, S.; Hintermeier, P. H.; Zhao, R.; Baráth, E.; Shi, H.; Liu, Y.; Lercher, J. A. Influence of Hydronium Ions in Zeolites on Sorption. *Angew. Chemie - Int. Ed.* **2019**, *58* (11), 3450–3455. https://doi.org/10.1002/anie.201812184.

(6) Mei, D.; Lercher, J. A. Mechanistic Insights into Aqueous Phase Propanol Dehydration in H-ZSM-5 Zeolite. *AIChE J.* **2017**, *63* (1), 172–184. https://doi.org/10.1002/aic.15517.

(7) Mei, D.; Lercher, J. A. Effects of Local Water Concentrations on Cyclohexanol Dehydration in H-BEA Zeolites. *J. Phys. Chem. C* **2019**, *123* (41), 25255–25266. https://doi.org/10.1021/acs.jpcc.9b07738.

(8) Zhi, Y.; Shi, H.; Mu, L.; Liu, Y.; Mei, D.; Camaioni, D. M.; Lercher, J. A. Dehydration Pathways of 1-Propanol on HZSM-5 in the Presence and Absence of Water. *J. Am. Chem. Soc.* **2015**, *137* (50), 15781–15794. https://doi.org/10.1021/jacs.5b09107.

(9) Wang, Q.; Fan, H.; Wu, S.; Zhang, Z.; Zhang, P.; Han, B. Water as an Additive to Enhance the Ring Opening of Naphthalene. *Green Chem.* **2012**, *14* (4), 1152–1158. https://doi.org/10.1039/c2gc16554f.

(10) Chen, K.; Damron, J.; Pearson, C.; Resasco, D.; Zhang, L.; White, J. L. Zeolite Catalysis: Water Can Dramatically Increase or Suppress Alkane C-H Bond Activation. *ACS Catal.* **2014**, *4* (9), 3039–3044. https://doi.org/10.1021/cs500858d.

(11) Li, G.; Wang, B.; Resasco, D. E. Water-Mediated Heterogeneously Catalyzed Reactions. *ACS Catal.* **2020**, *10* (2), 1294–1309. https://doi.org/10.1021/acscatal.9b04637.

(12) Jentys, A.; Warecka, G.; Derewinski, M.; Lercher, J. A. Adsorption of Water on ZSM5 Zeolites. *J. Phys. Chem.* **1989**, *93* (12), 4837–4843. https://doi.org/10.1021/j100349a032.

(13) Pelmenschikov, A. G.; Van Santen, R. A. Water Adsorption on Zeolites: Ab-Initio Interpretation of IR Data. *J. Phys. Chem.* **1993**, *97* (41), 10678–10680. https://doi.org/10.1021/j100143a025.

(14) Wang, M.; Jaegers, N. R.; Lee, M. S.; Wan, C.; Hu, J. Z.; Shi, H.; Mei, D.; Burton, S. D.; Camaioni, D. M.; Gutiérrez, O. Y.; Glezakou, V. A.; Rousseau, R.; Wang, Y.; Lercher, J.

A. Genesis and Stability of Hydronium Ions in Zeolite Channels. *J. Am. Chem. Soc.* **2019**, *141* (8), 3444–3455. https://doi.org/10.1021/jacs.8b07969.

(15) Bordiga, S.; Lamberti, C.; Bonino, F.; Travert, A.; Thibault-Starzyk, F. Probing Zeolites by Vibrational Spectroscopies. *Chem. Soc. Rev.* **2015**, *44* (20), 7262–7341. https://doi.org/10.1039/c5cs00396b.

(16) Pelmenschikov, A. G.; van Wolput, J. H. M. C.; Jaenchen, J.; van Santen, R. A. (A,B,C) Triplet of Infrared OH Bands of Zeolitic H-Complexes. *J. Phys. Chem.* **1995**, *99* (11), 3612–3617. https://doi.org/10.1021/j100011a031.

(17) Krossner, M.; Sauer, J. Interaction of Water with Brønsted Acidic Sites of Zeolite Catalysts. Ab Initio Study of 1:1 and 2:1 Surface Complexes. *J. Phys. Chem.* **1996**, *100* (15), 6199–6211. https://doi.org/10.1021/jp952775d.

(18) Zecchina, A.; Geobaldo, F.; Spoto, G.; Bordiga, S.; Ricchiardi, G.; Buzzoni, R.; Petrini, G. FTIR Investigation of the Formation of Neutral and Ionic Hydrogen-Bonded Complexes by Interaction of H-ZSM-5 and H-Mordenite with CH3CN and H2O: Comparison with the H-NAFION Superacidic System. *J. Phys. Chem.* **1996**, *100* (41), 16584–16599. https://doi.org/10.1021/jp960433h.

(19) Zecchina, A.; Bordiga, S.; Spoto, G.; Scarano, D.; Spanò, G.; Geobaldo, F. IR Spectroscopy of Neutral and Ionic Hydrogen-Bonded Complexes Formed upon Interaction of CH3OH, C2H5OH, (CH3)2O, (C2H5)2O and C4H8O with H-Y, H-ZSM-5 and H-Mordenite: Comparison with Analogous Adducts Formed on the H-Nafion Superacidic Membrane. *J. Chem. Soc. - Faraday Trans.* **1996**, *92* (23), 4863–4875. https://doi.org/10.1039/ft9969204863.

(20) Bordiga, S.; Regli, L.; Lamberti, C.; Zecchina, A.; Bjorgen, M.; Lillerud, K. P. FTIR Adsorption Studies of H2O and CH3OH in the Isostructural H-SSZ-13 and H-SAPO-34: Formation of H-Bonded Adducts and Protonated Clusters. *J. Phys. Chem. B* **2005**, *109*, 7724–7732. https://doi.org/10.1021/jp04432b.

(21) Mihaleva, V. V.; Van Santen, R. A.; Jansen, A. P. J. Quantum Chemical Calculation of Infrared Spectra of Acidic Groups in Chabazite in the Presence of Water. *J. Chem. Phys.* **2004**, *120* (19), 9212–9221. https://doi.org/10.1063/1.1709896.

(22) Vjunov, A.; Wang, M.; Govind, N.; Huthwelker, T.; Shi, H.; Mei, D.; Fulton, J. L.; Lercher, J. A. Tracking the Chemical Transformations at the Brønsted Acid Site upon Water-Induced Deprotonation in a Zeolite Pore. *Chem. Mater.* **2017**, *29* (21), 9030–9042. https://doi.org/10.1021/acs.chemmater.7b02133.

(23) Grifoni, E.; Piccini, G. M.; Lercher, J. A.; Glezakou, V. A.; Rousseau, R.; Parrinello, M.

Confinement Effects and Acid Strength in Zeolites. *Nat. Commun.* **2021**, *12*. https://doi.org/10.1038/s41467-021-22936-0.

(24) Hadzi, D. Infrared Spectra of Strongly Hydrogen-Bonded Systems. *Pure Appl. Chem.* **1965**, *11*, 435–453.

(25) Blinc, R.; Hadži, D. The Infra-Red Spectra of Some Ferroelectric Compounds with Short Hydrogen Bonds. *Mol. Phys.* **1958**, *1* (4), 391–405. https://doi.org/10.1080/00268975800100461.

(26) Huang, Q. R.; Shishido, R.; Lin, C. K.; Tsai, C. W.; Tan, J. A.; Fujii, A.; Kuo, J. L. Strong Fermi Resonance Associated with Proton Motions Revealed by Vibrational Spectra of Asymmetric Proton-Bound Dimers. *Angew. Chemie - Int. Ed.* **2021**, *60* (4), 1936–1941. https://doi.org/10.1002/anie.202012665.

(27) Van Hoozen, B. L.; Petersen, P. B. Origin of the 900 Cm-1 Broad Double-Hump OH Vibrational Feature of Strongly Hydrogen-Bonded Carboxylic Acids. *J. Chem. Phys.* **2015**, *142* (10). https://doi.org/10.1063/1.4914147.

(28) Van Hoozen, B. L.; Petersen, P. B. Vibrational Tug-of-War: The PKA Dependence of the Broad Vibrational Features of Strongly Hydrogen-Bonded Carboxylic Acids. *J. Chem. Phys.* **2018**, *148* (13). https://doi.org/10.1063/1.5026675.

(29) Somorjai, R. L.; Horning, D. F. Double-Minimum Potentials in Hydrogen-Bonded Solids. *J. Chem. Phys.* **1962**, *36*, 1980–1987. https://doi.org/https://doi.org/10.1063/1.1732814.

(30) Parker, L. M.; Bibby, D. M.; Burns, G. R. An Infrared Study of H2O and D2O on HZSM-5 and DZSM-5. *Zeolites* **1993**, *13* (2), 107–112. https://doi.org/10.1016/0144-2449(93)90069-F.

(31) Hack, J. H.; Ma, X.; Chen, Y.; Dombrowski, J.; Lewis, N. H. C.; Kung, H. H.; Voth, G. A.; Tokmakoff, A. Proton Dissociation and Delocalization under Stepwise Hydration of Zeolite HZSM-5. *Prep.*

(32) Dereka, B.; Yu, Q.; Lewis, N. H. C.; Carpenter, W. B.; Bowman, J. M.; Tokmakoff, A. Crossover from Hydrogen to Chemical Bonding. *Science* **2021**, *371* (6525), 160–164. https://doi.org/10.1126/science.abe1951.

(33) Yu, Q.; Carpenter, W. B.; Lewis, N. H. C.; Tokmakoff, A.; Bowman, J. M. High-Level VSCF/VCI Calculations Decode the Vibrational Spectrum of the Aqueous Proton. *J. Phys. Chem. B* **2019**, *123* (33), 7214–7224. https://doi.org/10.1021/acs.jpcb.9b05723.

(34) Fournier, J. A.; Carpenter, W. B.; Lewis, N. H. C.; Tokmakoff, A. Broadband 2D IR Spectroscopy Reveals Dominant Asymmetric H5O2+ Proton Hydration Structures in Acid

Solutions. *Nat. Chem.* **2018**, *10*, 932–937. https://doi.org/10.1038/s41557-018-0091-y.

(35) Carpenter, W. B.; Yu, Q.; Hack, J. H.; Dereka, B.; Bowman, J. M.; Tokmakoff, A. Decoding the 2D IR Spectrum of the Aqueous Proton with High-Level VSCF/VCI Calculations. *J. Chem. Phys.* **2020**, *153* (12), 124506. https://doi.org/10.1063/5.0020279.

(36) Yu, Q.; Bowman, J. M. How the Zundel (H5O2+) Potential Can Be Used to Predict the Proton Stretch and Bend Frequencies of Larger Protonated Water Clusters. *J. Phys. Chem. Lett.* **2016**, *7* (24), 5259–5265. https://doi.org/10.1021/acs.jpclett.6b02561.

(37) Hack, J. H.; Dombrowski, J. P.; Ma, X.; Chen, Y.; Lewis, N. H. C.; Carpenter, W. B.; Li, C.; Voth, G. A.; Kung, H. H.; Tokmakoff, A. Structural Characterization of Protonated Water Clusters Confined in HZSM-5 Zeolites. *J. Am. Chem. Soc.* **2021**, *143* (27), 10203–10213. https://doi.org/10.1021/jacs.1c03205.

(38) Janićijević, D.; Uskoković-Marković, S.; Ranković, D.; Milenković, M.; Jevremović, A.; Nedić Vasiljević, B.; Milojević-Rakić, M.; Bajuk-Bogdanović, D. Double Active BEA Zeolite/Silver Tungstophosphates – Antimicrobial Effects and Pesticide Removal. *Sci. Total Environ.* **2020**, *735*, 139530. https://doi.org/10.1016/j.scitotenv.2020.139530.

(39) Fecko, C. J.; Loparo, J. J.; Tokmakoff, A. Generation of 45 Femtosecond Pulses at 3 Mm with a KNbO3 Optical Parametric Amplifier. *Opt. Commun.* **2004**, *241*, 521–528. https://doi.org/10.1016/j.optcom.2004.07.038.

(40) Petersen, P. B.; Tokmakoff, A. Source for Ultrafast Continuum Infrared and Terahertz Radiation. *Opt. Lett.* **2010**, *35* (12), 1962. https://doi.org/10.1364/OL.35.001962.

(41) DeFlores, L. P.; Nicodemus, R. A.; Tokmakoff, A. Two-Dimensional Fourier Transform Spectroscopy in the Pump-Probe Geometry. *Opt. Lett.* **2007**, *32* (20), 2966. https://doi.org/10.1364/ol.32.002966.

(42) Bloem, R.; Garrett-Roe, S.; Strzalka, H.; Hamm, P.; Donaldson, P. Enhancing Signal Detection and Completely Eliminating Scattering Using Quasi-Phase-Cycling in 2D IR Experiments. *Opt. Express* **2010**, *18* (26), 1747–1756. https://doi.org/10.1364/OE.18.027067.

(43) Eaves, J. D.; Tokmakoff, A.; Geissler, P. L. Electric Field Fluctuations Drive Vibrational Dephasing in Water. *J. Phys. Chem. A* **2005**, *109* (42), 9424–9436. https://doi.org/10.1021/jp051364m.

(44) Hamm, P.; Zanni, M. *Concepts and Methods of 2D Infrared Spectroscopy*; Cambridge University Press: Cambridge, UK and New York, NY, USA, 2011.

(45) Kondo, J. N.; Iizuka, M.; Domen, K.; Wakabayashi, F. IR Study of H2O Adsorbed on H-

ZSM-5. *Langmuir* **1997**, *13* (4), 747–749. https://doi.org/10.1021/la9607565.

(46) Lock, A. J.; Bakker, H. J. Temperature Dependence of Vibrational Relaxation in Liquid H2O. *J. Chem. Phys.* **2002**, *117* (4), 1708–1713. https://doi.org/10.1063/1.1485966.

(47) De Marco, L.; Fournier, J. A.; Thämer, M.; Carpenter, W.; Tokmakoff, A. Anharmonic Exciton Dynamics and Energy Dissipation in Liquid Water from Two-Dimensional Infrared Spectroscopy. *J. Chem. Phys.* **2016**, *145* (9), 094501. https://doi.org/10.1063/1.4961752.

(48) Mukamel, S. *Principles of Nonlinear Optical Spectroscopy*; New York, 1995.

(49) Khalil, M.; Demirdöven, N.; Tokmakoff, A. Coherent 2D IR Spectroscopy: Molecular Structure and Dynamics in Solution. *J. Phys. Chem. A* **2003**, *107* (27), 5258–5279. https://doi.org/10.1021/jp0219247.

(50) Edler, J.; Hamm, P. Two-Dimensional Vibrational Spectroscopy of the Amide I Band of Crystalline Acetanilide: Fermi Resonance, Conformational Substates, or Vibrational Self-Trapping? *J. Chem. Phys.* **2003**, *119* (5), 2709–2715. https://doi.org/10.1063/1.1586694.

(51) Tokmakoff, A. *Time-Dependent Quantum Mechanics and Spectroscopy*. http://tdqms.uchicago.edu/.

(52) Palma, A.; Morales, J. Franck–Condon Factors and Ladder Operators. I. Harmonic Oscillator. *Int. J. Quantum Chem.* **1983**, *24* (17 S), 393–400. https://doi.org/10.1002/qua.560240843.

(53) Arfken, G. B.; Weber, H. J.; Harris, F. E. *Mathematical Methods for Physicists*; Elsevier, 2013.

(54) Biswas, R.; Carpenter, W.; Fournier, J. A.; Voth, G. A.; Tokmakoff, A. IR Spectral Assignments for the Hydrated Excess Proton in Liquid Water. *J. Chem. Phys.* **2017**, *146* (15). https://doi.org/10.1063/1.4980121.

(55) Colbert, D. T.; Miller, W. H. A Novel Discrete Variable Representation for Quantum Mechanical Reactive Scattering via the S-Matrix Kohn Method. *J. Chem. Phys.* **1992**, *96* (3), 1982–1991. https://doi.org/10.1063/1.462100.

Appendix 7A: Liouville space pathways for 2D IR models

In the model 2D IR spectra, peak amplitudes depend on the number of Liouville space pathways contributing at each combination of (ω_{Exc}, ω_{Det}), according to Eq. (7.2). This number can be counted by enumerating each pathway over a chosen set of basis states. In all cases, we assumed that the system began in the ground state since the first excited state energy is many times $k_B T$ at room temperature. For the bilinear coupling model (Fig. 7.5) and the Fermi resonance model (Fig. 7.7), the set of mixed states is {$|0\rangle$, $|1_1\rangle$, $|1_2\rangle$, $|2_1\rangle$, $|2_2\rangle$, $|2_3\rangle$}. The Liouville pathways between these states were enumerated under the selection rules that transitions can occur only between successive excitation manifolds. In other words, the selection rules for transitions from $|a_i\rangle$ to $|b_j\rangle$ is $b = a \pm 1$. Furthermore, transitions from $|1_1\rangle$ to $|2_3\rangle$ and from $|1_2\rangle$ to $|2_1\rangle$ were ignored because the transition amplitudes are very small. (This is because they are close to dipole-forbidden transitions like $|10\rangle$ to $|02\rangle$ in the basis of unmixed states in the bilinear coupling model). Coherence pathways were also ignored because the two doublet peaks were not simultaneously pumped in the 2D IR experiment. The resulting set of pathways are reported in Fig. 7A.1. Peaks labeled i-iv are positively signed, with GSB or GSB + SE pathways contributing. Peaks labeled i'-iv' are negatively signed from ESA pathways.

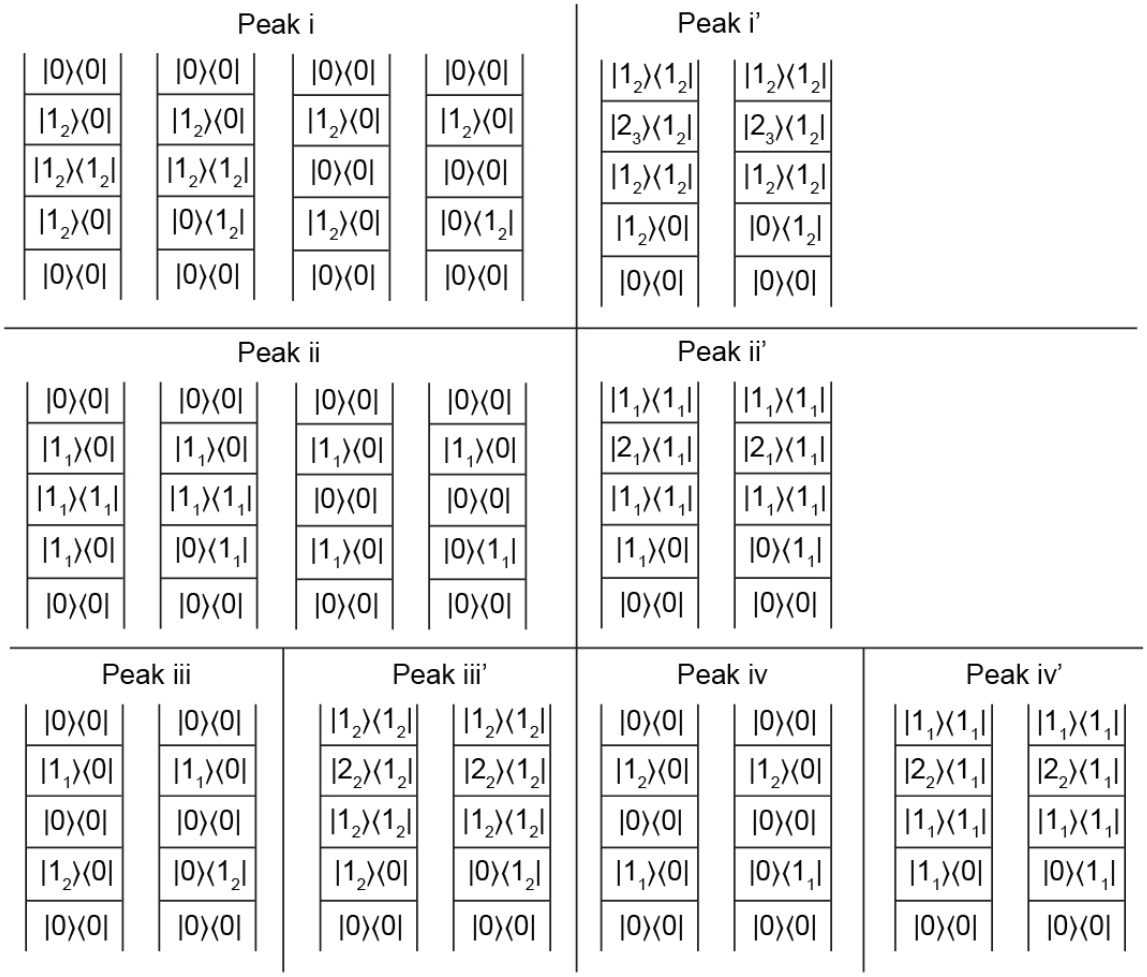

Figure 7A.1: Enumerated Liouville space pathways for the bilinear coupling and Fermi resonance models. The corresponding states and peaks are labeled in Figs. 7.5 and 7.7.

For the DHO model (Fig. 7.9), the structure of the Liouville space pathways is similar. But, transitions are allowed from $|0,n\rangle$ to $|1,m\rangle$ (or $|1,n\rangle$ to $|2,m\rangle$) for any n and m. This leads to the progression of peaks all spaced at ω_0. Harmonic selection rules are enforced by disallowing transitions from $|0,n\rangle$ to $|2,m\rangle$, or other transitions where the first index is not incremented by ± 1. Just like the result in Fig. 7A.1, the diagonal positive peaks have four contributing pathways (two ESA + two SE) and all other peaks have two pathways (two SE or two ESA).

The pathways for the labeled peaks in Fig. 7.9 (excited at $\omega_{00}^{(10)}$) are enumerated in Fig. 7A.2. Pathways for the other peaks can be constructed straightforwardly by replacing state |10⟩ with |11⟩ (i.e. excitation at $\omega_{10}^{(10)}$).

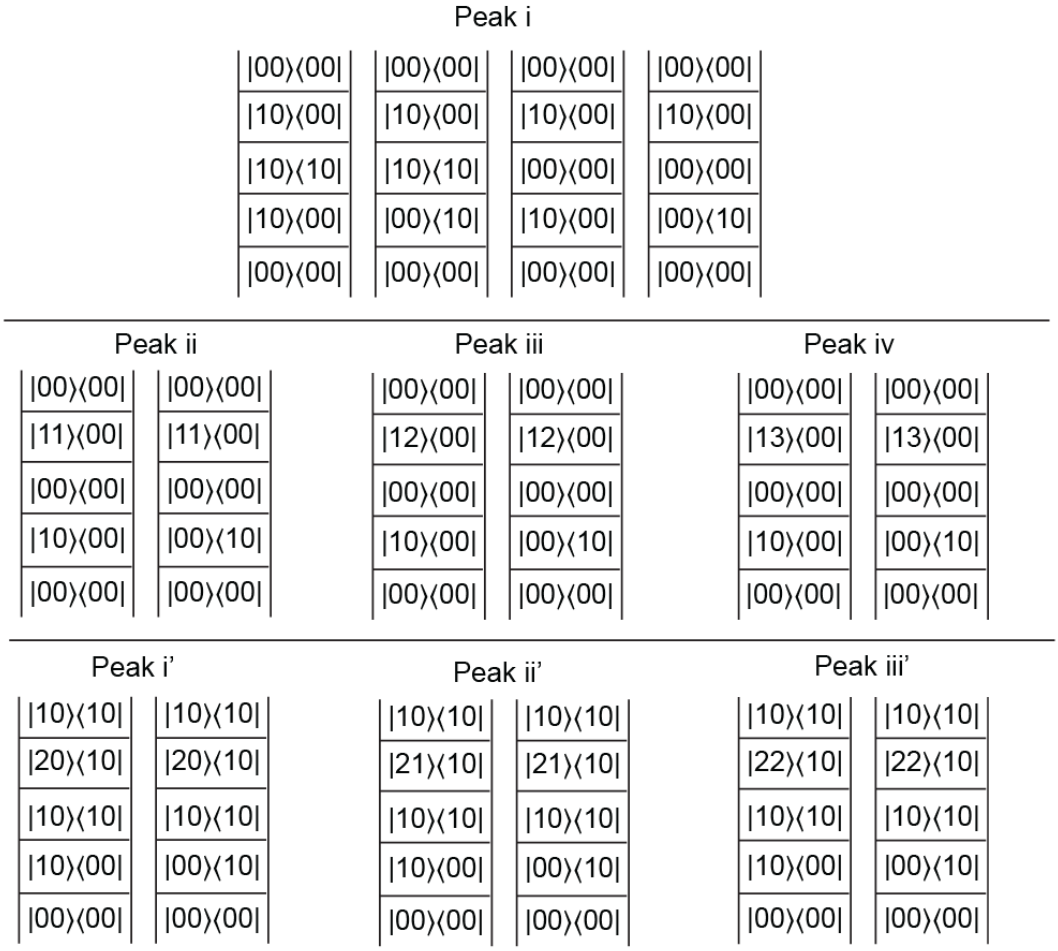

Figure 7A.2: Enumerated Liouville space pathways for the DHO model. The corresponding states and peaks are labeled in Fig. 7.9.

For the H-bond potential model (Fig. 7.11), the contributing pathways are enumerated in Fig. 7A.3. Only the first five states |0⟩-|4⟩ were included, since transitions involving higher-energy states fell outside of the experimental detection frequency range. Beginning in the ground state,

only excitations from $|0\rangle$ to $|1\rangle$ or $|2\rangle$ were considered, since other transitions fell outside of the experimental excitation frequency. While this model has only one vibration, there are still several possible pathways since no selection rules are enforced.

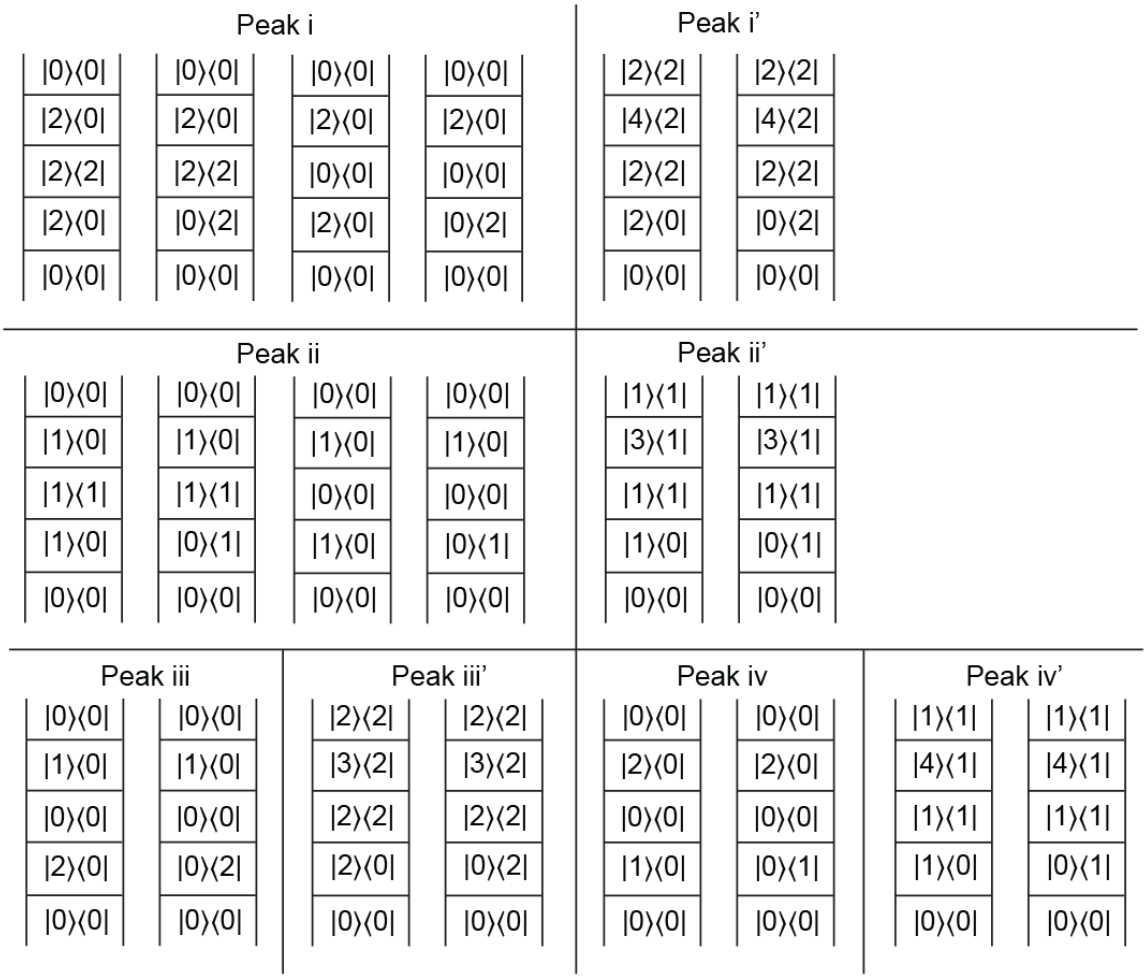

Figure 7A.3: Enumerated Liouville space pathways for the H-bonding potential model. The corresponding states and peaks are labeled in Fig. 7.11.